
Understanding Hysteresis Dynamics in Hybrid Organic-Inorganic Perovskite Solar Cells

Rana Yekani

260774491

Department of Mining and Materials Engineering,
McGill University



December 2023

A thesis submitted to McGill University in partial fulfillment of the
requirements for the degree of Doctor in Engineering in the Department of
Mining and Materials Engineering

© Rana Yekani 2023

Table of Contents

Table of Contents	i
List of Acronyms and Symbols.....	v
List of Figures.....	i
List of Tables.....	i
Abstract.....	i
Resume.....	iii
Acknowledgements.....	vi
Foreword.....	viii
Chapter 1: Introduction.....	1
1.1. Background on Perovskite Solar Cells.....	1
1.2. Overview of the Phenomenon of Hysteresis in PSCs.....	2
1.3. Thesis Objectives and Organization	2
1.4. References.....	4
Chapter 2: Literature Review.....	7
2.1. Fundamentals of Photovoltaic Energy Conversion.....	7
2.1.1. Absorption and Photoexcitation Processes	7
2.1.2. PV Metrics	9
2.1.3. Shockley-Queisser Limit	12
2.1.4. Non-Ideal Solar Cells.....	14
2.2. A Brief History of Solar Cell Development.....	16
2.3. Evolution of Perovskite Solar cells.....	20
2.3. Perovskite Crystal Structure	23
2.4. PSC Device Architecture	28
2.5. Peculiar Optoelectronic Properties of Halide Perovskites.....	30
2.6. Phenomenon of Hysteresis in PSCs.....	35

2.6.1. Parameters Affecting the Appearance of Hysteresis	36
2.6.2. Origin of Hysteresis	39
2.6.3. Strategies for Mitigating Hysteresis.....	46
2.7. Summary	53
2.8. References.....	53
Chapter 3: Methods.....	86
3.1. Assembly of PSCs.....	86
3.1.1. Preparation of the ETL.....	86
3.1.2. Preparation of the Perovskite Layer.....	89
3.1.3. Preparation of the HTL	91
3.1.4. Metal Contact.....	92
3.2. Characterization Techniques	92
3.2.1. J - V Curves and EIS Measurements.....	92
3.2.2. Space Charge Limited Current (SCLC).....	94
3.2.3. Conductivity Measurements	94
3.2.4 Scanning Electron Microscopy (SEM)	94
3.2.5. X-Ray Diffraction (XRD).....	95
3.2.6. External Quantum Efficiency (EQE).....	96
3.2.7. Photoluminescence (PL) and Time-Resolved Photoluminescence.....	98
3.2.8. Atomic Force Microscopy (AFM)	98
3.2.9. X-Ray Photoelectron Spectroscopy (XPS).....	98
3.2.10. Ultraviolet Photoelectron Spectroscopy (UPS)	98
3.3. Equipment.....	99
3.3.1. Shadow Mask.....	99
3.3.1. Testing Equipment	100

3.4. References.....	102
Chapter 4: Synergetic Interfacial Conductivity Modulation in Perovskite Solar Cells	103
4.1. Introduction.....	104
4.2. Experimental	106
4.3. Results and Discussion	109
4.4. Conclusion	122
4.5. Bridge.....	124
4.6. References.....	125
Chapter 5: Hysteresis Dynamics and Inductance in Perovskite Solar Cells.....	130
5.1. Introduction.....	131
5.2. Experimental	132
5.3. Results and Discussion	136
5.4. Conclusion	149
5.5. Bridge.....	150
5.6. References.....	151
Chapter 6: Controlling Photo-Induced Doping of Spiro-OMeTAD in Perovskite Solar Cells.....	157
6.1. Introduction.....	158
6.2. Experimental	160
6.3. Results and Discussion	163
6.4. Conclusion	181
6.5. References.....	182
Chapter 7: Global Discussion	189
7.1. Thesis Overview	189
7.2. References.....	200
Chapter 8: Synopsis	202

8.1. Global Conclusions.....	202
8.2. Contributions to the Original Knowledge.....	204
8.3. Future Research Direction	204
APPENDIXES: Supplementary Information for Chapters 4, 5 and 6.....	206
A.1. Supplementary Information- Chapter 4	206
A.2. Supplementary Information- Chapter 5	221
A.3. Supplementary Information- Chapter 6	229
A.4. References.....	243

List of Acronyms and Symbols

1D	One-Dimensional
2D	Two-Dimensional
3D	Three-Dimensional
4-TBP	4-Tert-Butylpyridine
AM	Air Mass
AR	Anatase-Rutile
A	Area
C	Capacitance
C_n	Auger Recombination Coefficient for Electrons
C_p	Auger Recombination Coefficient for Holes
c-Si	Crystalline Silicon
c-TiO ₂	Compact Titania
C_{LF}	Low Frequency Capacitance
C_{MF}	Mid Frequency Capacitance
C_{HF}	High Frequency Capacitance
C_s	Surface Capacitance
C_g	Geometrical Capacitance
c	speed of light
CIGS	Copper Indium Gallium Selenide
DI	De-Ionized
DMF	Dimethylformamide
DMSO	Dimethyl sulfoxide
D	Diffusion Coefficient
DFT	Density Functional Theory
DSSC	Dye-Sensitized Solar Cell
E_C	Conduction Band Energy
E_T	Phonon Energy
E_V	Valence Band Energy
E_F	Fermi Level Energy
E_G	Band Gap
EDS	Energy Dispersive X-ray Spectroscopy
EIS	Electrochemical Impedance Spectroscopy
EQE	External Quantum Efficiency
$E_{F,n}$	Fermi Level of Electrons
$E_{F,p}$	Fermi Level of Holes
ETL	Electron Transport Layer
E_{in}	Built-in Electric Field
e.m.f	Electromotive Force
FS	Forward Scan

FF	Fill Factor
FTO	Fluorine-Doped Tin Oxide
FF _{FS}	Fill Factor in Forward Scan
FF _{RS}	Fill Factor in Reverse Scan
FET	Field Effect Transistor
GGA	Generalized Gradient Approximation
HTL	Hole Transport Layer
\hbar	Planck's Constant
HI	Hysteresis Index
J-V	Current Density- Voltage
J _C	Capacitive Current
J _{SC}	Short-Circuit Current Density
J _{SC,SQ}	Short-Circuit Current Density in Shockley-Queisser Limit
J _{SS}	Steady State Current Density Sustained by the Solar Cell
J _{0,SQ}	Dark Recombination Current in Shockley-Queisser Limit
J _{inj}	Injection Current Density
J _e *	Modulated Electronic Current Density
J _e	Electronic Current Density
J _i	Ionic Current Density
J ₀	Reverse Saturation Current Density
K _B	Boltzmann Constant
k _{rad}	Coefficient of Radiative Recombination
LCAO	Linear Combination of Atomic Orbitals
LDA	Local Density Approximation
L	Thickness
LiTFSI	Lithium bis(trifluoromethanesulfonyl)imide
LED	Light Emitting Diode
MPP	Maximum Power Point
MAPI	Methylammonium Lead Iodide
m ₀	Free Electron Mass
m _e / m ₀	Effective Electron Mass
m _h / m ₀	Effective Hole Mass
n ₀	Equilibrium Charge Carrier Density
n	Free Electron Density
n _i	Intrinsic Charge Carrier Density
n _r	refractive index
<i>n</i>	Diode Ideality Factor
N _D	Defect Density
N _T	Trap Density
OPV	Organic Photovoltaics

PSC	Perovskite Solar Cell
PV	Photovoltaic
PCE	Power Conversion Efficiency
PL	Photoluminescence
P	Solar Cell Power Density
P_s	Incident Light Power Density
p	Free Hole Density
PTAA	Poly(triaryl amine), Poly[bis(4-phenyl)(2,4,6-trimethylphenyl)amine]
q	Unit Charge
R	Resistance
R_{LF}	Low Frequency Resistance
R_{MF}	Mid Frequency Resistance
R_{HF}	High Frequency Resistance
RA	Rutile-Anatase
R_{SRH}	Rate of Shockley-Read-Hall Recombination
R_{Surf}	Rate of Surface Recombination
R_L	Load Resistance
R_S	Series Resistance
R_{SH}	Shunt Resistance
R_{rad}	Rate of Radiative Recombination
r_A	Radius of the A-Site Cation
r_B	Radius of the B-Site Cation
r_X	Radius of the X-Site Cation
$r_{A, eff}$	Effective Radius of the A-Site Cation
$r_{X, eff}$	Effective Radius of the X-Site Cation
r_{mass}	Distance from the Molecular Center of Mass to the Furthest Non-Hydrogen Atom
r_{ion}	Ionic Radius of the Most Distant Atom
RS	Reverse Scan
S	Recombination Velocity
SQ	Shockley-Queisser
SRH	Shockley-Read-Hall
SCLC	Space Charge Limited Current Density
SECO	Secondary Electron Cut-Off
SEM	Scanning Electron Microscopy
SOC	Spin-Orbit Coupling
Spiro-OMeTAD	2,2',7,7'-Tetrakis[N,N-di(4-methoxyphenyl)amino]-9,9'-spirobifluorene
TCO	Transparent Conductive Oxide

T	Temperature
τ	Goldschmidt Tolerance Factor
TNR	Titania Nanorod
τ_{ave}	Average Lifetime
τ_p	Recombination Lifetime of Holes
τ_n	Recombination Lifetime of electrons
τ_{SRH}	Non-Radiative Recombination Lifetime
t_d	Voltage Settling Time
t_s	Current Sampling Time
TRPL	Time-Resolved Photoluminescence
TOPO	trioctylphosphine oxide
UPS	Ultraviolet Photoelectron Spectroscopy
UV-Vis	Ultraviolet-Visible
V_{in}	Built-in Potential
VBM	Valance Band Maximum
V	Voltage
V_{oc}	Open-Circuit Voltage
$V_{oc,SQ}$	Open-Circuit Current Density in Shockley-Queisser Limit
XRD	X-Ray Diffraction
W	Width of the Depletion Layer
ω	Radial Frequency
μ	Mobility
ϕ	Work Function
Φ_{sun}	Solar Spectrum
Φ_{bb}	Black Body Spectrum at the Solar Cell Temperature of T
α	Absorption Coefficient
μ_{oct}	Octahedral Factor
σ_T	Carrier Capture Cross-Section
ϵ	Dielectric Constant
ϵ_s	Static Limit of the Dielectric Constant
ϵ_∞	Optical Limit of the Dielectric Constant
σ	Conductivity

List of Figures

Figure 2.1. Schematic representation of excitation of an electron (a) into the conduction band (E_C) of a metal through absorption of a photon with energy $\hbar\omega$ and the subsequent loss of energy by releasing phonons of energy E_T , and (b) from valence band (E_V) into the conduction band of a semiconductor through absorption of a photon with energy $\hbar\omega$. E_F and E_G indicate Fermi energy and band gap energy, respectively.7

Figure 2.2: Comparison of the extra-terrestrial (AM 0) solar spectrum with standard terrestrial AM 1.5 in the case of both Global and Direct spectra.(5).....9

Figure 2.3: Illustration of a solar cell, under illumination, attached to a load through an external circuit.(6).....10

Figure 2.4: Current-voltage characteristics of a solar cell under illumination (light current) and dark (dark current). Based on the superposition approximation, the net current is obtained by shifting the bias-dependent dark current up by an amount equal to short-circuit current density. The sign convention is such that photocurrent is positive.(1) 11

Figure 2.5: Illustration of the equilibrium between optical charge carrier generation rate (G) and various recombination mechanisms at open-circuit.(4) 15

Figure 2.6: Equivalent circuit for a solar cell taking into account the effect of series resistance (R_S) as well as shunting resistance (R_{SH}).(1) 16

Figure 2.7: Schematic description of the setup employed by Edmond Becquerel which led to the first ever reported observation of photovoltaic effect.(29) 17

Figure 2.8: Schematic description of the setup employed by Adams and Dey in observing photogenerated current in an all-solid-state system for the first time.(29) 17

Figure 2.9: Schematic description of the first large-area ($\sim 30 \text{ cm}^2$) solar cell by Fritts in 1883, by pressing a thin selenium layer between gold and another metallic plate.(29) 18

Figure 2.10: The cubic perovskite crystal structure with ABX_3 formula, where A is a monovalent cation, B is a divalent cation and X is a halide.(74) 24

Figure 2.11: Formability of 3D lead (red) and tin (blue) halide perovskites as a function of A-site cation and halide anion radii. Solid and dashed lines mark the boundaries of the tolerance and octahedral factors, respectively. (42) 26

Figure 2.12: Schematics of the three most commonly utilized PSC architectures, comprising planar regular (n-i-p), mesoporous (n-i-p), and planar inverted (p-i-n) architectures.(133).....29

Figure 2.13: Schematics of some of the less-frequently utilized PSC architectures including ETL-free, HTL-free and HTL-free with a carbon electrode. (134).....30

Figure 2.14: The divergence between J-V curves in RS and FS, known as hysteresis, in MAPbI₃-based PSCs as a function of (a) scan rate, and (b) illumination intensity during measurements.(178)35

Figure 2.15 :Schematic comparison of static dielectric constant (ϵ_s) and high frequency dielectric constant (ϵ_∞) for orthorhombic and tetragonal phases of MAPbI₃. Contributions to ϵ_∞ arise from vibrational polar phonon modes associated with the inorganic lattice, which then negate any major temperature-dependence behavior in this region.(163)40

Figure 2.16 :(a) Illustration of the relationship between polarization (P) and electric field (E) in forward scan (FS) spanning A→B→C and reverse scan (RS) spanning C→D→A. (b) The influence of excess polarization (ΔP) on the built-in (V_{in}) and open-circuit voltage (V_{oc}), where the solid line is the energy diagram in the stabilized p-n diode and the dotted line is the changed energy diagram due to ΔP induced by non-relaxed ferroelectric domain under FS and moderate scan rate). (c) Schematic illustration of the relationship between E and ϵ , which is independent of the scan direction. (d) Schematic representation of the depletion region in halide perovskites which is heavily dependent on ϵ .(198).....41

Figure 2.17: Simplified band diagram of perovskite solar cell under illumination (quasi-Fermi levels dashed, e^- =electrons, h^+ =holes, CB=conduction band edge, VB=valence band edge) to illustrate changes in built-in potential and band-bending upon ion accumulation at interfaces that impede charge carrier extraction at selective contacts.(233)44

Figure 2.18: Device parameters for cells of different compositions [(A₁,A₂)B(X₁,X₂)₃]. (a) PCE; (b) V_{oc} ; (c) J_{sc} ; and (d) FF, as well as e) HI.(190) (Where A₁=FA, A₂=MA, B=Pb, X₁=, Br, X₂=I).47

Figure 3.1- (a) Schematic representation of the laser patterning design for the PSCs substrates, whereby the part highlighted in yellow denotes glass while the remainder indicates FTO, (b) example of a substrate used for assembling PSCs.86

Figure 3.2: (a) arrangement of the substrates inside the Teflon lining, (b) the Teflon lining (left) is then sealed inside the metal encasing (right) and placed inside the oven for hydrothermal synthesis.87

Figure 3.3- The spray pyrolysis setup.....	88
Figure 3.4: (a) The nitrogen-filled glovebox utilized for making the precursor and synthesizing perovskite layer as well as HTL. (b) the spin coater and hot plate/stirrer inside the glovebox.....	90
Figure 3.5: (a) the Class A solar simulator utilized throughout this thesis for PSC characterization, (b) schematics of different components of a solar simulator.	93
Figure 3.6: The Biologic SP-300 potentiostat used for characterization of PSCs.	94
Figure 3.7: The SU8230 microscope utilized for obtaining SEM and EDX images.	95
Figure 3.8: (a) The EQE setup utilized for characterization of PSCs, (b) schematics of different components of EQE.	97
Figure 3.9: (a) The shadow mask used during gold evaporation to obtain the desired contact pattern, (b) the detailed description of the shadow mask.....	100
Figure 3.10: (a) Side view, (b) top-view of the testing apparatus , (c) the top plate with four apertures for defining the area of active device to 0.09 cm^2 , and (d) detailed design specifications of the testing apparatus utilized in testing PSC devices reported in this thesis	101
Figure 4.1: (a-d) Top-view SEM images of the Planar and TNR ETLs; (e and f) cross-section SEM images of TNR and TNR (x4) structures; (g) XRD patterns, (h) cyclic voltammograms, (i) high binding energy part of the UPS spectra showing secondary electron cut-off (SECO) edge, and (j) the low binding energy part of UPS spectra for Planar and TNR type ETL structures.	111
Figure 4.2: Top view SEM images for (a) Planar c-TiO ₂ , (b) Planar c-TiO ₂ (x4), (c) TNR and (d) TNR(x4) at 15k and 50 k magnification; (e) EDS elemental mappings of the secondary phase precipitating out of the perovskite lattice.....	112
Figure 4.3: Comparison of PV metrics, at 100 and 10 mV/s scan rate, for PSCs based on different ETL configurations: (a) J_{SC} , (b) V_{OC} , (c) FF , and (d) PCE	113
Figure 4.4: (a) External quantum efficiency (EQE) spectra and (b) hysteresis index (HI_{PCE}) for PSCs based on different ETL structures.	114
Figure 4.5: Comparison of $J-V$ curves before and after prolonged light soaking (LS) under 1 Sun illumination, for PSCs based on different ETL structures.	117
Figure 4.6: Comparison of the high binding energy part (a,b), as well as the low binding energy segment (c,d) of the UPS spectra of perovskite layer interfacing each ETL configuration for before and after light soaking.....	118

Figure 4.7: Comparison of Nyquist plots for PSCs based on different ETL structures as a function of applied bias and light soaking (LS). 120

Figure 5.1: Schematics of synthesis methodology for (a) RA and (b) AR ETL structures. 137

Figure 5.2: Cross section (a) and top view (b) SEM images, as well as the corresponding AFM images (c) of AR and RA structures, and (d) cross section SEM images of the full stack PSC devices as well as (e) the corresponding perovskite layer coating AR and RA structures. The scale bar on SEM and AFM images denotes 500 nm and 1 μ m, respectively. 138

Figure 5.3: Comparison of the PV metrics in reverse scan (RS) as well as forward scan (FS) for PSCs based on AR and RA ETL structures: (a) J_{SC} , (b) V_{OC} , (c) FF , and (d) PCE , PL spectra with emission centered around 760 nm (e) and TRPL profiles (f) with excitation wavelength set to 504nm. **Error! Bookmark not defined.**

Figure 5.4: Representative current-voltage (J - V curves) measured under 100 mV/s and 10 mV/s in RS and FS for PSCs utilizing AR (a,c) and RA (b,d) as ETL structure 143

Figure 5.5: Comparison of Nyquist plots measured under 1 Sun illumination and increasing forward bias for PSCs based on (a) AR and (b) RA as ETL. The panel on the right columns show the zoomed-in view of the adjacent panel on the left, C-f plots for PSCs based on (c) AR and (d) RA. 144

Figure 5.6: Charge carrier dynamics in PSCs under 1 Sun illumination; a) generalized scheme of ETL/perovskite interface and band energy alignment in the high frequency region of EIS under V_{OC} (before the effect of ionic charge appears), and under ionic pile up upon longer illumination times at lower frequencies for b) RA and c) AR ETL structures under V_{OC} , d) the dynamics under increased forward bias leading to the appearance of low frequency hook in EIS spectra of AR. 146

Figure 6.1: (a) The n - i - p configuration used in constructing the PSCs in this work; SEM images of (b) cross-section and (c) top-view of the TiO_2 (AR) structure serving as ETL; (d) cyclic voltammogram and (e) XRD pattern of FTO/ETL; (f) cross-sectional image of the FTO/ ETL/ Perovskite/ HTL/Au and (g) top-view image of the perovskite layer covering the AR ETL; (h) UV-Vis spectrum of FTO/ETL and (i) the XRD pattern of FTO/ETL/Perovskite. 165

Figure 6.2: Optoelectronic characterization of the spiro-OMeTAD films: (a) UV-Vis absorbance, (b) space-charge limited current density (SCLC), conductivity of glass/HTL films (c) under dark and (d) under 1 Sun illumination..... 167

Figure 6.3: Distribution of PV metrics of PSCs assembled with HTL doped under the different conditions listed in Table 6.1: (a) J_{SC} , (b) V_{OC} , (c) FF , and (d) PCE obtained from $J-V$ scans under 100 mV/s and 10 mV/s speeds, (e) EQE spectra, and (f) hysteresis index (HI).169

Figure 6.4- Representative $J-V$ curves for PSCs using spiro-OMeTAD as HTL, doped according to the conditions listed in Table 6.1. The curves are displayed at either 100 or 10 mV/s scan speed, as well before and after 60 minutes of light soaking, denoted as Before and After, respectively.173

Figure 6.5: Proposed band diagrams at Perovskite/HTL interface: (a) favorable upward band bending which aids with the movement of photogenerated holes into HTL, (b) flat band conditions as a result of ionic accumulation at the interface and screening the built-in field, and (c) unfavorable inverted band alignment which inhibits efficient extraction of photogenerated holes by HTL. E_V , E_F and $E_{F,p}$ denote valance band, Fermi level in spiro-OMeTAD, and quasi hole Fermi level in the perovskite layer, respectively, in addition to comparison of XPS spectra obtained over the FTO/ETL/perovskite/HTL stacks before (d-g) and after (h-k) 60 minutes of light soaking under 1 Sun illumination.174

Figure 6.6: Comparison of Nyquist plots for HTL exposed to different doping conditions, obtained under open-circuit condition and 1 Sun illumination before and after 60 min of light soaking.177

Figure 6.7: Characterization of PSCs left under dark before and after gold deposition (DD): (a) Nyquist plots obtained under open-circuit condition and 1 Sun illumination, and (b) $J-V$ curves under 100 and 10 mV/s scan speed before and after 60 min of light soaking.179

Figure 7.1: Illustration of band bending at ETL/perovskite interface showing the dominant recombination mechanism giving rise to the hysteresis locus observed on $J-V$ curves at 10 mV/s, as well as probing the corresponding charge carrier dynamics using EIS under 1 Sun illumination and increasing forward bias in excess of V_{OC} for PSCs based on (a) AR and (b) RA as ETL.194

Figure 7.2: PV metrics for PSCs with quadruple perovskite composition in $n-i-p$ architecture assembled using c-TiO₂, c-TiO₂ (x4), TNR (same as RA in Chapter 5), TNR (x4) and AR.195

Figure 7.3: Comparison of $J-V$ curves at 100 and 10 mV/s before and after light soaking (LS) for PSCs with quadruple perovskite composition in $n-i-p$ architecture assembled using c-TiO₂, c-TiO₂ (x4), TNR (same as RA in Chapter 5), TNR (x4) and AR.197

Figure A.1- 1: Schematic illustration of n-i-p PSCs studied in this work based on the ETL configuration: (a) planar c-TiO₂, (b) planar c-TiO₂ (x4), (c) TNR and (d) TNR(x4).206

Figure A.1-2: Cross-section SEM image of the full stack PSC in n-i-p architecture, using TNR as ETL207

Figure A.1- 3: Results of the conductivity measurements on glass/spiro-OMeTAD film under dark, illumination and light soaking for 60 minutes.212

Figure A.1- 4: Comparison of the XPS core-level spectra for perovskite layers interfacing different ETLS before light soaking: (a) C1s, (b) Cs3d, (c) Rb3d, (d) Pb4f, (e) I3d and (f) Br3d.213

Figure A.1- 5: Comparison of the XPS core-level spectra for perovskite layers interfacing different ETLS after light soaking: (a) C1s, (b) Cs3d, (c) Rb3d, (d) Pb4f, (e) I3d and (f) Br3d.215

Figure A.1- 6: Top-view SEM image of the perovskite layer, interfacing c-TiO₂ as ETL, after light soaking at (a) 15k and (b) 50k magnification, as well EDS mapping (c) obtained over the precipitate displaying similar morphology and composition to Figure 4.2 a.217

Figure A.1- 7: Equivalent circuit used in fitting the EIS patterns of Figure 4.7.....217

Figure A.2- 1: a) XRD patterns (peaks marked by filled triangle and circle denote diffraction from rutile titania and FTO, respectively), b) cyclic voltammetry scans, (c) effective conductivity of the ETL structures, (d) the UV-Vis absorbance spectra. All the presented results are obtained over FTO/ETL stacks.221

Figure A.2- 2: (a) XRD pattern of the perovskite layer infiltrating AR and RA ETL structures. (b) dark current- voltage curve for FTO/spiro-OMeTAD/Au architecture.....222

Figure A.2- 3: (a) EQE spectra obtained for PSCs based on AR and RA ETL structures (b) Distribution of HI_{FF} for PSCs based on AR and RA ETL structures.224

Figure A.2- 4: (a) Equivalent circuit used for fitting the EIS spectra recorded under open-circuit condition, comparison of (b) R_{Series} , (c) R_{HF} , and (d) R_{LF} for PSCs based on AR and RA.....225

Figure A.2- 5: The distribution of PV metrics after storing the devices for 200 hours under dark and 25% relative humidity: (a) J_{SC} , (b) V_{OC} , (c) FF, (d) PCE.....226

Figure A.3- 1: Comparison of conductivity trends, performed after 60 minutes of light soaking....231

Figure A.3- 2: Fittings of XPS spectra obtained over FTO/ETL/perovskite/HTL films prior to light soaking.232

Figure A.3- 3: Fittings of XPS spectra obtained over FTO/ETL/perovskite/HTL films after light soaking for 60 minutes.....233

Figure A.3- 4: Equivalent circuits utilized for fitting the Nyquist plots of Figure 6.6, with R_{Series} being the series resistance. Equivalent circuits shown in (a) and (b) include elements in low frequency (LF), as well as high frequency (HF). The equivalent circuit displayed in (b) has additional mid frequency (MF) components.....236

Figure A.3- 5: Characterization results obtained from DD doping condition: (a) comparison of UV-Vis spectra for DD and pristine spiro-OMeTAD, (b) SCLC trend, and (c) evolution of conductivity for DD from dark to 1 Sun illumination238

Figure A.3- 6: Distribution of PV metrics obtained for PSCs using DD as the doping process for spiro-OMeTAD films: (a) J_{SC} , (b) V_{OC} , (c) FF , and (d) PCE , as well as (e) HI values, under scan rates of 100 and 10 mV/s.239

List of Tables

Table 3.1- Composition of the HTL precursor for Chapters 4-6.....	91
Table 3.2: List of the doping conditions utilized for increasing p-type conductivity of spiro-OMeTAD in Chapter 6.....	92
Table 5.1: Extracted charge carrier lifetimes from fitting TRPL decays.	141
Table 6.1: Different doping conditions tested.	165
Table A.1-1:Valence band energy (E_{VB}) and work function (Φ) values of different ETL structures	207
Table A.1- 2: Change of PV metrics for PSCs based on Planar c-TiO ₂ before and after 60 minutes light soaking. In each column, 100 and 10 denote the scan speeds of 100 mV/s and 10 mV/s, respectively. Additionally, LS stands for light soaking.....	208
Table A.1- 3:Change of PV metrics for PSCs based on Planar c-TiO ₂ (x4) before and after 60 minutes light soaking. In each column, 100 and 10 denote the scan speeds of 100 mV/s and 10 mV/s, respectively. Additionally, LS stands for light soaking.....	209
Table A.1- 4:Change of PV metrics for PSCs based on TNR before and after 60 minutes light soaking. In each column, 100 and 10 denote the scan speeds of 100 mV/s and 10 mV/s, respectively. Additionally, LS stands for light soaking.	210
Table A.1- 5:Change of PV metrics for PSCs based on TNR (x4) before and after 60 minutes light soaking. In each column, 100 and 10 denote the scan speeds of 100 mV/s and 10 mV/s, respectively. Additionally, LS stands for light soaking.	211
Table A.1- 6:Valence band energy E_{VB} and Φ values of perovskite layer interfacing different ETL structures. LS stands for light soaking.....	212
Table A.1- 7: Summary of the values obtained through fitting the XPS spectra displayed in Figure A.1- 4.	214
Table A.1- 8:Summary of the values obtained through fitting the XPS spectra displayed inFigure A.1- 5	216
Table A.1- 9: The extracted parameters from fitting the Nyquist plots of Figure 4.7 a with the equivalent circuits of Figure A.1- 7 , for PSCs based on c-TiO ₂	218
Table A.1- 10: The extracted parameters from fitting the Nyquist plots of Figure 4.7 b with the equivalent circuits of Figure A.1- 7, for PSCs based on c-TiO ₂ (x4).	218

Table A.1- 11: The extracted parameters from fitting the Nyquist plots of Figure 4.7 c with the equivalent circuits of Figure A.1- 7, for PSCs based on TNR.219

Table A.1- 12: The extracted parameters from fitting the Nyquist plots of Figure 4.7 d with the equivalent circuits of Figure A.1- 7, for PSCs based on TNR (x4).219

Table A.2- 1: PV metrics variation of PSCs based on AR and RA ETL structure for forward scan (FS) and reverse scan (RS), under 100 and 10 mV/s scan rates. The champion device in each case is highlighted in the row underneath.223

Table A.2- 2: PV metrics variation of PSCs based on AR and RA ETL structure for forward scan (FS) and reverse scan (RS), under 100 and 10 mV/s scan rates, corresponding to storing the devices for 200 hours under dark and 25% relative humidity. The champion device in each case is highlighted in the row underneath.227

Table A.3- 1: Conductivity values obtained for HTL films doped according to processes of Table 6.1, under dark as well as 1 Sun illumination.229

Table A.3- 2: Change of PV metrics for the LL process before and after 60 minutes of light soaking. In each column, 100 and 10 denote the scan speeds of 100 mV/s and 10 mV/s, respectively.229

Table A.3- 3: Change of PV metrics for the LD process before and after 60 of minutes light soaking. In each column, 100 and 10 denote the scan speeds of 100 mV/s and 10 mV/s, respectively.230

Table A.3- 4: Change of PV metrics for the DL process before and after 60 minutes of light soaking. In each column, 100 and 10 denote the scan speeds of 100 mV/s and 10 mV/s, respectively.230

Table A.3- 5: Change of PV metrics for the DL(15) process before and after 60 of minutes light soaking. In each column, 100 and 10 denote the scan speeds of 100 mV/s and 10 mV/s, respectively.231

Table A.3- 6: Conductivity values obtained for HTL films doped according to processes of Table 6.1, after 60 minutes of light soaking.232

Table A.3- 7: Binding energy (BE) and full-width half maximum (FWHM) values obtained from XPS spectra of the HTL films deposited over FTO/ETL/perovskite stacks, prior to light soaking for 60 minutes.234

Table A.3- 8: Binding energy (BE) and full-width half maximum (FWHM) values obtained from XPS spectra of the HTL films deposited over FTO/ETL/perovskite stacks, after light soaking for 60 minutes.....235

Table A.3- 9: The extracted parameters from fitting the Nyquist plots of Figure 6.6 with the equivalent circuits of Figure A.3- 4.237

Table A.3- 10: Conductivity values obtained for spiro-OMeTAD film doped according to DD process.....238

Table A.3- 11: Change of PV metrics for the DD process before and after 60 minutes light soaking. In each column, 100 and 10 denote the scan speeds of 100 mV/s and 10 mV/s, respectively. Additionally, RS and FS indicate forward and reverse scan directions, respectively.....240

Table A.3- 12: The extracted parameters from fitting the Nyquist plots for DD with the equivalent circuits of Figure A.3- 4b.241

Abstract

Perovskite solar cells (PSCs), reported first in 2009, have emerged as a potentially low-cost and scalable alternative to crystalline silicon solar cells. PSCs are named after the absorber layer of perovskite crystal structure ABX_3 , where A is a monovalent cation, B is a divalent cation and X is a halide. Upon the absorption of light, photogenerated electrons and holes in the perovskite layer are extracted by the electron transport layer (ETL) and hole transport layer (HTL), respectively. One of the most critical shortcomings hampering industrialization of PSCs is a phenomenon called hysteresis, defined as the mismatch between current-voltage ($J-V$) curves when the solar cell is scanned under reverse and forward scan directions. In this thesis, the evolution of hysteresis is investigated from the perspective of the transport layers, in the $n-i-p$ architecture of PSCs.

Firstly, the influence of compact titania (c-TiO₂) interfacing within the ETL in determining loss and gain in fill factor (FF) and the corresponding hysteresis modulation, as a function of light soaking, scan rate and applied bias was studied. For this purpose, c-TiO₂ (synthesized through spray pyrolysis), was utilized in the *i*) planar, and *ii*) scaffold-based configuration where it coats hydrothermally grown titania nanorods. The tolerance of ETL/perovskite interface under light soaking in planar PSCs allows for enhanced p -doping of spiro-OMeTAD to be reflected as overall improved FF , in contrast to scaffold-based PSCs. Better sustaining of FF at low scan speed in the planar configuration can be obtained by either supporting c-TiO₂ with a nanorod scaffold underneath or increasing its thickness. Conversely, open-circuit voltage (V_{OC}) values for all ETLs increased with scan rate and decreased with light soaking. Using electrochemical impedance spectroscopy (EIS), the application of forward bias was deemed to result in inverted band alignment for planar PSCs while increasing conductivity in scaffold-based configurations.

Secondly, a TiO₂ nanorod scaffold was investigated as ETL by using a combination of hydrothermal synthesized titania nanorods and c-TiO₂. Conducting hydrothermal synthesis over c-TiO₂ generated vertically aligned titania nanorods which were in direct contact with the perovskite layer. On the other hand, performing spray pyrolysis over hydrothermally synthesized scaffold resulted in randomly oriented titania nanorods coated with c-TiO₂. Through analyzing the hysteresis locus on $J-V$ curves and the corresponding EIS patterns obtained under 1 Sun illumination and voltages exceeding V_{OC} , it was demonstrated that the configuration of ETL scaffold can play a considerable role in determining the voltage range under which non-radiative recombination dominates. Particularly, low ETL

conductivity was correlated with band inversion under increasing forward bias and giving rise to inductive hysteresis as a result.

Thirdly, PSCs built on rutile titania nanorod scaffold grown over $c\text{-TiO}_2$ were further investigated to understand the influence of doping conditions of the spiro-OMeTAD, that is used as HTL, on evolution of hysteresis dynamics as a function of scan rate and light soaking. Several doping strategies were studied which differed with respect to length of the doping process, as well as the sequence in combining the type of storage before and after gold deposition. Using EIS, it was demonstrated that depending on the underlying cause for poor PSC performance, either a loss or gain in FF can be expected under operation which would then modify the appearance of hysteresis. For an HTL with low hole conductivity, light soaking can increase p -doping correlated with the reduction of the high frequency semicircle in the Nyquist plot. However, low HTL conductivity combined with undesirable interfacial electrochemical reactions lead to the propagation of the low frequency EIS features linked with diminished performance in forward scan.

Resume

Les cellules solaires à pérovskite (PSC), présentées pour la première fois en 2009, sont apparues comme une alternative potentiellement peu coûteuse et évolutive aux cellules solaires au silicium cristallin. Les PSC tirent leur nom de la couche absorbante de la structure cristalline de la pérovskite ABX_3 , où A est un cation monovalent, B un cation divalent et X un halogénure. Lors de l'absorption de la lumière, les électrons et les trous photogénérés dans la couche de pérovskite sont extraits par la couche de transport d'électrons (ETL) et la couche de transport de trous (HTL), respectivement. L'une des lacunes les plus critiques qui entravent l'industrialisation des PCS est un phénomène appelé hystérésis, défini comme le décalage entre les courbes courant-tension ($J-V$) lorsque la cellule solaire est balayée dans le sens inverse et dans le sens inverse. Dans cette thèse, l'évolution de l'hystérésis est étudiée du point de vue des couches de transport, dans l'architecture $n-i-p$ des PSC.

Tout d'abord, l'influence de l'interfaçage du titane compact (c-TiO₂) dans l'ETL pour déterminer la perte et le gain dans le facteur de remplissage (FF) et la modulation de l'hystérésis correspondante, en fonction de l'absorption de lumière, de la vitesse de balayage et de la polarisation appliquée, a été étudiée. À cette fin, le c-TiO₂ (synthétisé par pyrolyse par pulvérisation) a été utilisé dans une configuration i) planaire et ii) à base d'échafaudage où il recouvre des nanorods de titane cultivés par voie hydrothermale. La tolérance de l'interface ETL/perovskite sous l'effet de la lumière dans les PSC plans permet d'améliorer le dopage p du spiro-OMeTAD, ce qui se traduit par une amélioration globale de la FF , contrairement aux PSC à base d'échafaudages. Un meilleur maintien de la FF à faible vitesse de balayage dans la configuration planaire peut être obtenu soit en soutenant le c-TiO₂ avec un échafaudage de nanorods en dessous, soit en augmentant son épaisseur. Inversement, les valeurs de tension en circuit ouvert (V_{oc}) pour tous les ETL augmentent avec la vitesse de balayage et diminuent avec le trempage dans la lumière. En utilisant la spectroscopie d'impédance électrochimique (EIS), l'application d'une polarisation directe a été considérée comme entraînant un alignement de bande inversé pour les PSC plans tout en augmentant la conductivité dans les configurations à base d'échafaudages.

Deuxièmement, un échafaudage de nanorods de TiO₂ a été étudié comme ETL en utilisant une combinaison de nanorods de titane synthétisés par voie hydrothermale et de c-TiO₂. La synthèse hydrothermale sur c-TiO₂ a généré des nanorods de titane alignés verticalement qui étaient en

contact direct avec la couche de pérovskite. D'autre part, la pyrolyse par pulvérisation sur l'échafaudage synthétisé par voie hydrothermale a produit des nanorods de titane orientés de manière aléatoire et recouverts de c-TiO₂. En analysant le lieu d'hystérésis sur les courbes $J-V$ et les schémas EIS correspondants obtenus sous une illumination de 1 soleil et des tensions supérieures à V_{oc} , il a été démontré que la configuration de l'échafaudage ETL peut jouer un rôle considérable dans la détermination de la plage de tension dans laquelle la recombinaison non radiative domine. En particulier, une faible conductivité de l'ETL a été corrélée à l'inversion de bande sous une polarisation directe croissante, ce qui a donné lieu à une hystérésis inductive.

Troisièmement, les PSC construites sur un échafaudage de nanorods de titane rutile cultivé sur c-TiO₂ ont été étudiées plus avant pour comprendre l'influence des conditions de dopage du spiro-OMeTAD, utilisé comme HTL, sur l'évolution de la dynamique de l'hystérésis en fonction de la vitesse de balayage et de l'imprégnation lumineuse. Plusieurs stratégies de dopage ont été étudiées, qui diffèrent en ce qui concerne la durée du processus de dopage, ainsi que la séquence combinant le type de stockage avant et après le dépôt d'or. En utilisant l'EIS, il a été démontré qu'en fonction de la cause sous-jacente de la mauvaise performance de la PSC, on peut s'attendre à une perte ou à un gain de FF en fonctionnement, ce qui modifierait alors l'apparition de l'hystérésis. Pour une HTL avec une faible conductivité des trous, l'imbibition de lumière peut augmenter le dopage p en corrélation avec la réduction du demi-cercle à haute fréquence dans le tracé de Nyquist. Cependant, une faible conductivité de la HTL combinée à des réactions électrochimiques interfaciales indésirables conduit à la propagation des caractéristiques EIS à basse fréquence liées à une diminution des performances dans le balayage avant.

This thesis is dedicated to the courageous Iranian and Afghani women in their awe-inspiring fight against religious tyranny.

In loving memory of the members of Flight PS752.

Acknowledgements

First and foremost, I would like to express my immense gratitude towards my PhD supervisor, Professor George P. Demopoulos, for giving me the opportunity to conduct my doctoral studies at hydrothermal materials for environmental & energy technologies (HydroMet) laboratory. I'm especially grateful that he trusted me with choosing my research direction. His incredible display of patience with my mistakes, as well as perseverance and passion in research throughout his fruitful career have been nothing short of inspiring. I will always be indebted to him for his incredible support and compassion. Above all, he has been a father figure to me and helped me grow so much as a person.

I spent six memorable years at the HydroMet laboratory. I'd like to thank Han Wang, Moohyun Woo, Fan Yu, Senhao Wang, Arian Norouzi, Joon Kyung Koong, Dr. Andrea La Monaca, Aristya Marzuki, Philip Gamboa, and Gocke Kilic. I deeply appreciate their support, insight, and above all friendship over the years. I wish my time at McGill had overlapped with theirs for longer than it did. I would also like to thank the former lab members including Dr. Zhuoran Wang and Dr. Fuqiang Guo. I have learned so much from their manners and work etiquettes.

My sincere gratitude goes towards Prof. Sidney Omelon, Prof. Nathaniel Quitarano, Prof. Phillippe Ouzilleau, Prof. Kristian Waters, Prof. Dmytro Perepichka, Prof. Peter Grutter, Prof. Raynald Gauvin, Dr. Omur Dagdeviren, Nicholas Brodusch, Stephanie Bessette, Dr. Zhao Lu and Jun Li for the extremely helpful discussions, as well as selfless insight and guidance throughout the years.

I had the privilege of working with extremely talented and helpful technicians; Raymond Langlois, Alexandra Djuric, Frank Caporuscio, Ranjan Roy, Andrew Golsztajn, Gerald Lepkyj and Richard Talbot. It is because of their integral help that my doctoral work moved forward. Thank you for going out of your way to troubleshoot equipment, being patient with me and teaching me technical knowledge from scratch.

I would like to extend my appreciation to the wonderful admin staff of the Materials Engineering department. I am much thankful for Barbara Hanley, June Persaud and Leslie Bernier, for always watching out for me, being my friend and helping me get through tough times. I also like to acknowledge the very insightful conversations I have had over the years with Heather Holowathy and Genevieve Snider.

It would have been impossible to get through long hours at the lab, failing experiments and personal matters if it was not for my incredible friends Paniz Soltani, Dr. Abhi Ghosh, Dr. Hsien-chieh Chiu, Mahsa Ebrahimi, Saeede Taffazoli, Payam Shahsavari, Dr. Ozan Kokkilich, Ute Salzberger, Siegfried Schwartz, Robert Bianci, Dr. Jacob Lee, Dr. Bruno Castilho, Dr. Meng Zhou, Ronghao Li, Jeff Opoku, Tian Zhao, and Dane Beamsley among many others.

Finishing my PhD journey would not have been possible without my incredible partner, Andrew Walker, by my side who has always been rooting for my success more than myself and reprogramming everything to accommodate me. Seeing his hard work, discipline and perseverance has always inspired me to keep moving forward. I am also incredibly grateful to his loving family for the unconditional support.

Above all, I would like to thank my superwoman of a mother, Tahereh Rajabi, who has been my biggest supporter. She is without a doubt my role model. There are not enough words for me to ever thank her enough for the sacrifices she has had to make for me. I hope that one day, I can be just as graceful and strong as she is.

Foreword

This thesis has been presented in a manuscript-based format. Chapter 4 to Chapter 6 are individual manuscripts that have either been published, submitted for publication, or are in review towards publication in peer-reviewed journals. The chapters have been formatted and replicated as published or submitted. The research was carried out in the materials engineering department of McGill University under supervision of Prof. George P. Demopoulos, who was the principal investigator and administrator for the thesis project, as well as the associated funding. The following describes the contribution of various co-authors involved with the manuscript chapters.

Chapter 4: Candidate conceived the project idea and developed the required strategies with help of Prof. Demopoulos. Candidate performed the synthesis of all layers and device assembly, as well as XRD, cyclic voltammetry, J - V , EQE, UPS, and XPS characterization. The electron microscopy measurements were facilitated by Prof. Raynald Gauvin and Ms. Stephanie Bessette conducted imaging with Hitachi SU8230. Candidate analyzed the results and provided discussion with the help of Mr. Han Wang and Prof. Demopoulos.

Chapter 5: Candidate conceived the project idea and developed the required strategies with help of Prof. Demopoulos. Candidate performed the synthesis of all layers and device assembly, as well as XRD, cyclic voltammetry, J - V , EQE, UV-Vis, conductivity, AFM, PL and SCLC characterization. The electron microscopy measurements were facilitated by Prof. Raynald Gauvin and Ms. Stephanie Bessette conducted imaging with Hitachi SU8230. Prof. Patanjali Kambhampati provided the setup for TRPL, and Dr. Dallas Strandell conducted the corresponding measurements Candidate analyzed the results and provided discussion with the help of Dr. Hsien-chieh Chiu and Dr. Zhuoran Wang and Prof. Demopoulos.

Chapter 6: Candidate conceived the project idea and developed the required strategies with help of Prof. Demopoulos. Candidate performed the synthesis of all layers and device assembly, as well as XRD, cyclic voltammetry, J - V , EQE, UV-Vis, conductivity, and XPS characterization. Dr. Pegah Ghamari assisted with conducting some of the SCLC measurements. The electron microscopy measurements were facilitated by Prof. Raynald Gauvin and Ms. Stephanie Bessette conducted imaging with Hitachi SU8230. Mr. Jonathan Sharir-Smith helped with some of experimental work. Candidate analyzed the results and provided discussion with the help of Mr. Han Wang and Prof. Demopoulos.

Chapter 1: Introduction

1.1. Background on Perovskite Solar Cells

Perovskite solar cells (PSCs) were first introduced in 2009 by Kojima et al.(1) as a part of ongoing research on dye-sensitized solar cells (DSSCs).(2) What had triggered the research into both of these classes of photovoltaic (PV) devices was the high manufacturing cost and considerably negative environmental impact of the solar cells based on monocrystalline silicon (c-Si) and other types of high performing solar cells such as cadmium telluride (CdTe).(3) PSCs started their photovoltaic journey with a mere 3.8% power conversion efficiency (*PCE*),(1) while today they furnish cell scale efficiencies above 25% (4) on par with c-Si solar cells(5). PSCs are multi-layered devices, with each layer serving a very distinct purpose. At the heart of the solar cell, there is an absorber layer which as the name suggests is tasked with absorbing the sunlight. The absorber layer has perovskite crystal structure with the general formula of ABX_3 , where A is a monovalent cation, B is a divalent cation and X is a halide.(6) The perovskite layer (assumed to be an intrinsic semiconductor, *i*) is then sandwiched between an electron transport layer (ETL, a *n*-type semiconductor) and a hole transport layer (HTL, a *p*-type semiconductor) for separation of photogenerated charge carriers and eventually extracting them into the outer circuit. PSCs are, most commonly, assembled in two architectures: 1) *n-i-p* (or the normal structure) where the ETL is deposited over transparent conductive oxide (TCO), followed by the deposition of perovskite layer and HTL, and 2) *p-i-n* (or the inverted structure) where the HTL is deposited over the TCO, followed by deposition of perovskite layer and ETL. In both cases, light enters through the TCO to reach the perovskite layer.

The unparalleled progress in PSCs has been largely due to the exceptional optoelectronic properties of the perovskite semiconductors including being direct gap semiconductor,(7) having long charge carrier diffusion lengths,(8) high absorption coefficient,(9, 10) low exciton binding energies,(11) and etc. to name a few. What makes such a combination of favourable characteristics in perovskites rather peculiar is that these materials are mostly obtained from solution synthesis at low temperatures. Therefore, next to delivering competitive performance as that of c-Si, PSCs also offer an edge with respect to cost-effectiveness. However, before the full potential of PSCs can be realized in industrial scale, some challenges would have to be overcome including the phenomenon of hysteresis which is considerable contributing factor towards the overall instability problems prevalent in this class of solar cells. (12, 13)

1.2. Overview of the Phenomenon of Hysteresis in PSCs

Hysteresis is the term ascribed to the mismatch in the current-voltage (J - V) curves between reverse scan (RS) and forward scan (FS) directions. This phenomenon has been, above all, correlated with unreliable PSC performance values since the PCE tends to be overestimated in one scan direction and underestimated in the other.(14) What renders hysteresis a very complex issue is that the recorded dynamics can be far different depending on device architecture and choice of contact layers. To make matters worse, the said dynamics can evolve in unexpected directions under light soaking and change in temperature.(15) For example, in the n - i - p architecture, the FS usually renders lower photovoltaic metrics and overall PCE than that of RS (this situation is otherwise known as normal hysteresis), which is the opposite of what is commonly observed for the p - i - n architecture (otherwise known as inverted hysteresis). However, by leaving the devices (of either architecture) under prolonged illumination and forward/reverse bias, the originally observed dynamics can reverse course and evolve in complex ways.(16)

Apart from the aforementioned factors, other parameters have also been experimentally shown to affect the appearance and magnitude of hysteresis including scan rate, scan direction, pre-conditioning and measurement history of the device.(17, 18, 19, 20) Over the years different origins for hysteresis have been suggested including ferroelectricity, charge trapping/de-trapping, non-radiative recombination and ionic migration.(21, 22, 23, 24, 25, 26, 27, 28) Replicating the experimental observations using only one isolated origin has proved to be futile.(14) Consequently, a combination of origins has been proposed which contribute to the different time scales obtained from time-transient measuring techniques.(14) As such, the origin of hysteresis in PSCs remains an elusive and a debated topic in the community. This necessitates a deeper look into this phenomenon from the perspective of different PSC device components which has motivated the research presented in this thesis.

1.3. Thesis Objectives and Organization

After this introductory chapter (Chapter 1), Chapter 2 presents a literature review on the photovoltaic energy conversion process, history of solar cells and PSC operational mechanisms as well as the peculiar optoelectronic properties of metal halide perovskites. Finally, Chapter 2 offers a comprehensive overview on the phenomenon of hysteresis. Chapter 3 details deposition methods and

characterization techniques. In view of the existing gaps in better understanding the hysteresis dynamics and their origin in PSCs, several objectives are addressed in Chapter 4 to Chapter 6.

The first objective of this thesis is to understand the role of commonly employed compact TiO₂ layer (c-TiO₂, synthesized through spray pyrolysis) interfacing within the ETL structure on the loss and gain in FF , and the correlated hysteresis evolution, as a function of prolonged illumination, scan rate and applied bias. In addressing this objective, in **Chapter 4**, two different configurations of the $n-i-p$ architectures are studied: *i*) planar structure where the ETL is comprised solely of c-TiO₂, and *ii*) scaffold-based structure where c-TiO₂ coats hydrothermally grown titania nanorods. In this chapter, the ETL films are characterized by scanning electron microscopy (SEM), X-ray diffraction (XRD), cyclic voltammetry and ultraviolet photoelectron spectroscopy (UPS). The light soaking-induced changes to perovskite surface are evaluated using UPS, SEM and energy dispersive X-ray spectroscopy (EDS). Moreover, the charge transfer resistance values extracted from electrochemical impedance (EIS) are correlated with the FF evolution from $J-V$ curves. Through careful analysis of the change in the locus and magnitude of hysteresis as a function of testing conditions, this chapter establishes a link between the thickness of c-TiO₂ and the ETL configuration it is employed in, to hysteresis dynamics in PSCs. Chapter 4 is a reproduction of the original manuscript and is currently under peer review process.

The second objective of this thesis is to investigate the influence of the type of titania nanorod scaffold, as ETL, interfacing with the perovskite layer over locus of hysteresis in PSCs and specifically under voltages exceeding V_{OC} . To address this objective, **Chapter 5** investigates two ETL ensembles which are generated by varying the sequence between spray pyrolysis and hydrothermal synthesis. The synthesized ETL scaffolds differ with respect to their degree of vertical alignment versus the substrate as well as the layer directly interfacing the perovskite layer. The two ETL structures are characterized by XRD, cyclic voltammetry, ultraviolet-visible (UV-Vis) spectroscopy and SEM. The role of the TiO₂ nanorod scaffold in dictating the interfacial band alignment, non-radiative recombination and eventually inductive hysteresis is investigated through studying photoluminescence (PL), time-resolved photoluminescence (TRPL) spectra, $J-V$ curves under two different scan rates as well as EIS patterns under 1 Sun illumination and increasing forward bias in excess of V_{OC} . Chapter 5 is a reproduction of the original manuscript and is published in a peer-reviewed journal.

The third objective of this thesis is to understand the influence of doping parameters utilized in enhancing *p*-type conductivity of spiro-OMeTAD (as HTL) on the evolution of hysteresis dynamics in PSCs under light soaking and different scan rates. In that respect, **Chapter 6** offers a thorough analysis of the PSCs using different doping conditions (with respect to doping time and type of storage environment) via comparing *J-V* curves under two different scan rates, as well as before and after prolonged light soaking. The HTL films are characterized by conductivity measurements, as well as space-charge limited current density (SCLC) and UV-Vis spectroscopy. Moreover, the corresponding changes to the bonding environment of HTL films interfacing the perovskite layer is evaluated using XPS and are correlated with EIS measurements (at open circuit under 1 Sun) to identify signatures of HTL conductivity modulation depending on the utilized doping condition. Chapter 6 is a reproduction of the original manuscript is currently under peer review process.

At the end of each Chapter 4 and Chapter 5, a *Bridge* section is presented which connects the manuscript in each of the two chapters to the following one. Chapter 7 connects the findings of this thesis work to the objectives laid out in Chapter 1 and topics discussed in Chapter 2, to offer a global discussion of hysteresis dynamics, as studied from the perspective of both transport layers in quadruple perovskite based-PSCs with *n-i-p* architecture. The summary of the work conducted in this thesis is presented in Chapter 8 in terms of major conclusions, contributions to the original knowledge, and ideas for further work. The supplementary information for Chapters 4 to 6 is presented in the APPENDIX section.

1.4. References

1. Kojima A, Teshima K, Shirai Y, Miyasaka T. Organometal Halide Perovskites as Visible-Light Sensitizers for Photovoltaic Cells. *Journal of the American Chemical Society*. 2009;131(17):6050-1.
2. O'regan B, Grätzel M. A low-cost, high-efficiency solar cell based on dye-sensitized colloidal TiO₂ films. *nature*. 1991;353(6346):737-40.
3. Yoo JJ, Seo G, Chua MR, Park TG, Lu Y, Rotermund F, et al. Efficient perovskite solar cells via improved carrier management. *Nature*. 2021;590(7847):587-93.
4. Min H, Lee DY, Kim J, Kim G, Lee KS, Kim J, et al. Perovskite solar cells with atomically coherent interlayers on SnO₂ electrodes. *Nature*. 2021;598(7881):444-50.
5. Best Research-Cell Efficiency Chart [Available from: <https://www.nrel.gov/pv/cell-efficiency.html>].

6. Park N-G. Organic-inorganic halide perovskite photovoltaics.
7. Unger EL. The PV-Researcher's Siren: Hybrid metal halide perovskites. *Current Opinion in Green and Sustainable Chemistry*. 2017;4:72-6.
8. Xing G, Mathews N, Sun S, Lim SS, Lam YM, Grätzel M, et al. Long-range balanced electron- and hole-transport lengths in organic-inorganic CH₃NH₃PbI₃. *Science*. 2013;342(6156):344-7.
9. Park N-G. Perovskite solar cells: an emerging photovoltaic technology. *Materials Today*. 2015;18(2):65-72.
10. Lin Q, Armin A, Nagiri RCR, Burn PL, Meredith P. Electro-optics of perovskite solar cells. *Nature Photonics*. 2015;9(2):106-12.
11. Ponceca CS, Jr., Savenije TJ, Abdellah M, Zheng K, Yartsev A, Pascher T, et al. Organometal Halide Perovskite Solar Cell Materials Rationalized: Ultrafast Charge Generation, High and Microsecond-Long Balanced Mobilities, and Slow Recombination. *Journal of the American Chemical Society*. 2014;136(14):5189-92.
12. Leijtens T, Eperon GE, Noel NK, Habisreutinger SN, Petrozza A, Snaith HJ. Stability of metal halide perovskite solar cells. *Advanced Energy Materials*. 2015;5(20):1500963.
13. Boyd CC, Checharoen R, Leijtens T, McGehee MD. Understanding degradation mechanisms and improving stability of perovskite photovoltaics. *Chemical reviews*. 2018;119(5):3418-51.
14. Unger EL, Czudek A, Kim H-S, Tress W. Chapter 4 - Current-voltage analysis: lessons learned from hysteresis. In: Pazoki M, Hagfeldt A, Edvinsson T, editors. *Characterization Techniques for Perovskite Solar Cell Materials*: Elsevier; 2020. p. 81-108.
15. Miyasaka T. *Perovskite Photovoltaics and Optoelectronics: From Fundamentals to Advanced Applications*: John Wiley & Sons; 2021.
16. Kim S-G, Park N-G. Hysteresis of I – V Performance: Its Origin and Engineering for Elimination. *Perovskite Photovoltaics and Optoelectronics*2022. p. 215-32.
17. Unger EL, Hoke ET, Bailie CD, Nguyen WH, Bowring AR, Heumüller T, et al. Hysteresis and transient behavior in current–voltage measurements of hybrid-perovskite absorber solar cells. *Energy & Environmental Science*. 2014;7(11):3690-8.
18. Tress W, Marinova N, Moehl T, Zakeeruddin SM, Nazeeruddin MK, Grätzel M. Understanding the rate-dependent J–V hysteresis, slow time component, and aging in CH₃NH₃PbI₃ perovskite solar cells: the role of a compensated electric field. *Energy & Environmental Science*. 2015;8(3):995-1004.

19. Tress W. Metal Halide Perovskites as Mixed Electronic–Ionic Conductors: Challenges and Opportunities □ From Hysteresis to Memristivity. *The journal of physical chemistry letters*. 2017;8(13):3106-14.
20. Cao X, Li Y, Li C, Fang F, Yao Y, Cui X, et al. Modulating hysteresis of perovskite solar cells by a poling voltage. *The Journal of Physical Chemistry C*. 2016;120(40):22784-92.
21. Jacobs DA, Wu Y, Shen H, Barugkin C, Beck FJ, White TP, et al. Hysteresis phenomena in perovskite solar cells: the many and varied effects of ionic accumulation. *Physical Chemistry Chemical Physics*. 2017;19(4):3094-103.
22. Lee J-W, Kim S-G, Bae S-H, Lee D-K, Lin O, Yang Y, et al. The interplay between trap density and hysteresis in planar heterojunction perovskite solar cells. *Nano letters*. 2017;17(7):4270-6.
23. Liu P, Wang W, Liu S, Yang H, Shao Z. Fundamental understanding of photocurrent hysteresis in perovskite solar cells. *Advanced Energy Materials*. 2019;9(13):1803017.
24. Frost JM, Butler KT, Walsh A. Molecular ferroelectric contributions to anomalous hysteresis in hybrid perovskite solar cells. *Apl Materials*. 2014;2(8):081506.
25. Wei J, Zhao Y, Li H, Li G, Pan J, Xu D, et al. Hysteresis analysis based on the ferroelectric effect in hybrid perovskite solar cells. *The journal of physical chemistry letters*. 2014;5(21):3937-45.
26. Snaith HJ, Abate A, Ball JM, Eperon GE, Leijtens T, Noel NK, et al. Anomalous Hysteresis in Perovskite Solar Cells. *The Journal of Physical Chemistry Letters*. 2014;5(9):1511-5.
27. Richardson G, O'Kane SE, Niemann RG, Peltola TA, Foster JM, Cameron PJ, et al. Can slow-moving ions explain hysteresis in the current–voltage curves of perovskite solar cells? *Energy & Environmental Science*. 2016;9(4):1476-85.
28. Weber SA, Hermes IM, Turren-Cruz S-H, Gort C, Bergmann VW, Gilson L, et al. How the formation of interfacial charge causes hysteresis in perovskite solar cells. *Energy & Environmental Science*. 2018;11(9):2404-13.

Chapter 2: Literature Review

2.1. Fundamentals of Photovoltaic Energy Conversion

2.1.1. Absorption and Photoexcitation Processes

Solar photovoltaic (PV) energy conversion is a one-step process generating electrical energy from light energy, which is made of quanta called photons. This process relies on charge generation, charge separation and charge transport.(1)

During an excitation event, an electron in the ground state absorbs the energy of an incoming photon. This process generates a photoexcited electron in the excited state, and a photoexcited hole in the ground state.(1) For photons of all energies to be absorbed, uninterrupted range of excitation energies need to be available to the free charge carriers which is the case for metals. During relaxation, photoexcited charge carriers in metals lose their energy step by step, due to the continuous energy range available to them, to move back into the ground state by releasing phonons(2). The relaxation process in metals is typically in order of 10^{-12} seconds and is schematically shown in Figure 2.1(a).

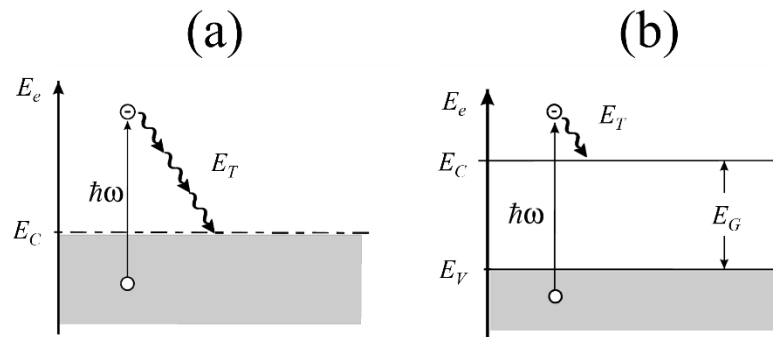


Figure 2.1. Schematic representation of excitation of an electron (a) into the conduction band (E_C) of a metal through absorption of a photon with energy $\hbar\omega$ and the subsequent loss of energy by releasing phonons of energy E_T , and (b) from valence band (E_V) into the conduction band of a semiconductor through absorption of a photon with energy $\hbar\omega$. E_F and E_G indicate Fermi energy and band gap energy, respectively.

It is precisely due to this uninterrupted continuous energy states that the photoexcited charge carriers in a metal can only remain in the electron gas for a short time before relaxation, which

makes their direct utilization rather cumbersome. In the case of semiconductor materials, on the other hand, the range of excitation energies is interrupted by an energy band gap (or forbidden gap, E_G) in which no energy states is allowed to exist, as schematically shown in Figure 2.1 (b). The energy states situated below and above the band gap are called the valance band (E_V) and conduction band (E_C), respectively. For an absorption event to occur in semiconductors, the energy of an incoming photon must be equal to at least that of the band gap ($\hbar\omega = E_G$, where \hbar is the Planck's constant and ω is the radial frequency). In this case, the electrons that have been excited to the upper states within the conduction band will start to lose their energy in a step-by-step fashion through generating phonons, like that of metals. However, once they reach the edge of E_C , they face the energy gap. At this point, they can no longer lose their energy stepwise, and they must release either many phonons or a photon. This is the reason that photoexcited electrons last longer in the excited state (lifetime in the order of 10^{-3} seconds) compared with metal, which therefore provides a window of opportunity to extract the excited electrons and convert their energy into electricity.(2) The extra energy of the excited electron generates a potential difference or electromotive force (e.m.f) which is the driving force behind the movement of an electron through a load in the external circuit.(1) This movement has to be in the opposite direction to that of a hole to generate electrical current.(3) For the photoexcited charge carriers to exit the absorber in the first place, there needs to be some built-in asymmetry at the two sides of the absorber medium which pulls them away. One way to achieve this, would be to generate a built-in field under dark equilibrium as a result of gradient in the work function, electron affinity or band gap between the two terminals of the device. In the case of electron affinity and band gap, a junction must be established at the interface between two different materials (heterojunction). However, the fields obtained with these methods are limited. In the case of work function, either a heterojunction or homojunction (when the same material on both sides of the junction is used). This method is the most widely used for solar cells and usually leads to large fields(1), with the most prominent example being p - n junctions (a junction established at the interface between an n - and a p -type semiconductor).

Within the context of light absorption, it is important to discuss solar irradiance, which is defined as the incoming power per area with a unit of $\text{mW}\cdot\text{cm}^{-2}$. Solar spectrum reaches the earth as thermal radiation emitted from the sun with a spectrum that resembles that of a black body radiation at 5900 K. During passing through the earth atmosphere, extra-terrestrial solar spectrum is filtered

out by the various atmospheric constituents. Therefore, the spectrum reaching the earth is attenuated both in shape and intensity, resulting in air mass (AM) 1.5 to be obtained, which corresponds to the Sun situated at an elevation angle of 42° . The attenuation of solar spectrum by the earth's atmosphere should result in a mean irradiance of 90 mW.cm^{-2} . However, per convention, the standard Global (G) terrestrial spectrum (AM 1.5G) is set to 100 mW.cm^{-2} .(1, 2, 4) The AM 1.5 Direct (D) spectrum is defined for solar concentrator work. The extra-terrestrial solar spectrum is known as AM 0. The three spectra are shown in Figure 2.2.

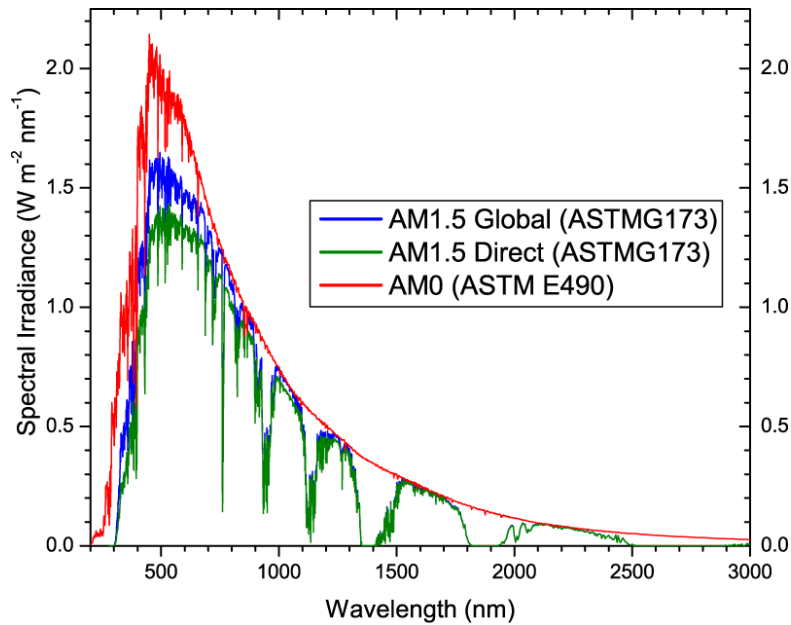


Figure 2.2: Comparison of the extra-terrestrial (AM 0) solar spectrum with standard terrestrial AM 1.5 in the case of both Global and Direct spectra.(5)

2.1.2. PV Metrics

A solar cell is characterized by four PV metrics (also called performance metrics). Figure 2.3 shows a typical $p-n$ junction solar cell during operation, *i.e.*, under illumination and connected to an external load resistance. This circuit will be discussed in more specific details later in this section.

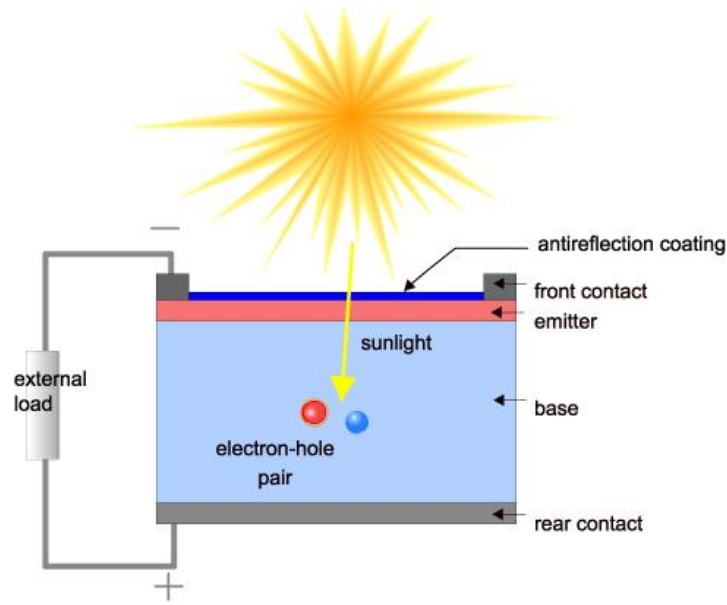


Figure 2.3: Illustration of a solar cell, under illumination, attached to a load through an external circuit.(6)

Under illumination, a voltage is developed across the circuit. If the terminals of the solar cell are isolated (which is the case for infinite load resistance), then the developed voltage (V) is called the *open-circuit voltage* (V_{OC}). The current drawn from the solar cell when its terminals are connected (zero load resistance), is called the *short-circuit current density* (J_{SC}). For any intermediate load resistance (R_L , between 0 and infinity), the solar cell generates a voltage value between 0 and V_{OC} , and a photocurrent density of $J = \frac{R_L}{V}$. Under dark, for the equivalent circuit of Figure 2.3, a potential difference is generated between the terminals of the solar cell like when the cell is placed under illumination. However, in this case because of any intermediate R_L , the generated current (also called the dark current) flows in the opposite direction of the photocurrent and therefore reduces the net value of J_{SC} . Correspondingly, the dark current-voltage (J - V) behavior is determined through Equation 1:(1)

$$J_{Dark}(V) = J_0(e^{\frac{qV}{nK_B T}} - 1) \quad (\text{Equation 1})$$

Where n is the ideality factor, K_B is the Boltzmann's constant, T is the temperature in degrees Kelvin and J_0 is the reverse saturation current density. The overall J - V characteristic of a solar cell is given by the sum of J_{SC} and $J_{Dark}(V)$, known as the superposition approximation, per Equation 2:(1)

$$J(V) = J_{SC} - J_0 \left(e^{\frac{qV}{n k_B T}} - 1 \right) \quad (\text{Equation 2})$$

Although the current that flows in the opposite direction of photocurrent in response to voltage in an illuminated solar cell is not formally equal to $J_{Dark}(V)$, the superposition principle is a reasonable assumption for many photovoltaic devices.

The dark and overall J - V response of a solar cell are shown in Figure 2.4. The cell generates power in the first quadrant (positive product of J and V) for voltages between 0 and V_{OC} . Conversely, for $V < 0$, the solar cell device acts as a photodetector which means it consumes power to generate a photocurrent. For $V > V_{OC}$ the solar cell is placed in the light emitting diode (LED) regime where it again consumes power.(1)

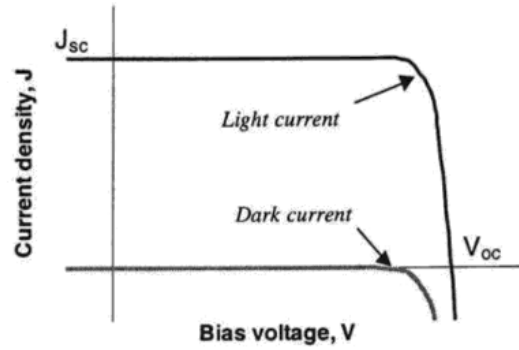


Figure 2.4: Current-voltage characteristics of a solar cell under illumination (light current) and dark (dark current). Based on the superposition approximation, the net current is obtained by shifting the bias-dependent dark current up by an amount equal to short-circuit current density.

The sign convention is such that photocurrent is positive.(1)

The third PV metric is called *fill factor (FF)* which defines the squareness of the J - V curves shown in Figure 2.4. The solar cell power density, P , is calculated from the product of J - V in the bias range where the cell generates power (0 to V_{OC}) and is given by Equation 3:(1)

$$P = JV \quad (\text{Equation 3})$$

The point on the J - V curve where the solar cell delivers maximum power, is called the *maximum power point (MPP)*, with the corresponding current density and voltage being J_m and V_m . Correspondingly, the FF is calculated through Equation 4:(1)

$$FF = \frac{J_m V_m}{J_{sc} V_{oc}} \quad (\text{Equation 4})$$

The fourth and final PV metric is called *power conversion efficiency* (*PCE*, or efficiency for short) is the power generated at MPP as a fraction of incident light power density, P_s , per Equation 5:(1)

$$PCE = \frac{J_m V_m}{P_s} = \frac{J_{sc} V_{oc} FF}{P_s} \quad (\text{Equation 5})$$

2.1.3. Shockley-Queisser Limit

It is important to note that the *PCE* and power output of a solar cell cannot indefinitely increase. For the case of an ideal solar cell with a single absorber, the maximum obtainable *PCE* is defined by the Shockley-Queisser (SQ) limit(7) with the following assumptions:

- Every incoming photon that has an energy exceeding the band gap is absorbed. This would make absorptivity a step function; 0 for $E < E_g$ and 1 for $E > E_g$
- Absorption of a photon with $E > E_g$ leads to the generation of exactly one electron-hole pair in the outer circuit contributing to J_{sc} . From assumptions 1 and 2, the J_{sc} of a solar cell in the SQ limit follows from Equation 6:(8)

$$J_{sc,SQ} = q \int_{E_g}^{\infty} \Phi_{sun}(E) dE \quad (\text{Equation 6})$$

where q is the elementary charge and Φ_{sun} is the solar spectrum.

- The generated electron-hole pairs lose their energy in excess of E_g , to the average energy of a thermalized electron-hole pair, which places them in thermal equilibrium with the solar cell as a result. The luminescence emitted by thermalized carriers in this case is calculated via Equation 7:(8)

$$\Delta\Phi_{lum} = \int_{E_g}^{\infty} \Phi_{bb}(E) dE \left[\exp\left(\frac{qV}{kT}\right) - 1 \right] \quad (\text{Equation 7})$$

where Φ_{bb} is the black body spectrum at temperature T of the solar cell, and is calculated through Equation 8:(8)

$$\Phi_{bb} \approx \frac{2\pi E^2}{h^3 c^2} \exp\left(\frac{-E}{kT}\right) \quad (\text{Equation 8})$$

with c being the speed of light.

The electron-hole pairs can either be collected at the respective contacts or they recombine radiatively, whereby a photon is generated.

within the SQ limit the only permitted form of recombination is radiative, also called bimolecular since only two particles are involved in this process. The principles of detailed balance necessitate that an absorption event can take place only when emission of a photon is allowed.(9) Therefore, by equating the rate of absorption with that of recombination in equilibrium, the radiative recombination coefficient (k_{rad}) is obtained through Equation 9:(10)

$$k_{rad}n_i^2 = \int_0^\infty 4\alpha n_r^2 \Phi_{bb} dE \text{ (Equation 9)}$$

Where α is the absorption coefficient, n_r is the real part of refractive index, and n_i is the intrinsic carrier density. The rate of radiative recombination is calculated from Equation 10:(8)

$$R_{rad} = k_{rad}(np - n_i^2) \text{ (Equation 10)}$$

- Some of the emitted photons are re-absorbed back into the solar cell which contribute to the PV action. This is called photon recycling. In an ideal solar cell, the dark current is the recombination current in the dark and is defined per Equation 11:(8)

$$J_{0,SQ} = q \int_{E_g}^\infty \Phi_{bb}(E, T = 300 K) dE \text{ (Equation 11)}$$

Consequently, the J - V curve under illumination in the SQ limit follows as Equation 12:(8)

$$J = J_{0,SQ} \left[\exp\left(\frac{qV}{kT}\right) - 1 \right] - J_{sc,SQ} \text{ (Equation 12)}$$

Finally, the V_{OC} in the SQ limit is defined per Equation 13: (8)

$$V_{OC,SQ} = \frac{kT}{q} \ln \left(\frac{J_{sc,SQ}}{J_{0,SQ}} + 1 \right) \text{ (Equation 13)}$$

- The contacts interfacing absorber material are ideal since they only exchange one type of charge carrier (electron or hole) with the absorber and operate with negligible resistance.

While the work of Shockley and Queisser is arguably the most important theoretical contribution to PV energy conversion, it also relies heavily on idealized assumptions as mentioned above which can never be fully met in real world solar cells.(11)

2.1.4. Non-Ideal Solar Cells

Thus far, we have been considering the case of an ideal solar cell. However, real cells deviate from the idealized framework of SQ limit (Section 2.1.3). As an example, the absorptivity is smeared out close to the band edge due to parasitic absorption and sub-gap states(12, 13, 14), therefore deviating from the step-function assumption. Additionally, while the only allowed recombination mechanism within the SQ limit is radiative, majority of recombination in real solar cells are non-radiative.(4) In general, three sources of non-radiative recombination can be identified(1, 2, 4, 15, 16):

- Auger recombination: This process is inherent to all semiconductor materials but is more prominent for indirect-gap types. This is because in semiconductors with indirect band gap, recombination would require exchange of a momentum that cannot otherwise be compensated by emitting a photon during a radiative recombination event. Since both momentum and energy must be conserved, then they will be transferred to another electron in the conduction band (or hole in the valence band), increasing its energy. This is then followed by thermalization of the charge carrier to the band edge. Since three particles are involved in this process (either two holes and one electron, or two electrons and one hole) then Auger process is a third-order recombination mechanism, becoming more likely for increased charge carrier concentration. The total rate for Auger recombination is given by Equation 14:(17)

$$R_{Auger} = C_n n^2 p + C_p n p^2 \text{ (Equation 14)}$$

Where n and p are the free electron and hole concentrations, C_n and C_p are the Auger coefficients. The term $C_n n^2 p$ indicates an Auger process where the excess energy is transferred to another electron, while the term $C_p n p^2$ denotes the Auger process for when the excess energy is transferred to another hole.

- Shockley-Read-hall (SRH) recombination: This is a first-order recombination process since it involves a charge carrier and a defect state in the band gap (electronic traps), and it is generally expressed as a bulk mechanism. The general rate for SRH is expressed per Equation 15:

$$R_{SRH} = \frac{np - n_i^2}{\tau_p(n + n_i) + \tau_n(p + p_i)} \quad (\text{Equation 15})$$

Where τ_p and τ_n denote hole and electron lifetimes, respectively. For a p -doped semiconductor having similar electron and hole lifetimes, the Equation 15 can be simplified to:

$$R_{SRH} \propto \frac{n}{\tau_{SRH}} \propto N_T \sigma_T \quad (\text{Equation 16})$$

Where τ_{SRH} is the time constant for SRH recombination and depends on trap density (N_T), carrier capture cross section (σ_T) and thermal velocity (v_{th}). Defect states could arise from crystal imperfections, impurities, grain boundaries, etc.

- Surface recombination: As the name suggests, this process takes place at the surface of the semiconductor according to Equation 17:

$$R_{surf} = S(n - n_0) \quad (\text{Equation 17})$$

Where S is the surface recombination velocity and n_0 is the equilibrium charge carrier density at the interface. This type of recombination becomes most relevant at the surface of the absorber adjacent to the contacts, where high S values can lead to loss of the charge carriers at their non-selective interface. In this regard, surface passivation as well as contact selectivity and conductivity for their respective charge carriers become important.

Radiative and non-radiative recombination mechanisms are displayed schematically in Figure 2.5.

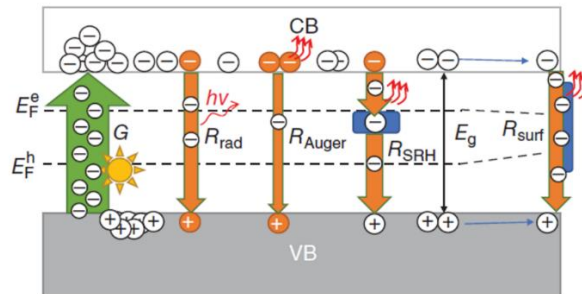


Figure 2.5: Illustration of the equilibrium between optical charge carrier generation rate (G) and various recombination mechanisms at open-circuit.(4)

Overall, the contacts can substantially dissipate the output power through parasitic resistances as well as other loss sources such as shunting. Series resistance (R_S) heavily affects the FF and, as the name suggests, arises from the resistance of the cell components. This effect is strongly correlated with non-selective and low conductivity contact materials, amongst other causes.(18, 19, 20, 21) Parallel or shunting resistance (R_{SH}) results from leakage of the current through the cell, around the edges of the device and between contacts of different polarity. This parameter also affects FF and is majorly witnessed in devices with poor rectification as well as direct contact between anode and cathode resulting (due to pin holes) in otherwise well-functioning cells.(22, 23, 24, 25, 26) For an optimal device, R_S and R_{SH} need to be as low, and as high as possible, respectively.

Considering the parasitic resistances, the more generalized equation for a solar cell is given by:(1)

$$J = J_{SC} - J_0 \left(e^{\frac{q(V+J A R_S)}{K T}} - 1 \right) - \frac{V+J A R_S}{R_{SH}} \quad (\text{Equation 18})$$

As such, a representation of the equivalent circuit for a solar cell under operation is displayed in Figure 2.6.

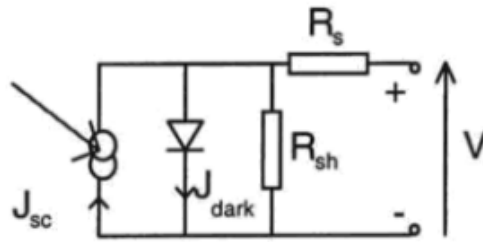


Figure 2.6: Equivalent circuit for a solar cell taking into account the effect of series resistance (R_S) as well as shunting resistance (R_{SH}). (1)

2.2. A Brief History of Solar Cell Development

The photovoltaic effect, which is the basic principle behind operation of solar cells as explained in Section 2.1, was first reported in 1839 by the French physicist, Edmund Becquerel.(27, 28) In his experiments, light of different wavelengths were incident on a platinum (as well as silver) electrode coated with silver chloride ($AgCl$) and silver bromide ($AgBr$) immersed in electrolyte. This

resulted in the generation of an electric current. The setup employed by Becquerel is schematically shown in Figure 2.7.

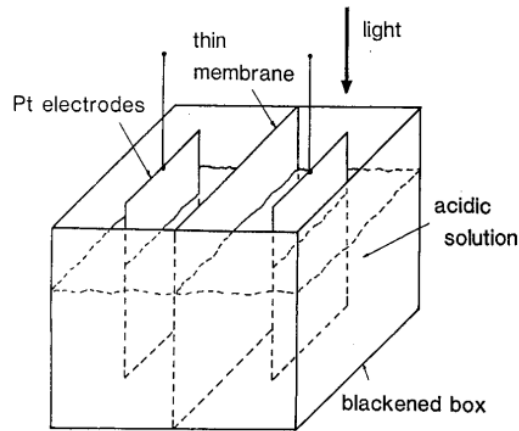


Figure 2.7: Schematic description of the setup employed by Edmond Becquerel which led to the first ever reported observation of photovoltaic effect.(29)

Despite this development, it was not until 1876 where the first photovoltaic device was constructed by British scientists William Adams and Richard Day.(30) In their device, light incident on a cylindrical vitreous selenium pressed from two sides by heated platinum wires generated electric current, as seen on Figure 2.8.

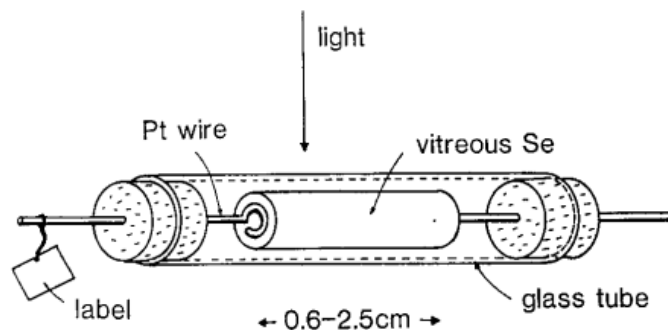


Figure 2.8: Schematic description of the setup employed by Adams and Day in observing photogenerated current in an all-solid-state system for the first time.(29)

This effect was initially attributed to light-induced crystallization of selenium in contact with heated platinum. However, the actual reason, as discovered by Goldman and Brodsky in 1914(31), was the barrier against current flow at one of the semiconductor-metal interfaces. Later in 1930s,

the theory of metal-semiconductor junction was laid out by Neville Mott and Walter Schottky.(29) The same underlying principle would then explain the generation of photocurrent from the first ever solar cell in 1894 made by Charles Fritts.(32) The cell was prepared from selenium contacted by gold on one side and another metallic contact (e.g. brass) on the other, as schematically displayed in Figure 2.9. This was the first ever report of a thin film solar cell with a large area of around 30 cm².

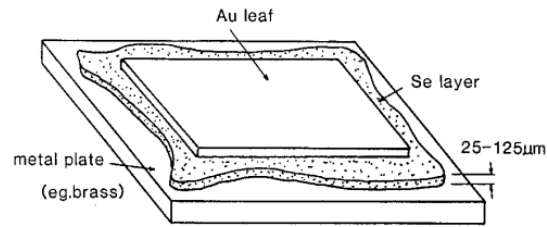


Figure 2.9: Schematic description of the first large-area ($\sim 30 \text{ cm}^2$) solar cell by Fritts in 1883, by pressing a thin selenium layer between gold and another metallic plate.(29)

At the same time as the developments with selenium, copper-copper oxide, lead sulphide and thallium sulphide heterojunctions were showing rectifying behavior. From 1930 onward, and with the development of metal-semiconductor junction theories and improvement in metal contact patterning, selenium-based photovoltaics were refined and in fact showed superior performance to copper-copper oxide devices, with *PCE* of about 0.4%.(29, 33) However, the major development in the 1930s was related to silicon, which was the subject of intense research in point-contact rectifiers of metal to crystal surface. For the purpose of ultra-high frequency applications, the point contact rectifiers of tungsten to silicon were in high demand which therefore incentivized production of high purity silicon. The first ever report on silicon-based solar cell devices was in 1941. In that device, a cast silicon ingot was used, prepared from acid-leached metallurgical grade silicon which was cooled from top melting. The efficiency offered by this device was around the same as that of the thin film-based devices available at the time. Next to that, the costly fabrication method for Si solar cells did not grant them any advantage over thin film technology.(29) Despite the slow progress of silicon solar cells, in 1941, Ohl found out that ingots of cast silicon had a natural barrier forming on them, resulting in the formation of rectifying junction. This discovery eventually led to the understanding of *n* and *p* doped silicon. Further studies focused on the

properties of donors and acceptors, as well as how to introduce them in a controlled fashion. Although the preliminary understanding of doping took place after the first silicon device was developed, it nevertheless helped with achieving the efficiency of 6% in 1954 for Si-based solar cell, as the *p-n* junction offered a much better rectifying action, and therefore photovoltaic performance than Schottky barriers. Around the same time, theoretical research on the maximum achievable efficiency based on the light absorber band gap had started taking off. These studies, in turn, indicated the high potential of semiconductor compounds such as cadmium sulphide, cadmium telluride and gallium arsenide due to their superior optoelectronic properties.(29) Although other alternatives such as CuInSe₂ were introduced, the photovoltaic was (and still is) dominated by Si-based solar cells due to the inevitable fact that the research in the microelectronics field had given silicon a jump start. Regardless of these developments, the complexities involved with preparing silicon solar cells, as well as the high cost of production (~~ca. \$ 200 per Watt~~) rendered them an attractive candidate majorly for space applications and remote locations where the transport of fuel were cumbersome.(1) However, in mid 1970s the table finally turned in favor of photovoltaics as the energy crisis took place. Considerations of costs coupled with energy balance favored thin film technologies over crystalline ones (c-Si and gallium arsenide- GaAs). The thin film devices that actually entered production were cadmium sulphide (CdS)/copper sulphide (Cu_xS), CdS/cadmium telluride (CdTe), CdS/copper (indium, gallium) diselenide - Cu(In,Ga)Se₂- and hydrogenated amorphous silicon (a-Si:H).(34) Despite promising predictions and two decades of research on CdS/Cu_xS, it eventually was ruled out as a suitable absorber material due to stability issues as well as drastic reduction of efficiencies when produced in large scale. Since a-Si:H matured earlier than the other remaining candidates in production, it led the thin film technology production.

As the research on photovoltaics started to expand driven from the menace of climate change, candidates other than purely inorganic materials were also explored. In particular, research into organic photovoltaics (OPVs) started from the 1990s. In an all-organic solar cell, a polymeric (or small molecule) light absorber (which also acts a hole transport medium) is interfaced with an organic transport layer tasked with conducting the electrons through it.(35, 36, 37) A variant of OPVs, was introduced in 1991 by Graetzel and O'Regan, termed dye-sensitized solar cells (DSSCs)(38), as a low-cost alternative to previous solar cell generations. This type of solar cell utilizes an organic dye as light absorber infiltrating an inorganic mesoporous scaffold with a high

surface area as the electron transport layer (ETL), interfaced with a liquid electrolyte which acts as the hole transport layer (HTL). Due to leakage concerns, later the liquid electrolyte was substituted with a molecular-type solid state HTL, such as 2,20,7,70-tetrakis (N, N-p-dimethoxy-phenylamino)-9,90-spirobifluorene (known as spiro-OMeTAD). The underlying principles for both categories are similar, with the exception of electron hopping through the HTL in solid state DSSC.(39)

In 2009, a variant of DSSCs was introduced by Kojima et al.(40), in which the organic dye was replaced with hybrid organic-inorganic compounds with the composition of methylammonium lead iodide ($\text{CH}_3\text{NH}_3\text{PbI}_3$, also referred to as MAPI) and methylammonium lead bromide ($\text{CH}_3\text{NH}_3\text{PbBr}_3$), both having perovskite crystal structure, which eventually resulted in this class of photovoltaics to be called perovskite solar cells. The research on perovskite-based PV certainly capitalized on over 20 years of research on DSSCs and OPVs, providing it with a jump start in the power conversion efficiency game.

2.3. Evolution of Perovskite Solar cells

Although perovskites were first introduced as a photovoltaic candidate in 2009, the discovery of perovskite crystal form dates to 1839. At that time, the first ever perovskite type mineral was collected by August Alexander Kaemmerer in Russia. He sent the samples for analysis to Gustave Rose in Germany who then determined the composition to be calcium titania (CaTiO_3).(41) This new mineral was named after the Napoleonic Wars veteran, Count Lev A. Perovskiy.(4) Further interest in CaTiO_3 and perovskite-type minerals was reignited in 1922 through the works of Victor Goldschmidt which led to what is known today as Goldschmidt tolerance factor. Apart from their application in paint and pigment industries, titanate-based oxide perovskite were also studied for the structural and biaxial optical properties.(42, 43) The actual research interest in electronic properties of oxide perovskites was ignited in 1940s with the discovery of ferroelectricity in BaTiO_3 .(44, 45) Meanwhile back in 1893 another class than titanates perovskite compounds were synthesized that of inorganic cesium lead halide perovskites of formula CsPbX_3 ($\text{X}=\text{Cl}, \text{Br}, \text{I}$). (46) The first X-ray diffraction studies demonstrating that their crystallization in tetragonal/orthorhombic and cubic phase, at room temperature and high temperature, respectively, were conducted around 60 years later.(47, 48) Around the same time, discovery of CsPbX_3 intense

luminescence attracted research interest into the electronic properties which revealed its frequency-dependent photoconductive response.(4) At this point, research into 2D perovskites had already been initiated, showing very interesting ferro and anti-ferromagnetic characteristics(49, 50, 51, 52), as well as elucidating the underlying causes for such behaviors (these structures are discussed in Section 2.3).

The venture into halide perovskite-based optoelectronics was initiated with hybrid organic-inorganic two-dimensional (2D) structures, and particularly the natural self-assembly of quantum well structures in $(\text{RNH}_3)_2\text{MX}_4$ compounds.(53, 54, 55, 56, 57, 58, 59) These structures were particularly attractive for a few reasons. One was the ease of fabrication and the ability to tune the structure at the molecular level which considered to be an advantage over artificial quantum wells, in which thickness fluctuations broadened the optical properties.(42) In addition, the organic cation spacer in between the inorganic sheets offered quantum confinement effects capable of enhancing exciton binding energy, oscillation strength and lifetime.(56, 60) Moreover, for tin-based hybrid compounds, a transition from semiconducting to metallic behavior was observed as a function of adjacent organic layers. This pointed to the electronic tunability of these structures.(61, 62) With further exploration of the unique optoelectronic properties of hybrid perovskites, they started to find their way into organic-inorganic light emitting diodes (LEDs) and semiconducting channels in thin film field-effect transistors (FET).(63, 64, 65, 66, 67, 68) Despite such advances, however, it took some more years before the research into perovskite-based photovoltaics commenced.

The original research on PSCs started in Japan back in 2005. The process started with Akihiro Kojima, a then-graduate student at Tokyo Polytechnique University, visiting the laboratories of Miyasaka at Toin University of Yokohama. The purpose of Kojima's visit was to study the possibility of employing lead halide perovskite material as a sensitizing medium on titania (TiO_2) electrodes. This project was also, in part, a continuation of Kenjiro Teshima's work from 1997 to 2002 on quantum photochemistry of self-organized quantum conferring structures using 2D halide perovskites. At the time of Kojima's visit at Miyasaka's laboratory, Teshima worked as a researcher at Peccell Technologies, Miyasaka's venture company specializing in the application of DSSCs had been established on the campus of Toin University of Yokohama. Therefore, the collaboration between Kojima and Teshima can be considered as the first seed of perovskite-based photovoltaic research. In 2006, results corresponding to the use of $\text{CH}_3\text{NH}_3\text{PbBr}_3$ perovskite

nanoparticles as sensitizer in DSSCs with *PCE* of 2.2% was showcased in Electrochemical Society's Annual Meeting.(69) Further research on perovskite sensitizers was carried by Kojima in University of Tokyo, from 2005 to 2010. Back then, perovskites were assumed to behave as a quantum dot structure which meant the loading of precursor solution and its deposition through spin coating was adjusted in a way to yield the thinnest possible coverage over the thick TiO₂ mesoporous scaffold in DSSCs architecture. The optimized cell structure rendered a mere *PCE* of 3.8% which led to the first peer-reviewed paper on perovskite-based photovoltaics in 2009.(40) However, at this point in time, the perovskite-based photovoltaics were not attracting much attention due to the fact the liquid electrolyte (containing lithium halide) was very corrosive towards the perovskite layer. This issue resulted in a two-year hiatus in perovskite-based photovoltaics research until in 2011 an international collaboration between Nam Gyu Park and Michael Graetzel's research groups lead to the first-ever published work on all solid-state DSSCs(70) using perovskites as sensitizer and spiro-OMeTAD as the organic hole transport layer. Spiro-OMeTAD was originally developed for organic LEDs back in 1997(71) but later introduced as an effective replacement for the organic electrolyte in DSSCs(72). Demonstration of all solid-state DSSCs garden a solid foot hold for halide perovskites in the field of photovoltaics. Up until this point, all the published work on perovskite-based PV was on sensitization type. In 2012, there came a pivotal shift from DSSCs to PSCs upon another international collaboration, between Takuro Murakami from Japan (supervised by Miyasaka) and Michael Lee (from Henry Snaith's group at Oxford) which led to a publication by Snaith et al. in which they reported a mixed halide perovskite composition of CH₃NH₃PbI_{3-x}Cl_x coating an insulating alumina scaffold, showing a *PCE* of 10.9%.(73) This mixed perovskite composition demonstrated better stability and carrier transport than MAPI. Additionally, the authors coated the mesoporous TiO₂ scaffold with a thin layer of perovskite medium as opposed to the conventional nanocrystals. Moreover, in that work, it was demonstrated that the presence of a TiO₂ porous network in conjunction with a non-conducting Al₂O₃ scaffold, not only did not suppress PV action but also boosted the *V_{OC}*. Therefore, halide perovskites proved to be more than mere sensitizers.(74) Additionally, the results showcased that the perovskite material was capable of transporting photogenerated charges by itself and even operate without the presence of any metal oxide scaffold. This is known as the ambipolar transport behavior which is used for explaining the absence of photoluminescence intermittency in isolated perovskite nanoparticles.(75) This is the reason 2D and three-dimensional

(3D) halide perovskites are believed to behave as an intrinsic semiconductor between *n*- and *p*-type layers in the PSC architecture, as explained in Section 2.3.

In 2013, application of sequential deposition method for MAPbI₃(76) and two-source vapor deposition(77) for CH₃NH₃PbI_{3-x}Cl_x resulted in optimized *PCE* values exceeding 15%. Later in 2014, Sang Seok's group reported 16.2% efficiency by using CH₃NH₃PbI_{3-x}Br_x as the perovskite absorber and a poly-triarylamine-based HTL.(78) This *PCE* value was increased to 17.9% in 2015.(79) Adjusting the thickness of the perovskite medium infiltrated in the TiO₂ scaffold versus that of the capping layer was cited as the strategy for the enhanced efficiency. Over the years, PSCs have become one of the most intensely researched topics with new developments, breakthroughs and new record efficiencies reported at an unprecedented speed. The highest efficiency reported for PSCs, at the time of writing this thesis, is 25.8%(80), rendering comparable *PCEs* with that of the leading technologies such as c-Si, CdTe and Cu(In,Ga)Se₂ (also known as CIGS).

Metal halide perovskite compounds are endowed with high absorption coefficient,(39, 81) defect tolerance,(82, 83) ambipolar transport,(73, 84) exceptionally long charge carrier diffusion lengths,(85) and spontaneous exciton dissociation,(86) to name a few, which kickstarted the next decade of PSCs research. Such impeccable optoelectronic properties of halide perovskites have enabled them to gain momentum in other applications such as tandem PVs(87, 88, 89), water-splitting(90, 91, 92), photodetectors(93, 94, 95), scintillators,(96) X-ray detectors,(97, 98) optical gain media(99, 100, 101, 102, 103, 104) and LEDs,(105, 106). In fact, there comes a greater level of appreciation for the unique properties of metal halide perovskites when considering that these materials are solution-processed at low temperatures and reduced manufacturing costs. Yet, they show comparable beneficial properties, at least in some respects, as top semiconductor performers such as GaAs(107, 108, 109, 110) which are manufactured through complex, expensive and energy exhaustive processes.

2.3. Perovskite Crystal Structure

One of the features of PSCs that have attracted interest is their compositional tunability (Further addressed in Section 2.6.3.1), which in turn enables the modifying of their electrical, optical, chemical and physical properties. However, only some elements can come together to form a stable perovskite crystal structure. The restrictions imposed on formability are reflected in the works of

Goldschmidt, who first described the perovskite crystal structure and the considerations regarding the so called tolerance factor as defined back in 1920s.(111) The Goldschmidt tolerance factor (τ) is a semi-empirical geometric parameter. It is also one of the major contributors in determining the intrinsic structural stability of the 3D perovskite structure and is defined based on the effective ionic radius (r) of the constituents, per Equation 19(112)that applies to the ABX_3 structure where A and B are cations and X is either a halogen or oxygen.

$$\tau = \frac{r_A + r_X}{\sqrt{2}(r_B + r_X)} \quad (\text{Equation 19})$$

When oxygen is used as the anion then A and B tend to be divalent and trivalent cations, respectively. However, when a halogen is used as anion, then A and B sites are occupied by monovalent and divalent cations, respectively.(39) In their structure, the B-site cation is octahedrally coordinated in a corner-sharing BX_6 configuration, and the A-site cation fits into the cubo-octahedral sites formed between them, forming an AX_{12} polyhedron. The cubic perovskite crystal structure is shown in Figure 2.10. The size of the A-site element has important implications over the dimensionality of the octahedral framework (*vide infra*)(67), as explained later in this section. It should be noted that halide perovskite composition having a mix of organic molecules and inorganic atoms on their A-site are referred to as “*hybrid organic-inorganic*”. This common nomenclature differentiates hybrid perovskites from related organometallic structures such as metal-organic frameworks due to the absence of covalent interaction between organic and inorganic species.

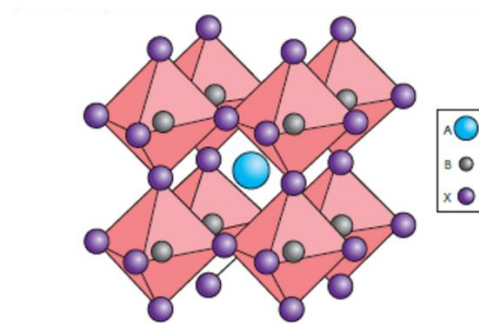


Figure 2.10: The cubic perovskite crystal structure with ABX_3 formula, where A is a monovalent cation, B is a divalent cation and X is a halide.(74)

The ideal perovskite structure $0.9 < \tau < 1$ exhibits cubic symmetry, in which the A site cation fits within the cages provided by the corner-sharing BX_6 octahedra. For the range of $0.8 < \tau < 0.9$, distorted perovskite structure with distorted octahedra is obtained. That being considered, a compound such as $MAPbI_3$ with $\tau=0.9$, in the middle of stability range, would be expected to have stable photoactive perovskite formation. This is in fact confirmed by the single crystal data showing that this material crystallizes in tetragonal space group of $I4cm$ at room temperature. At temperatures around -113°C , MAPI undergoes a phase transition to orthorhombic phase (with space group $Pnma$). This phase is outside the operation window for terrestrial applications and therefore its inferior PV properties are not of concern. The high temperature phase of MAPI is cubic which is observed at 54°C . The corresponding phase transition is slow and reversible and seems to be unproblematic for PV applications. The tolerance factors of $\tau > 1$ and $\tau < 0.8$ indicate that perovskite structure is not feasible. Moreover, having a tolerance factor that is equal to the boundaries of 0.8 or 1 can result in structural instability and therefore degradation into non-perovskite (and photoinactive) phases.(113) The two most notable examples of such an effect are formamidinium lead iodide ($FAPbI_3$) with $\tau=1$ and $CsPbI_3$ with $\tau=0.8$, with both decompose into hexagonal δ -phase. As will be discussed in Section 2.6.3.1, an effective strategy in improving the PSC stability (as well as performance) has been using mixed-cation and anion composition that effectively brings τ closer to the middle of the stability zone. For mixed perovskites with a general composition of $A_xA'_{1-x}B(X_yX'_{1-y})_3$, the effective cation radius on the A site and anion radius on the X site, denoted as $r_A(eff)$ and $r_x(eff)$, respectively, is calculated via the following equations(4):

$$r_A(eff) = xr_A + (1 - x)r_{A'} \quad (\text{Equation 20})$$

$$r_x(eff) = yr_x + (1 - y)r_{x'} \quad (\text{Equation 21})$$

These are then plugged into the equation for calculating Goldschmidt tolerance factor (Equation 19).

The second geometrical constraint (less frequently used) is called the octahedral factor (μ_{oct}) which coupled with τ provides a more defined framework for perovskite stability. μ_{oct} is defined as per Equation 22:(114)

$$\mu_{oct} = \frac{r_B}{r_x} \quad (\text{Equation 22})$$

with the typical range being $0.44 \leq \mu \leq 0.9$, indicating octahedral stability. Figure 2.11 shows the stable formation range for the A and X site combinations in the case of lead (Pb) and tin (Sn)-based perovskites.

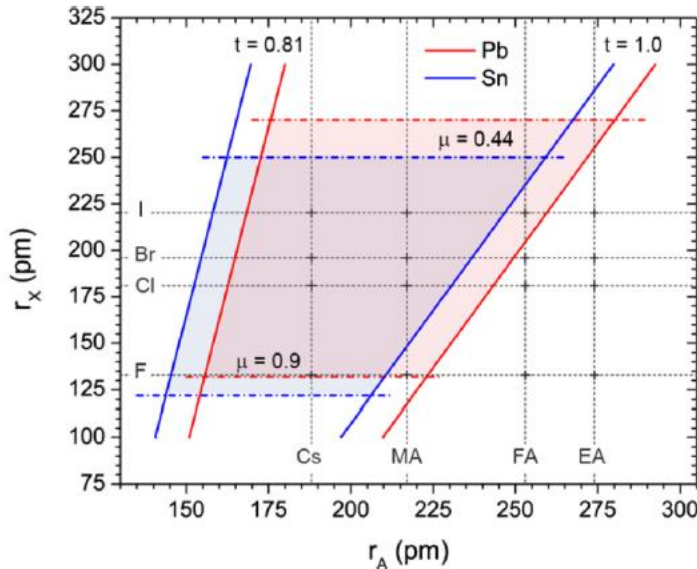


Figure 2.11: Formability of 3D lead (red) and tin (blue) halide perovskites as a function of A-site cation and halide anion radii. Solid and dashed lines mark the boundaries of the tolerance and octahedral factors, respectively. (42)

On this Figure, the approximate ionic radius for some of the most commonly used A-site cations such as methylammonium/MA (CH_3NH_3^+), formamidinium/FA ($\text{HC}(\text{NH}_2)_2^+$), ethylammonium/EA ($\text{CH}_3\text{C}_2\text{NH}_3^+$), as well as X-site anions are provided along the abscissa and ordinate, respectively.(115). If the intersection of the corresponding lines falls within the limits of formation (shaded region on Figure 2.11) then the desired perovskite composition is likely to form.

The Goldschmidt's tolerance factor and cubo-octahedral factor were discussed in their classical forms above. However, over the years there have been some modification proposed to both factors (116, 117, 118), due to two level of complexities when analyzing 3D halide perovskites. First one is that in the case of hybrid organic-inorganic compounds, the A-site organic molecule is in fact non-spherical which adds uncertainty to the analysis. To take this matter into effect, a rigid sphere

model has been proposed to determine the effective molecular cation radius, per Equation 23:(116, 118)

$$r_{A,eff} = r_{mass} + r_{ion} \text{ (Equation 23)}$$

where r_{mass} is the distance from the molecular center of mass to the furthest non-hydrogen atom, and r_{ion} is the ionic radius of the most distant atom. Thus, for a more accurate calculation of the tolerance factor, the $r_{A,eff}$ is plugged into Equation 19. Secondly, for all types of halide perovskites, the issue of reduced electronegativity of X-site anion (compared with oxide-type perovskites) has to be considered. When highly electronegative anions such as oxide and fluoride are replaced by less electronegative heavy halide such as iodide, then a larger degree of covalency results than what is predicted from a rigid sphere model. This, in turn, shortens the metal-halide bond length relative to Shannon metal cation radii, which was originally calculated strictly from oxide and fluoride coordination environments.(115) This issue was resolved by fixing the halide radii to those given by Shannon, which resulted in a series f divalent B-site cations whose radius changes as a function of halide chemistry.(117) This outcome pointed to the fact that the difference in electronegativity of B- and X-site components, certainly affects the deviation from Shannon radii which means modifications to bond ionicity are in fact responsible for the observed discrepancies in ionic radius. By correcting for both above-mentioned issues, the accuracy of predicting the formation of new halide perovskite compounds can be improved.(42)

It is of immense importance to note that, a favourable formation predicted by Goldschmidt tolerance factor and the cubo-octahedral factor, cannot predict other aspects of stability as well as phase transitions. For instance, MAPbI₃ despite showing formational stability, lacks thermal stability.(4) It is widely known that the highest symmetry phase for fully inorganic halide perovskites (e.g. CsPbI₃) is cubic (space group $pm3m$). Sequential transitions to other phases lowers the cubic symmetry through octahedral rotations that can be described using Glazer's notation(113, 119, 120, 121) (with smaller cations such as cesium (Cs), MA and FA causing larger rotations).(113, 122) Such distortions can sometimes be drastic enough so that the perovskite structure is no longer stable even despite favorable formation criteria.(113, 119, 123)

Apart from formability, the effective ionic radius also impacts the dimensionality of perovskite. Particularly, by tuning the radius of the A-site cation, symmetry and therefore optical band gap can

be modulated, which then affects the overall properties.(4) As an example, when large alkylammonium cations are used in the A-site, the tolerance factor exceeds one, which causes the 3D structure (which is most commonly studied for PV applications) to be broken down into sheets of 2D $[MX_4]^{2-}$ separated by the organic cation layers. Depending on the valence of the large organic cation, distinct structures are obtained. In the case of monovalent cation, A_2PbX_4 is formed where the inorganic sheets are separated by two layers of the cations which are stabilized through van der Waals forces. When divalent cation is utilized, $APbX_4$ is obtained where each organic cation bonds to the two inorganic layers sandwiching it from the two sides.(4) In both cases, these 2D perovskite structures are stabilized through hydrogen bonding between halogens in the inorganic sheets and the organic cations. Due to having a much larger band gap than the inorganic sheets, the organic cation acts as an insulating barrier. This renders the inorganic sheets to behave as isolated semiconductor with excitons believed to be confined within this part of the structure(124). Therefore, the width of the barrier formed by the organic cations becomes relevant to quantum confinement effects which grants 2D perovskites unique electrical and optical properties, as well as moisture stability (due to the hydrophobic nature of the organic cation). Another important aspect regarding the choice of organic cation is generating an organic-inorganic quantum well structure of type I and type II band offset which influences the flowing direction of photogenerated charge carriers.(125, 126, 127, 128) However, the most important criterion for the organic A site cation even in lower dimensional perovskites, remains to be its ability to fit within the cage formed by four-nearest neighbour MX_6 octahedra.(129) Apart from 2D perovskites, an additional category of quasi-2D perovskites (also known as Ruddlesden-Popper series) can also be identified. These structures have the general formula of $A_2B_{m-1}M_mX_{3m+1}$.(61, 130) In addition to the described symmetries, one-dimensional (1D) chain materials, zero-dimensional (0D) isolated octahedra, as well as a large library of superstructures and compositions including Aurivillius and Dion-Jacobson phases have also been introduced.(131, 132, 133)

2.4. PSC Device Architecture

In understanding differences in operational principles between PSCs and previous solar cell generations, we start with the three major types of architecture used for assembling PSCs as shown in Figure 2.12.

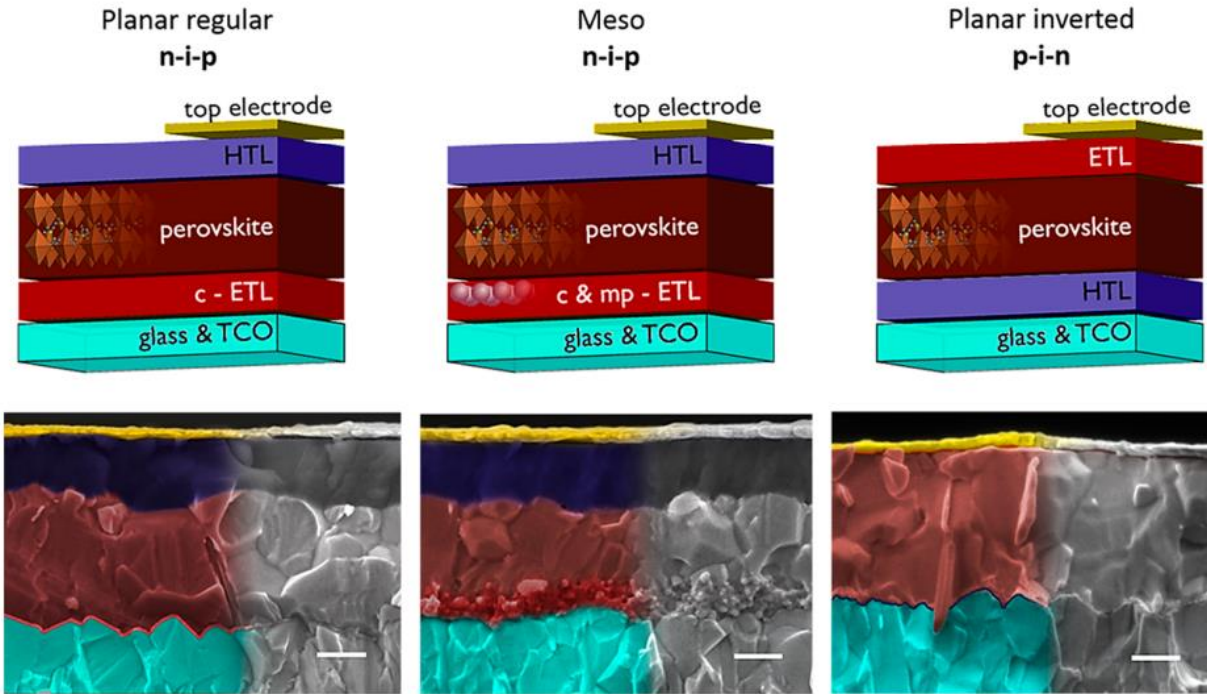


Figure 2.12: Schematics of the three most commonly utilized PSC architectures, comprising planar regular (*n-i-p*), mesoporous (*n-i-p*), and planar inverted (*p-i-n*) architectures.(134)

In all architectures, the perovskite layer is sandwiched between an *n*-type semiconductor (as ETL, e.g., TiO₂) and a *p*-type semiconductor (as HTL, e.g., spiro-OMeTAD) which are tasked with transporting photogenerated electrons and holes, respectively. What sets the different architectures apart is firstly the order with which the layers are stacked. In the *n-i-p* category (also, known as the regular type), it is the *n*-type semiconductor that is deposited over the transparent conductive oxide (TCO), while in the *p-i-n* category (also known as the inverted type), the *p*-type semiconductor directly interfaces the TCO. Secondly, depending on the presence of a scaffold within the *n-i-p* category, two types of PSC architectures can be differentiated: planar *n-i-p* (where the ETL is composed of only a thin compact layer, without any scaffold) and mesoporous *n-i-p* (where the ETL is a combination of a thin compact layer as well as a mesoporous scaffold). In all cases, the stack is fully finished by depositing a metal contact over the topmost layer.

Apart from the architectures explained above, there are other structures that have been used for assembling PCSs for example the ETL-free or the HTL-free types which as the name suggests, do not utilize an ETL or HTL, respectively, in their assembly. These structures are schematically shown in Figure 2.13.

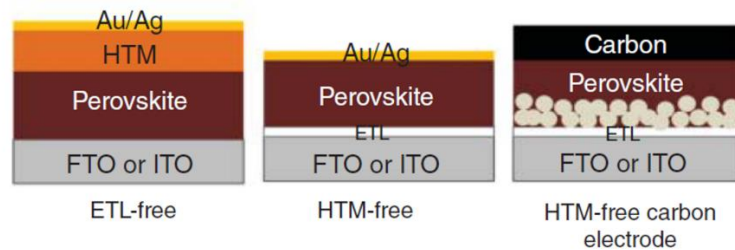


Figure 2.13: Schematics of some of the less-frequently utilized PSC architectures including ETL-free, HTL-free and HTL-free with a carbon electrode. (135)

It was precisely the functionality of such type of architectures (as well as replacing TiO_2 scaffold with an insulating alumina $-\text{Al}_2\text{O}_3-$ one) rather early on, that pointed towards properties in the perovskite layer that were beyond a mere sensitizer.(74)

2.5. Peculiar Optoelectronic Properties of Halide Perovskites

Halide perovskites and especially the compositions utilizing Sn and Pb on the B lattice site, possess unique electronic properties that differ from tetrahedrally coordinated III-V semiconductors from previous generations of solar cells.(42) Most importantly, it should be noted that determining the electronic structure and band gap of halide perovskites has to be a rather challenging task. Firstly, this is due to the fact for such calculations a periodic crystal structure needs to be defined which is hard to achieve in high temperature halide perovskites, due to displaying time-averaged symmetry. Other contributing factors include disordered structure, and presence of heavy elements (B site) in the composition of halide perovskites. Concomitantly, the attempts to model the electronic structure of halide perovskites, which were initiated since the 1970s, have only been somewhat successful. For example, linear combination of atomic orbitals (LCAO), was used to investigate the electronic structure of CsBX_3 (B=Sn, Pb) by excluding the A-site cation interactions.(136, 137, 138) Yet the rendered band gaps were so severely underestimated that CsSnBr_3 was predicted to be a semimetal, while it is in fact a medium gap semiconductor.(138, 139, 140) Other methods such as applying extended Huckel model (which were also applied by excluding the A-site interaction) to hybrid compounds, led to severe inaccuracies due to the bands having antibonding character.(139). Although later on, DFT calculations corrected for many-body effects managed to predict correct band gap energies for MAPbI_3 , it cannot accurately describe the

dispersion in the valence band for Pb-based perovskites, in addition to its ineffectiveness in calculating the correct bandgap for Sn-based perovskites.(42) Despite these shortcomings, DFT can still be useful in providing semi-quantitative information for the sake of comparing electronic properties of similar lead halide perovskite compounds. Overall, for improved calculations of perovskite band structure, two relativistic effects would have to be considered, since these compositions utilize heavy elements such as lead. The first important consequence of employing such a heavy element, is that Pb (II) will be stabilized against oxidation due to contraction of the 6s orbital. As a natural consequence of this effect, when placing Sn in the B site, the valence band maximum moves higher up which renders the 6s orbital less contracted.(42) As a result, the tendency of Sn (II) to Sn (IV) oxidation is greatly enhanced compared with its Pb counterpart.(141, 142) The second relativistic effect is spin-orbit coupling (SOC). This phenomenon basically exists due to mixing of two sources of electron angular momentum which are: 1- electron motion in p, d , and f orbitals and 2- electron spin around its own axis in a clockwise or counter-clockwise. Thus, electron orbital and spin angular momentum would be coupled in either a partially destructive or partially constructive way.(143) The most important implication of SOC in halide perovskites would be splitting and loss of degeneracy near conduction band minimum which results in a drastic narrowing of band gap.(144, 145, 146, 147) SOC takes place in non-spherical atomic orbitals and is directly correlated with atomic mass, which means this effect is nearly tripled in Pb-based perovskites compared to their Sn counterpart.(148) In halide perovskites, this is the direct result of Pb p orbital contribution to the conduction band minimum. Yet, in conventional sp semiconductors such as GaAs, SOC results in splitting of the valence band maximum due to the contribution of anion p orbital. This is why metal halide perovskite are known as a special case of sp semiconductors. A calculation method that has been able to capture the complexities of lead halide perovskites, is the state-of-the-art quasiparticle self-consistent GW with SOC corrections (SOC-QSGW).(140, 141, 149, 150) Including SOC in GW calculations, considerably enhances dispersion which consequently reduces the electron and hole effective masses.(141) Some studies have suggested that SOC affects the band dispersion to such an extent that the renders the application of parabolic approximation to band extrema invalid. This would mean that effective masses of charge carriers would substantially vary with direction in k -space.(141, 149) However, the experimental results obtained from magneto absorption spectroscopy still find the parabolic band extrema in MAPbI₃.(151, 152)

Electronic structure near the band edge is predominantly determined by the basic BX_6 building blocks of the inorganic lattice.(137, 150, 153, 154) The states that correspond to the organic cation are situated far from the band edges and therefore do not contribute much to the band gap (except for contributing through modifying the bond angles in the inorganic lattice(122, 144)), however they have a dominant effect in stabilizing the perovskite structure. The valence band in $MAPbI_3$ (and generally for $[PbI_6]^{4-}$ units in general) consist of in-plane I $5p$ orbitals that form σ -antibonding states with Pb $6s$ orbitals (with a ratio of 3:1 for I $5p$ to Pb $6s$). (149) The nonbonding conduction band constitutes of Pb $6p$ - I $5p$ π -antibonding and Pb $6p$ - I $5s$ σ -antibonding orbitals, with the majority of contribution from Pb orbitals. Low energy transition across the band gap would involve electron excitation from I $5p$ to Pb $6p$.(58, 155) In conventional III-V semiconductors like GaAs, the upper valence band is majorly formed through As $4p$ orbitals while the lower conduction band mostly constitutes of As $4s$ and Ga orbitals.(136, 145, 156, 157, 158)

Early perovskite compositions and those most relevant for optoelectronics have been shown to have a direct optical band gap(141, 147), similar to that of III-V compound semiconductors(159), which was a significant advantage over silicon. Several studies have suggested that there may be a Rashba, Rashba/Dresselhaus or Dresselhaus splitting in some non-centrosymmetric hybrid compounds leading to indirect gap perovskites.(144, 148, 149, 160, 161, 162, 163) As an example, 3D Ge-based halide perovskites are direct gap semiconductors while their 1D counterpart are indirect gap materials, displaying weak and broad absorption near the band edge.(160)

For III-V semiconductors, the signatures of direct band gap are two strong spin-orbit split excitonic absorption thresholds, which is due to the splitting of valence band. However, in the case of halide perovskite, due to the reverse ordering of the band edge states, in particular the p -like conduction band(145), the splitting occurs in the lowermost conduction band (which is originally triple degenerate) into upper and lower bands separated by about 1 eV. This phenomenon is otherwise referred to as the inverted electronic structure. This effect was neglected in the early DFT calculations, which resulted in predicting optical properties at the band edge to be three times higher than what was measured in practice.(164) Interestingly, the reverse ordering of the band edge is the reason behind increase of the band gap with increased temperature(165, 166) which would result in excitonic absorption edge to become more broadened and shift monotonically to higher energies.(167) To be more specific, the unique characteristic at the band edge of halide

perovskites gives rise to a positive deformation potential(140, 168, 169). In the event of expansion, the Pb 6s and I 5p antibonding orbitals in the valence band experience reduced interactions which decrease the energy of the antibonding states and therefore lowers the valence band maximum. However, because the conduction band is of non-bonding character, then it is negligibly affected by lattice deformations.(42) As a result, the absorption edge monochromatically shifts with lattice expansion. This is opposite of the effect observed for III-V semiconductors where the valence band maximum and conduction band minimum are almost exclusively made of bonding and antibonding interaction, respectively.(170) However, this dependence of absorbance on temperature in MAPbI₃ becomes almost negligible at energies higher than the excitonic peak.(167) It is important to note that the shift of absorption with temperature are calculated to be primarily due to modified lattice dimensions rather than modified electron-phonon interactions.(171) Because of the strong excitonic absorption edge for perovskites, the band gap is determined by a broadened excitonic impulse response, with the unbroadened part described by Elliot's theory(159, 172) (instead of using Tauc plot(173)), similar to that of III-V semiconductors. The higher exciton binding energies for halide perovskites (35-75 meV(146, 165)) lowers the absorption threshold and at the same time increases the strength of above bandgap absorption compared with III-V semiconductors. Since above bandgap absorption generates unbound electron-hole pairs, density functional theory (DFT) calculations predicts that this type of absorption should be stronger than in many III-V direct gap semiconductors such as GaAs.(74) However, in practice, only a marginal advantage is witnessed. This is because early DFT and other types of calculations such as local density approximation (LDA) and generalized gradient approximation (GGA), underestimated bandgaps due to neglecting many-body interactions associated with transitions to the excited states.(42) Yet they have proved to be very effective in describing ground state properties.(167) Even when DFT calculations take SOC effects into consideration, the band gap is still underestimated unless corrected for many-body effects. Apart from potentially enhancing absorption, excitons could provide the device with an extra population of carriers that may assist carrier transport. Therefore, if the lifetime of exciton diffusion or recombination exceeds that of free carriers, then it could provide beneficial for the device.(174) However, as shown by D'Innocenzo et al.(165), exciton concentration is low compared with free carriers, except for extreme circumstances. Despite being higher than III-V semiconductors, the binding energy is still low enough for photogeneration of excitons and their thermal dissociation into free charge carriers (as well as their

reassociation/recombination back into excitons). The degree to which each effect contributes to the photocurrent would then ideally depend on the coupling between them, as characterized by the intrinsic excitonic dissociation time. This property is of immense importance when the perovskite layer is embedded within a planar architecture or deposited into an insulating scaffold. If the dissociation time is larger than the recombination time (otherwise known as the low-coupling limit), then the corresponding populations will be independent from each other, and the relative concentrations will be determined by the spectral features of the illumination. Under standard illumination conditions, most generated species are expected to be free electron-hole pairs. In this case, the exciton generation will only occur at wavelengths close to the band edges which means in order for them to contribute to the photocurrent, they would need to dissociate at an interface (ETL or HTL), which is the case with OPVs. For the high coupling limit (rapid dissociation), the concentration of free charge carriers and excitons will equilibrate. In this case the concentrations, in theory, would be determined by a mass action law rather than by illumination. Under this limit, the excitons will flow with either electrons or holes (depending on which specie has a higher electrochemical gradient).(175) However, since electrons and holes flow in the opposite direction, at some point in the device their gradient will be equal which results in the total flux to be determined purely by the free carriers. For a coupling range lying somewhere in between the two described extremes, an intermediate behavior would be expected.(174)

Another very important feature of the band structure in halide perovskites is the comparable parabolicity in conduction band and valence band which effectively results in comparable effective masses for electrons and holes.(42) Although parabolic approximation is generally valid, there could be non-negligible contributions from relativistic effects in Pb and Sn-based perovskites. Therefore, theoretically calculated values could differ from numbers obtained in practice. Despite that, in good agreement with experimental results(151), SOC-GW calculations have predicted effective electron mass of $m_e/m_0=0.19$, and hole effective mass of $m_h/m_0=0.25$ for MAPbI₃, where m_0 is the free electron mass.(141) In sharp contrast, there is a large imbalance between effective masses in GaAs ($m_e/m_0=0.07$, $m_h/m_0=0.5$) and CdTe ($m_e/m_0=0.11$, $m_h/m_0=0.35$).(176) Note that a lower effective mass corresponds to higher mobility for a given specie which therefore explains the ambipolar carrier transport behavior.(85, 177)

2.6. Phenomenon of Hysteresis in PSCs

In 2013, for the first time, the mismatch of J - V curves between FS and RS was reported in PSCs by Snaith et al.(178) This phenomenon was termed “hysteresis”, derived from an ancient Greek word, meaning lagging behind. A representation of hysteresis is shown in Figure 2.14.

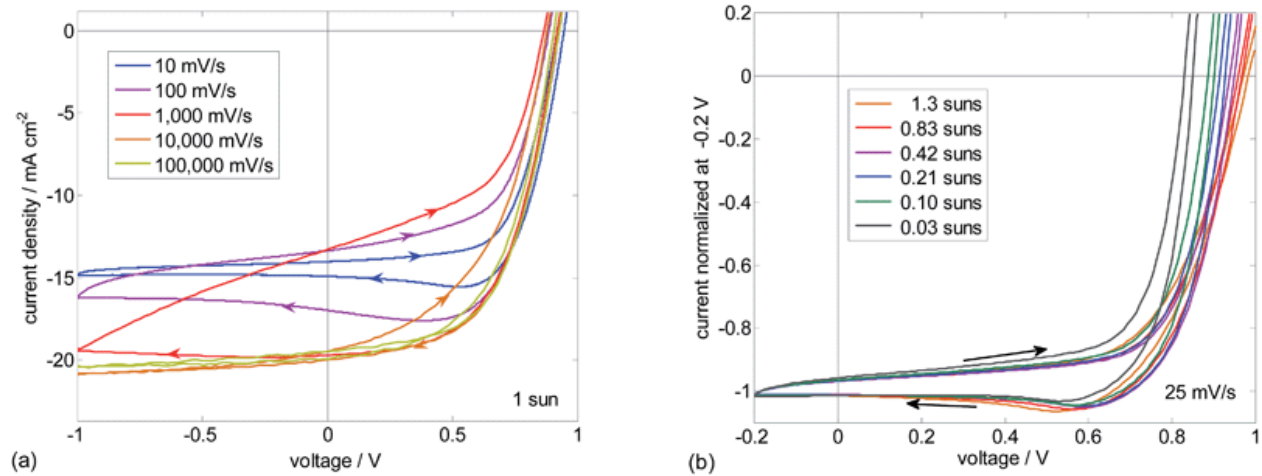


Figure 2.14: The divergence between J - V curves in RS and FS, known as hysteresis, in MAPbI₃-based PSCs as a function of (a) scan rate, and (b) illumination intensity during measurements.(179)

Interestingly, prior to the first report, hysteresis had gone completely unreported in the halide perovskite-related literature. It should be noted that the phenomenon of hysteresis is not unique to PSCs. The capacitance-voltage curves for CdTe devices exhibits hysteresis, upon degradation, due to the mobile Cu_i^+ ions acting as deep trap states.(180) As well, high performing Si-based solar cells with high internal capacitance display hysteretic behavior when their J - V curves is measured under fast scan rates.(181) Moreover, liquid-based DSSCs also show capacitive effects once charge carrier transport across the electrolyte becomes the rate limiting step. What is peculiar, however, about hysteresis in PSCs is not its presence but rather how it manifests itself whereby the electronic response can be slowed down from pico-second time scales to hours, affecting the device reliability and stability.(182)

Many researchers have detailed the importance of indicating experimental parameters as well as the active area employed for recording the J - V curves and calculating PV metrics, respectively. The reason behind enforcing such constraint was that hysteresis was leading to potentially

incorrect assessment of power conversion efficiency, by rendering over-estimated and under-estimated *PCE* in the two scan directions.(178, 179, 183) To overcome the uncertainties in data reporting as a result of hysteresis, alternative PSCs measurements such as comparing *MPP* tracking results, comparing J_{SC} from *J-V* curves with that of external quantum efficiency (EQE) measurements, as well as scanning PSCs under both fast and slow scan rates, have been proposed.(178, 183, 184, 185)

2.6.1. Parameters Affecting the Appearance of Hysteresis

Considering that hysteresis has been shown to be heavily affected by scan rate, scan direction and pre-conditioning of the cell prior to measurements, as well as measurement history, then it becomes crucial to have all such considerations specified when reporting the *PCE*. Yet, it should be noted that often the absence of hysteresis in *J-V* curves under one scan rate does not equal its absence under all other testing conditions.(183) Therefore, if the *J-V* scan is not conducted under linear-sweep condition, then it is not sufficient to specify the scan rate as the only ‘scan condition’. Within the category of scan rate what becomes immensely important is considering the delay time (or voltage settling time, t_d), prior to recording the current for a certain amount of time (or current sampling time, t_s), for reporting the correct scan rate. This means the total time (Δt) spanning prior to next voltage step to be applied is the sum of t_d , t_s and possibly an additional waiting time (t_{wait}). According to Equation 24, this would render the scan rate to be:(182)

$$S = \frac{dV}{dt} = \frac{\Delta V}{\Delta t} = \frac{\Delta V}{t_d + t_s + t_{wait}} \quad (\text{Equation 24})$$

One consequence of using very short t_d , is that the recorded current would be over-estimated in one scan direction while under-estimated in the opposite direction, due to the transient capacitive response of the device.(186) Therefore, for the actual steady-state response of the PSC to be recorded, the *J-V* scan has to be conducted with a long enough t_d that would let the transient response of the device to stabilize. However, there is no one correct delay time that can be applied for the measurement of all PSCs but rather as a rule of thumb t_d should be at least three times larger than the longest transient time constant of a given device to place the measurement in the steady-state window.(182) Overall, for any scan rate, the current response of a PSC device can be expressed, per Equation 25, as the sum of two components, one being the transient components $J_{trans}(t)$, and the time-independent steady state current sustained by the device, J_{SS} :

$$J(t) = J_{SS} + J_{trans}(t) = J_{SS} + \sum_{i=0}^n A_i e^{-\left(\frac{t-t_0}{\tau_i}\right)} \quad (\text{Equation 25})$$

Where A_i is the amplitude and τ_i is the time constant for the longest transient response.(186) Once t_d becomes sufficiently large to allow stabilization of the longest transient in the device, $J_{trans}(t)$ practically vanishes. For a stepwise change in the applied potential, this analysis can be utilized to exhibit how the step size and total duration of its application can modulate the hysteresis response. In addition, during the staircase voltammetry scan itself, this analysis can be applied to obtain transient time constant as well as amplitude as a function of the applied potential. (187, 188)Such analyses would then render a minimum t_d which can be applied to scan the PSC in quasi steady-state condition. Thus, analyzing the transients in the $J-V$ curves become integrally important not just for determining a suitable t_d , but also for gaining valuable insight into the dynamic response of the device.(186, 187, 188, 189, 190)

Over the years, various metrics have been proposed to quantify hysteresis, known as hysteresis index (HI), per Equations 26-30:(189, 190, 191, 192)

$$HI_{0.5V_{OC}} = \frac{J_{RS}(0.5V_{OC}) - J_{FS}(0.5V_{OC})}{J_{RS}(0.5V_{OC})} \quad (\text{Equation 26})$$

$$HI_{0.8V_{OC}} = \frac{J_{RS}(0.8V_{OC}) - J_{FS}(0.8V_{OC})}{J_{RS}(0.8V_{OC})} \quad (\text{Equation 27})$$

$$HI_{int} = \frac{\int_0^{V_{OC}} J_{RS}(V) dV - \int_0^{V_{OC}} J_{FS}(V) dV}{\int_0^{V_{OC}} J_{RS}(V) dV} \quad (\text{Equation 28})$$

$$HI_{FF} = \frac{FF_{RS} - FF_{FS}}{FF_{RS}} \quad \text{Equation (Equation 29)}$$

$$HI_{PCE} = \frac{PCE_{RS} - PCE_{FS}}{PCE_{RS}} \quad (\text{Equation 30})$$

However, analogous to the single-rate $J-V$ scan, the claim of negligible hysteresis, based on HI , is not a sufficient claim for deciding whether the measurement conditions have been chosen correctly, with respect to the steady-state of the device.(192) In fact, the device could appear practically ‘hysteresis-free’ at either very short or very long delay times while the absolute device performance might diverge a lot from both cases. This is the reason why, often, journals require $J-V$ data of PSCs from multiple scan rates to be able to validate the discussion on hysteresis. On the positive

side, if the coupled analysis of J - V response and delay time is conducted, it can yield very useful information on dynamics of device operation.(182)

In general, two types of hysteresis can be distinguished which are predominantly determined by the device architecture(178, 183, 193) as well as the choice of ETL and HTL materials (as will be discussed later in Section 2.6.3.2 and Section 2.6.3.3, respectively). The magnitude of hysteresis tends to be higher in devices employing n - i - p than those with p - i - n architecture (first introduced by Docampo et al.(194)). However, as stated earlier, this behavior is heavily dictated by the choice of contacts. Particularly, the n - i - p device architecture of FTO/TiO₂/MAPbI₃/Spiro-OMeTAD/gold (Au) displays a large hysteresis which was shown to be drastically improved by either completely replacing the TiO₂ ETL with phenyl-C61-butyric-methyl-ester (PCBM)(195) or using PCBM surface passivation over TiO₂(196). One of the most striking differences between the two PSC architectures of normal and inverted type, is the evolution of their scan rate-dependent hysteresis.(197). In addition, the PSC architecture can even influence the temperature-dependent hysteresis behavior of the device. For example, hysteresis in n - i - p structures is shown to have a more pronounced dependence on temperature than their p - i - n counterparts.(182) This indicates that the activation energy of the mechanism responsible for hysteresis is quite different for the different architectures.(198) In addition to device architecture, the physical and chemical nature of the PSC interfaces affects not only the layer adhesion but also density and type of interfacial defects formed.(182) Moreover, the underlying transport layer can influence the crystallinity of the perovskite medium atop which has been demonstrated to influence hysteresis.(195)

As already mentioned, another factor that can heavily impact the appearance of hysteresis is the pre-conditioning and measurement history that the device had been subjected to prior to recording the J - V curves.(179, 183, 199) As an example, devices that have been stored in the dark prior to J - V measurements, can display an S -shaped curve (typically in the forward scan direction) which is indicative of loss in contact selectivity and results in a large divergence between FS and RS curves. However, this situation can be counteracted by leaving the device under light soaking and forward bias to restore contact selectivity (and therefore FF), upon which the device exhibits a more diode-like behavior.(183) Inversely, the same S -shaped behavior can be induced by holding the device under illumination and reverse bias before recording the J - V curves. It has also been shown that very strong poling can even reverse the selectivity of the PSC, whereby charge carriers are

collected at the ‘wrong’ contact.(200) Therefore pre-conditioning (storage, light soaking, pre-biasing and etc.) can modulate the time transients of the device compared to a pristine cell.

2.6.2. Origin of Hysteresis

Over the years, different origins for the hysteresis behavior of PSCs have been proposed including ferroelectricity(178, 201, 202), charge carrier trapping/de-trapping(178, 183) and ion migration(178, 179, 183). As explained before, hysteresis is also observed in other types of solar cells with high internal capacitance. Therefore, the observation of hysteresis in PSCs was hinting that it might be caused by accumulation of charge carriers and/or defect states, correlating it with the conventional understanding of capacitive behavior.(203) In addition to that, the difference in magnitude of hysteresis in PSCs, observed between the different scan rates is partly a signature of capacitive behavior, and is by itself indicative of charge carrier storage.(182) As such, capacitive current (J_C) which is a scan rate-dependent parameter, can be defined using Equation 31 as a function of capacitance (C), and voltage step size per time:(204)

$$J_C = C \frac{dV}{dt} = C \frac{\Delta V}{\Delta t} \text{ (Equation 31)}$$

Capacitive current is a current that flows into a capacitor, which occurs when it is being charged (voltage varying through it with time).(203) Therefore, in this case, the experimentally obtained hysteretic J - V curves can be modelled with an equivalent circuit that has two diodes and two capacitors.(182)

One attribute that could give rise to capacitive currents is the dielectric response of the halide perovskite absorber which is believed to be resulting in ferroelectricity that could explain hysteresis. This viewpoint mainly originated from the work of Poglitsch and Weber on MAPbI₃ back in 1987.(205) The authors attributed the temperature-dependent frequency dispersion of complex permittivity to dynamic disorder in the perovskite material.(205) This work has motivated a large number of studies ever since to elucidate the dynamic disorder of MA cation (which is asymmetric with a sizeable permanent dipole of 2.3 D)(169) in the MAPbI₃ structure.(206, 207, 208, 209, 210) The outcomes indicated that the MA cation undergoes rotation along C-N bond and tumbling reorientation in higher temperature phases. This reorientation is inhibited in the low-temperature orthorhombic phase and therefore dynamic reorientation is not observed there.(209) It is this rotational freedom of the A-site cation that allows it to respond to external perturbation.

In particular, it was hypothesized that the MA cations screen the free charge carriers and create ferroelectric domains,(211) which has important consequence for the dielectric characteristic of these materials. The complex dielectric function is defined according to Equation 32(42):

$$\varepsilon(\omega) = \varepsilon_1(\omega) + i\varepsilon_2(\omega) \text{ (Equation 32)}$$

Where ε_1 and ε_2 are the real and imaginary parts of the dielectric function, respectively, and ω is the angular frequency. The frequency dispersion of ε_1 for the low temperature orthorhombic and high temperature tetragonal phase of MAPbI₃ is shown in Figure 2.15 (164). ε_1 is related to the polarizability of the material in response to an oscillating electric field. The low frequency (or the static limit, ε_s) is related to the coupling of all polarizable elements within the lattice which include dipoles, ions and electrons. However, the high frequency (optical limit, ε_∞), only has electronic contribution.(212) In the optical limit, the major contribution to the real part of complex dielectric function comes from vibrational polar phonon modes within the inorganic lattice. This effectively renders ε_∞ to be comparable for the two phases.

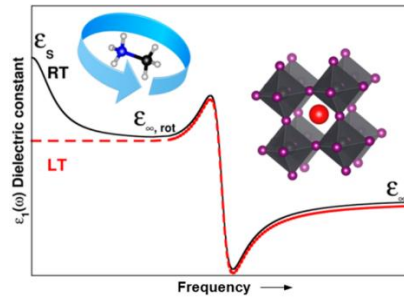


Figure 2.15 :Schematic comparison of static dielectric constant (ε_s) and high frequency dielectric constant (ε_∞) for orthorhombic and tetragonal phases of MAPbI₃. Contributions to ε_∞ arise from vibrational polar phonon modes associated with the inorganic lattice, which then negate any major temperature-dependence behavior in this region.(164)

However, in the low frequency limit, ε_s for the tetragonal phase increases rapidly. This discrepancy between the two phases under the low frequency limit is attributed to the rotation of MA cation which is inactive in the orthorhombic phase.(164) Thus based on these observations, a ferroelectric diode model was proposed to explain hysteresis dynamics in PSCs.(199) X-ray diffraction (XRD) patterns and Raman studies seemingly confirmed that MAPbI₃ contains ferroelectric domains in relation with an acentro-symmetric structure (without an inversion center). Next to that, electric

field-polarization measurements (E - P), whereby the total charge quantity (including the polarized charge) as a function of electric field, displayed ferroelectric behavior (Figure 2.16 a). The corresponding P - E loop shows how the state of P and E , based on how the state changes from short-circuit to open-circuit ($A \rightarrow B \rightarrow C$ in forward scan) and open-circuit to short-circuit ($C \rightarrow D \rightarrow A$ in reverse scan). In such a scheme, points B and D are transient states.

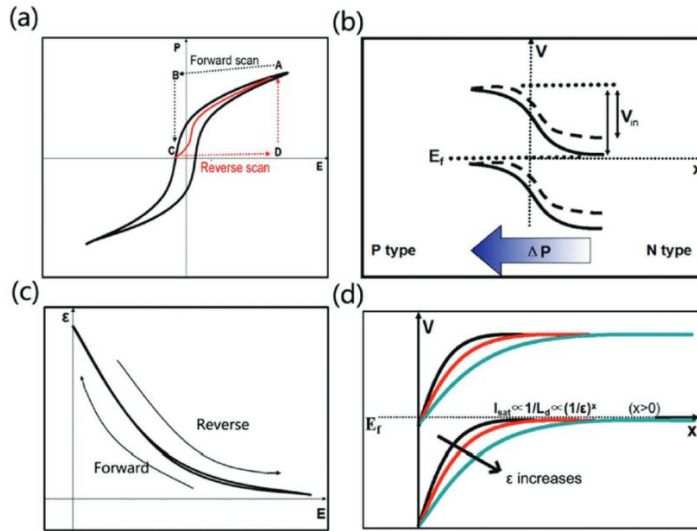


Figure 2.16 : (a) Illustration of the relationship between polarization (P) and electric field (E) in forward scan (FS) spanning $A \rightarrow B \rightarrow C$ and reverse scan (RS) spanning $C \rightarrow D \rightarrow A$. (b) The influence of excess polarization (ΔP) on the built-in (V_{in}) and open-circuit voltage (V_{OC}), where the solid line is the energy diagram in the stabilized p-n diode and the dotted line is the changed energy diagram due to ΔP induced by non-relaxed ferroelectric domain under FS and moderate scan rate). (c) Schematic illustration of the relationship between E and ϵ , which is independent of the scan direction. (d) Schematic representation of the depletion region in halide perovskites which is heavily dependent on ϵ .(199)

For FS, the built-in electric field is large in the beginning (because of zero applied bias). Excess polarization (ΔP , which is built-up due to the long relaxation time of ferroelectric domain) would be pronounced in FS, because as electric field decreases then polarization has enough time to drop. Therefore, the built-in potential (V_{in}), and concomitantly V_{OC} , will decrease (Figure 2.16 b). This is because E_{in} varies according to:(199)

$$E_{in} = (V_{OC} - V)/W \text{ (Equation 33)}$$

where W is the width of the depletion layer. Because polarization cannot follow the scan rate (since it is faster than the relaxation time), then a transient state B will exist when going from A to C, in the forward scan. This results in the presence of excess polarization in FS. In the reverse scan, point C has almost zero E_{in} because $V \geq V_{OC}$ which creates a small ε . In RS, when going from state C back to A with increasing the external field, a transient state (D) will appear that has small ΔP with large ε , which leads to enhanced V_{OC} and J_{SC} compared with FS. Since $\varepsilon = dP/dE$, then ε is expected to decrease at forward scan but increase under reverse scan (Figure 2.16 c). With respect to semiconductor behavior, the larger the dielectric constant then the larger portion of the electric field that material (Figure 2.16 d) will take up which results in larger J_{SC} and V_{OC} . In ferroelectric materials, the change of dielectric constant under different poling conditions can affect charge collection efficiency, which if true in the case MAPbI₃ could explain the hysteresis behavior. In other words, polarization and de-polarization of MAPbI₃ is expected to be dictated by the external field if this material is intrinsically ferroelectric. What in fact fueled a lot of such arguments was the observation that hysteresis was being modulated by the poling voltage (pre-biasing prior to measuring the J - V curves).(213, 214, 215) Furthermore such arguments were supported by quasi-elastic neutron scattering and pump-probe vibrational spectroscopy, showing that the rotations of MA cation occurs within 3 ps.(209, 211) Additionally, the presence of ferroelectric domains equal to the grain size upon biasing, through piezo-response force microscopy were reported.(216, 217) However, considering that the transients observed in J - V curves of PSCs is in order of seconds to hours, then the ferroelectricity explanation is unlikely to be the dominant cause of hysteresis (if at all plausible).(218, 219, 220, 221)

Another possible explanation, for the slow time transients in PSCs, is ionic defect formation and migration.(178, 179, 184, 211) This was rather intuitive since halide perovskites were known to be ionic conductors since decades ago,(222) which motivated later studies. In a general scheme, ionic migration could involve all the constituents of the organic cation (A-site), inorganic lead cation (B-Site) and halide anions (X-site). The observation of ionic electromigration through photothermal-induced resonance microscopy, confirms the electric field induced by photovoltage in PSCs is sufficient to induce ion migration.(223) In addition movement of ionic species, proton migration was also reported to occur,(224) which resulted in the deprotonation of the organic cation as a result, and were hypothesized to contribute to hysteresis by diffusing through the perovskite layer.(225, 226) The ionic conductivity of a given material (σ) would depend on defect

density (N_D), ionic mobility (μ) and diffusion coefficient (D) for a given defect species. μ primarily depends on the activation energy (EA), while N_D is mostly determined by energy of formation. Defect densities in the order of 10^{17} - 10^{20} cm⁻³ are predicted for halide perovskites (ref). Since halide vacancies show the lowest energy of formation and activation energies,(227, 228, 229) they are projected to contribute the most to the calculated defect densities for perovskite materials. Most importantly, halide vacancy/interstitial pairs can form under operation in PSCs which could result in enhancement of N_D .(230, 231) Cation diffusion is also considered to be a potential source of ion migration. MA (which migrates along the diagonal $\langle 110 \rangle$ direction on the cubic unit cell and jumps into a neighbouring vacant A-site) has a higher activation energy than iodine vacancies (migrating along the lead octahedron, similar to Pb^{2+}). (227) Therefore, large A-site organic cations are expected to affect the hysteresis response at longer time scales (minutes to hours),(223) and has been shown to contribute to reversible performance losses during day/night cycling of PSCs(232).

Most researchers in the field tend to agree that hysteresis in PSCs is mostly attributable to the redistribution of ionic charge (through drift and diffusion) in the perovskite layer, upon the application of external perturbation, and accumulate at the interface in order to screen the built-in field in the perovskite layer.(179, 233, 234). The perspective of ion migration could explain some experimental observations such as deterioration of hysteresis as a function of storage time, during which time interfacial ionic accumulation takes place especially in the presence of O_2 /moisture.(235) As mentioned before, the choice of transport layers can influence the type and extent of hysteresis. This is, however, not in contradiction with the ion migration hypothesis. Different transport layers exhibit different conductivities which would then change the ionic distribution within the perovskite layer as a result. This influences not only the carrier collection efficiency but also the capture cross section of photogenerated charges. (182)

This behavior and the resulting implications are shown in Figure 2.17.

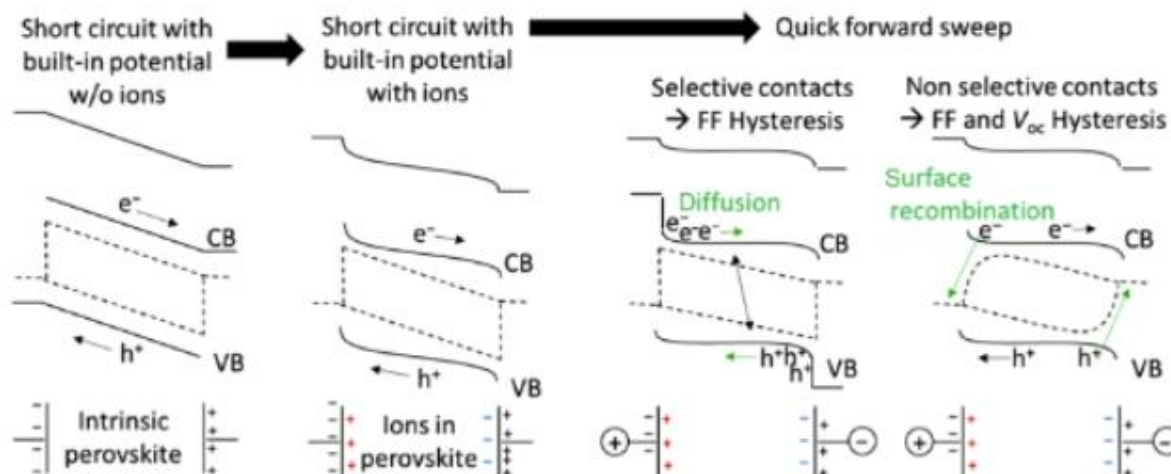


Figure 2.17: Simplified band diagram of perovskite solar cell under illumination (quasi-Fermi levels dashed, e^- =electrons, h^+ =holes, CB=conduction band edge, VB=valence band edge) to illustrate changes in built-in potential and band-bending upon ion accumulation at interfaces that impede charge carrier extraction at selective contacts.(234)

Based on this viewpoint, during FS (as well as by holding the PSC under negative bias prior to measuring $J-V$ curves), negatively charged ions would preferentially pile up at the ETL interface (and vice versa for HTL), impeding efficient charge carrier extraction at the corresponding interfaces. This would, in turn, result in a lower extracted charge density and an overall reduced *PCE*. It has been argued that accumulation of negatively charged ionic species at the ETL, leads to *p*-doping of the perovskite layer at the interface vicinity due to attracting holes for preserving charge neutrality (and vice versa for HTL) which therefore lowers the charge extraction capability of that interface.(236, 237) However, during RS (as well as by holding the PSC under a positive bias prior to measuring $J-V$ curves), negatively charged ions would accumulate at the HTL (and vice versa for the positive ions) which leads to enhanced charge carrier extraction (and therefore higher *PCE*) in RS than FS. What has started to become more evident with time is that it is not directly the ionic effects that are causing hysteresis but rather their modulation of electronic response through changing the interfacial charge carrier extraction efficiency, electric field distribution within the device, trapping/de-trapping of charges carriers through ionic defects and non-radiative recombination rates that is giving rise to this issue.(198, 238, 239, 240)

One of the common approaches to model hysteresis has been drift-diffusion simulations. With respect to classical semiconductors, in this modeling approach, electrons and holes are considered

to be mobile while ionized dopant atoms give rise to a localized space charge.(182) In order to account for the mixed electron-ionic conducting nature of perovskites, mobile ionic species have been analogously modeled as that of mobile charge carriers, albeit with lower diffusion constant and mobility.(240, 241, 242, 243, 244) The problem is that such an approach would require a high number of parameters with many amongst them being unknown. As a result, many different combinations of such parameters, reproduce the same hysteresis which leads to various claims on how a given hysteresis appearance is caused.(182) As an example, some studies claim that hysteresis cannot be a result of ionic migration alone, and that this effect has to be combined with a high density of surface traps promoting non-radiative recombination.(240, 242) Taking both factors into account becomes particularly essential when explaining the *S*-shaped *J-V* curve (commonly in FS) and as a result a large magnitude of hysteresis.(236) The presence of both shallow and deep traps has been detected in MAPbI₃, using thermally simulated current measurements.(245) It is hypothesized that traps (which can predominantly exist at the interfaces as well as perovskite grain boundaries) can trap photogenerated charge carriers under forward bias. These charges might be released under short-circuit as they get separated by the transport layers. This is the slow charge trapping/de-trapping process that has proved to be essential for producing hysteresis in some cases.(246) In support of such a hypothesis, trap passivation/reduction strategies in PSCs have been beneficial in reducing hysteresis.(247, 248) On the other hand, other works reproduced hysteresis by assuming only mobile ionic defects without necessarily the need for interfacial recombination.(239) It has also been argued that charge extraction in PSCs is heavily dependent on the electric field. Yet, because such a trend is reproduced by considering low diffusion length and high surface recombination, the work concludes that high magnitude of hysteresis is correlated with low performing device,(244) a perspective that cannot be generalized. Overall, the phenomenon of hysteresis tends to be a multi-faceted issue that can have multiple origins happening on overlapping time scales, as opposed to an isolated process.(236, 249, 250). Also it is worth mentioning that some contact layers are assumed to be less permeable and/or experience less ionic accumulation, such as PCBM, copper (I) iodide (CuI) and copper (I) thiocyanate (CuSCN).(251, 252, 253) However, this does not imply absence of mobile ionic species within the perovskite layer.(240, 254) Of importance, is to note that in addition to the intrinsic ion migration in the perovskite film, extrinsic atomic and ionic migration such as Au, lithium ion (Li⁺), hydrogen ion (H⁺), sodium cation (Na⁺, when used in the contact layers) also

takes place which can affect the PSC performance.(255) Such observations, rendered the ionic migration explanation for hysteresis in PSCs to be interwind with defects and their formation.

Thus far we discussed ferroelectricity, ionic accumulation, and charge trapping/de-trapping within the framework of capacitive hysteresis. In general, for a purely capacitive response, the magnitude of hysteresis is expected to drop for scan rate with t_d that does not coincide with the response time of the device, which is however not always the case. Importantly, the capacitive currents that have been calculated for devices operating at 0V and under dark, are in the range of nA/cm² which are too small to explain the hysteresis on their own. This necessitates considering non-capacitive effects for a better understanding of hysteresis dynamics. These would be rather secondary effects and include changes in the charge carrier collection efficiency and recombination rates of electrons and holes due to changes in the built-in potential (as a result of ionic re-equilibration).(179, 256) In general, capacitive effects can be distinguished from their non-capacitive counterparts in J - V curves, through their high frequency dependence.(197, 257)

Overall, the mechanisms giving rise to hysteresis can have serious implications with respect to long-term stability of PSC. In addition to showing more sever hysteresis, n - i - p architectures also seem to exhibit light-induced performance losses that have been shown to only partially recover under dark.(258) Concomitantly, reversible device performance after dark storage on the time scale of few hours, has been suggested to be related to mobile ionic species,(232, 259) or light-induced formation of deep-level traps.(260) In another example, aging PSCs under open-circuit condition and 1 Sun illumination can considerably modify the hysteresis dynamics compared with the pristine device (reduced hysteresis under slow scan rates and increased hysteresis under fast scan rates).(179) However, such behaviors are heavily dependent on the architecture of the PSC as well as the employed charge transport layers.(182) Therefore, considering the instability and unreliability associated with the hysteresis phenomenon, it is of crucial importance to develop strategies for mitigating hysteresis.

2.6.3. Strategies for Mitigating Hysteresis

2.6.3.1. Strategies Concerning the Perovskite Layer

The stabilization of the perovskite layer, and the subsequent alleviation of hysteresis from that perspective, has been tackled from multiple fronts, one being its composition.(79, 191, 261) Figure 2.18 shows the PV metrics and HI corresponding to 49 different compositions in a matrix of

cation/anion alloys of MA/FA on the A site, Pb on the B-site and Br/I on the X-site.(191) It should be noted that some of the studied compositions in Figure 2.18, were determined to be unstable due to photo-induced phase segregation occurring through halide migration. In turn, such compositions yield a higher *HI* than others. Also noteworthy, is the more pronounced hysteresis of MA-based devices compared with FA-based devices which could be related to the higher mobility of the MA cation.(262) However, care must be taken in correlating compositional variance with hysteresis since changing the elements ratio in the precursor not only affects the formation kinetics but also the morphology of the resulting perovskite layer.(182)

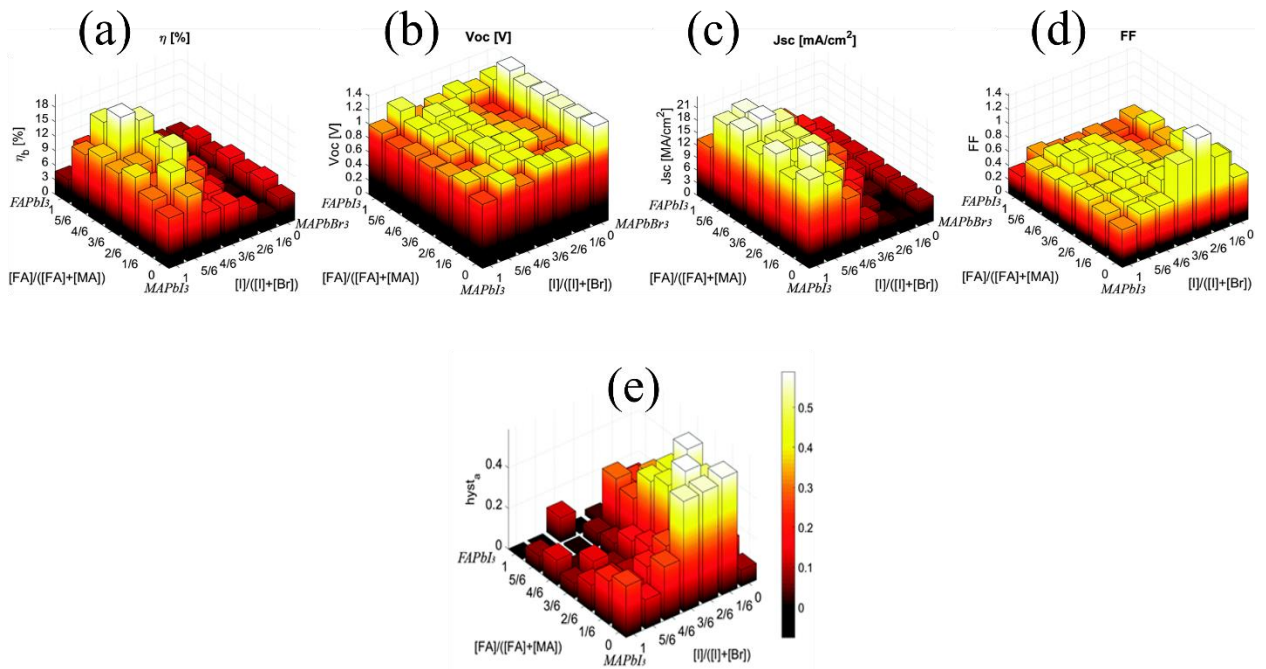


Figure 2.18: Device parameters for cells of different compositions $[(A_1A_2)B(X_1X_2)_3]$. (a) *PCE*; (b) V_{oc} ; (c) J_{sc} ; and (d) *FF*, as well as e) *HI*.(191) (Where $A_1=FA$, $A_2=MA$, $B=Pb$, $X_1=$, Br , $X_2=I$).

Using a mixed A-site cation composition for the perovskite layer has been shown to exhibit better performance, with respect to stability, *PCE* and hysteresis.(191, 261, 263) For example, FA can be alloyed with MA and Cs cations. As well, the B-site, cations can be mixed by combining Pb and Sn, to render complex compositions of $FA_{0.7}Cs_{0.3}Pb_{0.7}Sn_{0.3}I_3$ and $FA_{0.7}MA_{0.3}Sn_{0.3}Pb_{0.7}I_3$ (265). PSCs using the aforementioned compositions in *p-i-n* architectures render negligible hysteresis in J_{sc} between RS and FS. Similarly, the simultaneous alloying of A and X-site elements can prove

beneficial for PCS performance. This is done through combining I⁻ with Br⁻ or Cl⁻ on the X-site for optimizing the optical and electronic properties of the perovskite film (and hence the corresponding PSC performance).(266) The mixed perovskite composition of MA_{0.17}FA_{0.83}Pb(I_{0.83}Br_{0.17})₃, within mesoporous and planar *n-i-p* architectures, yields efficient devices with little hysteresis. More complex perovskite compositions employing four cations of rubidium (Rb⁺), Cs⁺, MA⁺ and FA⁺ in the A-site and having a mix of I⁻ and Br⁻ on the X-site (known as the quadruple perovskite composition or RbCsMAFA) exhibit elevated performance compared with most other compositions.(263) Rb⁺ is believed to be increasing the charge carrier mobility in the perovskite film, and therefore reducing the resistance as well as capacitance associated with charge transport. It has also been suggested that Rb⁺ enhances the crystallinity of the perovskite layer, through which the ionic defect migration is suppressed and therefore the dynamic response of the corresponding PSCs is altered.(267) On the other hand, the suggested role for Cs⁺ is assumed to be reducing the trap density and therefore non-radiative recombination rate of charge carriers within the perovskite film.(261, 263, 268, 269). Above all, potassium cation (K⁺) has been shown to have the most positive influence in reducing the trap density, through enlarged crystallite size and raising the conduction band minimum.(270) In particular, by using potassium iodide (KI) as the source of potassium cations, the enhanced performance and improved hysteresis behavior in the corresponding PSCs is attributed to the compensation of halide deficiency (and therefore enhanced crystalline quality) and substitution of bromide by iodide.(271) Although K⁺ has exhibited a positive influence on PSC performance for a wide range of compositions, its contribution in particular to the perovskite composition of K_xCs_{0.05}(FA_{0.85}MA_{0.15})_{0.95}Pb(I_{0.85}Br_{0.15}) has resulted in a large reduction of hysteresis. It should be noted that, as opposed to Cs⁺, the smaller size cations of K⁺ and Rb⁺ are less likely to be incorporated into the A-site. Through nuclear magnetic resonance (NMR) studies, they are suggested to occupy interstitial lattice sites instead, which is believed to prevent Frenkel defects formation.(270, 271, 272)

Another aspect of optimization has been the morphology of the perovskite layer, especially in the case of planar structures where a uniform, smooth and full coverage of the perovskite layer with large monolithic crystallites are considered to determine parameters not only with respect to *PCE* but also hysteresis.(269, 273, 274). The morphology of the perovskite layer can be adjusted through additive engineering.(275, 276, 277, 278, 279, 280, 281, 282, 283) As an example, addition of 3-5 wt.% lead (II) thiocyanate- Pb (SCN)₂- into the perovskite precursor considerably

increases the crystallite size and passivates the grain boundaries in $\text{MA}_{0.7}\text{FA}_{0.3}\text{PbI}_3$. This is achieved through $\text{Pb}(\text{SCN})_2$ reacting with iodide ions and forming PbI_2 by, which enhances PSC performance and leads to reduced hysteresis.(278, 279)

Generally, the methods employed for synthesizing the perovskite layer render polycrystalline morphology consisting of grains and grain boundaries. Grain boundaries, and overall defects, seem to be less detrimental in the case of perovskites compared with conventional semiconductors.(109, 284, 285, 286) However, they are still largely believed to hamper charge transport and be a source of recombination, which therefore becomes important in controlling hysteresis.(287) The synthesis method, through governing nucleation and growth process, also determines the perovskite crystallite size and overall morphology.(288) Therefore, tuning of parameters affecting the perovskite crystallite size and quality can have a significant effect in alleviating hysteresis.(289, 290) The two most common techniques for synthesizing the perovskite layer are the one-step (also known as the anti-solvent technique) and two-step deposition methods. The one step process is conducted through spin coating which usually consists of an initial stage with lower rounds per minute (rpm) for a few seconds, immediately followed by a longer spinning segment at a higher rpm. The synthesis is completed by spin casting an anti-solvent (most commonly chlorobenzene, toluene and diethyl ether) over the spinning substrate a few seconds before the end of the spinning program.(78) In the two-step process, the inorganic component (for example lead iodide, PbI_2 , in the case of MAPbI_3) is deposited through spin coating. This is followed by deposition of the organic precursor solution (methylammonium iodide, MAI, in the case of PbI_2) to obtain the final perovskite composition.(76) However, while the one-step deposition is more convenient than the spin coating process, it requires the involvement of anti-solvent method. Other deposition methods to have rendered promising results are vapor-based(291) and room temperature-based crystallization(292) methods. Interestingly, vapor-based methods typically render smaller crystallites and therefore larger area of grain boundaries, and yet exhibit smaller hysteresis.(293) As such, the discussion over the role of grain boundaries in PSCs is an open debate.

2D perovskites (as discussed in Section 2.3), have been an area of interest to alleviate hysteresis, due to their impressive stability.(294) In this type of perovskites, the organic cations are attracted to the inorganic cations by van der Waals forces which due to being too strong for ionic movement, inhibit ion migration. On the other hand, as mentioned in Section 2.3, the major issue with 2D

perovskites is that their organic component confines the charges and therefore gives rise to insulating properties. However, if the orientation of the organic component with the respect to the inorganic one can be controlled (for example, preferential out of plane), then charge transport can be promoted which can help with reducing hysteresis.(295) This has been the case for 2D perovskites based on butylammonium (BA) and phenethylamine (PEA) bulky organic cations with the compositions of $(X)_2(MA)_3Pb_4I_{13}$ (with $X= BA$ or PEA) in *p-i-n* configuration rendering efficiencies of around 12% without hysteresis and improved stability.(296, 297) Despite such results, ultimately, the bulky spacer organic cation would limit the performance of the corresponding PSCs by inhibiting the out-of-plane charge transport.(298) Nevertheless, over the past years, an effective strategy that has arisen, has been combining the stable 2D and efficient 3D perovskites to obtain the so-called mixed 2D-3D heterostructures. Prominent examples include $BA_{0.09}(FA_{0.83}Cs_{0.17})_{0.91}Pb(I_{0.6}Br_{0.4})_3$ and $(PEA_2PbI_4)_{0.017}(MAPbI_3)_{0.983}$ mixed compositions which deliver smaller hysteresis than their pure 3D counterparts.(299, 300)

2.6.3.2. Strategies Concerning the ETL

The most widely used ETL material for PSCs is TiO_2 which has been employed in the form of conformal blocking layer, mesoporous scaffold, nanorods and nanowires, and other nanostructures.(261, 263, 301, 302, 303) However, despite beneficial properties, the conductivity of TiO_2 remains relatively low in addition to the fact that the presence of oxygen vacancies in the corresponding film can trap charges and contribute to hysteresis.(304, 305) For these reasons, other ETL materials have been tested to understand their influence over the hysteresis dynamics in PCSs. The second most commonly utilized ETL is SnO_2 which is effective in reducing hysteresis and demonstrates excellent electron selection and conduction capabilities, in addition to having a deeper conduction band edge than titania.(238, 306, 307, 308) Additionally, the low temperature requirements for synthesizing SnO_2 through low-temperature plasma-enhanced atomic layer deposition (PE-ALD) makes them a suitable candidate for utilization in normal and flexible PSCs.(309) Moreover, ZnO films which exhibit higher conductivity and require lower annealing temperatures have been shown to be effective ETL for relieving hysteresis in planar *n-i-p* architectures.(310) Another metal oxide candidate has been $\alpha-Fe_2O_3$, whose nano-island structure in mesoporous *n-i-p* architecture allows for efficient charge extraction between ETL and perovskite layer which therefore reduces hysteresis.(311, 312) In addition to inorganic materials, organic compounds have also been researched. In particular, both Buckminsterfullerene (C_{60}) and PCBM

have been tested in planar *n-i-p* structures (with and without TiO₂) and have resulted in reduced hysteresis due to reduced trap density and passivating perovskite grain boundaries.(313, 314, 315, 316, 317). Moreover, other organic materials such as N,N'-bis(3-(dimethylamino)propyl)-5,11-dioctylcoronene-2,3,8,9-tetracarboxdiimide (CDIN), C₆₀ pyrrolidine tris-acid and solid-state ionic liquid (ss-ILs) have shown great promise in reducing hysteresis for *n-i-p* architecture, due to their high electronic conductivity, mobility and good thermal stability.(318)

Moreover, multi-layered ETL structures have been developed, as a form of interfacial engineering, to improve band alignment at the interface, passivate defects, facilitate photogenerated electron collection, as well as blocking holes from entering ETL and overall reduce hysteresis. As an example, a combination of mesoporous titania with hole-blocking amorphous SnO_x or niobium (V) oxide (Nb₂O₅) with controlled thickness has been shown to alleviate hysteresis.(319) In the case of planar PSCs, utilizing ethanolamine-functionalized fullerene bilayer and a biopolymer heparin sodium (HS) thin layer in conjunction with compact TiO₂ has shown to considerably reduce hysteresis, through facilitating electron transfer from perovskite and ETL and passivating interfacial traps.(320, 321, 322)

2.6.3.3. Strategies Concerning the HTL

The most common choice for the HTL in PSCs is spiro-OMeTAD which often renders highest efficiencies in *n-i-p* architecture PSCs (323, 324) and is in fact passed down from DSSCs(72). However, despite its widespread popularity, this material suffers from low hole mobility and conductivity due to lack of molecular ordering.(325, 326) To counteract such problems, the spiro-OMeTAD precursor is doped with a combination of lithium bis(trifluoromethylsulfonyl)imide (LiTFSI) and 4-tert-butylpyridine (4-TBP).(327, 328, 329) The same combination is also employed to enhance hole mobility and conductivity of another organic HTL material called PTAA, which is also a popular choice in the perovskite photovoltaic community.(330, 331) Although the presence LiTFSI and 4-TBP in the resulting HTL film can lead to enhanced performance with respect to both *PCE* and hysteresis of the corresponding PSCs, they can negatively impact the long-term operational stability and therefore hysteresis dynamics.(332) Counteracting the contributions of hysteresis stemming from HTL based on spiro-OMeTAD has been two fold. One set of solutions has focused on alternative dopants.(333, 334, 335, 336, 337, 338, 339, 340) The most prominent example is 2,3,5,6-tetrafluoro-7,7,8,8-

tetracyanoquinodimethane (F4-TCNQ), where the corresponding PSCs display lower hysteresis compared with that of LiFTSI/4-TBP combination. It is suggested that the strong electron acceptor properties of F4-TCNQ, enables spiro-OMeTAD to form supramolecular interactions with Γ at the perovskite surface, through halogen bonding, and therefore passivating the traps and reducing hysteresis.(341) Another set of strategies revolve around replacing spiro-OMeTAD as HTL altogether. In this regard, many organic replacements such as PEDOT:PSS,(342) poly(3-hexylthiophene-2,5-diyl) (P3HT),(343) and poly[5,5'-bis(2-butyloctyl)-(2,2'-bithiophene)-4,4'-dicarboxylate-alt-5,5'-2,2'-bithiophene] (PCDBT)(344) have been applied as HTL. Despite promising results with respect to both *PCE* and hysteresis dynamics, the high cost of organic HTLs, remains a challenge.(246) In capitalizing on the front of cost-effectiveness, many suitable inorganic *p*-type semiconductors have been developed as HTL, especially for *p-i-n* structure. In this case, the most widely used compound is nickel oxide (NiO_x).(345, 346) The PSCs based on this HTL show relatively small hysteresis, which has shown to be tunable depending on the employed synthesis method.(347) Other choices of inorganic HTLs include CuI ,(251, 348) CuSCN ,(349) copper (II) sulfide (CuS),(350) as well as copper oxide (CuO_x)(351, 352). Despite the very promising hysteresis reduction observed by utilizing the above mentioned inorganic HTL materials, their *PCE* often lacks behind that of organic HTL-based PSCs.(246)

In addition to the aforementioned strategies, and similar to the concepts applied for ETL, interfacial engineering practices have also been employed for the HTL interface. For instance, Al_2O_3 and diethanolamine (DEA) have been shown to positively influence the interface between NiO_x and the perovskite layer, resulting in reduced hysteresis. The proposed mechanism in the case of Al_2O_3 is the blocking of electron back transfer to the E_V of NiO_x , due to better band alignment. In the case of DEA, it is suggested that it can improve the interfacial contact, through which hole extraction is promoted.(353, 354) For PSCs employing PEDOT:PSS as HTL, the interface with the perovskite layer could be modified using 3-aminopropionic acid. This forms an ambipolar self-assembled monolayer, which reduces the energy level mismatch at perovskite/HTL interface. The resulting PSCs are shown to be less sensitive to scan direction and scan rate.(355) With regards to the conventional spiro-OMeTAD, considerable mitigation of hysteresis has been achieved through insertion of a passivating layer, which consists of FAI, bulk iBAI, or a polystyrene layer. (356, 357)

2.7. Summary

In this chapter, after providing an overview on the photovoltaic effect and history of solar cell development, PSCs were introduced. As detailed throughout this chapter, PSCs utilize a metal halide perovskite layer absorber with ABX_3 crystal structure, where A and B are monovalent and divalent cations, respectively, and X is a halide. Despite many advantageous properties that halide perovskites impart on PSCs, enabling them to deliver competitive *PCE* values with solar cells based on c-Si, the development of PSCs is yet to be realized in large scale due to the prevalence of a phenomenon called hysteresis, which is defined as the mismatch between $J-V$ in the reverse and forward scan directions.

The phenomenon of hysteresis is largely believed to be caused by the mixed ionic-electronic conducting properties of the perovskite layer. The myriad of studies in the literature has shown that hysteresis can be modulated depending on not only the perovskite absorber layer but also the charge transport layers (ETL and HTL). Despite such reports, however, a systematic study linking the transport layer properties with the appearance of hysteresis is still lacking.

Correspondingly, the research work in Chapters 4, 5 and 6 were undertaken to correlate the modulation of hysteresis with respect to hysteresis locus and magnitude, to the change of electronic conductivity at the interface of perovskite layer with the transport layers, because of electronic-ionic coupling, depending on the contact layer properties such as doping density, conductivity, thickness, and morphology.

2.8. References

1. Nelson JA. The physics of solar cells: World Scientific Publishing Company; 2003.
2. Würfel P, Würfel U. Physics of solar cells: from basic principles to advanced concepts: John Wiley & Sons; 2016.
3. Würfel U, Cuevas A, Würfel P. Charge carrier separation in solar cells. IEEE Journal of Photovoltaics. 2014;5(1):461-9.
4. Miyasaka T. Perovskite Photovoltaics and Optoelectronics: From Fundamentals to Advanced Applications: John Wiley & Sons; 2021.
5. Standard Solar Spectra [Available from: <https://www.pveducation.org/pvcdrom/appendices/standard-solar-spectra>].

6. Solar Cell Structure [Available from: <https://www.pveducation.org/pvcdrom/solar-cell-operation/solar-cell-structure>].
7. Shockley W, Queisser HJ. Detailed balance limit of efficiency of p-n junction solar cells. *Journal of applied physics*. 1961;32(3):510-9.
8. Kirchartz T, Rau U. What Makes a Good Solar Cell? *Advanced Energy Materials*. 2018;8(28):1703385.
9. Bridgman P. Note on the principle of detailed balancing. *Physical Review*. 1928;31(1):101.
10. Van Roosbroeck W, Shockley W. Photon-radiative recombination of electrons and holes in germanium. *Physical Review*. 1954;94(6):1558.
11. Guillemoles J-F, Kirchartz T, Cahen D, Rau U. Guide for the perplexed to the Shockley–Queisser model for solar cells. *Nature photonics*. 2019;13(8):501-5.
12. Urbach F. The long-wavelength edge of photographic sensitivity and of the electronic absorption of solids. *Physical Review*. 1953;92(5):1324.
13. Cody G, Tiedje T, Abeles B, Brooks B, Goldstein Y. Disorder and the optical-absorption edge of hydrogenated amorphous silicon. *Physical Review Letters*. 1981;47(20):1480.
14. De Wolf S, Holovsky J, Moon S-J, Loper P, Niesen B, Ledinsky M, et al. Organometallic halide perovskites: sharp optical absorption edge and its relation to photovoltaic performance. *The journal of physical chemistry letters*. 2014;5(6):1035-9.
15. Sze SM, Li Y, Ng KK. *Physics of semiconductor devices*: John wiley & sons; 2021.
16. Dittrich T. *Materials concepts for solar cells*: World Scientific; 2015.
17. Kerr MJ, Cuevas A. General parameterization of Auger recombination in crystalline silicon. *Journal of Applied Physics*. 2002;91(4):2473-80.
18. Greulich J, Glatthaar M, Rein S. Fill factor analysis of solar cells' current–voltage curves. *Progress in Photovoltaics: Research and Applications*. 2010;18(7):511-5.
19. Khanna A, Mueller T, Stangl RA, Hoex B, Basu PK, Aberle AG. A fill factor loss analysis method for silicon wafer solar cells. *IEEE Journal of Photovoltaics*. 2013;3(4):1170-7.
20. Qi B, Wang J. Fill factor in organic solar cells. *Physical Chemistry Chemical Physics*. 2013;15(23):8972-82.
21. Boccard M, Ballif C. Influence of the subcell properties on the fill factor of two-terminal perovskite–silicon tandem solar cells. *ACS Energy Letters*. 2020;5(4):1077-82.

22. Dhass AD, Natarajan E, Ponnusamy L, editors. Influence of shunt resistance on the performance of solar photovoltaic cell. 2012 International Conference on Emerging Trends in Electrical Engineering and Energy Management (ICETEEEM); 2012 13-15 Dec. 2012.
23. Dongaonkar S, Servaites JD, Ford GM, Loser S, Moore J, Gelfand RM, et al. Universality of non-Ohmic shunt leakage in thin-film solar cells. *Journal of Applied Physics*. 2010;108(12).
24. Bouzidi K, Chegaar M, Bouhemadou A. Solar cells parameters evaluation considering the series and shunt resistance. *Solar Energy Materials and Solar Cells*. 2007;91(18):1647-51.
25. Proctor CM, Nguyen T-Q. Effect of leakage current and shunt resistance on the light intensity dependence of organic solar cells. *Applied Physics Letters*. 2015;106(8).
26. Barbato M, Meneghini M, Cester A, Mura G, Zanoni E, Meneghesso G. Influence of shunt resistance on the performance of an illuminated string of solar cells: Theory, simulation, and experimental analysis. *IEEE Transactions on Device and Materials Reliability*. 2014;14(4):942-50.
27. Becquerel A-E. Recherches sur les effets de la radiation chimique de la lumiere solaire au moyen des courants electriques. *CR Acad Sci*. 1839;9(145):1.
28. Becquerel M. Mémoire sur les effets électriques produits sous l'influence des rayons solaires. *Comptes rendus hebdomadaires des séances de l'Académie des sciences*. 1839;9:561-7.
29. Green MA, editor *Photovoltaics: coming of age*. IEEE Conference on Photovoltaic Specialists; 1990: IEEE.
30. Adams WG, Day RE. V. The action of light on selenium. *Proceedings of the Royal Society of London*. 1877;25(171-178):113-7.
31. Goldmann A, Brodsky J. Zur Theorie des Becquereleffektes. I. Lichtelektrische Untersuchungen an oxydierten Kupferelektroden. *Annalen der Physik*. 1914;349(14):849-900.
32. Fritts CE. On a new form of selenium cell, and some electrical discoveries made by its use. *American Journal of Science*. 1883;3(156):465-72.
33. Bergmann L. Uber eine neue Selen-Sperrschicht Photozelle. *Physikalische Zeitschrift*. 1931;32:286-9.
34. Abou-Ras D, Kirchartz T, Rau U. *Advanced characterization techniques for thin film solar cells*: Wiley Online Library; 2011.

35. Su Y-W, Lan S-C, Wei K-H. Organic photovoltaics. *Materials Today*. 2012;15(12):554-62.
36. Mazzi KA, Luscombe CK. The future of organic photovoltaics. *Chemical Society Reviews*. 2015;44(1):78-90.
37. Leo K. Organic photovoltaics. *Nature Reviews Materials*. 2016;1(8):1-2.
38. O'regan B, Grätzel M. A low-cost, high-efficiency solar cell based on dye-sensitized colloidal TiO₂ films. *nature*. 1991;353(6346):737-40.
39. Park N-G. Perovskite solar cells: an emerging photovoltaic technology. *Materials Today*. 2015;18(2):65-72.
40. Kojima A, Teshima K, Shirai Y, Miyasaka T. Organometal Halide Perovskites as Visible-Light Sensitizers for Photovoltaic Cells. *Journal of the American Chemical Society*. 2009;131(17):6050-1.
41. Rose G. De novis quibusdam fossilibus quae in montibus Uraliis inveniuntur: typis AG Schadii; 1839.
42. Manser JS, Christians JA, Kamat PV. Intriguing optoelectronic properties of metal halide perovskites. *Chemical reviews*. 2016;116(21):12956-3008.
43. Bowman H. On the structure of perovskite from the Burgumer alp, Pfitschthal, tyrol. *Mineralogical magazine and journal of the Mineralogical Society*. 1908;15(69):156-76.
44. Wainer E. High titania dielectrics. *Transactions of the Electrochemical Society*. 1946;89(1):331.
45. Cross L, Newnham R. History of ferroelectrics. *Ceramics and civilization*. 1987;3:289-305.
46. Wells HL. Über die cäsium-und kalium-bleihalogenide. *Zeitschrift für anorganische Chemie*. 1893;3(1):195-210.
47. Møller CK. A phase transition in cæsium plumbochloride. *Nature*. 1957;180(4593):981-2.
48. Møller CK. Crystal structure and photoconductivity of caesium plumbohalides. *Nature*. 1958;182:1436-.
49. De Jongh LJ, Miedema AR. Experiments on simple magnetic model systems. *Advances in Physics*. 2001;50(8):947-1170.

50. Willett R, Place H, Middleton M. Crystal structures of three new copper (II) halide layered perovskites: structural, crystallographic, and magnetic correlations. *Journal of the American chemical society*. 1988;110(26):8639-50.
51. Mostafa MF, Willett RD. Magnetic properties of ferrous chloride complexes with two-dimensional structures. *Physical Review B*. 1971;4(7):2213.
52. Geick R, Strobel K. Phonons in perovskite-type layer structures. *Journal of Physics C: Solid State Physics*. 1979;12(1):27.
53. Ishihara T, Takahashi J, Goto T. Exciton state in two-dimensional perovskite semiconductor (C₁₀H₂₁NH₃)₂PbI₄. *Solid state communications*. 1989;69(9):933-6.
54. Xu C-q, Fukuta Sy, Sakakura H, Kondo T, Ito R, Takahashi Y, et al. Anomalous electro-absorption in the low-temperature phase of (C₁₀H₂₁NH₃)₂PbI₄. *Solid state communications*. 1991;77(12):923-6.
55. Xu C-q, Kondo T, Sakakura H, Kumata K, Takahashi Y, Ito R. Optical third-harmonic generation in layered perovskite-type material (C₁₀H₂₁NH₃)₂PbI₄. *Solid state communications*. 1991;79(3):245-8.
56. Hong X, Ishihara T, Nurmikko A. Dielectric confinement effect on excitons in PbI₄-based layered semiconductors. *Physical Review B*. 1992;45(12):6961.
57. Hirasawa M, Ishihara T, Goto T, Sasaki S, Uchida K, Miura N. Magnetoreflexion of the lowest exciton in a layered perovskite-type compound (C₁₀H₂₁NH₃)₂PbI₄. *Solid state communications*. 1993;86(8):479-83.
58. Papavassiliou GC, Koutselas I, Terzis A, Whangbo M-H. Structural and electronic properties of the natural quantum-well system (C₆H₅CH₂CH₂NH₃)₂SnI₄. *Solid state communications*. 1994;91(9):695-8.
59. Ishihara T, Hong X, Ding J, Nurmikko A. Dielectric confinement effect for exciton and biexciton states in PbI₄-based two-dimensional semiconductor structures. *Surface science*. 1992;267(1-3):323-6.
60. Hanamura E, Nagaosa N, Kumagai M, Takagahara T. Quantum wells with enhanced exciton effects and optical non-linearity. *Materials Science and Engineering: B*. 1988;1(3-4):255-8.
61. Mitzi DB, Feild C, Harrison W, Guloy A. Conducting tin halides with a layered organic-based perovskite structure. *Nature*. 1994;369(6480):467-9.

62. Mitzi D, Wang S, Feild C, Chess C, Guloy A. Conducting layered organic-inorganic halides containing $\langle 110 \rangle$ -oriented perovskite sheets. *Science*. 1995;267(5203):1473-6.
63. Era M, Morimoto S, Tsutsui T, Saito S. Electroluminescent device using two dimensional semiconductor $(\text{C}_6\text{H}_5\text{C}_2\text{H}_4\text{NH}_3)_2\text{PbI}_4$ as an emitter. *Synthetic Metals*. 1995;71(1-3):2013-4.
64. Hattori T, Taira T, Era M, Tsutsui T, Saito S. Highly efficient electroluminescence from a heterostructure device combined with emissive layered-perovskite and an electron-transporting organic compound. *Chemical physics letters*. 1996;254(1-2):103-8.
65. Chondroudis K, Mitzi DB. Electroluminescence from an organic-inorganic perovskite incorporating a quaterthiophene dye within lead halide perovskite layers. *Chemistry of materials*. 1999;11(11):3028-30.
66. Kagan CR, Mitzi DB, Dimitrakopoulos CD. Organic-inorganic hybrid materials as semiconducting channels in thin-film field-effect transistors. *Science*. 1999;286(5441):945-7.
67. Mitzi DB, Dimitrakopoulos CD, Kosbar LL. Structurally tailored organic-inorganic perovskites: optical properties and solution-processed channel materials for thin-film transistors. *Chemistry of materials*. 2001;13(10):3728-40.
68. Mitzi DB, Dimitrakopoulos CD, Rosner J, Medeiros DR, Xu Z, Noyan C. Hybrid field-effect transistor based on a low-temperature melt-processed channel layer. *Advanced Materials*. 2002;14(23):1772-6.
69. Kojima A, Teshima K, Miyasaka T, Shirai Y. Novel Photoelectrochemical Cell with Mesoscopic Electrodes Sensitized by Lead-Halide Compounds (2). *ECS Meeting Abstracts*. 2006;MA2006-02(7):397.
70. Kim H-S, Lee C-R, Im J-H, Lee K-B, Moehl T, Marchioro A, et al. Lead iodide perovskite sensitized all-solid-state submicron thin film mesoscopic solar cell with efficiency exceeding 9%. *Scientific reports*. 2012;2(1):591.
71. Salbeck J, Yu N, Bauer J, Weissörtel F, Bestgen H. Low molecular organic glasses for blue electroluminescence. *Synthetic Metals*. 1997;91(1-3):209-15.
72. Bach U, Lupo D, Comte P, Moser JE, Weissörtel F, Salbeck J, et al. Solid-state dye-sensitized mesoporous TiO_2 solar cells with high photon-to-electron conversion efficiencies. *Nature*. 1998;395(6702):583-5.

73. Lee MM, Teuscher J, Miyasaka T, Murakami TN, Snaith HJ. Efficient Hybrid Solar Cells Based on Meso-Superstructured Organometal Halide Perovskites. *Science*. 2012;338(6107):643-7.
74. Green MA, Ho-Baillie A, Snaith HJ. The emergence of perovskite solar cells. *Nature Photonics*. 2014;8(7):506-14.
75. Wen X, Ho-Baillie A, Huang S, Sheng R, Chen S, Ko H-c, et al. Mobile charge-induced fluorescence intermittency in methylammonium lead bromide perovskite. *Nano Letters*. 2015;15(7):4644-9.
76. Burschka J, Pellet N, Moon S-J, Humphry-Baker R, Gao P, Nazeeruddin MK, et al. Sequential deposition as a route to high-performance perovskite-sensitized solar cells. *Nature*. 2013;499(7458):316-9.
77. Liu M, Johnston MB, Snaith HJ. Efficient planar heterojunction perovskite solar cells by vapour deposition. *Nature*. 2013;501(7467):395-8.
78. Jeon NJ, Noh JH, Kim YC, Yang WS, Ryu S, Seok SI. Solvent engineering for high-performance inorganic–organic hybrid perovskite solar cells. *Nature Materials*. 2014;13(9):897-903.
79. Jeon NJ, Noh JH, Yang WS, Kim YC, Ryu S, Seo J, et al. Compositional engineering of perovskite materials for high-performance solar cells. *Nature*. 2015;517(7535):476-80.
80. Min H, Lee DY, Kim J, Kim G, Lee KS, Kim J, et al. Perovskite solar cells with atomically coherent interlayers on SnO₂ electrodes. *Nature*. 2021;598(7881):444-50.
81. Lin Q, Armin A, Nagiri RCR, Burn PL, Meredith P. Electro-optics of perovskite solar cells. *Nature Photonics*. 2015;9(2):106-12.
82. Huang H, Bodnarchuk MI, Kershaw SV, Kovalenko MV, Rogach AL. Lead halide perovskite nanocrystals in the research spotlight: stability and defect tolerance. *ACS energy letters*. 2017;2(9):2071-83.
83. Das B, Liu Z, Aguilera I, Rau U, Kirchartz T. Defect tolerant device geometries for lead-halide perovskites. *Materials advances*. 2021;2(11):3655-70.
84. Etgar L, Gao P, Xue Z, Peng Q, Chandiran AK, Liu B, et al. Mesoscopic CH₃NH₃PbI₃/TiO₂ Heterojunction Solar Cells. *Journal of the American Chemical Society*. 2012;134(42):17396-9.

85. Xing G, Mathews N, Sun S, Lim SS, Lam YM, Grätzel M, et al. Long-range balanced electron-and hole-transport lengths in organic-inorganic CH₃NH₃PbI₃. *Science*. 2013;342(6156):344-7.
86. Ponceca CS, Jr., Savenije TJ, Abdellah M, Zheng K, Yartsev A, Pascher T, et al. Organometal Halide Perovskite Solar Cell Materials Rationalized: Ultrafast Charge Generation, High and Microsecond-Long Balanced Mobilities, and Slow Recombination. *Journal of the American Chemical Society*. 2014;136(14):5189-92.
87. McMeekin DP, Sadoughi G, Rehman W, Eperon GE, Saliba M, Hörantner MT, et al. A mixed-cation lead mixed-halide perovskite absorber for tandem solar cells. *Science*. 2016;351(6269):151-5.
88. Bailie CD, Christoforo MG, Mailoa JP, Bowring AR, Unger EL, Nguyen WH, et al. Semi-transparent perovskite solar cells for tandems with silicon and CIGS. *Energy & Environmental Science*. 2015;8(3):956-63.
89. Werner J, Weng C-H, Walter A, Fesquet L, Seif JP, De Wolf S, et al. Efficient monolithic perovskite/silicon tandem solar cell with cell area > 1 cm². *The journal of physical chemistry letters*. 2016;7(1):161-6.
90. Chen Y-S, Manser JS, Kamat PV. All solution-processed lead halide perovskite-BiVO₄ tandem assembly for photolytic solar fuels production. *Journal of the American Chemical Society*. 2015;137(2):974-81.
91. Luo J, Im J-H, Mayer MT, Schreier M, Nazeeruddin MK, Park N-G, et al. Water photolysis at 12.3% efficiency via perovskite photovoltaics and Earth-abundant catalysts. *Science*. 2014;345(6204):1593-6.
92. Sabba D, Kumar MH, Wong LH, Barber J, Grätzel M, Mathews N. Perovskite-hematite tandem cells for efficient overall solar driven water splitting. *Nano letters*. 2015;15(6):3833-9.
93. Maculan G, Sheikh AD, Abdelhady AL, Saidaminov MI, Haque MA, Murali B, et al. CH₃NH₃PbCl₃ single crystals: inverse temperature crystallization and visible-blind UV-photodetector. *The journal of physical chemistry letters*. 2015;6(19):3781-6.
94. Lin Q, Armin A, Burn PL, Meredith P. Filterless narrowband visible photodetectors. *Nature Photonics*. 2015;9(10):687-94.

95. Moehl T, Im JH, Lee YH, Domanski K, Giordano F, Zakeeruddin SM, et al. Strong photocurrent amplification in perovskite solar cells with a porous TiO₂ blocking layer under reverse bias. *The journal of physical chemistry letters*. 2014;5(21):3931-6.
96. Chen Q, Wu J, Ou X, Huang B, Almutlaq J, Zhumeckenov AA, et al. All-inorganic perovskite nanocrystal scintillators. *Nature*. 2018;561(7721):88-93.
97. Náfrádi B, Náfrádi Gb, Forró Ls, Horváth E. Methylammonium lead iodide for efficient X-ray energy conversion. *The Journal of Physical Chemistry C*. 2015;119(45):25204-8.
98. Yakunin S, Sytnyk M, Kriegner D, Shrestha S, Richter M, Matt GJ, et al. Detection of X-ray photons by solution-processed lead halide perovskites. *Nature photonics*. 2015;9(7):444-9.
99. Xing G, Mathews N, Lim SS, Yantara N, Liu X, Sabba D, et al. Low-temperature solution-processed wavelength-tunable perovskites for lasing. *Nature materials*. 2014;13(5):476-80.
100. Deschler F, Price M, Pathak S, Klintberg LE, Jarausch D-D, Higler R, et al. High photoluminescence efficiency and optically pumped lasing in solution-processed mixed halide perovskite semiconductors. *The journal of physical chemistry letters*. 2014;5(8):1421-6.
101. Fu Y, Zhu H, Schrader AW, Liang D, Ding Q, Joshi P, et al. Nanowire lasers of formamidinium lead halide perovskites and their stabilized alloys with improved stability. *Nano letters*. 2016;16(2):1000-8.
102. Zhu H, Fu Y, Meng F, Wu X, Gong Z, Ding Q, et al. Lead halide perovskite nanowire lasers with low lasing thresholds and high quality factors. *Nature materials*. 2015;14(6):636-42.
103. Sutherland BR, Hoogland S, Adachi MM, Wong CT, Sargent EH. Conformal organohalide perovskites enable lasing on spherical resonators. *ACS nano*. 2014;8(10):10947-52.
104. Yakunin S, Protesescu L, Krieg F, Bodnarchuk MI, Nedelcu G, Humer M, et al. Low-threshold amplified spontaneous emission and lasing from colloidal nanocrystals of caesium lead halide perovskites. *Nature communications*. 2015;6(1):8056.
105. Liu Y, Cui J, Du K, Tian H, He Z, Zhou Q, et al. Efficient blue light-emitting diodes based on quantum-confined bromide perovskite nanostructures. *Nature Photonics*. 2019;13(11):760-4.
106. Xiao Z, Kerner RA, Zhao L, Tran NL, Lee KM, Koh T-W, et al. Efficient perovskite light-emitting diodes featuring nanometre-sized crystallites. *Nature Photonics*. 2017;11(2):108-15.

107. Yang Y, Yan Y, Yang M, Choi S, Zhu K, Luther JM, et al. Low surface recombination velocity in solution-grown $\text{CH}_3\text{NH}_3\text{PbBr}_3$ perovskite single crystal. *Nature communications*. 2015;6(1):7961.
108. Yang Y, Ostrowski DP, France RM, Zhu K, Van De Lagemaat J, Luther JM, et al. Observation of a hot-phonon bottleneck in lead-iodide perovskites. *Nature Photonics*. 2016;10(1):53-9.
109. Shi D, Adinolfi V, Comin R, Yuan M, Alarousu E, Buin A, et al. Low trap-state density and long carrier diffusion in organolead trihalide perovskite single crystals. *Science*. 2015;347(6221):519-22.
110. Brenner TM, Egger DA, Kronik L, Hodes G, Cahen D. Hybrid organic–inorganic perovskites: low-cost semiconductors with intriguing charge-transport properties. *Nature Reviews Materials*. 2016;1(1):1-16.
111. Goldschmidt VM. Die gesetze der kristallochemie. *Naturwissenschaften*. 1926;14(21):477-85.
112. Park N-G, Miyasaka T, Grätzel M. Organic-inorganic halide perovskite photovoltaics. Cham, Switzerland: Springer. 2016.
113. Stoumpos CC, Kanatzidis MG. The renaissance of halide perovskites and their evolution as emerging semiconductors. *Accounts of chemical research*. 2015;48(10):2791-802.
114. Li C, Lu X, Ding W, Feng L, Gao Y, Guo Z. Formability of abx_3 (x= f, cl, br, i) halide perovskites. *Acta Crystallographica Section B: Structural Science*. 2008;64(6):702-7.
115. Shannon RD. Revised effective ionic radii and systematic studies of interatomic distances in halides and chalcogenides. *Acta crystallographica section A: crystal physics, diffraction, theoretical and general crystallography*. 1976;32(5):751-67.
116. Kieslich G, Sun S, Cheetham AK. Solid-state principles applied to organic–inorganic perovskites: new tricks for an old dog. *Chemical Science*. 2014;5(12):4712-5.
117. Travis W, Glover E, Bronstein H, Scanlon D, Palgrave R. On the application of the tolerance factor to inorganic and hybrid halide perovskites: a revised system. *Chemical Science*. 2016;7(7):4548-56.
118. Kieslich G, Sun S, Cheetham AK. An extended tolerance factor approach for organic–inorganic perovskites. *Chemical science*. 2015;6(6):3430-3.

119. Stoumpos CC, Malliakas CD, Kanatzidis MG. Semiconducting tin and lead iodide perovskites with organic cations: phase transitions, high mobilities, and near-infrared photoluminescent properties. *Inorganic chemistry*. 2013;52(15):9019-38.
120. Salje EKH. Characteristics of perovskite-related materials. *Philosophical Transactions of the Royal Society of London Series A, Mathematical and Physical Sciences*. 1989;328(1599):409-16.
121. Glazer A. Simple ways of determining perovskite structures. *Acta Crystallographica Section A: Crystal Physics, Diffraction, Theoretical and General Crystallography*. 1975;31(6):756-62.
122. Filip MR, Eperon GE, Snaith HJ, Giustino F. Steric engineering of metal-halide perovskites with tunable optical band gaps. *Nature communications*. 2014;5(1):5757.
123. Li Z, Yang M, Park J-S, Wei S-H, Berry JJ, Zhu K. Stabilizing perovskite structures by tuning tolerance factor: formation of formamidinium and cesium lead iodide solid-state alloys. *Chemistry of Materials*. 2016;28(1):284-92.
124. Tanaka K, Sano F, Takahashi T, Kondo T, Ito R, Ema K. Two-dimensional Wannier excitons in a layered-perovskite-type crystal (C₆H₁₃NH₃)₂PbI₄. *Solid state communications*. 2002;122(5):249-52.
125. Dunlap-Shohl WA, Barraza ET, Barrette A, Dovletgeldi S, Findik G, Dirkes DJ, et al. Tunable internal quantum well alignment in rationally designed oligomer-based perovskite films deposited by resonant infrared matrix-assisted pulsed laser evaporation. *Materials Horizons*. 2019;6(8):1707-16.
126. Gao Y, Shi E, Deng S, Shiring SB, Snaider JM, Liang C, et al. Molecular engineering of organic–inorganic hybrid perovskites quantum wells. *Nature chemistry*. 2019;11(12):1151-7.
127. Liu C, Huhn W, Du K-Z, Vazquez-Mayagoitia A, Dirkes D, You W, et al. Tunable semiconductors: control over carrier states and excitations in layered hybrid organic-inorganic perovskites. *Physical Review Letters*. 2018;121(14):146401.
128. Mitzi DB, Chondroudis K, Kagan CR. Design, structure, and optical properties of organic– inorganic perovskites containing an oligothiophene chromophore. *Inorganic chemistry*. 1999;38(26):6246-56.
129. Mitzi DB. Synthesis, structure, and properties of organic-inorganic perovskites and related materials. *Progress in inorganic chemistry*. 1999:1-121.

130. Takeoka Y, Asai K, Rikukawa M, Sanui K. Systematic studies on chain lengths, halide species, and well thicknesses for lead halide layered perovskite thin films. *Bulletin of the Chemical Society of Japan*. 2006;79(10):1607-13.
131. Kim HG, Becker OS, Jang JS, Ji SM, Borse PH, Lee JS. A generic method of visible light sensitization for perovskite-related layered oxides: Substitution effect of lead. *Journal of Solid State Chemistry*. 2006;179(4):1214-8.
132. Saparov B, Mitzi DB. Organic–inorganic perovskites: structural versatility for functional materials design. *Chemical reviews*. 2016;116(7):4558-96.
133. Wang S, Mitzi DB, Feild CA, Guloy A. Synthesis and characterization of [NH₂C (I): NH₂] 3MI₅ (M= Sn, Pb): stereochemical activity in divalent tin and lead halides containing Single. Itbbrac. 110. rtbbrac. Perovskite sheets. *Journal of the American Chemical Society*. 1995;117(19):5297-302.
134. Saliba M, Correa-Baena J-P, Wolff CM, Stolterfoht M, Phung N, Albrecht S, et al. How to Make over 20% Efficient Perovskite Solar Cells in Regular (n–i–p) and Inverted (p–i–n) Architectures. *Chemistry of Materials*. 2018;30(13):4193-201.
135. Jena AK, Kulkarni A, Miyasaka T. Halide Perovskite Photovoltaics: Background, Status, and Future Prospects. *Chem Rev*. 2019;119(5):3036-103.
136. Fröhlich D, Heidrich K, Künzel H, Trendel G, Treusch J. Cesium-trihalogen-plumbates a new class of ionic semiconductors. *Journal of Luminescence*. 1979;18:385-8.
137. Koutselas IB, Ducasse L, Papavassiliou GC. Electronic properties of three- and low-dimensional semiconducting materials with Pb halide and Sn halide units. *Journal of Physics: Condensed Matter*. 1996;8(9):1217.
138. Parry D, Tricker M, Donaldson J. The electronic structure of CsSnBr₃ and related trihalides; Studies using XPS and band theory. *Journal of Solid State Chemistry*. 1979;28(3):401-8.
139. Lefebvre I, Lippens P, Lannoo M, Allan G. Band structure of CsSnBr₃. *Physical Review B*. 1990;42(14):9174.
140. Huang L-y, Lambrecht WR. Electronic band structure, phonons, and exciton binding energies of halide perovskites CsSnCl₃, CsSnBr₃, and CsSnI₃. *Physical Review B*. 2013;88(16):165203.

141. Umari P, Mosconi E, De Angelis F. Relativistic GW calculations on CH₃NH₃PbI₃ and CH₃NH₃SnI₃ perovskites for solar cell applications. *Scientific reports*. 2014;4(1):4467.
142. Papavassiliou GC, Koutselas I. Structural, optical and related properties of some natural three-and lower-dimensional semiconductor systems. *Synthetic Metals*. 1995;71(1-3):1713-4.
143. Wulfsberg G. *Inorganic chemistry: university Science books*; 2000.
144. Amat A, Mosconi E, Ronca E, Quarti C, Umari P, Nazeeruddin MK, et al. Cation-induced band-gap tuning in organohalide perovskites: interplay of spin-orbit coupling and octahedra tilting. *Nano letters*. 2014;14(6):3608-16.
145. Even J, Pedesseau L, Dupertuis M-A, Jancu J-M, Katan C. Electronic model for self-assembled hybrid organic/perovskite semiconductors: Reverse band edge electronic states ordering and spin-orbit coupling. *Physical Review B*. 2012;86(20):205301.
146. Tanaka K, Takahashi T, Ban T, Kondo T, Uchida K, Miura N. Comparative study on the excitons in lead-halide-based perovskite-type crystals CH₃NH₃PbBr₃ CH₃NH₃PbI₃. *Solid state communications*. 2003;127(9-10):619-23.
147. Even J, Pedesseau L, Jancu J-M, Katan C. Importance of spin-orbit coupling in hybrid organic/inorganic perovskites for photovoltaic applications. *The Journal of Physical Chemistry Letters*. 2013;4(17):2999-3005.
148. Even J, Pedesseau L, Jancu JM, Katan C. DFT and $k \cdot p$ modelling of the phase transitions of lead and tin halide perovskites for photovoltaic cells. *physica status solidi (RRL)–Rapid Research Letters*. 2014;8(1):31-5.
149. Brivio F, Butler KT, Walsh A, Van Schilfgaarde M. Relativistic quasiparticle self-consistent electronic structure of hybrid halide perovskite photovoltaic absorbers. *Physical Review B*. 2014;89(15):155204.
150. Chiarella F, Zappettini A, Licci F, Borriello I, Cantele G, Ninno D, et al. Combined experimental and theoretical investigation of optical, structural, and electronic properties of CH₃NH₃SnX₃ thin films (X= Cl, Br). *Physical Review B*. 2008;77(4):045129.
151. Miyata A, Mitioglu A, Plochocka P, Portugall O, Wang JT-W, Stranks SD, et al. Direct measurement of the exciton binding energy and effective masses for charge carriers in organic-inorganic tri-halide perovskites. *Nature Physics*. 2015;11(7):582-7.
152. Galkowski K, Mitioglu A, Miyata A, Plochocka P, Portugall O, Eperon GE, et al. Determination of the exciton binding energy and effective masses for methylammonium and

- formamidinium lead tri-halide perovskite semiconductors. *Energy & Environmental Science*. 2016;9(3):962-70.
153. Brivio F, Walker AB, Walsh A. Structural and electronic properties of hybrid perovskites for high-efficiency thin-film photovoltaics from first-principles. *Apl Materials*. 2013;1(4):042111.
154. Borriello I, Cantele G, Ninno D. Ab initio investigation of hybrid organic-inorganic perovskites based on tin halides. *Physical Review B*. 2008;77(23):235214.
155. Jishi RA, Ta OB, Sharif AA. Modeling of lead halide perovskites for photovoltaic applications. *The Journal of Physical Chemistry C*. 2014;118(49):28344-9.
156. Yin W-J, Yang J-H, Kang J, Yan Y, Wei S-H. Halide perovskite materials for solar cells: a theoretical review. *Journal of Materials Chemistry A*. 2015;3(17):8926-42.
157. Gray A, Papp C, Ueda S, Balke B, Yamashita Y, Plucinski L, et al. Probing bulk electronic structure with hard X-ray angle-resolved photoemission. *Nature materials*. 2011;10(10):759-64.
158. Yan Y, Wang Q, Shu W, Jia Z, Ren X, Zhang X, et al. First-principle study of the electronic and optical properties of BInGaAs quaternary alloy lattice-matched to GaAs. *Physica B: Condensed Matter*. 2012;407(23):4570-3.
159. Sell D, Lawaetz P. New analysis of direct exciton transitions: application to GaP. *Physical Review Letters*. 1971;26(6):311.
160. Stoumpos CC, Frazer L, Clark DJ, Kim YS, Rhim SH, Freeman AJ, et al. Hybrid germanium iodide perovskite semiconductors: active lone pairs, structural distortions, direct and indirect energy gaps, and strong nonlinear optical properties. *Journal of the American Chemical Society*. 2015;137(21):6804-19.
161. Kepenekian M, Robles R, Katan C, Saponi D, Pedesseau L, Even J. Rashba and Dresselhaus effects in hybrid organic-inorganic perovskites: from basics to devices. *ACS nano*. 2015;9(12):11557-67.
162. Kim M, Im J, Freeman AJ, Ihm J, Jin H. Switchable $S = 1/2$ and $J = 1/2$ Rashba bands in ferroelectric halide perovskites. *Proceedings of the National Academy of Sciences*. 2014;111(19):6900-4.
163. Even J. Pedestrian guide to symmetry properties of the reference cubic structure of 3D all-inorganic and hybrid perovskites. ACS Publications; 2015. p. 2238-42.

164. Even J, Pedesseau L, Katan C. Analysis of multivalley and multibandgap absorption and enhancement of free carriers related to exciton screening in hybrid perovskites. *The Journal of Physical Chemistry C*. 2014;118(22):11566-72.
165. D'innocenzo V, Grancini G, Alcocer MJ, Kandada ARS, Stranks SD, Lee MM, et al. Excitons versus free charges in organo-lead tri-halide perovskites. *Nature communications*. 2014;5(1):3586.
166. Ishihara T. Optical properties of PbI₂-based perovskite structures. *Journal of luminescence*. 1994;60:269-74.
167. Green MA, Jiang Y, Soufiani AM, Ho-Baillie A. Optical properties of photovoltaic organic-inorganic lead halide perovskites. *The journal of physical chemistry letters*. 2015;6(23):4774-85.
168. Bardeen J, Shockley W. Deformation potentials and mobilities in non-polar crystals. *Physical review*. 1950;80(1):72.
169. Frost JM, Butler KT, Brivio F, Hendon CH, Van Schilfgaarde M, Walsh A. Atomistic origins of high-performance in hybrid halide perovskite solar cells. *Nano letters*. 2014;14(5):2584-90.
170. Maintz S, Deringer VL, Tchougréeff AL, Dronskowski R. Analytic projection from plane-wave and PAW wavefunctions and application to chemical-bonding analysis in solids. *Journal of computational chemistry*. 2013;34(29):2557-67.
171. Yu C, Chen Z, J. Wang J, Pfenninger W, Vockic N, Kenney JT, et al. Temperature dependence of the band gap of perovskite semiconductor compound CsSnI₃. *Journal of Applied Physics*. 2011;110(6):063526.
172. Elliott R. Intensity of optical absorption by excitons. *Physical Review*. 1957;108(6):1384.
173. Tauc J, Grigorovici R, Vancu A. Optical properties and electronic structure of amorphous germanium. *physica status solidi (b)*. 1966;15(2):627-37.
174. Corkish R, Chan DSP, Green MA. Excitons in silicon diodes and solar cells: A three-particle theory. *Journal of applied physics*. 1996;79(1):195-203.
175. Green MA, editor Many-body theory applied to solar cells: excitonic and related carrier correlation effects. *Conference Record of the Twenty Sixth IEEE Photovoltaic Specialists Conference-1997*; 1997: IEEE.
176. Pankove JI. *Optical processes in semiconductors*: Courier Corporation; 1975.

177. Stranks SD, Eperon GE, Grancini G, Menelaou C, Alcocer MJ, Leijtens T, et al. Electron-hole diffusion lengths exceeding 1 micrometer in an organometal trihalide perovskite absorber. *Science*. 2013;342(6156):341-4.
178. Snaith HJ, Abate A, Ball JM, Eperon GE, Leijtens T, Noel NK, et al. Anomalous Hysteresis in Perovskite Solar Cells. *The Journal of Physical Chemistry Letters*. 2014;5(9):1511-5.
179. Tress W, Marinova N, Moehl T, Zakeeruddin SM, Nazeeruddin MK, Grätzel M. Understanding the rate-dependent J–V hysteresis, slow time component, and aging in CH₃NH₃PbI₃ perovskite solar cells: the role of a compensated electric field. *Energy & Environmental Science*. 2015;8(3):995-1004.
180. Albin DS, del Cueto JA, editors. Correlations of capacitance-voltage hysteresis with thin-film CdTe solar cell performance during accelerated lifetime testing. 2010 IEEE International Reliability Physics Symposium; 2010: IEEE.
181. Herman M, Jankovec M, Topič M. Optimisation of the I–V measurement scan time through dynamic modelling of solar cells. *IET Renewable power generation*. 2013;7(1):63-70.
182. Unger EL, Czudek A, Kim H-S, Tress W. Chapter 4 - Current-voltage analysis: lessons learned from hysteresis. In: Pazoki M, Hagfeldt A, Edvinsson T, editors. *Characterization Techniques for Perovskite Solar Cell Materials*: Elsevier; 2020. p. 81-108.
183. Unger EL, Hoke ET, Bailie CD, Nguyen WH, Bowring AR, Heumüller T, et al. Hysteresis and transient behavior in current–voltage measurements of hybrid-perovskite absorber solar cells. *Energy & Environmental Science*. 2014;7(11):3690-8.
184. Contreras L, Idígoras J, Todinova A, Salado M, Kazim S, Ahmad S, et al. Specific cation interactions as the cause of slow dynamics and hysteresis in dye and perovskite solar cells: a small-perturbation study. *Physical Chemistry Chemical Physics*. 2016;18(45):31033-42.
185. Christians JA, Manser JS, Kamat PV. Best practices in perovskite solar cell efficiency measurements. Avoiding the error of making bad cells look good. ACS Publications; 2015. p. 852-7.
186. Chen B, Yang M, Zheng X, Wu C, Li W, Yan Y, et al. Impact of capacitive effect and ion migration on the hysteretic behavior of perovskite solar cells. *The journal of physical chemistry letters*. 2015;6(23):4693-700.

187. Ono LK, Raga SR, Wang S, Kato Y, Qi Y. Temperature-dependent hysteresis effects in perovskite-based solar cells. *Journal of Materials Chemistry A*. 2015;3(17):9074-80.
188. Christoforo MG, Hoke ET, McGehee MD, Unger EL, editors. Transient response of organo-metal-halide solar cells analyzed by time-resolved current-voltage measurements. *Photonics*; 2015: MDPI.
189. Kim H-S, Park N-G. Parameters affecting I–V hysteresis of CH₃NH₃PbI₃ perovskite solar cells: effects of perovskite crystal size and mesoporous TiO₂ layer. *The journal of physical chemistry letters*. 2014;5(17):2927-34.
190. Sanchez RS, Gonzalez-Pedro V, Lee J-W, Park N-G, Kang YS, Mora-Sero I, et al. Slow dynamic processes in lead halide perovskite solar cells. Characteristic times and hysteresis. *The journal of physical chemistry letters*. 2014;5(13):2357-63.
191. Jacobsson TJ, Correa-Baena J-P, Pazoki M, Saliba M, Schenk K, Grätzel M, et al. Exploration of the compositional space for mixed lead halogen perovskites for high efficiency solar cells. *Energy & Environmental Science*. 2016;9(5):1706-24.
192. Habisreutinger SN, Noel NK, Snaith HJ. Hysteresis index: A figure without merit for quantifying hysteresis in perovskite solar cells. *ACS Energy Letters*. 2018;3(10):2472-6.
193. Kim H-S, Jang I-H, Ahn N, Choi M, Guerrero A, Bisquert J, et al. Control of I–V hysteresis in CH₃NH₃PbI₃ perovskite solar cell. *The journal of physical chemistry letters*. 2015;6(22):4633-9.
194. Docampo P, Ball JM, Darwich M, Eperon GE, Snaith HJ. Efficient organometal trihalide perovskite planar-heterojunction solar cells on flexible polymer substrates. *Nature communications*. 2013;4(1):2761.
195. Patel JB, Wong-Leung J, Van Reenen S, Sakai N, Wang JTW, Parrott ES, et al. Influence of interface morphology on hysteresis in vapor-deposited perovskite solar cells. *Advanced Electronic Materials*. 2017;3(2):1600470.
196. Kegelman L, Wolff CM, Awino C, Lang F, Unger EL, Korte L, et al. It Takes Two to Tango □ Double-Layer Selective Contacts in Perovskite Solar Cells for Improved Device Performance and Reduced Hysteresis. *ACS applied materials & interfaces*. 2017;9(20):17245-55.
197. Garcia-Belmonte G, Bisquert J. Distinction between capacitive and noncapacitive hysteretic currents in operation and degradation of perovskite solar cells. *ACS Energy Letters*. 2016;1(4):683-8.

198. Levine I, Nayak PK, Wang JT-W, Sakai N, Van Reenen S, Brenner TM, et al. Interface-dependent ion migration/accumulation controls hysteresis in MAPbI₃ solar cells. *The Journal of Physical Chemistry C*. 2016;120(30):16399-411.
199. Wei J, Zhao Y, Li H, Li G, Pan J, Xu D, et al. Hysteresis analysis based on the ferroelectric effect in hybrid perovskite solar cells. *The journal of physical chemistry letters*. 2014;5(21):3937-45.
200. Xiao Z, Yuan Y, Shao Y, Wang Q, Dong Q, Bi C, et al. Giant switchable photovoltaic effect in organometal trihalide perovskite devices. *Nature materials*. 2015;14(2):193-8.
201. Dualeh A, Moehl T, Tétreault N, Teuscher J, Gao P, Nazeeruddin MK, et al. Impedance spectroscopic analysis of lead iodide perovskite-sensitized solid-state solar cells. *ACS nano*. 2014;8(1):362-73.
202. Butler KT, Frost JM, Walsh A. Ferroelectric materials for solar energy conversion: photoferroics revisited. *Energy & Environmental Science*. 2015;8(3):838-48.
203. Kang DH, Park NG. On the current–voltage hysteresis in perovskite solar cells: dependence on perovskite composition and methods to remove hysteresis. *Advanced Materials*. 2019;31(34):1805214.
204. Bisquert J, Garcia-Belmonte G, Guerrero A. Impedance characteristics of hybrid organometal halide perovskite solar cells. *Organic-inorganic halide perovskite photovoltaics: from fundamentals to device architectures*. 2016:163-99.
205. Poglitsch A, Weber D. Dynamic disorder in methylammoniumtrihalogenoplumbates (II) observed by millimeter-wave spectroscopy. *The Journal of chemical physics*. 1987;87(11):6373-8.
206. Weller MT, Weber OJ, Henry PF, Di Pumpo AM, Hansen TC. Complete structure and cation orientation in the perovskite photovoltaic methylammonium lead iodide between 100 and 352 K. *Chemical communications*. 2015;51(20):4180-3.
207. Onoda-Yamamuro N, Matsuo T, Suga H. Dielectric study of CH₃NH₃PbX₃ (X= Cl, Br, I). *Journal of Physics and Chemistry of Solids*. 1992;53(7):935-9.
208. Onoda-Yamamuro N, Matsuo T, Suga H. Calorimetric and IR spectroscopic studies of phase transitions in methylammonium trihalogenoplumbates (II). *Journal of Physics and Chemistry of Solids*. 1990;51(12):1383-95.

209. Leguy AM, Frost JM, McMahon AP, Sakai VG, Kockelmann W, Law C, et al. The dynamics of methylammonium ions in hybrid organic–inorganic perovskite solar cells. *Nature communications*. 2015;6(1):7124.
210. Bakulin AA, Selig O, Bakker HJ, Rezus YL, Müller C, Glaser T, et al. Real-time observation of organic cation reorientation in methylammonium lead iodide perovskites. *The journal of physical chemistry letters*. 2015;6(18):3663-9.
211. Frost JM, Butler KT, Walsh A. Molecular ferroelectric contributions to anomalous hysteresis in hybrid perovskite solar cells. *Apl Materials*. 2014;2(8):081506.
212. Kim H-S, Im SH, Park N-G. Organolead halide perovskite: new horizons in solar cell research. *The Journal of Physical Chemistry C*. 2014;118(11):5615-25.
213. Yuan Y, Li T, Wang Q, Xing J, Gruverman A, Huang J. Anomalous photovoltaic effect in organic-inorganic hybrid perovskite solar cells. *Science advances*. 2017;3(3):e1602164.
214. Cao X, Li Y, Li C, Fang F, Yao Y, Cui X, et al. Modulating hysteresis of perovskite solar cells by a poling voltage. *The Journal of Physical Chemistry C*. 2016;120(40):22784-92.
215. Nemnes GA, Besleaga C, Tomulescu AG, Pintilie I, Pintilie L, Torfason K, et al. Dynamic electrical behavior of halide perovskite based solar cells. *Solar Energy Materials and Solar Cells*. 2017;159:197-203.
216. Röhm H, Leonhard T, Hoffmann MJ, Colsmann A. Ferroelectric domains in methylammonium lead iodide perovskite thin-films. *Energy & Environmental Science*. 2017;10(4):950-5.
217. Fan Z, Xiao J, Sun K, Chen L, Hu Y, Ouyang J, et al. Ferroelectricity of CH₃NH₃PbI₃ perovskite. *The journal of physical chemistry letters*. 2015;6(7):1155-61.
218. Sharada G, Mahale P, Kore BP, Mukherjee S, Pavan MS, De C, et al. Is CH₃NH₃PbI₃ polar. *J Phys Chem Lett*. 2016;7(13):2412-9.
219. Sajedi Alvar M, Kumar M, Blom PWM, Wetzelaer G-JAH, Asadi K. Absence of ferroelectricity in methylammonium lead iodide perovskite. *AIP Advances*. 2017;7(9):095110.
220. Anusca I, Balčiūnas S, Gemeiner P, Svirskas Š, Sanlialp M, Lackner G, et al. Dielectric response: answer to many questions in the methylammonium lead halide solar cell absorbers. *Advanced Energy Materials*. 2017;7(19):1700600.

221. Meloni S, Moehl T, Tress W, Franckevičius M, Saliba M, Lee YH, et al. Ionic polarization-induced current–voltage hysteresis in $\text{CH}_3\text{NH}_3\text{PbX}_3$ perovskite solar cells. *Nature communications*. 2016;7(1):10334.
222. Verwey J, Westerink N. Photoconductivity in lead chloride and lead bromide. *Physica*. 1969;42(2):293-302.
223. Yuan Y, Chae J, Shao Y, Wang Q, Xiao Z, Centrone A, et al. Photovoltaic switching mechanism in lateral structure hybrid perovskite solar cells. *Advanced Energy Materials*. 2015;5(15):1500615.
224. Nickel NH, Lang F, Brus VV, Shargaieva O, Rappich J. Unraveling the light-induced degradation mechanisms of $\text{CH}_3\text{NH}_3\text{PbI}_3$ perovskite films. *Advanced Electronic Materials*. 2017;3(12):1700158.
225. Egger DA, Kronik L, Rappe AM. Theory of hydrogen migration in organic–inorganic halide perovskites. *Angewandte Chemie International Edition*. 2015;54(42):12437-41.
226. Egger DA, Rappe AM, Kronik L. Hybrid organic–inorganic perovskites on the move. *Accounts of chemical research*. 2016;49(3):573-81.
227. Eames C, Frost JM, Barnes PR, O’regan BC, Walsh A, Islam MS. Ionic transport in hybrid lead iodide perovskite solar cells. *Nature communications*. 2015;6(1):7497.
228. Walsh A, Stranks SD. Taking control of ion transport in halide perovskite solar cells. *ACS Energy Letters*. 2018;3(8):1983-90.
229. Frost JM, Walsh A. What is moving in hybrid halide perovskite solar cells? *Accounts of chemical research*. 2016;49(3):528-35.
230. Meggiolaro D, Motti SG, Mosconi E, Barker AJ, Ball J, Perini CAR, et al. Iodine chemistry determines the defect tolerance of lead-halide perovskites. *Energy & Environmental Science*. 2018;11(3):702-13.
231. Stampelcoskie KG, Manser JS, Kamat PV. Dual nature of the excited state in organic–inorganic lead halide perovskites. *Energy & Environmental Science*. 2015;8(1):208-15.
232. Domanski K, Roose B, Matsui T, Saliba M, Turren-Cruz S-H, Correa-Baena J-P, et al. Migration of cations induces reversible performance losses over day/night cycling in perovskite solar cells. *Energy & Environmental Science*. 2017;10(2):604-13.
233. Belisle RA, Nguyen WH, Bowring AR, Calado P, Li X, Irvine SJ, et al. Interpretation of inverted photocurrent transients in organic lead halide perovskite solar cells: proof of the field

- screening by mobile ions and determination of the space charge layer widths. *Energy & Environmental Science*. 2017;10(1):192-204.
234. Tress W. Metal Halide Perovskites as Mixed Electronic–Ionic Conductors: Challenges and Opportunities □ From Hysteresis to Memristivity. *The journal of physical chemistry letters*. 2017;8(13):3106-14.
235. Ginting RT, Jeon M-K, Lee K-J, Jin W-Y, Kim T-W, Kang J-W. Degradation mechanism of planar-perovskite solar cells: correlating evolution of iodine distribution and photocurrent hysteresis. *Journal of Materials Chemistry A*. 2017;5(9):4527-34.
236. Jacobs DA, Wu Y, Shen H, Barugkin C, Beck FJ, White TP, et al. Hysteresis phenomena in perovskite solar cells: the many and varied effects of ionic accumulation. *Physical Chemistry Chemical Physics*. 2017;19(4):3094-103.
237. Kim J, Lee S-H, Lee JH, Hong K-H. The role of intrinsic defects in methylammonium lead iodide perovskite. *The journal of physical chemistry letters*. 2014;5(8):1312-7.
238. Baena JPC, Steier L, Tress W, Saliba M, Neutzner S, Matsui T, et al. Highly efficient planar perovskite solar cells through band alignment engineering. *Energy & Environmental Science*. 2015;8(10):2928-34.
239. Weber SA, Hermes IM, Turren-Cruz S-H, Gort C, Bergmann VW, Gilson L, et al. How the formation of interfacial charge causes hysteresis in perovskite solar cells. *Energy & environmental science*. 2018;11(9):2404-13.
240. Calado P, Telford AM, Bryant D, Li X, Nelson J, O'Regan BC, et al. Evidence for ion migration in hybrid perovskite solar cells with minimal hysteresis. *Nature communications*. 2016;7(1):13831.
241. Richardson G, O'Kane SE, Niemann RG, Peltola TA, Foster JM, Cameron PJ, et al. Can slow-moving ions explain hysteresis in the current–voltage curves of perovskite solar cells? *Energy & Environmental Science*. 2016;9(4):1476-85.
242. van Reenen S, Kemerink M, Snaith HJ. Modeling anomalous hysteresis in perovskite solar cells. *The journal of physical chemistry letters*. 2015;6(19):3808-14.
243. Sherkar TS, Momblona C, Gil-Escrig L, Avila J, Sessolo M, Bolink HJ, et al. Recombination in perovskite solar cells: significance of grain boundaries, interface traps, and defect ions. *ACS energy letters*. 2017;2(5):1214-22.

244. Neukom MT, Züfle S, Knapp E, Makha M, Hany R, Ruhstaller B. Why perovskite solar cells with high efficiency show small IV-curve hysteresis. *Solar Energy Materials and Solar Cells*. 2017;169:159-66.
245. Baumann A, Väh S, Rieder P, Heiber MC, Tvingstedt K, Dyakonov V. Identification of trap states in perovskite solar cells. *The journal of physical chemistry letters*. 2015;6(12):2350-4.
246. Liu P, Wang W, Liu S, Yang H, Shao Z. Fundamental understanding of photocurrent hysteresis in perovskite solar cells. *Advanced Energy Materials*. 2019;9(13):1803017.
247. Lee J-W, Kim S-G, Bae S-H, Lee D-K, Lin O, Yang Y, et al. The interplay between trap density and hysteresis in planar heterojunction perovskite solar cells. *Nano letters*. 2017;17(7):4270-6.
248. Aygüler MF, Hufnagel AG, Rieder P, Wussler M, Jaegermann W, Bein T, et al. Influence of fermi level alignment with tin oxide on the hysteresis of perovskite solar cells. *ACS applied materials & interfaces*. 2018;10(14):11414-9.
249. Pockett A, Eperon GE, Sakai N, Snaith HJ, Peter LM, Cameron PJ. Microseconds, milliseconds and seconds: deconvoluting the dynamic behaviour of planar perovskite solar cells. *Physical Chemistry Chemical Physics*. 2017;19(8):5959-70.
250. Miyadera T, Sugita T, Chikamatsu M. Hysteresis Analysis of Organolead Halide Perovskite Solar Cells by Transient Current Measurement. *Electrochemistry*. 2017;85(5):276-9.
251. Sepalage GA, Meyer S, Pascoe A, Scully AD, Huang F, Bach U, et al. Copper (I) iodide as hole-conductor in planar perovskite solar cells: probing the origin of J–V hysteresis. *Advanced Functional Materials*. 2015;25(35):5650-61.
252. Tress W, Correa Baena JP, Saliba M, Abate A, Graetzel M. Inverted current–voltage hysteresis in mixed perovskite solar cells: polarization, energy barriers, and defect recombination. *Advanced Energy Materials*. 2016;6(19):1600396.
253. De Bastiani M, Dell'Erba G, Gandini M, D'Innocenzo V, Neutzner S, Kandada ARS, et al. Ion migration and the role of preconditioning cycles in the stabilization of the J–V characteristics of inverted hybrid perovskite solar cells. *Advanced Energy Materials*. 2016;6(2):1501453.
254. Bertoluzzi L, Belisle RA, Bush KA, Checharoen R, McGehee MD, O'Regan BC. In situ measurement of electric-field screening in hysteresis-free PTAA/FA0.83Cs0.17Pb (I)0.83Br0.17)3/C60 perovskite solar cells gives an ion mobility of $\sim 3 \times 10^{-7} \text{ cm}^2/(\text{V s})$, 2 orders of

- magnitude faster than reported for metal-oxide-contacted perovskite cells with hysteresis. *Journal of the American Chemical Society*. 2018;140(40):12775-84.
255. Li Z, Xiao C, Yang Y, Harvey SP, Kim DH, Christians JA, et al. Extrinsic ion migration in perovskite solar cells. *Energy & Environmental Science*. 2017;10(5):1234-42.
256. Jacobs DA, Shen H, Pfeffer F, Peng J, White TP, Beck FJ, et al. The two faces of capacitance: New interpretations for electrical impedance measurements of perovskite solar cells and their relation to hysteresis. *Journal of Applied Physics*. 2018;124(22):225702.
257. Almora O, Zarazua I, Mas-Marza E, Mora-Sero I, Bisquert J, Garcia-Belmonte G. Capacitive dark currents, hysteresis, and electrode polarization in lead halide perovskite solar cells. *The journal of physical chemistry letters*. 2015;6(9):1645-52.
258. Khenkin MV, Anoop K, Visoly-Fisher I, Galagan Y, Di Giacomo F, Patil BR, et al. Reconsidering figures of merit for performance and stability of perovskite photovoltaics. *Energy & Environmental Science*. 2018;11(4):739-43.
259. Mizusaki J, Arai K, Fueki K. Ionic conduction of the perovskite-type halides. *Solid State Ionics*. 1983;11(3):203-11.
260. Merdasa A, Tian Y, Camacho R, Dobrovolsky A, Debroye E, Unger EL, et al. “Supertrap” at work: extremely efficient nonradiative recombination channels in MAPbI₃ perovskites revealed by luminescence super-resolution imaging and spectroscopy. *ACS nano*. 2017;11(6):5391-404.
261. Saliba M, Matsui T, Seo J-Y, Domanski K, Correa-Baena J-P, Nazeeruddin MK, et al. Cesium-containing triple cation perovskite solar cells: improved stability, reproducibility and high efficiency. *Energy & environmental science*. 2016;9(6):1989-97.
262. Haruyama J, Sodeyama K, Han L, Tateyama Y. First-principles study of ion diffusion in perovskite solar cell sensitizers. *Journal of the American Chemical Society*. 2015;137(32):10048-51.
263. Saliba M, Matsui T, Domanski K, Seo J-Y, Ummadisingu A, Zakeeruddin SM, et al. Incorporation of rubidium cations into perovskite solar cells improves photovoltaic performance. *Science*. 2016;354(6309):206-9.
264. Zong Y, Wang N, Zhang L, Ju MG, Zeng XC, Sun XW, et al. Homogenous alloys of formamidinium lead triiodide and cesium tin triiodide for efficient ideal-bandgap perovskite solar cells. *Angewandte Chemie International Edition*. 2017;56(41):12658-62.

265. Wang Y, Fu W, Yan J, Chen J, Yang W, Chen H. Low-bandgap mixed tin–lead iodide perovskite with large grains for high performance solar cells. *Journal of Materials Chemistry A*. 2018;6(27):13090-5.
266. Tombe S, Adam G, Heilbrunner H, Apaydin DH, Ulbricht C, Sariciftci NS, et al. Optical and electronic properties of mixed halide (X= I, Cl, Br) methylammonium lead perovskite solar cells. *Journal of Materials Chemistry C*. 2017;5(7):1714-23.
267. Turren-Cruz S-H, Saliba M, Mayer MT, Juárez-Santiesteban H, Mathew X, Nienhaus L, et al. Enhanced charge carrier mobility and lifetime suppress hysteresis and improve efficiency in planar perovskite solar cells. *Energy & Environmental Science*. 2018;11(1):78-86.
268. Azam M, Yue S, Xu R, Liu K, Ren K, Sun Y, et al. Highly efficient solar cells based on Cl incorporated tri-cation perovskite materials. *Journal of Materials Chemistry A*. 2018;6(28):13725-34.
269. Hu Y, Hutter EM, Rieder P, Grill I, Hanisch J, Aygüler MF, et al. Understanding the role of cesium and rubidium additives in perovskite solar cells: trap states, charge transport, and recombination. *Advanced Energy Materials*. 2018;8(16):1703057.
270. Son D-Y, Kim S-G, Seo J-Y, Lee S-H, Shin H, Lee D, et al. Universal approach toward hysteresis-free perovskite solar cell via defect engineering. *Journal of the American Chemical Society*. 2018;140(4):1358-64.
271. Abdi-Jalebi M, Andaji-Garmaroudi Z, Cacovich S, Stavrakas C, Philippe B, Richter JM, et al. Maximizing and stabilizing luminescence from halide perovskites with potassium passivation. *Nature*. 2018;555(7697):497-501.
272. Kubicki DJ, Prochowicz D, Hofstetter A, Zakeeruddin SM, Grätzel M, Emsley L. Phase segregation in Cs-, Rb- and K-doped mixed-cation (MA) x (FA) $1-x$ PbI₃ hybrid perovskites from solid-state NMR. *Journal of the American Chemical Society*. 2017;139(40):14173-80.
273. Sharenko A, Toney MF. Relationships between lead halide perovskite thin-film fabrication, morphology, and performance in solar cells. *Journal of the American Chemical Society*. 2016;138(2):463-70.
274. Chen Q, Zhou H, Song T-B, Luo S, Hong Z, Duan H-S, et al. Controllable self-induced passivation of hybrid lead iodide perovskites toward high performance solar cells. *Nano letters*. 2014;14(7):4158-63.

275. Wu C-G, Chiang C-H, Tseng Z-L, Nazeeruddin MK, Hagfeldt A, Grätzel M. High efficiency stable inverted perovskite solar cells without current hysteresis. *Energy & Environmental Science*. 2015;8(9):2725-33.
276. Heo JH, Song DH, Im SH. Planar $\text{CH}_3\text{NH}_3\text{PbBr}_3$ hybrid solar cells with 10.4% power conversion efficiency, fabricated by controlled crystallization in the spin-coating process. *Advanced Materials*. 2014;26(48):8179-83.
277. Yu Y, Wang C, Grice CR, Shrestha N, Chen J, Zhao D, et al. Improving the performance of formamidinium and cesium lead triiodide perovskite solar cells using lead thiocyanate additives. *ChemSusChem*. 2016;9(23):3288-97.
278. Ke W, Zhao D, Xiao C, Wang C, Cimaroli AJ, Grice CR, et al. Cooperative tin oxide fullerene electron selective layers for high-performance planar perovskite solar cells. *Journal of Materials Chemistry A*. 2016;4(37):14276-83.
279. Wang C, Zhao D, Yu Y, Shrestha N, Grice CR, Liao W, et al. Compositional and morphological engineering of mixed cation perovskite films for highly efficient planar and flexible solar cells with reduced hysteresis. *Nano Energy*. 2017;35:223-32.
280. Yang L, Yan Y, Cai F, Li J, Wang T. Poly (9-vinylcarbazole) as a hole transport material for efficient and stable inverted planar heterojunction perovskite solar cells. *Solar Energy Materials and Solar Cells*. 2017;163:210-7.
281. Si H, Liao Q, Kang Z, Ou Y, Meng J, Liu Y, et al. Deciphering the NH_4PbI_3 intermediate phase for simultaneous improvement on nucleation and crystal growth of perovskite. *Advanced Functional Materials*. 2017;27(30):1701804.
282. Chen W, Sun K, Ma C, Leng C, Fu J, Hu L, et al. Eliminating JV hysteresis in perovskite solar cells via defect controlling. *Organic Electronics*. 2018;58:283-9.
283. Zhang H, Hou M, Xia Y, Wei Q, Wang Z, Cheng Y, et al. Synergistic effect of anions and cations in additives for highly efficient and stable perovskite solar cells. *Journal of Materials Chemistry A*. 2018;6(19):9264-70.
284. Edri E, Kirmayer S, Mukhopadhyay S, Gartsman K, Hodes G, Cahen D. Elucidating the charge carrier separation and working mechanism of $\text{CH}_3\text{NH}_3\text{PbI}_{3-x}\text{Cl}_x$ perovskite solar cells. *Nature communications*. 2014;5(1):3461.
285. Edri E, Kirmayer S, Henning A, Mukhopadhyay S, Gartsman K, Rosenwaks Y, et al. Why lead methylammonium tri-iodide perovskite-based solar cells require a mesoporous

electron transporting scaffold (but not necessarily a hole conductor). *Nano letters*.

2014;14(2):1000-4.

286. Dong Q, Fang Y, Shao Y, Mulligan P, Qiu J, Cao L, et al. Electron-hole diffusion lengths > 175 μm in solution-grown $\text{CH}_3\text{NH}_3\text{PbI}_3$ single crystals. *Science*. 2015;347(6225):967-70.

287. Bischak CG, Sanehira EM, Precht JT, Luther JM, Ginsberg NS. Heterogeneous charge carrier dynamics in organic–inorganic hybrid materials: nanoscale lateral and depth-dependent variation of recombination rates in methylammonium lead halide perovskite thin films. *Nano letters*. 2015;15(7):4799-807.

288. Bi D, Yi C, Luo J, Décoppet J-D, Zhang F, Zakeeruddin SM, et al. Polymer-templated nucleation and crystal growth of perovskite films for solar cells with efficiency greater than 21%. *Nature Energy*. 2016;1(10):1-5.

289. Chen Q, Zhou H, Hong Z, Luo S, Duan H-S, Wang H-H, et al. Planar heterojunction perovskite solar cells via vapor-assisted solution process. *Journal of the American Chemical Society*. 2014;136(2):622-5.

290. Li X, Bi D, Yi C, Décoppet J-D, Luo J, Zakeeruddin SM, et al. A vacuum flash–assisted solution process for high-efficiency large-area perovskite solar cells. *Science*. 2016;353(6294):58-62.

291. Abbas HA, Kottokkaran R, Ganapathy B, Samiee M, Zhang L, Kitahara A, et al. High efficiency sequentially vapor grown nip $\text{CH}_3\text{NH}_3\text{PbI}_3$ perovskite solar cells with undoped P3HT as p-type heterojunction layer. *APL materials*. 2015;3(1):016105.

292. Zhou Y, Yang M, Wu W, Vasiliev AL, Zhu K, Padture NP. Room-temperature crystallization of hybrid-perovskite thin films via solvent–solvent extraction for high-performance solar cells. *Journal of Materials Chemistry A*. 2015;3(15):8178-84.

293. Momblona C, Gil-Escrig L, Bandiello E, Hutter EM, Sessolo M, Lederer K, et al. Efficient vacuum deposited pin and nip perovskite solar cells employing doped charge transport layers. *Energy & Environmental Science*. 2016;9(11):3456-63.

294. Stoumpos CC, Cao DH, Clark DJ, Young J, Rondinelli JM, Jang JJ, et al. Ruddlesden–Popper hybrid lead iodide perovskite 2D homologous semiconductors. *Chemistry of Materials*. 2016;28(8):2852-67.

295. Zhu X, Xu Z, Zuo S, Feng J, Wang Z, Zhang X, et al. Vapor-fumigation for record efficiency two-dimensional perovskite solar cells with superior stability. *Energy & Environmental Science*. 2018;11(12):3349-57.
296. Tsai H, Nie W, Blancon J-C, Stoumpos CC, Asadpour R, Harutyunyan B, et al. High-efficiency two-dimensional Ruddlesden–Popper perovskite solar cells. *Nature*. 2016;536(7616):312-6.
297. Qing J, Liu XK, Li M, Liu F, Yuan Z, Tiukalova E, et al. Aligned and graded type-II Ruddlesden–Popper perovskite films for efficient solar cells. *Advanced Energy Materials*. 2018;8(21):1800185.
298. Smith IC, Hoke ET, Solis-Ibarra D, McGehee MD, Karunadasa HI. A layered hybrid perovskite solar-cell absorber with enhanced moisture stability. *Angewandte Chemie International Edition*. 2014;53(42):11232-5.
299. Wang Z, Lin Q, Chmiel FP, Sakai N, Herz LM, Snaith HJ. Efficient ambient-air-stable solar cells with 2D–3D heterostructured butylammonium-caesium-formamidinium lead halide perovskites. *Nature Energy*. 2017;2(9):1-10.
300. Chen J, Lee D, Park N-G. Stabilizing the Ag electrode and reducing J–V hysteresis through suppression of iodide migration in perovskite solar cells. *ACS applied materials & interfaces*. 2017;9(41):36338-49.
301. Wu WQ, Huang F, Chen D, Cheng YB, Caruso RA. Thin Films of Dendritic Anatase Titania Nanowires Enable Effective Hole-Blocking and Efficient Light-Harvesting for High-Performance Mesoscopic Perovskite Solar Cells. *Advanced Functional Materials*. 2015;25(21):3264-72.
302. Yu Y, Li J, Geng D, Wang J, Zhang L, Andrew TL, et al. Development of lead iodide perovskite solar cells using three-dimensional titanium dioxide nanowire architectures. *Acs Nano*. 2015;9(1):564-72.
303. Qin P, Paulose M, Dar MI, Moehl T, Arora N, Gao P, et al. Stable and efficient perovskite solar cells based on titania nanotube arrays. *Small*. 2015;11(41):5533-9.
304. Li Y, Zhao Y, Chen Q, Yang Y, Liu Y, Hong Z, et al. Multifunctional fullerene derivative for interface engineering in perovskite solar cells. *Journal of the American Chemical Society*. 2015;137(49):15540-7.

305. Ito S, Tanaka S, Manabe K, Nishino H. Effects of surface blocking layer of Sb₂S₃ on nanocrystalline TiO₂ for CH₃NH₃PbI₃ perovskite solar cells. *The Journal of Physical Chemistry C*. 2014;118(30):16995-7000.
306. Rao HS, Chen BX, Li WG, Xu YF, Chen HY, Kuang DB, et al. Improving the extraction of photogenerated electrons with SnO₂ nanocolloids for efficient planar perovskite solar cells. *Advanced Functional Materials*. 2015;25(46):7200-7.
307. Ke W, Fang G, Liu Q, Xiong L, Qin P, Tao H, et al. Low-temperature solution-processed tin oxide as an alternative electron transporting layer for efficient perovskite solar cells. *Journal of the American Chemical Society*. 2015;137(21):6730-3.
308. Bu T, Shi S, Li J, Liu Y, Shi J, Chen L, et al. Low-temperature presynthesized crystalline tin oxide for efficient flexible perovskite solar cells and modules. *ACS applied materials & interfaces*. 2018;10(17):14922-9.
309. Kuang Y, Zaretto V, van Gils R, Karwal S, Koushik D, Verheijen MA, et al. Low-Temperature Plasma-Assisted Atomic-Layer-Deposited SnO₂ as an Electron Transport Layer in Planar Perovskite Solar Cells. *ACS Applied Materials & Interfaces*. 2018;10(36):30367-78.
310. Heo JH, Lee MH, Han HJ, Patil BR, Yu JS, Im SH. Highly efficient low temperature solution processable planar type CH₃NH₃PbI₃ perovskite flexible solar cells. *Journal of Materials Chemistry A*. 2016;4(5):1572-8.
311. Liu J, Gao C, Luo L, Ye Q, He X, Ouyang L, et al. Low-temperature, solution processed metal sulfide as an electron transport layer for efficient planar perovskite solar cells. *Journal of Materials Chemistry A*. 2015;3(22):11750-5.
312. Wang L, Fu W, Gu Z, Fan C, Yang X, Li H, et al. Low temperature solution processed planar heterojunction perovskite solar cells with a CdSe nanocrystal as an electron transport/extraction layer. *Journal of Materials Chemistry C*. 2014;2(43):9087-90.
313. Wojciechowski K, Leijtens T, Siprova S, Schlueter C, Hörantner MT, Wang JT-W, et al. C₆₀ as an efficient n-type compact layer in perovskite solar cells. *The journal of physical chemistry letters*. 2015;6(12):2399-405.
314. Yoon H, Kang SM, Lee J-K, Choi M. Hysteresis-free low-temperature-processed planar perovskite solar cells with 19.1% efficiency. *Energy & Environmental Science*. 2016;9(7):2262-6.

315. Li H, Li X, Wang W, Huang J, Li J, Huang S, et al. Ultraflexible and biodegradable perovskite solar cells utilizing ultrathin cellophane paper substrates and TiO₂/Ag/TiO₂ transparent electrodes. *Solar Energy*. 2019;188:158-63.
316. Meng X, Zhou J, Hou J, Tao X, Cheung SH, So SK, et al. Versatility of carbon enables all carbon based perovskite solar cells to achieve high efficiency and high stability. *Advanced Materials*. 2018;30(21):1706975.
317. Yin X, Han J, Zhou Y, Nan H, Yao Z, Tai M, et al. Inverted Perovskite Solar Cells with Efficient Mixed-Fullerene Derivative Charge Extraction Layers. *ChemistrySelect*. 2018;3(24):6802-9.
318. Zhu Z, Xu JQ, Chueh CC, Liu H, Li Za, Li X, et al. A low-temperature, solution-processable organic electron-transporting layer based on planar coronene for high-performance conventional perovskite solar cells. *Advanced Materials*. 2016;28(48):10786-93.
319. Fernandes SL, Véron AC, Neto NF, Nüesch FA, da Silva JHD, Zaghete MA, et al. Nb₂O₅ hole blocking layer for hysteresis-free perovskite solar cells. *Materials Letters*. 2016;181:103-7.
320. Byranvand MM, Kim T, Song S, Kang G, Ryu SU, Park T. p-type CuI islands on TiO₂ electron transport layer for a highly efficient planar-perovskite solar cell with negligible hysteresis. *Advanced Energy Materials*. 2018;8(5):1702235.
321. Zhou W, Zhen J, Liu Q, Fang Z, Li D, Zhou P, et al. Successive surface engineering of TiO₂ compact layers via dual modification of fullerene derivatives affording hysteresis-suppressed high-performance perovskite solar cells. *Journal of Materials Chemistry A*. 2017;5(4):1724-33.
322. You S, Wang H, Bi S, Zhou J, Qin L, Qiu X, et al. A biopolymer heparin sodium interlayer anchoring TiO₂ and MAPbI₃ enhances trap passivation and device stability in perovskite solar cells. *Advanced materials*. 2018;30(22):1706924.
323. Yoo JJ, Wieghold S, Sponseller MC, Chua MR, Bertram SN, Hartono NTP, et al. An interface stabilized perovskite solar cell with high stabilized efficiency and low voltage loss. *Energy & Environmental Science*. 2019;12(7):2192-9.
324. Jiang Q, Zhao Y, Zhang X, Yang X, Chen Y, Chu Z, et al. Surface passivation of perovskite film for efficient solar cells. *Nature Photonics*. 2019;13(7):460-6.

325. Leijtens T, Ding I-K, Giovenzana T, Bloking JT, McGehee MD, Sellinger A. Hole transport materials with low glass transition temperatures and high solubility for application in solid-state dye-sensitized solar cells. *ACS nano*. 2012;6(2):1455-62.
326. Burschka J, Dualeh A, Kessler F, Baranoff E, Cevey-Ha N-L, Yi C, et al. Tris (2-(1 H-pyrazol-1-yl) pyridine) cobalt (III) as p-type dopant for organic semiconductors and its application in highly efficient solid-state dye-sensitized solar cells. *Journal of the American Chemical Society*. 2011;133(45):18042-5.
327. Snaith HJ, Grätzel M. Enhanced charge mobility in a molecular hole transporter via addition of redox inactive ionic dopant: Implication to dye-sensitized solar cells. *Applied physics letters*. 2006;89(26):262114.
328. Nguyen WH, Bailie CD, Unger EL, McGehee MD. Enhancing the hole-conductivity of spiro-OMeTAD without oxygen or lithium salts by using spiro (TFSI) 2 in perovskite and dye-sensitized solar cells. *Journal of the American Chemical Society*. 2014;136(31):10996-1001.
329. Wang S, Yuan W, Meng YS. Spectrum-dependent spiro-OMeTAD oxidation mechanism in perovskite solar cells. *ACS applied materials & interfaces*. 2015;7(44):24791-8.
330. Heo JH, Im SH, Noh JH, Mandal TN, Lim C-S, Chang JA, et al. Efficient inorganic-organic hybrid heterojunction solar cells containing perovskite compound and polymeric hole conductors. *Nature photonics*. 2013;7(6):486-91.
331. Yang WS, Park B-W, Jung EH, Jeon NJ, Kim YC, Lee DU, et al. Iodide management in formamidinium-lead-halide-based perovskite layers for efficient solar cells. *Science*. 2017;356(6345):1376-9.
332. Li W, Dong H, Wang L, Li N, Guo X, Li J, et al. Montmorillonite as bifunctional buffer layer material for hybrid perovskite solar cells with protection from corrosion and retarding recombination. *Journal of Materials Chemistry A*. 2014;2(33):13587-92.
333. Burschka J, Kessler F, Nazeeruddin MK, Grätzel M. Co (III) complexes as p-dopants in solid-state dye-sensitized solar cells. *Chemistry of Materials*. 2013;25(15):2986-90.
334. Calio L, Salado M, Kazim S, Ahmad S. A generic route of hydrophobic doping in hole transporting material to increase longevity of perovskite solar cells. *Joule*. 2018;2(9):1800-15.
335. Zhang J, Daniel Q, Zhang T, Wen X, Xu B, Sun L, et al. Chemical dopant engineering in hole transport layers for efficient perovskite solar cells: insight into the interfacial recombination. *ACS nano*. 2018;12(10):10452-62.

336. Leijtens T, Giovenzana T, Habisreutinger SN, Tinkham JS, Noel NK, Kamino BA, et al. Hydrophobic organic hole transporters for improved moisture resistance in metal halide perovskite solar cells. *ACS applied materials & interfaces*. 2016;8(9):5981-9.
337. Zhang J, Zhang T, Jiang L, Bach U, Cheng Y-B. 4-tert-Butylpyridine free hole transport materials for efficient perovskite solar cells: a new strategy to enhance the environmental and thermal stability. *ACS Energy Letters*. 2018;3(7):1677-82.
338. Yue Y, Salim N, Wu Y, Yang X, Islam A, Chen W, et al. Enhanced Stability of Perovskite Solar Cells through Corrosion-Free Pyridine Derivatives in Hole-Transporting Materials. *Advanced Materials*. 2016;28(48):10738-43.
339. Seo J-Y, Kim H-S, Akin S, Stojanovic M, Simon E, Fleischer M, et al. Novel p-dopant toward highly efficient and stable perovskite solar cells. *Energy & Environmental Science*. 2018;11(10):2985-92.
340. Wang X, Wu J, Yang Y, Liu X, Guo Q, Song Z, et al. High performance and stable perovskite solar cells using vanadic oxide as a dopant for spiro-OMeTAD. *Journal of Materials Chemistry A*. 2019;7(21):13256-64.
341. Luo J, Jia C, Wan Z, Han F, Zhao B, Wang R. The novel dopant for hole-transporting material opens a new processing route to efficiently reduce hysteresis and improve stability of planar perovskite solar cells. *Journal of power sources*. 2017;342:886-95.
342. Nie W, Tsai H, Asadpour R, Blancon J-C, Neukirch AJ, Gupta G, et al. High-efficiency solution-processed perovskite solar cells with millimeter-scale grains. *Science*. 2015;347(6221):522-5.
343. Di Giacomo F, Razza S, Matteocci F, D'Epifanio A, Licoccia S, Brown TM, et al. High efficiency CH₃NH₃PbI_{3-x}Cl_x perovskite solar cells with poly (3-hexylthiophene) hole transport layer. *Journal of Power Sources*. 2014;251:152-6.
344. Guerrero A, Bou A, Matt G, Almora O, Heumüller T, Garcia-Belmonte G, et al. Switching off hysteresis in perovskite solar cells by fine-tuning energy levels of extraction layers. *Advanced Energy Materials*. 2018;8(21):1703376.
345. You J, Meng L, Song T-B, Guo T-F, Yang Y, Chang W-H, et al. Improved air stability of perovskite solar cells via solution-processed metal oxide transport layers. *Nature nanotechnology*. 2016;11(1):75-81.

346. Zhu Z, Bai Y, Zhang T, Liu Z, Long X, Wei Z, et al. High-performance hole-extraction layer of sol-gel-processed NiO nanocrystals for inverted planar perovskite solar cells. *Angewandte Chemie International Edition*. 2014;53(46):12571-5.
347. Yin X, Liu J, Ma J, Zhang C, Chen P, Que M, et al. Solvothermal derived crystalline NiOx nanoparticles for high performance perovskite solar cells. *Journal of Power Sources*. 2016;329:398-405.
348. Christians JA, Fung RC, Kamat PV. An inorganic hole conductor for organo-lead halide perovskite solar cells. Improved hole conductivity with copper iodide. *Journal of the American Chemical Society*. 2014;136(2):758-64.
349. Ye S, Sun W, Li Y, Yan W, Peng H, Bian Z, et al. CuSCN-based inverted planar perovskite solar cell with an average PCE of 15.6%. *Nano letters*. 2015;15(6):3723-8.
350. Rao H, Sun W, Ye S, Yan W, Li Y, Peng H, et al. Solution-processed CuS NPs as an inorganic hole-selective contact material for inverted planar perovskite solar cells. *ACS applied materials & interfaces*. 2016;8(12):7800-5.
351. Zuo C, Ding L. Solution-processed Cu₂O and CuO as hole transport materials for efficient perovskite solar cells. *Small*. 2015;11(41):5528-32.
352. Sun W, Li Y, Ye S, Rao H, Yan W, Peng H, et al. High-performance inverted planar heterojunction perovskite solar cells based on a solution-processed CuO x hole transport layer. *Nanoscale*. 2016;8(20):10806-13.
353. Chen W, Wu Y, Liu J, Qin C, Yang X, Islam A, et al. Hybrid interfacial layer leads to solid performance improvement of inverted perovskite solar cells. *Energy & Environmental Science*. 2015;8(2):629-40.
354. He X, Bai Y, Chen H, Zheng X, Yang S. High performance perovskite solar cells through surface modification, mixed solvent engineering and nanobowl-assisted light harvesting. *MRS Advances*. 2016;1(47):3175-84.
355. Gu Z, Zuo L, Larsen-Olsen TT, Ye T, Wu G, Krebs FC, et al. Interfacial engineering of self-assembled monolayer modified semi-roll-to-roll planar heterojunction perovskite solar cells on flexible substrates. *Journal of Materials Chemistry A*. 2015;3(48):24254-60.
356. Cho Y, Soufiani AM, Yun JS, Kim J, Lee DS, Seidel J, et al. Mixed 3D-2D passivation treatment for mixed-cation lead mixed-halide perovskite solar cells for higher efficiency and better stability. *Advanced Energy Materials*. 2018;8(20):1703392.

357. Li M, Yan X, Kang Z, Huan Y, Li Y, Zhang R, et al. Hydrophobic polystyrene passivation layer for simultaneously improved efficiency and stability in perovskite solar cells. *ACS applied materials & interfaces*. 2018;10(22):18787-95.

Chapter 3: Methods

3.1. Assembly of PSCs

3.1.1. Preparation of the ETL

Throughout this thesis, TiO_2 was utilized as the ETL. In general, four ETL structures have been synthesized using a combination of hydrothermal synthesis and spray pyrolysis. Synthesis processes are performed on conductive low-iron soda lime glass pieces. The conductivity of the glass stems from a thin (about 550 nm) conformal fluorine-doped tin oxide (FTO) deposited over it. For the purpose of characterization, the FTO glass sheets (300 mm by 300 mm, 2.2 mm thick, surface resistivity of 7 Ohm/sq) are purchased from Sigma Aldrich (735167), and then cut using a diamond cutter into desired dimensions. For making solar cells devices, FTO glasses are purchased from Solaronix (TCO227/LI) pre-patterned and pre-cut into 2 cm by 2 cm pieces (2.2 mm thick). The etching pattern is shown in Figure 3.1(a) and an FTO substrate is displayed in Figure 3.1(b).

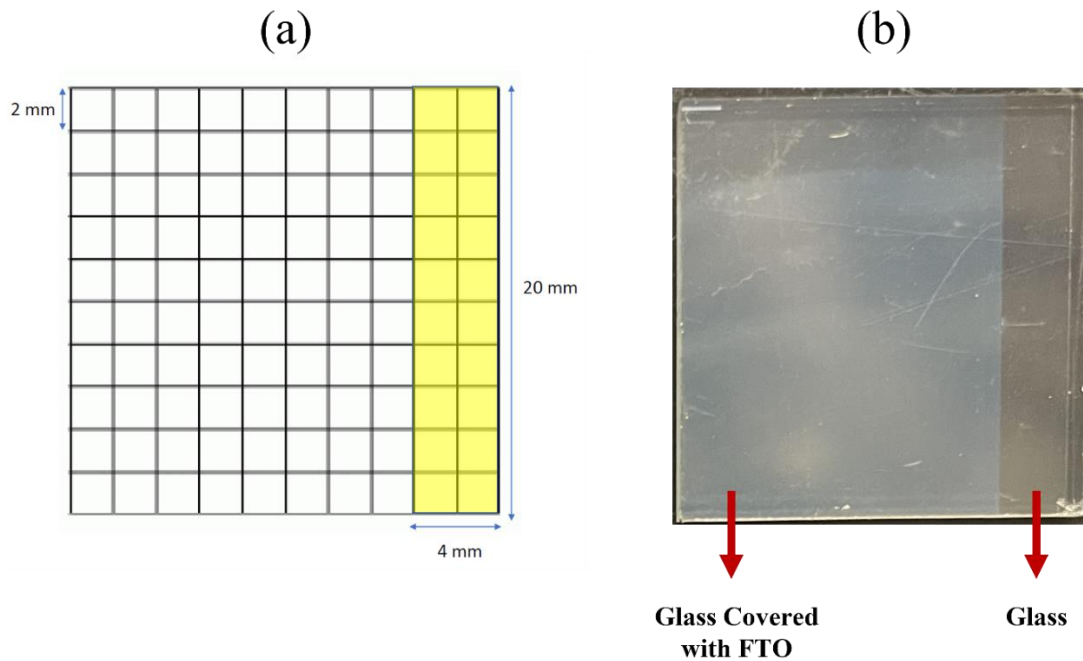


Figure 3.1- (a) Schematic representation of the laser patterning design for the PSCs substrates, whereby the part highlighted in yellow denotes glass while the remainder indicates FTO, (b) example of a substrate used for assembling PSCs.

The substrates are cleaned using three consecutive 15-min sonication steps of de-ionized (DI) water, 2-propanol and acetone. After drying them with a nitrogen gun, the glass pieces undergo a 15-min UV-Ozone treatment (Novascan, PSD Series) to remove the traces of any organic residues. Growth of the rutile titania nanorod films is carried out using hydrothermal synthesis(1). The reaction solution is made with 20 mL DI water and 20 mL concentrated hydrochloric acid (36.5%-38% by weight from Fisher Scientific). The mixture is stirred at room temperature in a sealed beaker for 5 minutes before the addition of 1 mL Ti (IV) butoxide. After stirring for another 40 min, the precursor solution was added to a Teflon-lined stainless-steel autoclave (125 mL volume, Parr Instrument Co.), where three FTO substrates are placed at an angle with their conductive sides facing the wall. A glass slide is placed in between the FTO pieces for separation (Figure 3.2 a). The autoclave is then sealed in a metal encasing (Figure 3.2 b) and placed in the oven (Yamato, DKN602C) with a heating ramp of 10°C/hour to reach the final temperature of 125°C where they are held for 60 minutes before cooling down inside the oven, which takes approximately 3 hours.



Figure 3.2: (a) Arrangement of the substrates inside the Teflon lining, (b) the Teflon lining (left) is then sealed inside the metal encasing (right) and placed inside the oven for hydrothermal synthesis.

After the synthesis is done, the samples are taken out and washed thoroughly with DI water and ethanol. Afterwards, they undergo an annealing step in a box furnace (Thermo Scientific, Lindberg

Blue M) at a heating ramp of 4°C/min to 550°C with holding time of 30 minutes before cooling down.

To synthesize the compact TiO₂ (c-TiO₂), spray pyrolysis is employed. The titania precursor solution contains 9 mL ethanol, 0.6 mL Ti(IV) diisopropoxide bis acetylacetonate and 0.4 mL acetylacetonate. After solution preparation, FTO substrates are placed on a hotplate and heated to 450°C at a ramp rate of 22°C/min. After the final temperature is reached, the substrates are left on the hotplate for an additional 10 min for temperature stabilization before starting the spray pyrolysis. The synthesis is conducted using a nebulizer gun (DWK Lifescience Kimble Kontes, 10 mL capacity, 19/22 thread) to spray the precursor mist over the samples using O₂ as carrier gas, inside the fume hood. This process takes about 10 minutes and is completed in roughly 20 number of rounds of spraying. The setup for spray pyrolysis is shown in Figure 3.3. When the spraying process is finished, the substrates were left on the hotplate for another 10 min before turning it off and letting the samples cool down to room temperature.



Figure 3.3- The spray pyrolysis setup.

In Chapter 4, two different ETL structures are utilized to assemble PSCs in *n-i-p* architecture. The ETL is generated through using: *i*) only spray pyrolysis to synthesize planar c-TiO₂ as ETL, and *ii*) a combination of hydrothermal synthesis and spray pyrolysis, whereby the rutile titania nanorods are coated with c-TiO₂, rendering titania nanorod scaffold as ETL. The latter ensemble is denoted as TNR. Additionally in this chapter, a precursor volume 4 times larger than the base level of the spraying precursor solution was also tested for both ETL planar and scaffold-based PSC configurations. This resulted in total of four ETL structures: c-TiO₂, c-TiO₂ (x4), TNR and TNR (x4). The “(x4)” next to the ETL indicates a higher thickness of compact titania utilized in the corresponding structure.

In Chapter 5, two types of scaffold-based ETL structures are generated through combining hydrothermal synthesis and spray pyrolysis. The first structure is synthesized by conducting hydrothermal synthesis over FTO substrate to obtain randomly oriented rutile titania nanorods, and then covering them with c-TiO₂ using spray pyrolysis. This ensemble is denoted as RA (**R**utile-**A**natase). The second ETL scaffold is generated by hydrothermal synthesis on an FTO substrate that is already covered with c-TiO₂, which renders vertically aligned titania nanorods which is denoted as AR (**A**natase-**R**utile).

In Chapter 6, the utilized ETL structure is AR.

3.1.2. Preparation of the Perovskite Layer

In Chapters 4 to 6, the perovskite layer has the composition of (Cs_{0.05}Rb_{0.05}MA_{0.15}FA_{0.75})Pb(I_{0.83}Br_{0.17})₃ and is synthesized inside a nitrogen-filled glovebox (MBraun, LabStar), as shown in Figure 3.4.



Figure 3.4: (a) The nitrogen-filled glovebox utilized for making the precursor and synthesizing perovskite layer as well as HTL. (b) the spin coater and hot plate/stirrer inside the glovebox.

To make the perovskite precursor, firstly, 1.5 M solutions of PbI_2 and $PbBr_2$ are obtained, in separate vials, in a mix of DMF/DMSO (4:1 V/V) by dissolving the salts through increasing the hot plate temperature from room temperature to 180°C . The solutions are left on the hot plate with constant stirring for 30 minutes before turning off the hot plate (the stirring is kept on). Separately, 1.5 M solutions of CsI in DMSO and RbI in DMF/DMSO mixture (4:1 V/V) are obtained by placing the vials on the hotplate and increasing the temperature from room temperature to 150°C . The vials are left on the hotplate and constant stirring for 30 minutes before turning the hotplate off and letting them cool down to room temperature. Afterwards PbI_2 is added to FAI (to render $FAPbI_3$), and $PbBr_2$ is added to MABr (to render $MAPbBr_3$) in the ratio of

$$\frac{PbI_2}{FAI} = \frac{PbBr_2}{MABr} = \frac{1.09}{1}$$

The resulting solutions are left to stir for 10 minutes. Then the resulting solutions are mixed in $FAPbI_3:MAPbBr_3$ (5:1 V/V) ratio. This renders $(FAPbI_3)_{0.83}(MAPbBr_3)_{0.17}$ perovskite composition. Then, through adding 5 vol.% of the CsI and 5 vol.% of the RbI stock solutions the final composition of $(Cs_{0.05}Rb_{0.05}MA_{0.15}FA_{0.75})Pb(I_{0.83}Br_{0.17})_3$ is obtained.

For all perovskite compositions, the deposition is conducted inside the glovebox, through the anti-solvent method by using $150 \mu\text{L}$ of the final perovskite precursor and a two-step spinning program;

1000 rpm for 10 seconds followed by 6000 rpm for 20 seconds. Five seconds before the end of spinning, 200 μ L of chlorobenzene was poured on the spinning substrate. The substrates were then annealed at 100 $^{\circ}$ C for 60 minutes.

3.1.3. Preparation of the HTL

In this thesis the HTL precursor is made by mixing 2,2',7,7'-tetrakis[*N,N*-di(4-methoxyphenyl)amino]-9,9'-spirobifluorene (spiro-OMeTAD), lithium bis(trifluoromethylsulfonyl)imide (LiTFSI) and 4-*tert*-butylpyridine (4-TBP), according to Table 3.1.

Table 3.1- Composition of the HTL precursor for Chapters 4-6

Spiro-OMeTAD	4-TBP	LiTFSI	Chlorobenzene
72 mg	28.3 μ L	17.5 μ L	1 mL

The preparation of the HTL precursor solution is conducted inside the glovebox, by adding chlorobenzene to spiro-OMeTAD and then addition of 4-TBP and LiTFSI (which is obtained by dissolving 520 mg in 1 ml acetonitrile). The precursor is stirred for 15 minutes before letting it rest for 30 minutes. Deposition of HTL is conducted by spin casting 30 μ L the precursor solution (dripping the solution while the substrate is already spinning) through a single step spinning program of 3000 rpm for 30 seconds, inside the glovebox.

In Chapter 4 and Chapter 5, *p*-doping of the spiro-OMeTAD film is accomplished by leaving the FTO/ETL/Perovskite/HTL stacks in a dark room with 20% RH for 12 hours. After gold deposition, devices are left to rest inside the glovebox for 9 hours before being stored under ambient illumination and 20% RH for 15 hours. In Chapter 6, two stage doping process according to Table 3.2 have been utilized:

Table 3.2: List of the doping conditions utilized for increasing p-type conductivity of spiro-OMeTAD in Chapter 6.

	Before Au Deposition	After Au Deposition
1	Dark and 20% RH-12 Hours	Dark and 20% RH-12 Hours
2	Light and 20% RH-12 Hours	Dark and 20% RH-12 Hours
3	Light and 20% RH-12 Hours	Light and 20% RH-12 Hours
4	Dark and 20% RH-12 Hours	Light and 20% RH-12 Hours
5	Dark and 20% RH-12 Hours	Light and 20% RH-15 Hours
6	Dark and 20% RH-12 Hours	Light and 20% RH-18 Hours

3.1.4. Metal Contact

For Chapter 4 to Chapter 6, gold (Au) is chosen as the back metal contact. The deposition is done at McGill University Nanotools Microfabrication Laboratory (MNM, Physics Department). The process is conducted through thermal evaporation of Au using NexDep (Angstrom Engineering) at a rate 1 Å/s to obtain a thickness of 80 nm. The evaporation process is initiated at vacuum level of at least 2.0×10^{-6} mbar.

3.2. Characterization Techniques

3.2.1. *J-V* Curves and EIS Measurements

J-V scans and EIS measurements were obtained using a class A solar simulator (Sol1A 94021A, Newport) which was calibrated with a silicon KG5 reference cell (Abet Technologies), in combination with a Biologic potentiostat (SP-300). The EC-Lab software was used for adjusting the measurement parameters. In Chapter 4 to Chapter 6, to measure the PV metrics¹, *J-V* curves were recorded under 100 and 10 mV/s from -0.2 V (vs. reference electrode) to 0.2 V above V_{OC} . For EIS measurements a frequency range of 1 MHz to 50 MHz, with a perturbation potential of 20

¹ To ensure statistically reliable data, multiple measurements were made for each device condition (at least 12). Plotted data are presented in boxes which are determined by the 25th and 75th percentiles. The whiskers are determined by the 5th and 95th percentiles. The mean is expressed with a solid horizontal line, and the outliers fall outside the box.

mV over 40 data points. All the J - V scans and EIS measurements² are conducted under 1 Sun illumination.

Figure 3.5 (a) shows the solar simulator used for conducting J - V scans. Figure 3.5 (b) schematically illustrates the different components of a solar simulator. Figure 3.6 displays the potentiostat utilized for the measurements in thesis.

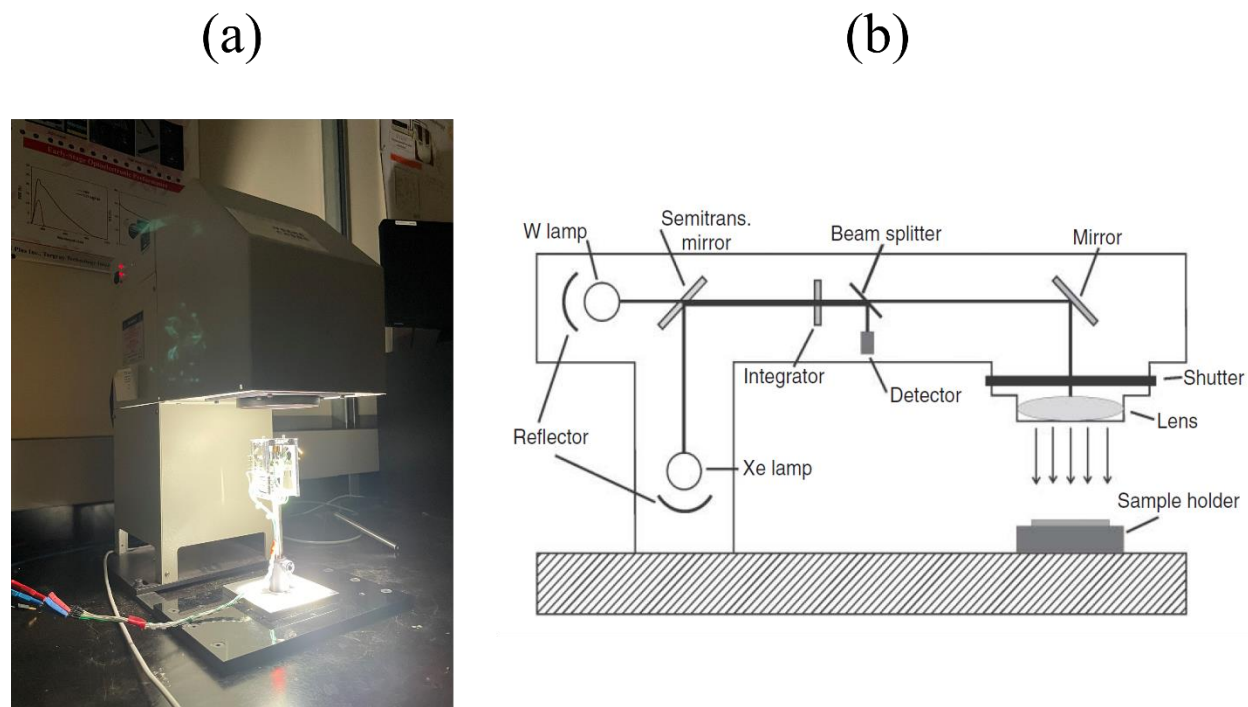


Figure 3.5: (a) the Class A solar simulator utilized throughout this thesis for PSC characterization, (b) schematics of different components of a solar simulator.

² Select fittings of the EIS data are provided in the corresponding Appendices for each of Chapters 4,5, and 6.

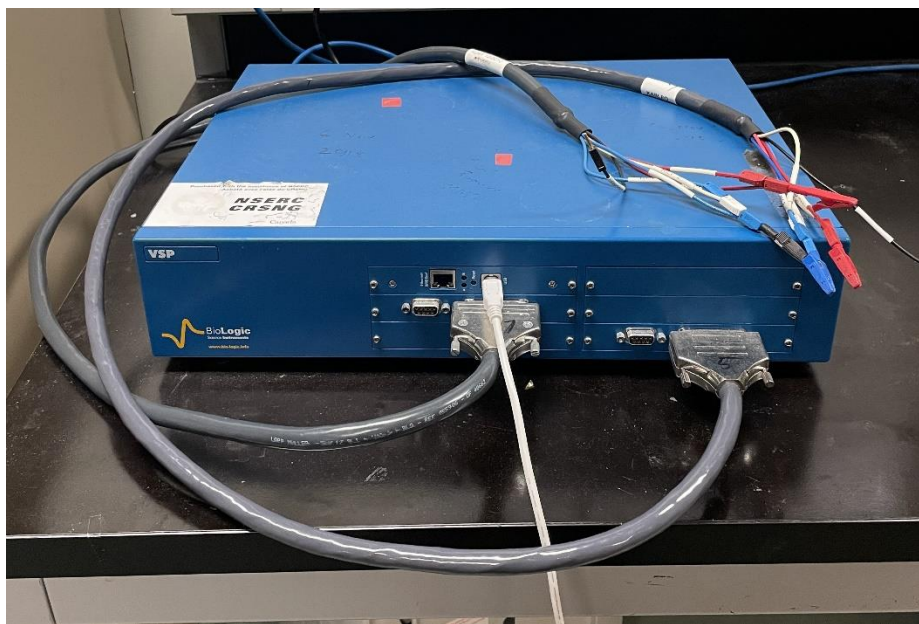


Figure 3.6: The Biologic SP-300 potentiostat used for characterization of PSCs.

3.2.2. Space Charge Limited Current (SCLC)

The SCLC measurements in Chapters 5,6 and 7 were conducted, to determine charge carrier mobility, using the Biologic SP-300 potentiostat (as explained in Section 3.2.1) under dark condition. The FTO/HTL/Au stacks were left to relax in the dark for 10 minutes prior to starting the measurements.

3.2.3. Conductivity Measurements

Two-probe effective conductivity measurements were conducted using the Biologic SP-300 potentiostat (as explained in Section 3.2.1). In Chapters 4 and 5, these measurements were conducted under dark over FTO/ETL/Au stacks. In Chapter 6, the measurements were conducted over Glass/spiro-OMeTAD/Au stacks under both dark condition as well as under 1 Sun illumination.

3.2.4 Scanning Electron Microscopy (SEM)

Cross sectional, top view SEM images as well as energy-dispersive spectroscopy (EDX) were obtained with a SU8230 Hitachi (Figure 3.7) cold-field emission scanning electron microscope

(CFE-SEM), utilizing the in-lens upper secondary electron detector, and using 2mm of working distance with 3 kV acceleration voltage and emission current of 20 μ A. To increase the conductivity of the cross-section specimen and help with drifting, 4 nm of platinum was sputtered on them with a Quorum Q150TS sputter coater. The cross-sectional samples were prepared by mechanically cleaving the specimen with diamond scribe. Energy dispersive X-ray spectroscopy (EDS) was performed with a Bruker Xflash 60 standard detector at 15mm working distance, 5kV accelerating voltage, high probe mode and 30uA emission current. Mappings were performed at 15kX magnification with 15 min acquisition time using integrated drift correction procedure to avoid drifting of the region of interest.



Figure 3.7: The SU8230 microscope utilized for obtaining SEM and EDX images.

3.2.5. X-Ray Diffraction (XRD)

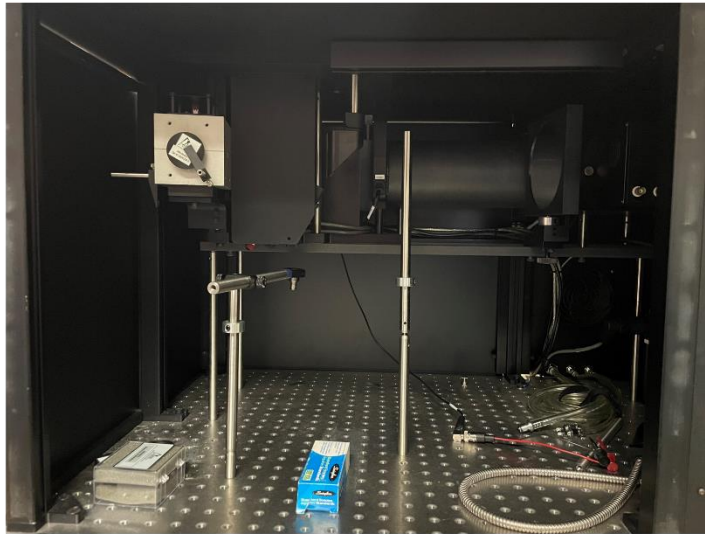
XRD patterns were acquired using a Bruker D8 Advance at Université du Québec à Montréal (UQAM). Copper source ($K\alpha$ line) was used with a voltage of 40 kV and a current of 40 mA. Scan parameters were 2Theta from 6° to 70° with an increment of 0.02° , and integration time of 1s. The

experiment was performed in the grazing incidence diffraction mode with a low incident angle of 3° . Both the primary and secondary axial soller was 2.5° while the secondary twin optic was set to soller 0.2° . The LynxEye detector was set to 0D mode.

3.2.6. External Quantum Efficiency (EQE)

To obtain EQE spectra, the setup from PV Measurements, Inc was utilized which was calibrated using a silicon diode. Additionally, the laser position on the devices was adjusted by maximizing the EQE intensity using green laser. The chopping frequency was set to 100 Hz for all measurements. Figure 3.8 (a) and Figure 3.8 (b), show the EQE setups utilized for obtaining the spectra in this thesis, and the schematic illustration of the EQE components, respectively.

(a)



(b)

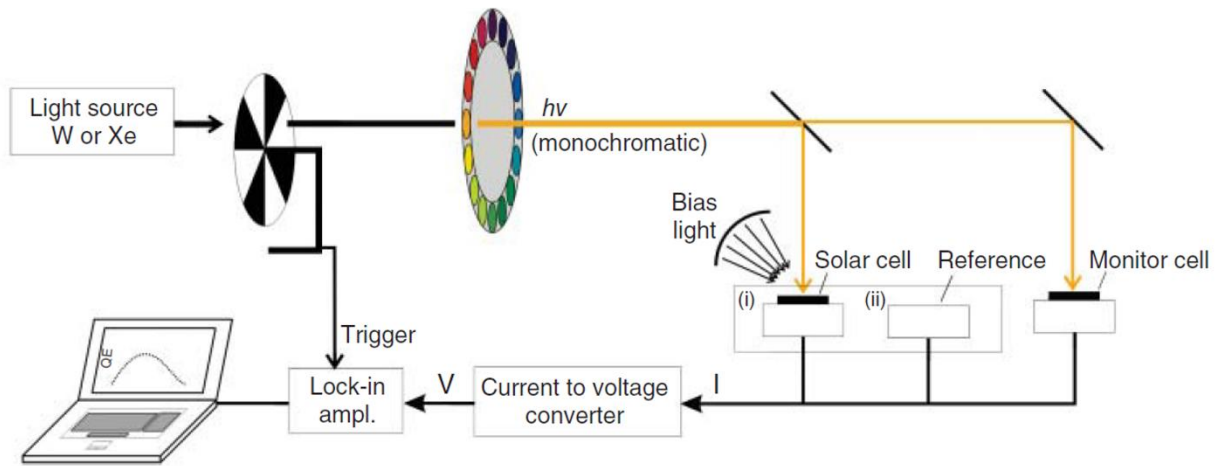


Figure 3.8: (a) The EQE setup utilized for characterization of PSCs, (b) schematics of different components of EQE.

3.2.7. Photoluminescence (PL) and Time-Resolved Photoluminescence

The PL spectra in Chapters 5 were collected with a Renishaw InVia Raman microscope using 514 nm excitation wavelength and x50 objective lens, at Université de Montréal with the help of Samir Elouatik. The TRPL measurements in Chapter 5 were conducted utilizing a streak camera (Axis TRS, Axis Photonique Inc.). The sample was excited at 504nm (1nJ) which was produced from a Coherent OperA Solo Optical Parametric Amplifier (OPA) pumped by a Ti:sapphire regenerative amplifier (Coherent Legend Elite Duo He+, 1 kHz rep. rate). The fluorescence is collected at 90°, collimated, and subsequently focused onto the streak camera slit using a pair of off-axis parabolic mirrors. The PL is dispersed by a spectrometer (Acton SP-2358i, 150g/mm, 600nm blaze), accelerated in a bilamellar streak tube (Photonis P820) and imaged using an air-cooled CCD (Spectral Instruments 1200 series). The trace, and its corresponding background measurement, is obtained from an average of 15 exposures lasting 10 seconds each. The decay profiles were fitted with the Origin Pro software using the built-in ExpDecay2 function.

3.2.8. Atomic Force Microscopy (AFM)

AFM measurements were conducted under tapping mode in air using Bruker MultiMode 8 with RTESPA-150 probes at 0.1 Hz scanning speed. These measurements were conducted at Université du Québec à Montréal (UQAM). The AFM images were processed using Gwyddion data analysis software.

3.2.9. X-Ray Photoelectron Spectroscopy (XPS)

The XPS spectra of Chapter 6 were collected with Nexsa G2 (Thermo Scientific), using Al K α radiation (1486.6 eV) and an X-ray spot size of 200 μ m. The flood gun was turned on for the measurements to prevent charging effects. Samples were sealed into the sample holder inside a nitrogen-filled glovebox to prevent oxidation of spiro-OMeTAD. For all elemental spectra, 20 scans with a dwell time of 50 ms and pass energy of 50 eV were used. Charge correction was carried out using adventitious C 1s set to a binding energy of 284.8 eV, while charge neutralization was carried out using an electron flood gun.

3.2.10. Ultraviolet Photoelectron Spectroscopy (UPS)

UPS spectra of Chapter 4 were collected with Nexsa G2 (Thermo Scientific). For the spectra obtained on ETLs, total of 10 scans were acquired using He II ($h\nu = 40.08$ eV) with a pass energy of 10 eV, energy step size of 0.1 eV and dwell time of 50 ms. In the case of perovskite layers, He

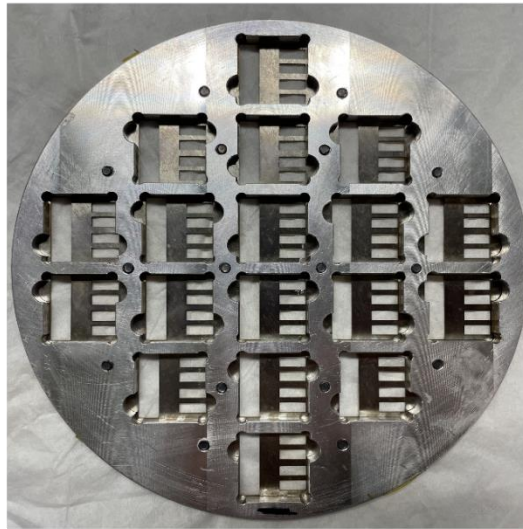
I ($h\nu = 21.22$ eV) was utilized for collecting 5 spectra with pass energy of 2 eV, energy step size of 0.05 eV and dwell time of 50 ms. In both cases, to obtain SECO, a bias of negative 10 V was applied. The spectra displayed in the manuscript are corrected for the bias. The Fermi energy ($E_F=0$) reference in UPS was calibrated with a clean polycrystalline Ag sample built into the sample holder.

3.3. Equipment

3.3.1. Shadow Mask

Evaporation of gold on the FTO/ETL/Perovskite/HTL stacks was conducted using a shadow mask, as seen on Figure 3.9 (a). The detailed design of this mask is displayed in Figure 3.9 (b). By utilizing this shadow mask, 4 devices on each sample are generated.

(a)



(b)

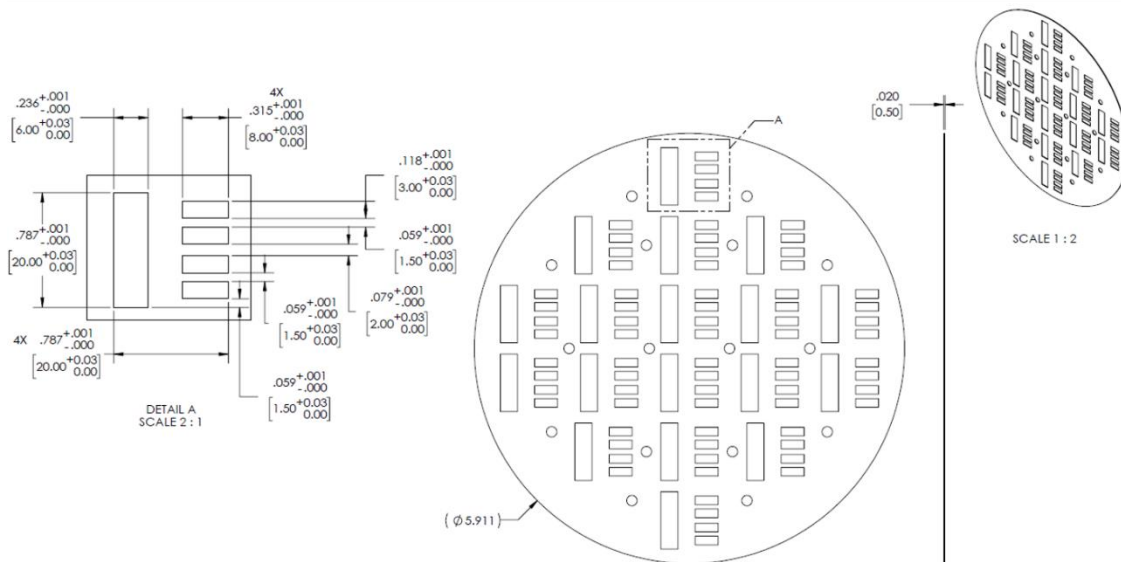


Figure 3.9: (a) The shadow mask used during gold evaporation to obtain the desired contact pattern, (b) the detailed description of the shadow mask.

3.3.1. Testing Equipment

To test the resulting PSCs for $J-V$ scans, EIS, SCLC and EQE, a testing apparatus was used which can be seen in Figure 3.10 (a) and Figure 3.10 (b). The devices are fixed into the equipment using a screw that fastens the top plate (with apertures defining the active area of 0.09 cm^2) to the base,

as seen in Figure 3.10 (c). The design of this equipment was done by Richard Talbot (Department of Physics, McGill University) and its detailed description is shown in Figure 3.10 (d).

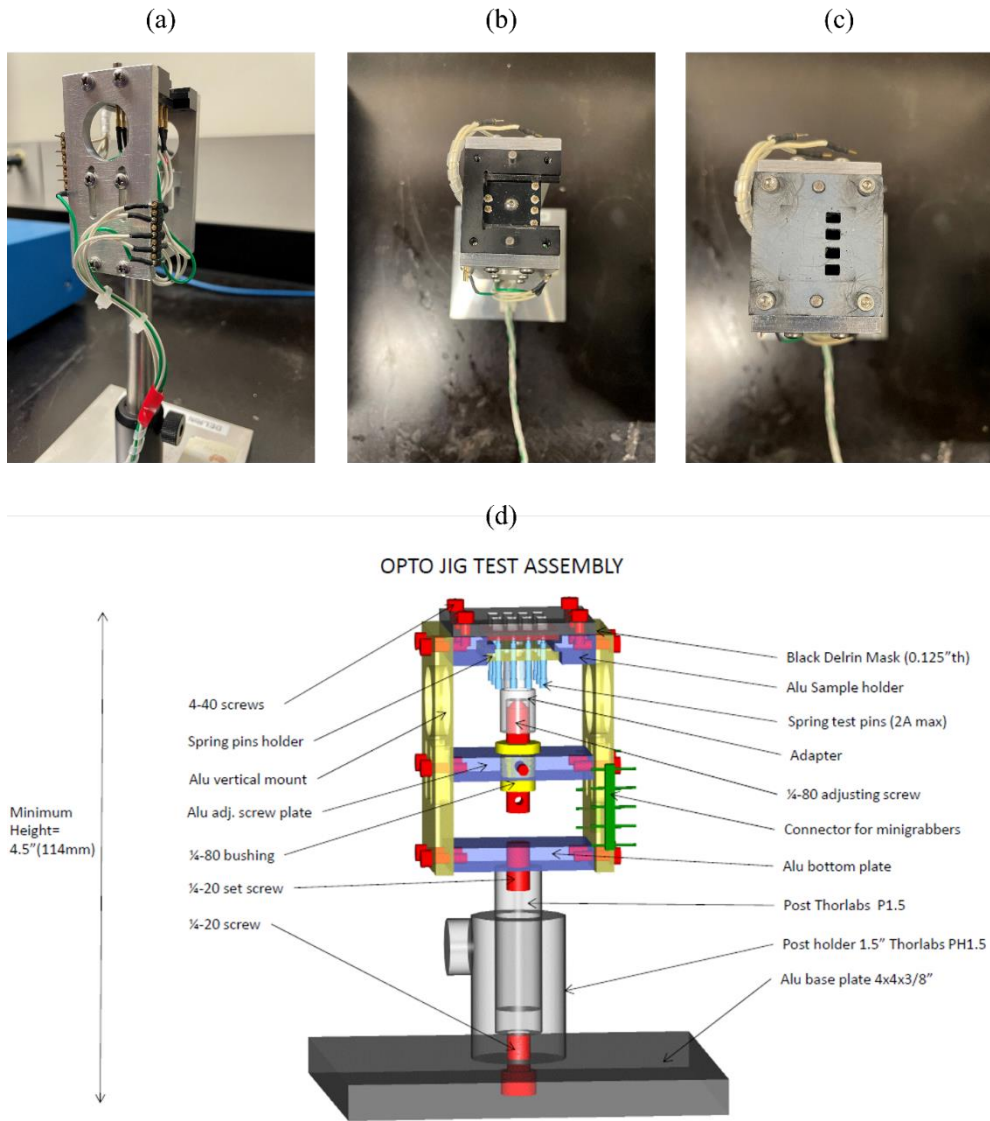


Figure 3.10: (a) Side view, (b) top-view of the testing apparatus, (c) the top plate with four apertures for defining the area of active device to 0.09 cm^2 , and (d) detailed design specifications of the testing apparatus utilized in testing PSC devices reported in this thesis

3.4. References

1. Liu B, Aydil ES. Growth of Oriented Single-Crystalline Rutile TiO₂ Nanorods on Transparent Conducting Substrates for Dye-Sensitized Solar Cells. *Journal of the American Chemical Society*. 2009;131(11):3985-90.

Chapter 4: Synergetic Interfacial Conductivity Modulation in Perovskite Solar Cells

This chapter addresses the 1st objective of the thesis aiming at understanding the role of commonly employed compact TiO₂ layer (c-TiO₂, synthesized through spray pyrolysis) interfacing within the ETL structure on the evolution of hysteresis dynamics in PSCs as a function of light soaking, scan speed and applied bias. This chapter is replication of a manuscript submitted for peer reviewed publication. The citation information for this chapter is provided below:

- Yekani, R., Wang, H., Bessette, S., Gauvin, R., and Demopoulos, G.P., 2023. “Synergetic Interfacial Conductivity Modulation Dictating Hysteresis Evolution in Perovskite Solar Cells under Operation”. *Submitted to ECS Journal of Solid-State Science and Technology*

Abstract

In this work, the configuration of compact TiO₂ coating (c-TiO₂) interface as electron transport layer (ETL) in giving rise to loss and gain of fill factor (*FF*) and therefore modulation of hysteresis behavior in perovskite solar cells (PSCs) is investigated. For this purpose, PSCs based on planar compact TiO₂ (c-TiO₂) as well as a scaffold-based architecture are studied. In the latter case c-TiO₂ coats a hydrothermally grown titania nanorod scaffold. The results demonstrate that when c-TiO₂ is used in planar configuration, *FF* considerably improves with prolonged light soaking which is in sharp contrast to what is observed for scaffold-based PSCs. Moreover, higher thickness of planar c-TiO₂ is shown to be beneficial for sustaining *FF* in forward scan. Finally, through studying the intricate interfacial dynamics utilizing electrochemical impedance spectroscopy (EIS), it was concluded that for a PSC under operation, the cumulative effect of conductivity modulation at the perovskite with transport layer interfaces, for their respective charge carriers, determines the loss and gain in performance depending on scan rate, applied bias and prolonged light soaking. This work points towards multiple factors affecting PSC output, which could work either in confluence or against one another depending on the interfacial configuration of transport layers.

Keywords

PSC, ETL interface, hysteresis, *FF*, planar, scaffold, light soaking, conductivity

4.1. Introduction

Over the past decade, perovskite solar cells (PSCs) have been the subject of accelerated research interest, emerging as a potential candidate to replace the previous generations of photovoltaics, including those based on silicon (Si) and cadmium-telluride (CdTe). Despite many positive attributes of PSCs such as long electron-hole diffusion lengths(1), high absorption coefficient(2) and defect tolerance(3), considerable challenges including hysteresis are still associated with this class of solar cells, hampering their large-scale development. Hysteresis is the term applied to the mismatch between current-voltage ($J-V$) curves recorded in the forward scan (FS) and reverse scan (RS) directions, which was first reported by Snaith et al. in 2015.(4) Over the years, this phenomenon has garnered much attention since it is closely related with stability and toxicity problems associated with PSCs.(5, 6, 7) Valuable research in the field has identified some of the parameters affecting hysteresis such as scan rate,(8, 9, 10, 11) device architecture,(12, 13, 14) chemistry of the perovskite layer,(15, 16, 17, 18) as well as the electron-transport layer (ETL) and hole-transport layer (HTL)(19, 20, 21, 22, 23). For $n-i-p$ architectures, the choice of ETL has been shown to exert a heavy influence over the microstructure of the perovskite layer, as well as the corresponding PSC performance with respect to efficiency, hysteresis and stability.(20, 24, 25, 26) Also of immense importance is the PSC architecture (planar vs. mesoporous) which, depending on the type of ETL interface, can heavily modulate the PSC performance.(27, 28, 29) In the planar architecture, the perovskite layer directly interfaces on the top surface of the dense hole blocking ETL coated on FTO. On the other hand, in the mesoporous configuration, the perovskite layer infiltrates within a TiO_2 scaffold (built on FTO) and contacts the dense blocking ETL through it.(30) The latter remains the most widely utilized ETL configuration which has been employed in combination with mixed cation and/or halide composition for the perovskite layer and spiro-OMeTAD or PTAA as HTL to render some of the highest PCE s ever reported.(31, 32, 33, 34). Multiple studies have shown that compared with the planar configuration, the appearance of hysteresis can be alleviated using the mesoporous structure.(4, 28, 35). However, a detailed perspective on this matter is still lacking.

In this work, to better differentiate the dynamics involved in each ETL interface configuration, PSCs with perovskite composition of $(\text{Cs}_5\text{Rb}_5\text{MA}_{0.15}\text{FA}_{0.75})\text{Pb}(\text{I}_{0.83}\text{Br}_{0.17})_3$ are assembled in *i*) planar architecture, whereby the compact TiO_2 layer (c- TiO_2) synthesized through spray pyrolysis

is the sole component of ETL, and *ii*) a scaffold-based architecture, whereby c-TiO₂ covers hydrothermally synthesized titania nanorods. The latter configuration is termed as TNR henceforth. This study builds on our earlier work³³ that considered hysteresis dynamics in scaffold-based ETL structures, and comparatively extends it into the planar ETL configuration. To obtain a comprehensive picture, two thicknesses of compact titania coating were considered by adjusting the volume of precursor solution during spray pyrolysis.

Through careful analysis of PV metrics evolution under light soaking at 100 mV/s and 10 mV/s, we showed that the interfacial configuration of ETL can heavily influence both the magnitude and locus of hysteresis. In a universal trend for all PSC devices, open-circuit voltage (V_{OC}) values dropped with light soaking but were enhanced with reduced scan rate. Moreover, short-circuit current density (J_{SC}) values were reduced upon decreasing the scan rate for all devices regardless of the employed ETL structure. PSCs with planar configuration experience a gain in fill factor (FF) in both scan directions as a result of light soaking, which overall resulted in reduced hysteresis index. Interestingly, PSCs having scaffold configuration within their ETL, also displayed a reduced hysteresis index with light soaking which however was far from a positive change since it stemmed from diminished PV metrics in both scan directions. Scan rate-dependent dynamics displayed a stronger trend on thickness of compact titania coating. Employing a supporting scaffold underneath the thin compact titania helped with minimizing the FF loss in FS especially under reduced scan rate. On the other hand, utilizing thicker planar c-TiO₂ enabled a gain in FF under reduced scan speed which was however to an extent negatively impacted when interfaced with a nanorod scaffold. Moreover, electrochemical impedance spectroscopy (EIS) patterns under 1 Sun illumination and open-circuit conditions were compared not only as a function of light soaking but also before and after J - V measurement, to isolate the effect of light from that of applied forward bias on the interfacial charge carrier dynamics. The corresponding results indicated that PSCs based on scaffold structure benefit from enhanced conductivity after J - V measurements which is in opposite to what is observed in planar-based PSCs, hypothesized to suffer from inverted band alignment at perovskite/ETL interface, hampering efficient charge transport.

This work offers three important findings. Firstly, not every reduction or increase in hysteresis index can be interpreted as a positive or negative change, respectively, in PSC performance. The changes in hysteresis index should be considered alongside corresponding changes in PV metrics

to obtain a reliable understanding of the charge carrier modulation and therefore hysteresis evolution. Secondly, despite utilizing the quadruple perovskite composition which has been shown to yield high *PCE* and low hysteresis,(31) charge carrier dynamics and hysteresis evolution can be considerably modulated depending on the interfacial configuration of the utilized ETL structure. Thirdly, the specific ETL configuration with respect to the layers involved, their thickness and resulting interfaces can heavily influence the operation of PSCs in terms of tolerance towards light soaking and applied forward bias as well as sustaining of stabilized performance.

4.2. Experimental

Synthesis of different types of Electron Transport Layers (ETL)

For all ETL-related synthesis paths, the fluorine-doped tin oxide (FTO) glass substrates (2 cm by 2 cm in dimension and pre-patterned) were purchased from Solaronix (with surface resistivity of 7 Ohm/ Square and thickness of 2.2 mm; part number: TCO22-7/LI). The substrates were ultrasonically cleaned sequentially in a 2% Hellmanex solution in DI water, 2-propanol, and acetone, for 15 min in each solvent. Eventually, the substrates were treated for 15 min with UV-ozone.

To synthesize the planar ETL configuration, spray pyrolysis was performed on cleaned FTO substrates placed on a hotplate and heated gradually to 450°C. The precursor solution containing 9 mL ethanol, 0.6 mL Ti(IV) di-isopropoxide bis acetylacetonate (Sigma Aldrich) and 0.4 mL acetylacetone (Sigma Aldrich) was sprayed over the hot FTO substrates using O₂ as carrier gas. When the spraying process was finished, the substrates were left on the hotplate for another 10 min before turning it off and letting the samples cool down to room temperature.

Growth of the titania nanorod was carried out using hydrothermal synthesis(36) over the anatase seed layer, as we reported elsewhere³³. The reaction solution was made with 20 mL DI water and 20 mL concentrated hydrochloric acid (36.5%-38% by weight from Fisher Scientific). The mixture was stirred at room temperature in a sealed beaker for 5 minutes before the addition of 1 mL Ti (IV) butoxide (Reagent grade 97%, Sigma Aldrich). After stirring for another 40 min, the precursor solution was added to a Teflon-lined stainless-steel autoclave (125 mL volume, Parr Instrument Co.), where two substrates (FTO covered with anatase layer previously deposited by spray pyrolysis) were placed at an angle with their conductive sides facing the wall. The autoclave was

then sealed and placed in the oven with a heating ramp of 10°C/hour to reach the final temperature of 150°C where they were held for 60 minutes before cooling down inside the oven, which took approximately 3 hours. After the synthesis was done, the substrates were taken out and washed thoroughly with DI water. Afterwards, they underwent an annealing step at a heating ramp of 4°C/min to 550°C with a holding time of 30 minutes before cooling down. To obtain the final scaffold, the titania nanorod films are coated by compact titania through spray pyrolysis.

Synthesis of Perovskite Layer and Hole Transport Layer (HTL)

The perovskite layer is synthesized and deposited according to the procedure described by Saliba et al.(37). In short, the perovskite precursor was prepared by mixing FAI (1M), PbI₂ (1.1 M), MABr (0.2M) and PbBr₂ (0.2M) in DMF/DMSO (4:1 v/v). CsI (1.5M in DMSO) and RbI (1.5M in DMF:DMSO 4:1 v/v) were added to the perovskite precursor solution prior to spin coating to obtain the final quadruple cation composition of (Cs₅Rb₅MA_{0.15}FA_{0.75})Pb(I_{0.83}Br_{0.17})₃. The perovskite layer is deposited through the anti-solvent method by using 150 μL of the final perovskite precursor solution and using a two-step spin coating program; 1000 rpm for 10 seconds followed by 6000 rpm for 20 seconds. Five seconds before the end of spinning, 200 μL of chlorobenzene was poured on the spinning substrate. The substrates were then annealed at 100 °C for 45 minutes. Except for PbI₂ and PbBr₂ which were sourced from TCI America, all other chemicals were purchased from Sigma Aldrich.

Spiro-OMeTAD was chosen as the HTL material. To make the precursor, 72.3 mg of spiro-OMeTAD, 28.3 μL 4-TBP and 17.5 μL LiTFSI (520 mg/mL in acetonitrile) are added to 1 mL chlorobenzene. Deposition of HTL was conducted by spin casting 30 μL of the precursor solution at 3000 rpm. Finally, 80 nm of gold was thermally evaporated (NexDep, Angstrom Engineering) in a 2x10⁻⁶ mbar vacuum at the rate of 1 Å/s. To *p*-dope spiro-OMeTAD, the FTO/ETL/perovskite/HTL stacks were left under dark for 12 hours, before gold deposition and 15 hours under ambient light after contact evaporation. The relative humidity for both stages was set at 20%.

Current Density- Voltage (J - V) and Electrochemical Impedance Spectroscopy (EIS)

Measurements

The illumination measurements were conducted with a class A solar simulator (Sol1A 94021A, Newport) which was calibrated with a silicon KG5 reference cell (Abet Technologies). To measure the PV metrics, J - V curves were recorded under 1 Sun at 100 and 10 mV/s from -0.2 V (vs. reference electrode) to 0.2 V above V_{OC} . All EIS measurements were conducted under 1 Sun illumination and various forward bias values with a Biologic potentiostat (SP-300) and controlled by EC lab software from 1 MHz to 50 MHz, with a perturbation potential of 20 mV over 40 data points. There was a total of four devices on each sample, with an active area each of 0.09 cm².

X-Ray Diffraction (XRD)

XRD patterns were acquired using a Bruker D8 Advance. Copper source ($K\alpha$ line) was used with a voltage of 40 kV and a current of 40 mA. Scan parameters were 2θ from 6° to 70° with an increment of 0.02°, and integration time of 1s. The experiment was performed in the grazing incidence diffraction mode with a low incident angle of 3°. Both the primary and secondary axial soller was 2.5° while the secondary twin optic was set to soller 0.2°. The LynxEye detector was set to 0D mode.

Cyclic Voltammetry

Cyclic voltammetry measurements were carried out in a one-compartment cell using Biologic potentiostat (SP-300) and controlled by EC lab software. Ag/AgCl (sat. KCl) and Au were used as reference and counter electrode, respectively. The electrolyte was 0.5 mM $K_4Fe(CN)_6$ (Sigma Aldrich) + 0.5mM $K_3Fe(CN)_6$ (Sigma Aldrich) in aqueous 0.5 M KCl (Sigma Aldrich). The voltage was scanned from -1 V to 1V at a rate of 25 mV/s. The effective electrode area was 1 cm².

Scanning Electron Microscopy (SEM)

Cross sectional and top view SEM images were obtained with a SU8230 Hitachi cold-field emission scanning electron microscope (CFE-SEM), utilizing the in-lens upper secondary electron detector, and using 2mm of working distance with 3 kV accelerating voltage and emission current of 20 μ A. To increase the conductivity of the cross-section specimen and help with drifting, 4 nm of platinum was sputtered on them with a Quorum Q150TS sputter coater. The cross-sectional

samples were prepared by mechanically cleaving the specimen with diamond scribe. Energy dispersive X-ray spectroscopy (EDS) was performed with a Bruker XFlash 60 standard detector at 15mm working distance, 5kV accelerating voltage, high probe mode and 30uA emission current. Mappings were performed at 15kX magnification with 15 min acquisition time using integrated drift correction procedure to avoid drifting of the region of interest.

X-Ray Photoelectron Spectroscopy (XPS)

XPS spectra were collected with Nexsa G2 (Thermo Scientific), using Al K α radiation (1486.6 eV) and an X-ray spot size of 200 μ m. The flood gun was turned on for the measurements to prevent charging effects. For all elemental spectra, 20 scans with a dwell time of 50 ms and pass energy of 50 eV were used. Charge correction was carried out using adventitious C1s set to a binding energy of 284.8 eV, while charge neutralization was carried out using an electron flood gun.

Ultraviolet Photoelectron Spectroscopy (UPS)

UPS spectra were collected with Nexsa G2 (Thermo Scientific). For the spectra obtained on ETLs, total of 10 scans were acquired using He II ($h\nu = 40.08$ eV) with a pass energy of 10 eV, energy step size of 0.1 eV and dwell time of 50 ms. In the case of perovskite layers, He I ($h\nu = 21.22$ eV) was utilized for collecting 5 spectra with pass energy of 2 eV, energy step size of 0.05 eV and dwell time of 50 ms. In both cases, to obtain secondary electron cut-off (SECO), a bias of negative 10 V was applied. The spectra displayed in the manuscript are corrected for the bias. The Fermi energy ($E_F=0$) reference in UPS was calibrated with a clean polycrystalline Ag sample built-into the sample holder.

4.3. Results and Discussion

In this work, the modulation of charge carrier dynamics at perovskite/ electron transport layer (ETL) interface in PSCs with *n-i-p* architecture are studied. More specifically, two sets of PSC/ETL interfacial configurations are considered: (i) planar, where the perovskite layer directly interfaces on the compact titania(c-TiO₂) film coated on FTO, ii) scaffold-based, where the perovskite layer infiltrates and makes contact with c-TiO₂ coated over hydrothermally grown rutile

TiO₂ nanorods on FTO (which will be referred to as TNR). For both configurations, the thickness of c-TiO₂ was controlled by increasing the volume of the spray pyrolysis solution to four times higher than the base volume. The corresponding ETLs are denoted with “(x4)” next to their abbreviation to indicate a thicker compact titania layer. Thus, the following ETL structures are considered: Planar c-TiO₂, Planar c-TiO₂ (x4), TNR and TNR(x4). Schematics of the planar and scaffold-based PSC architectures are presented in Figure A.1-1 (*Supporting Information*).

The top-view scanning electron microscopy (SEM) images of the different ETL structures are shown in Figure 4.1 a-d. The cross-section SEM images of TNR and TNR (x4) configurations are displayed in Figure 4.1 e and Figure 4.1 f, respectively. The X-ray diffraction (XRD) patterns for the ETL structures are shown in Figure 4.1 g. For the c-TiO₂ (x4) and TNR (x4) an anatase titania peak is detected at 2θ of 25°, marked by (#), while both TNR structures show rutile titania peak at 36°, marked by (*) corresponding to the [001] crystallographic direction indicating the vertical alignment of rutile titania nanorods with respect to FTO, (36) which is marked by (•). Cyclic voltammetry measurements (Figure 4.1 h) confirm full coverage of all ETL structures over the FTO substrate. The low binding energy part of the ultraviolet photoelectron spectroscopy (UPS), as well as its high binding energy segment (i.e., secondary electron cut-off, SECO) are displayed in Figure 4.1 i and Figure 4.1 j, respectively. The work function (Φ) is determined from the difference between energy of UV photons (in this case 40.08 eV, He II) and that of the binding energy corresponding to SECO. The valence band maximum (VBM) (rising edge in the low energy part of UPS near E_F=0 eV) is used for obtaining ionization potential (IE) of filled states (IE=VBM+ Φ). The corresponding results are summarized in Table A.1-1. Overall, the studied ETL structures demonstrate negligible difference in their VBM and Φ values.

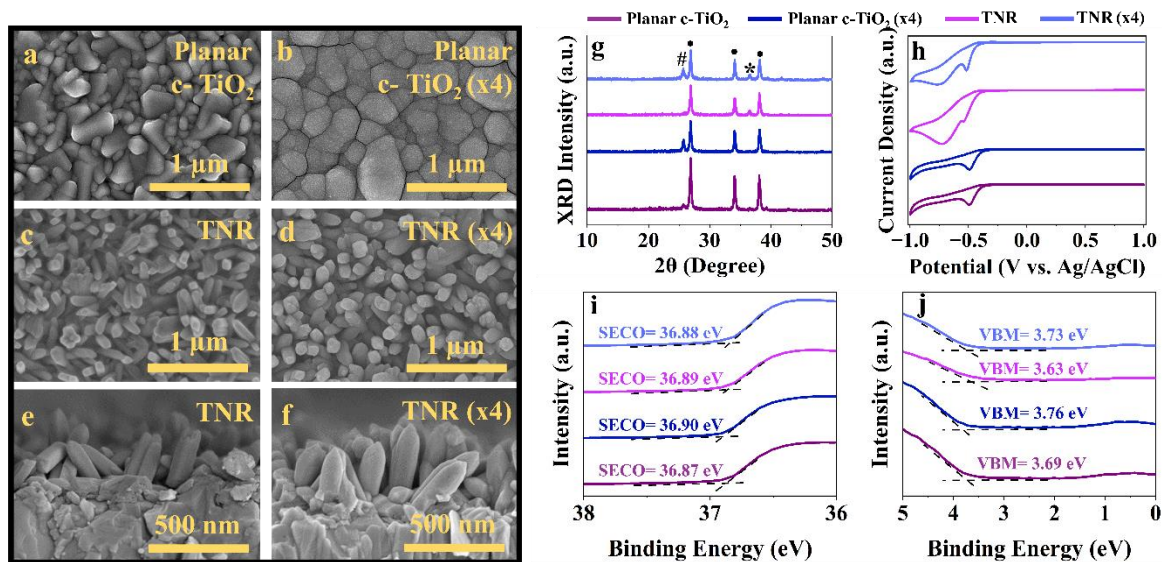


Figure 4.1: Characterization of the ETLs. (a-d) Top-view SEM images of the Planar and TNR ETLs; (e and f) cross-section SEM images of TNR and TNR (x4) structures; (g) XRD patterns with * corresponding to rutile and • corresponding to anatase modifications, (h) cyclic voltammograms, (i) high binding energy part of the UPS spectra showing secondary electron cut-off (SECO) edge, and (j) the low binding energy part of UPS spectra for Planar and TNR type ETL structures.

Figure 4.2 a-d displays the top-view SEM images (in two different magnifications) of the perovskite layer capping/infiltrating each ETL structure. When using thinner compact titania coatings, larger perovskite crystals are obtained (Planar c-TiO₂ and TNR). The zoomed-out view (15k magnification) SEM images of the perovskite layers are shown in lower panels of Figure 4.2 a-d. The energy dispersive X-ray spectroscopy (EDS) results obtained over the surface of perovskite layer (Figure 4.2 e) indicate that the precipitates with bright contrast in SEM images are rich in Rb, I, and Cs. Depending on the underlying ETL film, different crystallization patterns for this secondary phase are obtained. In the case of Planar c-TiO₂ (Figure 4.2 a), this phase shows chain like patterns. In TNR-based perovskite layer (Figure 4.2 c), the crystallites seem to be a mix of islands and chains. For thicker compact titania films in both planar and scaffold type ETLs (Figure 4.2 b and Figure 4.2 d), the chains are no longer visible. Therefore, the interfacial ETL configuration not only impacts the perovskite crystal size but also crystallization pattern of other constituents out of the perovskite lattice. To make the full-stack device, spiro-OMeTAD (as HTL) is spin cast over the perovskite layer and finally 80 nm of gold (Au) is thermally evaporated over

the HTL. The cross-section SEM image for the full-stack PSC devices using TNR as ETL is displayed in Figure A.1-2.

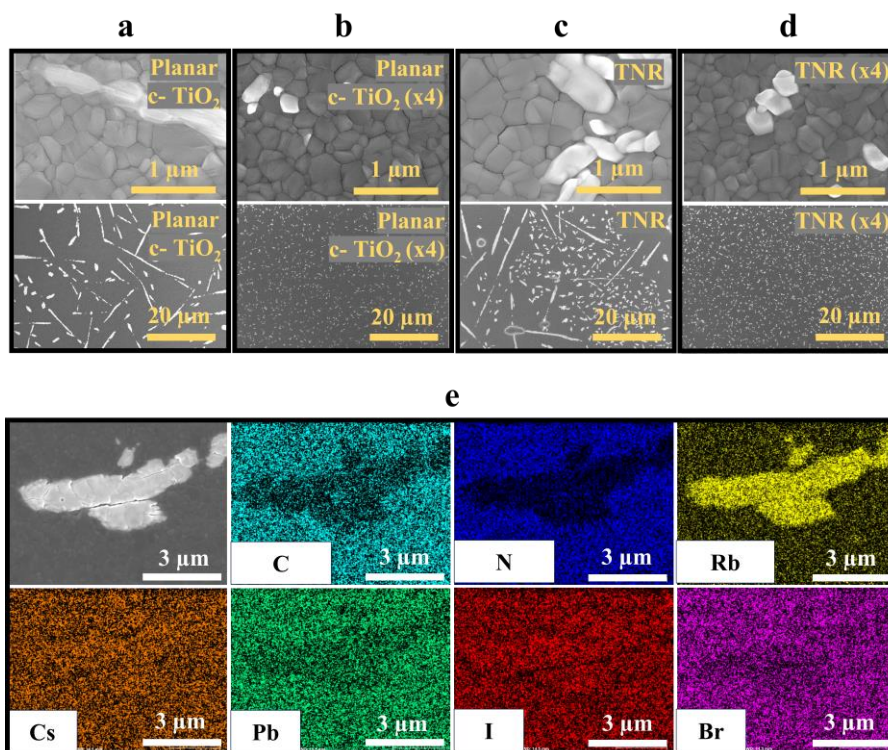


Figure 4.2: Top view SEM images for the perovskite layer deposited over (a) Planar c-TiO₂, (b) Planar c-TiO₂ (x4), (c) TNR and (d) TNR(x4) at 15k and 50 k magnification; (e) EDS elemental mappings of the secondary phase precipitating out of the perovskite lattice for Planar c-TiO₂ (x4) as ETL.

To obtain PV metrics, each PSC type (comprising four devices) was exposed to increasing pre-illumination time ranging from 0 to 60 minutes, with a 20-minute interval, before recording the $J-V$ curves. The corresponding PV metrics at two different scan rates of 10 and 100 mV/s are shown in Figure 4.3.

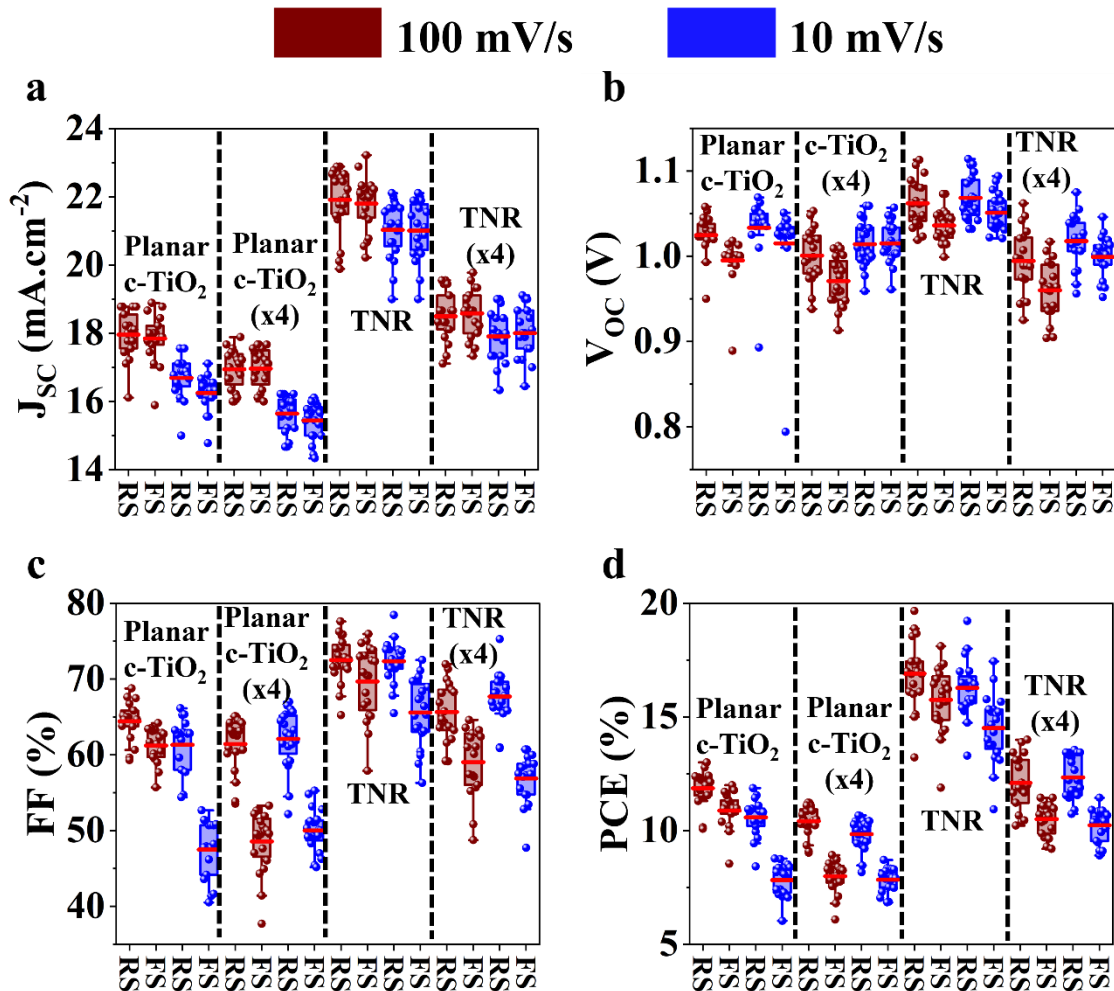


Figure 4.3: Comparison of PV metrics, at 100 and 10 mV/s scan rate, for PSCs based on different ETL configurations: (a) J_{SC} , (b) V_{OC} , (c) FF , and (d) PCE .

For both scan directions and rate, increasing the thickness of titania coating in the two ETL configurations leads to reduced J_{SC} , as can be seen on Figure 4.3 a. TNR structures obtain considerably higher J_{SC} values than their Planar c-TiO₂ counterparts. In addition, decreasing the scan rate results in J_{SC} reduction. Concomitant with the trends of J_{SC} , PSCs based on TNR display the highest external quantum efficiency (EQE) plateau of over 80 % (Figure 4.4 a), followed by TNR (x4), Planar c-TiO₂ and finally Planar c-TiO₂ (x4).

As seen in Figure 4.3 b, increasing thickness of titania coating diminishes V_{OC} , for both scan rates and directions, while reducing the scan rate enhances V_{OC} (albeit to a considerably larger extent when a thicker titania coating is utilized). Although PSCs based on TNR obtain higher V_{OC} than

the Planar c-TiO₂ counterpart, increased thickness of compact titania layer renders relatively similar values for TNR (x4) and Planar c-TiO₂ (x4). From Figure 4.3 c, in the case of both ETL configurations, higher *FF* values are obtained for thinner titania coating layers (TNR and Planar c-TiO₂). For both scan rates, the *FF* radically drops under FS when thicker titania coatings are utilized. This drop is more prominent under 10 mV/s when a thinner coating layer is employed. Finally, with respect to *PCE*, TNR and TNR(x4)-based-PSCs deliver higher values than their planar counterparts. Overall, increasing the thickness of titania coating layer results in a *PCE* drop for both ETL configurations, albeit more pronounced in scaffold-based PSCs (Figure 4.3 d). Additionally, when thicker titania coating is employed in the ETL ensemble, the *PCE* is better retained upon switching to 10 mV/s. Conversely, for thinner titania coating and especially Planar c-TiO₂ a substantial drop in *PCE* in FS is observed. The champion device in this work obtains a *PCE* of 19.66 % which is based on TNR as ETL. Overall, it is evident that depending on the thickness of the titania coating layer and its combination with a nanorod scaffold, considerably enhanced PV metrics can be expected.

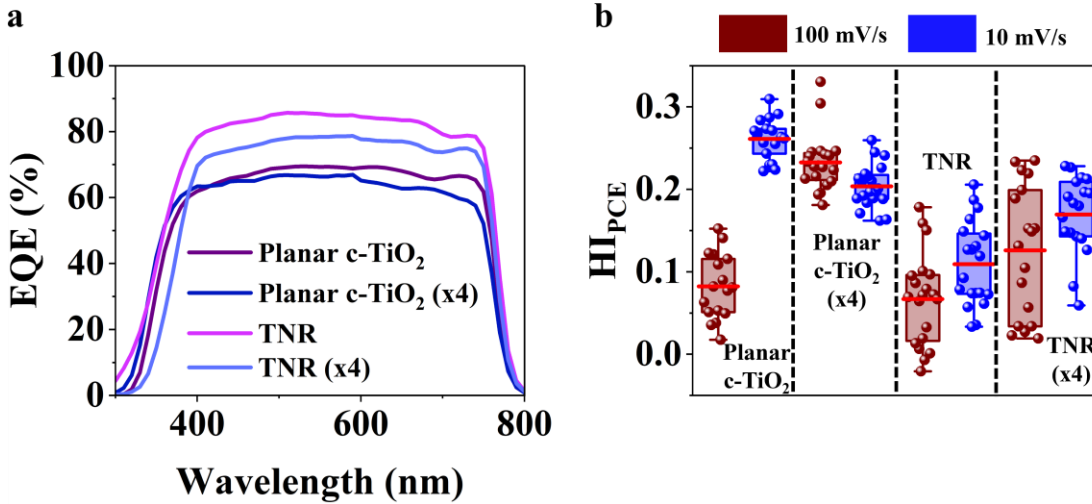


Figure 4.4: (a) External quantum efficiency (EQE) spectra and (b) hysteresis index (HI_{PCE}) for PSCs based on different ETL structures.

In this work, the hysteresis is also calculated using the following:(7)

$$HI_{PCE} = \frac{PCE_{RS} - PCE_{FS}}{PCE_{RS}} \quad (\text{Equation 4.1})$$

where PCE_{RS} and PCE_{FS} are the PCE values corresponding to FS and RS directions, respectively.

HI_{PCE} values calculated for the two PSCs architectures are shown in Figure 4.4 d, whereby Planar c-TiO₂ and c-TiO₂ (x4) configurations display the highest HI_{PCE} under 10 mV/s and 100 mV/s, respectively. As we have argued before and discussed elsewhere,(38, 39) this parameter cannot be utilized to fully comment on the dynamics of PSCs, since it does not take into account changes in metrics of FS and RS that resulted in a certain HI_{PCE} value. As such, reduction of HI_{PCE} values alone cannot necessarily be taken as an indication of improved performance or in general a better PSC. Hence, for a better understanding of the contribution of each ETL structure to loss and gain of PSC performance under 1 Sun illumination, $J-V$ scans (under 100 and 10 mV/s) before and after light soaking were compared (Figure 4.5 and 2- Table A.1- 5). For all studied PSCs, the V_{OC} values were reduced with light soaking but enhanced with lower scan rate. Moreover, the J_{SC} values displayed a universal decrease with reduced scan rate. Therefore, in the following, the changes to HI_{PCE} are assessed by considering the corresponding modulations to FF in FS (FF_{FS}) and FF in RS (FF_{RS}).

For PSCs based on Planar c-TiO₂ (Figure 4.5 a and Table A.1-2), under light soaking, the FF is improved for both scan directions, which can be attributed to the enhanced p -doping of spiro-OMeTAD as HTL under illumination (Figure A.1- 3) This enhancement is, however, more pronounced in FS than in RS (8.77% vs. 3.9% for 100 mV/s) and under reduced scan rate of 10 mV/s (18.40% in FS vs. 11.56% for RS), as compared with prior to light soaking. Concomitantly, the magnitude of HI_{PCE} for a given scan rate is reduced when comparing the values corresponding to before and after light soaking (0.12 vs. 0.08 for 100 mV/s, and 0.30 vs. 0.25 for 10 mV/s). From the perspective of FF , this can be indeed regarded as a positive change. However, when switching from 100 mV/s to 10 mV/s, a drastic reduction of FF for a given scan direction is observed (12.57% for RS and 42.61% for FS before light soaking, 3.6% for RS and 26.58% for FS after light soaking). The recorded decrease is more enhanced in the case of FS which leads to increased HI_{PCE} and therefore widening of $J-V$ curves upon lowering the scan rate (0.12 vs. 0.30 for before, and 0.08 vs. 0.25 for after light soaking). Therefore, the positive influence of enhanced spiro-OMeTAD p -doping, over FF for planar PSCs, under illumination is overcome by reduced scanning speed. Therefore, even though reduced scan speed leads to enhanced V_{OC} , it is nevertheless detrimental for FF . Similar effects under light soaking are observed for Planar c-TiO₂ (x4), albeit to a lesser

extent (Figure 4.5 b and Table A.1-3). In particular, the enhancement of FF under light soaking and 100 mV/s in Planar c-TiO₂ (x4) is 2.9% for RS and 5.2% for FS. Under 10 mV/s, a similar spike for FF_{RS} is observed as that of 100 mV/s, yet under FS it remains unchanged. Interestingly, reducing the scan speed from 100 to 10 mV/s results in enhanced FF for both scan directions before light soaking (2.2% under RS and 3.05% under FS). After light soaking, while the FF in RS increases by 2.2%, it decreases by 2.7% in FS. As a result, HI_{PCE} magnitude is reduced under light soaking for 100 mV/s (0.24 for before light soaking vs. 0.19 for after light soaking), however is enhanced under 10 mV/s (0.15 before light soaking vs. 0.21 after light soaking). In addition, for PSCs based on Planar c-TiO₂ (x4), HI_{PCE} is lowered with reduced scanning speed before light soaking (0.24 vs. 0.15) and enhanced after light soaking (0.19 vs. 0.21). In addition to displaying gain in FF under light soaking, PSCs based Planar c-TiO₂ (x4) possess the added benefit of enhanced FF under reduced scan speed of 10 mV/s (except for a slight decrease of FF_{FS} under 10 mV/s), compared with their Planar c-TiO₂ counterpart.

With respect to scaffold- based PSCs, different dynamics are observed under both light soaking and reduced scan speed. When TNR is utilized as ETL, light soaking diminishes FF in both scan directions and rates. As such, under 100 mV/s, a 5.81% drop in RS and 3.08% drop in FS was observed. Under light soaking and 10 mV/s, the FF_{FS} experiences a higher reduction than that of RS (5.66 % vs. 4.6%). Prior to light soaking, switching the scan rate from 100 mV/s to 10 mV/s, results in reduction of FF_{FS} by 2.7%, with negligible change in RS. After light soaking, reduced scan rate has negligible influence over the FF_{RS} while it decreases FF_{FS} by 5.31%. Overall, as a result of light soaking, the HI_{PCE} is reduced under 100 mV/s (0.095 for vs. 0.013) while under 10 mV/s no change is observed. For PSCs based on TNR(x4), under the influence of light soaking, the FF_{RS} is reduced by 15.81% under 100 mV/s while under 10 mV/s the change is negligible. Under 10 mV/s, the FF_{RS} and FF_{FS} are reduced by 4.6% and 5.66%, respectively. Interestingly switching the scan rate from 100 mV/s to 10 mV/s, results in negligible change prior to light soaking. However, after prolonged illumination, the FF_{RS} is enhanced by 7.14% while that of FS is reduced by 4.73%. Overall, the HI_{PCE} is reduced due to light soaking (0.21 vs. 0.1 for 100 mV/s, and 0.18 vs. 0.2 for 10 mV/s). Upon decreasing the scan rate, HI_{PCE} shows a negligible drop from 0.21 to 0.2 prior to light soaking and increases from 0.1 to 0.18 after light soaking. It should be noted that the reduction of HI_{PCE} under light soaking for PSCs based on scaffold type ETLs, is far from a positive change since it stems from the reduction in all performance metrics.

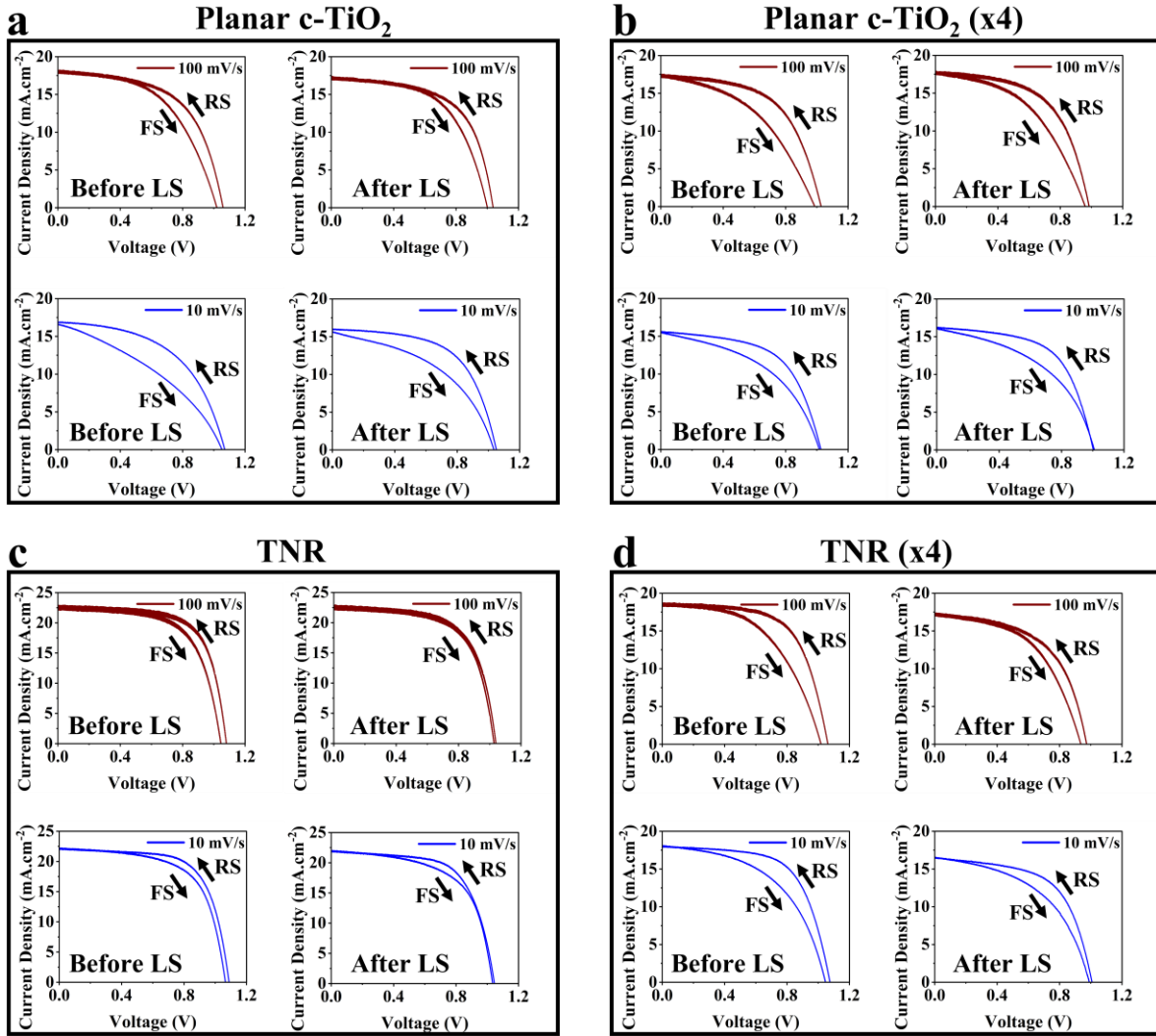


Figure 4.5: Comparison of J - V curves before and after prolonged light soaking (LS) under 1 Sun illumination, for PSCs based on different ETL structures.

To inspect the light-induced changes, UPS spectra are compared (Figure 4.6) for perovskite layer interfacing each ETL configuration. The results, summarized in Table A.1- 6, indicate that for all perovskite layers, the Φ values decrease as a result of light soaking while VBM values remain relatively similar. This suggests that E_F moves closer to the conduction band minimum, which therefore indicates n -doping in the perovskite layer in the vicinity of HTL. However, since this effect is present for all perovskite media, it cannot by itself explain the changes to PV metrics as a result of light soaking. Additionally, X-ray photoelectron spectroscopy (XPS) results are compared for before (Figure A.1- 4 and Table A.1- 7) and after light soaking (Figure A.1- 5 and Table A.1- 8). No new peaks are observed as a result of prolonged illumination (except for the peak appearing

around 292 eV in C1s spectrum of perovskite layer deposited over Planar c-TiO₂). Moreover, the top-view SEM images (Figure A.1- 6a and Figure A.1- 6b) and EDS mapping results (Figure A.1- 6c) obtained over the perovskite layer after light soaking display no changes in morphology or composition compared with those obtained prior to illumination (Figure 4.2).

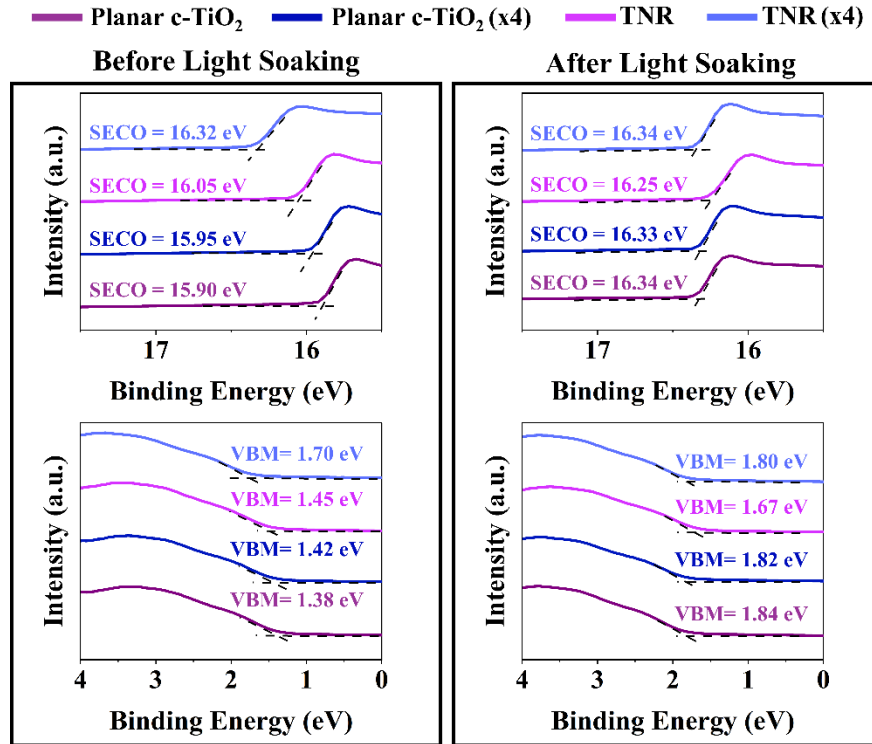


Figure 4.6: Comparison of the high binding energy part (a,b), as well as the low binding energy segment (c,d) of the UPS spectra of perovskite layer interfacing each ETL configuration for before and after light soaking.

To better inspect the ETL-dependent influence of applied bias from that of illumination for PSCs under operation, electrochemical impedance spectroscopy (EIS) spectra are compared not only for prolonged light soaking but also before and after $J-V$ scans. The results are displayed in Figure 4.7. It should be noted that our $J-V$ scans start with RS (starting at voltage exceeding V_{OC} and descending to -0.2 V, at 100 mV/s) followed by FS (starting at -0.2 V and ascending to voltages exceeding V_{OC} by 0.2 V, at 10 mV/s). Therefore, the EIS measurements conducted after $J-V$ scans reflect the influence of forward bias exceeding V_{OC} . All EIS spectra are fitted with the equivalent circuit of Figure A.1- 7, where R_{Series} denotes the series resistance by the wires and contacts. Additionally, to fit the low and high frequency features, resistive (R) and capacitive (C) elements

indicated by LF and HF are employed, respectively. The fitting results for PSCs based on different ETLs are summarized in Table A.1- 9- Table A.1- 12. Our arguments will be developed on the basis that both R_{HF} and R_{LF} indicate charge transfer resistance, as shown elsewhere(39, 40). In the following the extracted resistive parameters are compared for the starting point (the state before application of light and applied bias) with *i*) light soaking only, *ii*) $J-V$ scans only, and *iii*) cumulative effect of light soaking as well as $J-V$ scans. Finally, we compare the weight of the two effects by comparing the EIS spectra after $J-V$ curves, before and after light soaking. In principle, during the $J-V$ scans, PSCs undergo short light soaking time of about 5 minutes. However, since the light soaking time considered in this work is much longer (60 min vs. 5 min), therefore the observed effects after only the $J-V$ measurements can be attributed majorly to the applied bias.

In the case of Planar c-TiO₂, light soaking alone leads to reduction of R_{HF} , without changing R_{LF} . After $J-V$ scans are conducted R_{HF} is considerably enhanced, with negligible influence on R_{LF} . We attribute this effect to potentially unfavorable inverted band alignment at ETL/perovskite interface.(39, 40) After the application of light soaking and $J-V$, both resistive parameters increase with respect to the starting point. However, interestingly, in the case of PSCs based on Planar c-TiO₂, light soaking has a more considerable influence over the resistive parameters compared with applied bias. In Planar c-TiO₂ (x4), both R_{HF} and R_{LF} are subject to reduction with prolonged light soaking. After $J-V$ scans are conducted, both resistive parameters decrease. However, after the agglomerated influence of $J-V$ and light soaking, R_{LF} is unchanged while R_{HF} is reduced. Consequently, in this case, light soaking and applied bias seem to work in confluence. For nanorod-based PSCs, prior to $J-V$ scans, both R_{LF} and R_{HF} are enhanced with light soaking. Yet, after $J-V$, both resistance parameters are reduced. This indicates that when titania coating film, regardless of its thickness, is supported by a scaffold underneath then the light soaking and $J-V$ work against each other. Finally, after the cumulative effect of light soaking and $J-V$, R_{HF} and R_{LF} increase, signifying that weight of detrimental light soaking effect on ETL/perovskite in this case is higher than the conductivity enhancement by applied voltage.

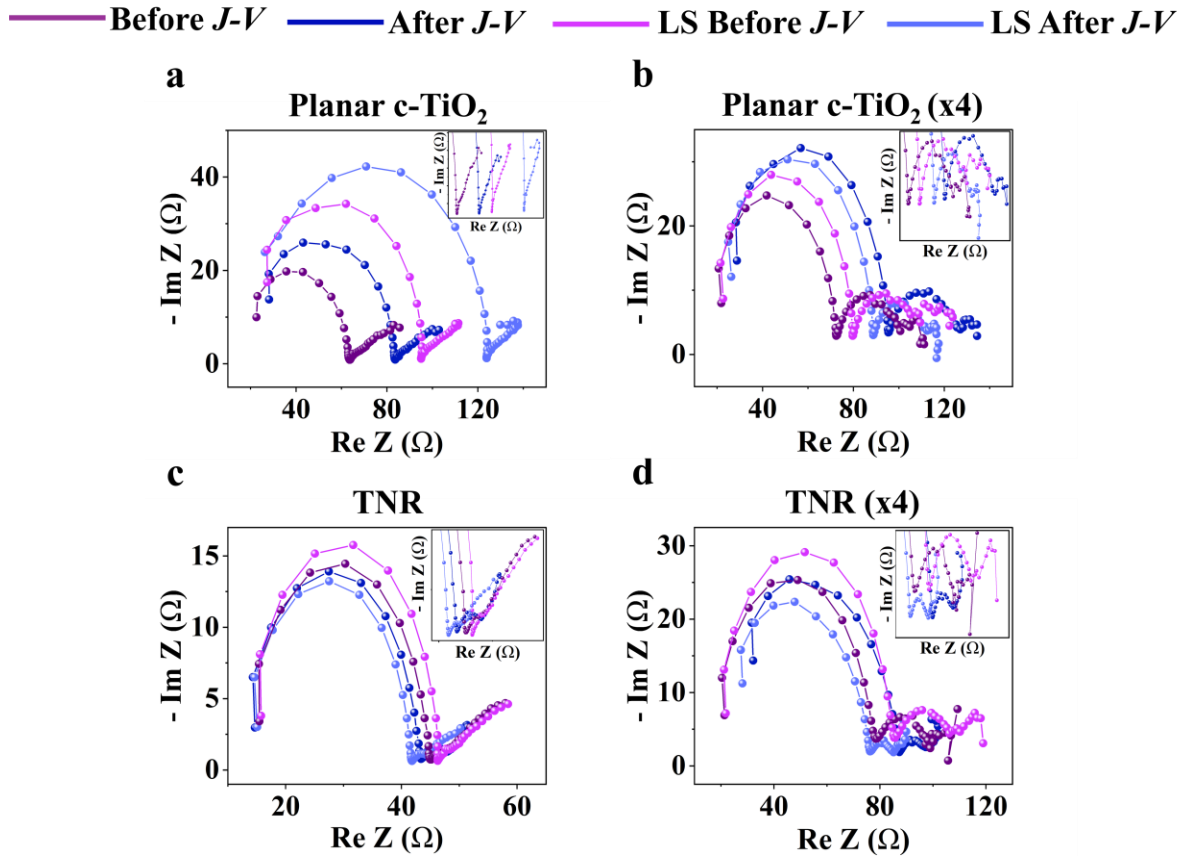


Figure 4.7: Comparison of Nyquist plots for PSCs based on different ETL structures as a function of applied bias and light soaking (LS).

In the following we bring all our observations together to offer a better understanding of operational charge carrier dynamics in PSCs depending on the interfacial configuration (planar vs. scaffold-based) and thickness of the compact titania coating layer.

Based on our results, light soaking works highly in favor of planar PSCs. Through conductivity measurements, it was demonstrated that the bulk conductivity of spiro-OMeTAD (as HTL) is enhanced under light soaking. This is in fact reflected in the reduction of R_{series} for all EIS spectra as a result of prolonged illumination. However, if this conductivity increase was the sole underlying mechanism behind FF increase, then all PSCs under both scan rates should have displayed improvement with light soaking, which as our results indicate is not the case. It is of crucial importance to note that for a net positive gain from p -doping of HTL under illumination to be reflected in FF , the conductivity of ETL/perovskite interface must be able to show tolerance (remain unchanged, if not ideally increasing) towards prolonged illumination which is only the

case for planar PSCs as they displayed improved FF under light soaking. Alternatively, if the conductivity at ETL/perovskite interface is adversely impacted by light soaking, the magnitude of this effect must be smaller than that of the positive HTL conductivity enhancement. This means the total gain in FF would depend on the net conductivity modulation at device interfaces. As such, the increase in R_{HF} and R_{LF} for nanorod-based PSCs is reflected in FF loss under light soaking. On the other hand, the reduction of both resistive parameters for planar-based PSCs is translated in FF gain under prolonged illumination.

Another important finding from this work was that applied forward bias and light soaking could work either together or against one another depending on the underlying ETL. More specifically we demonstrated that while light soaking improves device performance for Planar $c\text{-TiO}_2$, the application of forward bias could potentially result in inverted band alignment at the interface, hampering charge extraction which is reflected in the corresponding enhancement of R_{HF} and R_{LF} . By comparing the EIS fitting results, we concluded that the positive influence of illumination is larger than the negative impact of forward bias, which however is only reflected in the reduction of R_{HF} . Meanwhile, for PSCs based on thick $c\text{-TiO}_2$ (x4), the resulting planar PSC not only displayed FF gain under light soaking but also demonstrated increased conductivity after $J\text{-}V$ scans. Therefore, depending on the thickness of compact titania coating the resulting planar PSCs, applied bias and light soaking could work either together or against each other to modulate interfacial conductivity. For scaffold-based PSCs, applied voltage resulted in enhanced interfacial conductivity, while light soaking worked in the opposite direction, reflected in the decrease and increase of resistive parameters, respectively. However, in contrast to what was observed in Planar $c\text{-TiO}_2$, for scaffold-based PSCs the negative influence of prolonged illumination is larger than that of the positive effect of forward bias.

We also compared the influence of reduced scan speed of 10 mV/s in this work. By comparing scaffold-based PSCs with their planar counterpart it can be concluded that an underlying scaffold considerably helps with lowering the extent of FF loss under reduced scan rate. This effect has a heavier impact on interfacial charge extraction capability compared with the detrimental influence of light soaking, as reflected in the evolution of corresponding FF values. This points to the integral role of a scaffold within the ETL structure. Yet, when it comes to a thicker compact titania coating layer, presence of a scaffold results in FF loss under reduced scan rate as well as light soaking,

compared with its planar counterpart. Therefore, whether presence of scaffold within the ETL structure can be beneficial for FF evolution of PSC under operation, would depend on the thickness of compact titania.

Lastly, despite the intricate ETL interfacial configuration-dependent changes in FF , V_{OC} seemed to display a rather universal trend for all PSCs by reducing under light soaking and enhancing under slow scan rate. Although this trend is line with the observed changes in FF in some cases, (i.e., reduction of FF and V_{OC} under light soaking for TNR-based PSCs), no conclusive correlation can be obtained between the evolution of the two parameters under light soaking and slow scan speed. This observation points towards potentially different underlying phenomena for FF and V_{OC} under operation.

4.4. Conclusion

In the present study, the influence of the compact titania layer placement as well as its thickness within the ETL structure on the evolution of hysteresis dynamics as a function of light soaking, scan speed and applied bias was demonstrated. For this purpose, PSCs were assembled in planar configuration (whereby the ETL consists of only the compact titania coating) and scaffold configuration, where the compact titania coating is supported by titania nanorods underneath. For both configurations, the thickness of the compact titania coating was adjusted by controlling the volume of the precursor solution during spray pyrolysis. Our results reveal that, with respect to interfacial microstructure consideration, configuration of the underlying ETL can impact not only the perovskite crystallite size but also the size and pattern of a secondary phase rich in Rb, I and Cs crystallizing out of the perovskite lattice. The $J-V$ curves for the resulting devices were studied under 100 mV/s and 10 mV/s, before and after light soaking. For planar PSCs, FF is considerably improved as a result of light soaking which ultimately led to reduced hysteresis magnitude. On the other hand, in the case of scaffold configurations, prolonged illumination proved rather detrimental for ETL/perovskite interface as indicated by the diminished FF . Despite that, hysteresis magnitude was reduced which was, however, regarded as a negative change since it stemmed from diminished PV metrics. More complex dynamics were observed as a result of reduced scan rate. It was shown that utilizing a thicker compact titania coating layer within the scaffold type ETL structure can better sustain FF in FS under lower scanning speed in, while it even led to enhanced FF for the planar counterpart. Through SEM, EDX and XPS measurements we confirmed that the

composition and chemical state of perovskite surface was not altered under light soaking for any of the ETL structures. However, UPS measurements indicated n -doping in the perovskite surface as a result of prolonged illumination. By comparing EIS patterns before and after J - V scans, we showed that depending on the specific ETL configuration, factors such as light soaking, reduced scan rate and applied bias could work either together or against one another to impact the overall PSC performance. From Nyquist plots, the application of forward bias (exceeding V_{oc}) to planar PSCs was deemed to increase charge transport resistance, which was attributed to inverted band alignment, while it resulted in enhanced conductivity for PSCs based on scaffold ETL structure. Overall, in this work, we showed that the absolute magnitude of hysteresis index cannot necessarily be taken as an indication for improved or deteriorated PSC performance and needs to be considered in combination with changes in the PV metrics to enable deriving valid conclusion. Moreover, the obtained results indicate that the overall PSC performance is determined not by simply one optimized layer but rather a combination of components that work well together. As such, charge carrier dynamics and hysteresis evolution in PSCs under different testing conditions are determined by competing conductivity modulation effects at the perovskite interface with HTL and ETL.

4.5. Bridge

In Chapter 4, the role of compact titania layer (c-TiO₂, synthesized through spray pyrolysis) interfacing within the ETL structure in modulating the hysteresis behavior in quadruple perovskite-based PSCs with *n-i-p* architecture was studied. This was motivated in particular because of the current incomplete picture as to the synergistic effects of light soaking (under 1 Sun illumination), scan rate, and applied bias with ETL's interfacial structure in influencing PSC hysteresis behavior. To obtain a thorough insight of this interaction, the compact titania (c-TiO₂) layer was utilized on its own as the ETL (rendering the so-called planar configuration), as well as in conjunction with underlying titania nanorods synthesized through hydrothermal synthesis which resulted in a scaffold-based configuration. For both configurations, the thickness of the c-TiO₂ layer was varied through adjusting the volume of the precursor solution during spray pyrolysis. The results indicated that under light soaking, the evolution of hysteresis dynamics depends on the cumulative effect of conductivity modulation at both charge extraction interfaces (ETL and HTL) for respective charge carriers. Thus as a result of light soaking inducing increased hole conductivity in HTL (spiro-OMeTAD), a *FF* gain was attained suggesting the ETL/perovskite interface must be able to withstand prolonged illumination. This proved to be the case for PSCs with planar configuration. However, for the scaffold-based configuration, illumination proved to be detrimental for the ETL/perovskite interface manifested in *FF* loss. The reduction of hysteresis magnitude in planar PSCs was accompanied by improved *FF* in FS, while in the case of scaffold-based PSCs diminished metrics obtained. This finding, therefore, means that hysteresis index alone cannot be utilized as a reliable metric for gauging improved or deteriorated PSC performance. Moreover, to sustain the *FF* under reduced scan rate and especially under FS, c-TiO₂ either must be utilized with a nanorod scaffold underneath or with increased thickness in planar configuration. From EIS measurements, applied positive bias was deemed to negatively impact the planar configuration and negate the favourable light soaking effect. This was in sharp contrast to the scaffold-based PSCs displaying an increased conductivity at ETL/perovskite interface with applied forward bias, which however was not sufficient to compete with the negative impact of light soaking for these structures. It was suggested that the planar configurations could experience band inversion (on the perovskite side) under the application of forward bias exceeding V_{OC} . To this end, the evolution of charge carrier dynamics and the corresponding hysteresis modulation from the perspective of c-TiO₂ thickness

and interfacing within the ETL structure was elucidated. Continuing to explore the impact of ETL on hysteresis dynamics, we next set out to study the influence of the titania nanorod scaffold in determining the hysteresis locus and magnitude -a less understood issue. To this end, the work presented in Chapter 5 was conducted, whereby two types of titania nanorod scaffolds were built by combining spray pyrolysis and hydrothermal synthesis. In this case, the focus was placed on understanding inductive hysteresis as a function of the ETL/perovskite interface by correlating the gap between J - V curves with the presence of inductive features in the EIS patterns obtained under 1 Sun illumination and forward bias exceeding V_{OC} .

4.6. References

1. deQuilettes DW, Koch S, Burke S, Paranj R, Shropshire AJ, Ziffer ME, et al. Photoluminescence Lifetimes Exceeding 8 μ s and Quantum Yields Exceeding 30% in Hybrid Perovskite Thin Films by Ligand Passivation. *ACS Energy Letters*. 2016;1(2):438-44.
2. Park N-G. Perovskite solar cells: an emerging photovoltaic technology. *Materials Today*. 2015;18(2):65-72.
3. Das B, Liu Z, Aguilera I, Rau U, Kirchartz T. Defect tolerant device geometries for lead-halide perovskites. *Materials advances*. 2021;2(11):3655-70.
4. Snaith HJ, Abate A, Ball JM, Eperon GE, Leijtens T, Noel NK, et al. Anomalous Hysteresis in Perovskite Solar Cells. *The Journal of Physical Chemistry Letters*. 2014;5(9):1511-5.
5. Cui Y, Chen C, Li C, Chen L, Bista SS, Liu X, et al. Correlating Hysteresis and Stability with Organic Cation Composition in the Two-Step Solution-Processed Perovskite Solar Cells. *ACS Applied Materials & Interfaces*. 2020;12(9):10588-96.
6. Odabaşı Ç, Yıldırım R. Assessment of Reproducibility, Hysteresis, and Stability Relations in Perovskite Solar Cells Using Machine Learning. *Energy Technology*. 2020;8(12):1901449.
7. Unger EL, Czudek A, Kim H-S, Tress W. Chapter 4 - Current-voltage analysis: lessons learned from hysteresis. In: Pazoki M, Hagfeldt A, Edvinsson T, editors. *Characterization Techniques for Perovskite Solar Cell Materials*: Elsevier; 2020. p. 81-108.

8. Kang DH, Park NG. On the current–voltage hysteresis in perovskite solar cells: dependence on perovskite composition and methods to remove hysteresis. *Advanced Materials*. 2019;31(34):1805214.
9. Rong Y, Hu Y, Ravishankar S, Liu H, Hou X, Sheng Y, et al. Tunable hysteresis effect for perovskite solar cells. *Energy & Environmental Science*. 2017;10(11):2383-91.
10. Song DH, Jang MH, Lee MH, Heo JH, Park JK, Sung S-J, et al. A discussion on the origin and solutions of hysteresis in perovskite hybrid solar cells. *Journal of Physics D: Applied Physics*. 2016;49(47):473001.
11. Kim H-S, Jang I-H, Ahn N, Choi M, Guerrero A, Bisquert J, et al. Control of I–V hysteresis in CH₃NH₃PbI₃ perovskite solar cell. *The journal of physical chemistry letters*. 2015;6(22):4633-9.
12. Liu P, Wang W, Liu S, Yang H, Shao Z. Fundamental understanding of photocurrent hysteresis in perovskite solar cells. *Advanced Energy Materials*. 2019;9(13):1803017.
13. Seo J, Noh JH, Seok SI. Rational strategies for efficient perovskite solar cells. *Accounts of chemical research*. 2016;49(3):562-72.
14. Jena AK, Kulkarni A, Ikegami M, Miyasaka T. Steady state performance, photo-induced performance degradation and their relation to transient hysteresis in perovskite solar cells. *Journal of Power Sources*. 2016;309:1-10.
15. Li W, Rothmann MU, Zhu Y, Chen W, Yang C, Yuan Y, et al. The critical role of composition-dependent intragrain planar defects in the performance of MA_{1-x}FA_xPbI₃ perovskite solar cells. *Nature Energy*. 2021;6(6):624-32.
16. Contreras L, Idígoras J, Todinova A, Salado M, Kazim S, Ahmad S, et al. Specific cation interactions as the cause of slow dynamics and hysteresis in dye and perovskite solar cells: a small-perturbation study. *Physical Chemistry Chemical Physics*. 2016;18(45):31033-42.
17. Kim S-G, Li C, Guerrero A, Yang J-M, Zhong Y, Bisquert J, et al. Potassium ions as a kinetic controller in ionic double layers for hysteresis-free perovskite solar cells. *Journal of Materials Chemistry A*. 2019;7(32):18807-15.
18. Yoo H-S, Park N-G. Post-treatment of perovskite film with phenylalkylammonium iodide for hysteresis-less perovskite solar cells. *Solar Energy Materials and Solar Cells*. 2018;179:57-65.

19. Fakharuddin A, Schmidt-Mende L, Garcia-Belmonte G, Jose R, Mora-Sero I. Interfaces in perovskite solar cells. *Advanced Energy Materials*. 2017;7(22):1700623.
20. Patel JB, Wong-Leung J, Van Reenen S, Sakai N, Wang JTW, Parrott ES, et al. Influence of interface morphology on hysteresis in vapor-deposited perovskite solar cells. *Advanced Electronic Materials*. 2017;3(2):1600470.
21. Shao S, Loi MA. The role of the interfaces in perovskite solar cells. *Advanced Materials Interfaces*. 2020;7(1):1901469.
22. Weber SA, Hermes IM, Turren-Cruz S-H, Gort C, Bergmann VW, Gilson L, et al. How the formation of interfacial charge causes hysteresis in perovskite solar cells. *Energy & environmental science*. 2018;11(9):2404-13.
23. Zhao C, Chen B, Qiao X, Luan L, Lu K, Hu B. Revealing underlying processes involved in light soaking effects and hysteresis phenomena in perovskite solar cells. *Advanced Energy Materials*. 2015;5(14):1500279.
24. Guo Q, Xu Y, Xiao B, Zhang B, Zhou E, Wang F, et al. Effect of energy alignment, electron mobility, and film morphology of perylene diimide based polymers as electron transport layer on the performance of perovskite solar cells. *ACS applied materials & interfaces*. 2017;9(12):10983-91.
25. Thakur UK, Askar AM, Kisslinger R, Wiltshire BD, Kar P, Shankar K. Halide perovskite solar cells using monocrystalline TiO₂ nanorod arrays as electron transport layers: impact of nanorod morphology. *Nanotechnology*. 2017;28(27):274001.
26. Upama MB, Elumalai NK, Mahmud MA, Wang D, Haque F, Gonçalves VR, et al. Role of fullerene electron transport layer on the morphology and optoelectronic properties of perovskite solar cells. *Organic Electronics*. 2017;50:279-89.
27. Yang D, Zhou X, Yang R, Yang Z, Yu W, Wang X, et al. Surface optimization to eliminate hysteresis for record efficiency planar perovskite solar cells. *Energy & Environmental Science*. 2016;9(10):3071-8.
28. Zhang Y, Liu M, Eperon GE, Leijtens TC, McMeekin D, Saliba M, et al. Charge selective contacts, mobile ions and anomalous hysteresis in organic–inorganic perovskite solar cells. *Materials Horizons*. 2015;2(3):315-22.

29. Yang D, Yang R, Wang K, Wu C, Zhu X, Feng J, et al. High efficiency planar-type perovskite solar cells with negligible hysteresis using EDTA-complexed SnO₂. *Nature communications*. 2018;9(1):3239.
30. Miyasaka T. *Perovskite Photovoltaics and Optoelectronics: From Fundamentals to Advanced Applications*: John Wiley & Sons; 2021.
31. Saliba M, Matsui T, Domanski K, Seo J-Y, Ummadisingu A, Zakeeruddin SM, et al. Incorporation of rubidium cations into perovskite solar cells improves photovoltaic performance. *Science*. 2016;354(6309):206-9.
32. Jeon NJ, Noh JH, Kim YC, Yang WS, Ryu S, Seok SI. Solvent engineering for high-performance inorganic–organic hybrid perovskite solar cells. *Nature Materials*. 2014;13(9):897-903.
33. Heo S, Seo G, Lee Y, Seol M, Kim SH, Yun D-J, et al. Origins of High Performance and Degradation in the Mixed Perovskite Solar Cells. *Advanced Materials*. 2019;31(8):1805438.
34. Saliba M, Matsui T, Seo J-Y, Domanski K, Correa-Baena J-P, Nazeeruddin MK, et al. Cesium-containing triple cation perovskite solar cells: improved stability, reproducibility and high efficiency. *Energy & Environmental Science*. 2016;9(6):1989-97.
35. Kim H-S, Park N-G. Parameters affecting I–V hysteresis of CH₃NH₃PbI₃ perovskite solar cells: effects of perovskite crystal size and mesoporous TiO₂ layer. *The journal of physical chemistry letters*. 2014;5(17):2927-34.
36. Liu B, Aydil ES. Growth of oriented single-crystalline rutile TiO₂ nanorods on transparent conducting substrates for dye-sensitized solar cells. *Journal of the American Chemical Society*. 2009;131(11):3985-90.
37. Saliba M, Correa-Baena J-P, Wolff CM, Stolterfoht M, Phung N, Albrecht S, et al. How to Make over 20% Efficient Perovskite Solar Cells in Regular (n–i–p) and Inverted (p–i–n) Architectures. *Chemistry of Materials*. 2018;30(13):4193-201.
38. Habisreutinger SN, Noel NK, Snaith HJ. Hysteresis Index: A Figure without Merit for Quantifying Hysteresis in Perovskite Solar Cells. *ACS Energy Letters*. 2018;3(10):2472-6.
39. Yekani R, Chiu H-c, Strandell D, Wang Z, Bessette S, Gauvin R, et al. Correlation between hysteresis dynamics and inductance in hybrid perovskite solar cells: studying the dependency on ETL/perovskite interfaces. *Nanoscale*. 2023;15(5):2152-61.

40. Ebadi F, Taghavinia N, Mohammadpour R, Hagfeldt A, Tress W. Origin of apparent light-enhanced and negative capacitance in perovskite solar cells. *Nature communications*. 2019;10(1):1574.

Chapter 5: Hysteresis Dynamics and Inductance in Perovskite Solar Cells

This chapter addresses the 2nd objective of the thesis, which is to evaluate how the interfacial structure of the ETL (titania nanorod scaffold) leads to inductive hysteresis in PSCs with *n-i-p* architecture and quadruple perovskite composition. This chapter is replication of a manuscript published in a peer-reviewed journal. The citation information for this chapter is provided below:

- Yekani, R., Chiu, H.C., Strandell, D., Wang, Z., Bessette, S., Gauvin, R., Kambhampati, P. and Demopoulos, G.P., 2023. “Correlation between hysteresis dynamics and inductance in hybrid perovskite solar cells: studying the dependency on ETL/perovskite interfaces.” *Nanoscale*, 15(5), pp.2152-2161.

Abstract

In this study, to elucidate origin of inductance and its relation to the phenomenon of hysteresis in hybrid perovskite solar cells (PSCs), two electron transport layer (ETL) structures are utilized: (a) rutile titania nanorods grown over anatase titania (AR) and (b) anatase titania covering the rutile titania nanorods (RA). The rutile and anatase phases are prepared via hydrothermal synthesis and spray pyrolysis, respectively. PSCs based on ETL with RA structure attain higher short-circuit current density (J_{sc}) and open-circuit voltage (V_{oc}) while showing slightly lower fill factor (FF) compared with their AR counterpart. Using electrochemical impedance spectroscopy (EIS) measurements, we show that the ETL plays a major role in setting the tone for ionic migration speed and consequently accumulation. Moreover, we consider conductivity of the transport layers as a determining factor in not only giving rise to inductive features but also dictating the bias region under which recombination takes place, ultimately influencing hysteresis locus.

Keywords

Perovskite Solar Cells, Hysteresis, Electron Transport Layer, Electrochemical Impedance Spectroscopy, Inductance

5.1. Introduction

Since their initial breakthrough in 2009, hybrid organic-inorganic perovskite solar cells (PSCs) have come a long way from a mere 3.9% power conversion efficiency (*PCE*)⁽¹⁾ to over 25% in 2021⁽²⁾. After only a decade, PSCs have shown considerable potential to compete with silicon solar cells.⁽³⁾ In PSCs, the absorber possesses ABX₃ perovskite structure where A is a monovalent cation, B is a divalent cation and X is a halide. Due to exhibiting phenomenal properties such as long electron-hole diffusion length⁽⁴⁾, high absorption coefficient⁽⁵⁾, low exciton binding energies⁽⁶⁾ and defect tolerance⁽⁷⁾, PSCs have been receiving unparalleled research attention over the past decade. Unlocking their full potential, however, relies on overcoming major challenges such as hysteresis.

Hysteresis is the term applied to the mismatch between current-voltage (*J-V*) curves during reverse and forward scan⁽⁸⁾. The major culprit, as reported in literature, is the ionic charge redistribution within the perovskite film as a response to external stimuli^(9, 10), coupled with non-radiative recombination at the interfaces. Over the past decade, there has been a considerable improvement regarding devising various perovskite engineering and chemistry approaches to minimize hysteretic occurrences^(11, 12). Electron transport layer (ETL) and hole transport layer (HTL) are known to exert a heavy influence over hysteresis through their defect properties^(13, 14), passivation⁽¹⁵⁾, chemistry⁽¹⁶⁾ and utilization in various architectures⁽¹⁷⁾.

A probing method that has been commonly utilized to characterize PSCs, especially at the interfaces, and identify hysteretic features is electrochemical impedance spectroscopy (EIS).⁽¹⁸⁾ Yet, the interpretation of the resulting spectra has proved to be difficult and drawing intense debate in some cases. One example is the origin and implication of lower frequency capacitance under illumination. An early round of studies attributed this feature to accumulation of electronic charge at the interfaces.^(19, 20) A subset of lower frequency capacitance is called inductance (otherwise known as negative capacitance) (21, 22, 23, 24) that appears as a hook or loop in Nyquist plot representation of EIS measurements and is believed to be detrimental for PSC performance.⁽²⁵⁾ Inductance has had varying interpretations in the literature such as emptying rate of an intermediate state⁽¹⁹⁾ and interfacial charge transfer resistance⁽²⁶⁾. Recently, it has been shown^(27, 28, 29, 30) that the capacitance element in lower frequency is rather due to phase difference between applied voltage and recorded current density, yet, its response is manifested similar to that of a physical inductor.

Note that in this interpretation, the role of electrode polarization is not completely disregarded, however is believed to make a minor contribution towards the observed capacitance response. Based on this definition, inductance is mainly attributed to ionic modulation of potential barrier at perovskite interfaces and subsequent injection current from the contacts.⁽³⁰⁾

Apart from the observation of inductance in PSCs with normal planar⁽¹⁹⁾, mesoporous⁽²⁷⁾ and even ETL-free architecture⁽³¹⁾, other works⁽³²⁾ have deliberately utilized multi-layered ETL structures to boost the number of charge injection processes involved to induce the appearance of inductance in EIS spectra. In this work, to acquire a deeper understanding of the hysteresis phenomenon and its correlation with inductance, PSCs with two different titania ETL structures (that differ in crystallographic phase and sequence of deposition) are studied. The variation in ETL phase composition and structure is achieved by using spray pyrolysis (to deposit anatase phase film) and hydrothermal synthesis (for obtaining rutile phase in nanorod morphology). The two phases are then stacked alternatively in FTO/anatase/rutile and FTO/rutile/anatase architecture to yield AR and RA structures, respectively. The ETLs are characterized through a combination of techniques such as scanning electron microscopy (SEM), X-ray diffraction (XRD), cyclic voltammetry, atomic force microscopy (AFM), ultraviolet-visible (UV-Vis) absorption, photoluminescence (PL), time-resolved photoluminescence (TRPL) and EIS. Utilizing the mentioned ETL architectures allows us to build a theory for interpreting the inductance features appearing in mid and lower frequency part of Nyquist plot and correlating them with hysteresis dynamics in PSCs.

The obtained results demonstrate that, under fixed parameters corresponding to synthesis and deposition of perovskite layer and HTL, the locus of hysteresis is dictated by the ETL. Moreover, the bias range under which hysteresis locus appears is indicative of the corresponding electronic band structure. We postulate that the inductive hook at low frequency is a manifestation of non-radiative recombination under inverted bands at the ETL/perovskite interface.

5.2. Experimental

Synthesis of the ETL structures

For all ETL-related synthesis purposes, the FTO glass substrates (2 cm by 2 cm in dimension and pre-patterned) were purchased from Solaronix (with surface resistivity of 7 Ohm/ Square and

thickness of 2.2 mm-part number: TCO22-7/LI). The substrates were ultrasonically cleaned sequentially in a 2% Hellmanex solution in DI water, 2-propanol, and acetone, for 15 min in each solvent. Eventually, the substrates were treated for 15 min with UV-ozone.

Growth of the rutile nanorod film was carried out using hydrothermal synthesis.⁽³³⁾ The reaction solution was made with 0.02 L DI water and 0.02 L concentrated hydrochloric acid (36.5%-38% by weight from Fisher Scientific). The mixture was stirred at room temperature in a sealed beaker for 5 minutes before the addition of 0.001 L Ti (IV) butoxide (Reagent grade 97%, Sigma Aldrich). After stirring for another 40 min, the precursor solution was added to a Teflon-lined stainless-steel autoclave (0.125 L volume, Parr Instrument Co.), where two substrates were placed at an angle with their conductive sides facing the wall. The autoclave was then sealed and placed in the oven with a heating ramp of 10°C/hour to reach the final temperature of 150°C where they were held for 60 minutes before cooling down inside the oven, which took approximately 3 hours. After the synthesis was done, the substrates were taken out and washed thoroughly with DI water. Afterwards, they underwent an annealing step at a heating ramp of 4°C/min to 550°C with holding time of 30 minutes before cooling down.

The anatase phase was synthesized using spray pyrolysis. Cleaned FTO substrates were placed on a hot plate and heated gradually to 450°C. Then a precursor solution containing 9 mL ethanol, 0.6 mL Ti(IV) diisopropoxide bis acetylacetonate (Sigma Aldrich) and 0.4 mL acetylacetonate (Sigma Aldrich) was sprayed over the samples using O₂ as carrier gas.

Synthesis of perovskite layer and HTL

The perovskite layer is synthesized and deposited according to the procedure described by Saliba et al.⁽³⁴⁾ In short, the perovskite precursor was prepared by mixing FAI (1M), PbI₂ (1.1 M), MABr (0.2M) and PbBr₂ (0.2M) in DMF/DMSO (4:1 v/v). CsI (1.5M in DMSO) and RbI (1.5M in DMF:DMSO 4:1 v/v) were added to the perovskite precursor to obtain quadruple cation composition of (Cs₅Rb₅MA_{0.15}FA_{0.75})Pb(I_{0.83}Br_{0.17})₃. The perovskite layer is deposited through the anti-solvent method by using 150 μL of the final perovskite precursor and using a two-step spinning program; 1000 rpm for 10 seconds followed by 6000 rpm for 20 seconds. Five seconds before the end of spinning, 200 μL of chlorobenzene was poured on the spinning substrate. The substrates were then annealed at 100 °C for 45 minutes. Except for PbI₂ and PbBr₂ which were sourced from TCI America, all other chemicals were purchased from Sigma Aldrich.

Spiro-OMeTAD was chosen as the HTL material. The precursor solution is made from 72.3 mg of spiro-OMeTAD, 28.3 μL 4-TBP and 17.5 μL LiTFSI (520 mg/mL in acetonitrile) in 1 mL chlorobenzene. Deposition of HTL was conducted by spin casting 30 μL the precursor solution at 3000 rpm. Finally, 80 nm of gold was thermally evaporated (NexDep, Angstrom Engineering) in 2E-6 mbar vacuum at the rate of 1 $\text{\AA}/\text{s}$.

Current Density- Voltage (J - V) and Electrochemical Impedance Spectroscopy (EIS)

Measurements

The illumination measurements were conducted with a class A solar simulator (Sol1A 94021A, Newport) which was calibrated with a silicon KG5 reference cell (Abet Technologies). To measure the PV metrics, J - V curves were recorded under 1 Sun at 100 and 10 mV/s from -0.2 V (vs. reference electrode) to 0.2 V above V_{OC} . All EIS measurements were conducted under 1 Sun illumination and various forward bias values with a Biologic potentiostat (SP-300) and controlled by EC lab software from 1 MHz to 50 MHz, with a perturbation potential of 20 mV over 40 data points. There was a total of four devices on each sample, with an active area of 0.09 cm^2 . The illumination intensity for all J - V and EIS measurements was 1 Sun.

X-Ray Diffraction (XRD)

XRD patterns were acquired using a Bruker D8 Advance. Copper source ($K\alpha$ line) was used with a voltage of 40 kV and a current of 40 mA. Scan parameters were 2Theta from 6° to 70° with an increment of 0.02°, and integration time of 1s. The experiment was performed in the grazing incidence diffraction mode with a low incident angle of 3°. Both the primary and secondary axial soller was 2.5° while the secondary twin optic was set to soller 0.2°. The LynxEye detector was set to 0D mode.

Cyclic Voltammetry Measurements

Cyclic voltammetry measurements were carried out in a one-compartment cell using Biologic potentiostat (SP-300) and controlled by EC lab software. Ag/AgCl (sat. KCl) and Au were used as reference and counter electrode, respectively. The electrolyte was 0.5 mM $\text{K}_4\text{Fe}(\text{CN})_6$ (Sigma Aldrich) + 0.5mM $\text{K}_3\text{Fe}(\text{CN})_6$ (Sigma Aldrich) in aqueous 0.5 M KCl (Sigma Aldrich). The voltage was scanned from -1 V to 1V at a rate of 25 mV/s. The effective electrode area was 1 cm^2 .

Scanning Electron Microscopy (SEM)

Cross sectional and top view SEM images were obtained with a cold-field emission scanning electron microscope (CFE-SEM) SU8230 Hitachi, utilizing the in-lens upper secondary electron detector, and using 2mm of working distance with 3 kV acceleration voltage and emission current of 20 μ A. To increase the conductivity of the cross-section specimen and help with drifting, 4 nm of platinum was sputtered on them with a Quorum Q150TS sputter coater.

Atomic Force Microscopy (AFM)

AFM measurements were conducted under tapping mode in air using Bruker MultiMode 8 with RTESPA-150 probes at 0.1 Hz scanning speed. The AFM images were processed using Gwyddion data analysis software.

Photoluminescence (PL) and Time-Resolved Photoluminescence (TRPL)

Photoluminescence spectra were collected with a Renishaw InVia Raman microscope using 514 nm excitation wavelength and x50 objective lens. Time-resolved photoluminescence (TRPL) measurements were conducted utilizing a streak camera (Axis TRS, Axis Photonique Inc.). The sample was excited at 504nm (1nJ) which was produced from a Coherent OPerA Solo Optical Parametric Amplifier (OPA) pumped by a Ti:sapphire regenerative amplifier (Coherent Legend Elite Duo He⁺, 1 kHz rep. rate). The fluorescence is collected at 90^o, collimated, and subsequently focused onto the streak camera slit using a pair of off-axis parabolic mirrors. The PL is dispersed by a spectrometer (Acton SP-2358i, 150g/mm, 600nm blaze), accelerated in a bilamellar streak tube (Photonis P820) and imaged using an air-cooled CCD (Spectral Instruments 1200 series). The trace, and its corresponding background measurement, is obtained from an average of 15 exposures lasting 10 seconds each. The decay profiles were fitted with the Origin Pro software using the built-in ExpDecay2 function.

Ultraviolet-visible (UV-Vis) Spectroscopy

The absorptance spectra were measured using integrating sphere (PV Measurements, Inc.) and chopping frequency of 100 Hz. The specimens were obtained by spin casting spiro-OMeTAD precursor solution over FTO pieces (surface resistivity of 7 Ohm/Square from Sigma Aldrich).

External Quantum Efficiency (EQE)

To obtain EQE spectra, the setup from PV Measurements, Inc was utilized which was calibrated using a silicon diode. The chopping frequency was set to 100 Hz.

Determination of Space-Charge Limited Current Density (SCLC)

To prepare the samples for SCLC measurements, 30 μL of the spiro-OMeTAD precursor solution was spin casted atop FTO substrate at 3000 rpm for 30 seconds. Additionally, 80 nm of Au was thermally evaporated on top of spiro-OMeTAD films. The measurements were conducted by sweeping the voltage using Keithley 2400 source meter from 0 V to 10 V.

5.3. Results and Discussion

The ETL assembling process is provided schematically in Figure 5.1, whereby two different structures are deposited over fluorine-doped tin oxide (FTO) by varying the sequence of synthesis procedures (hydrothermal synthesis and spray pyrolysis), rendering the following ETL structures: RA (Figure 5.1 a) and AR (Figure 5.1 b). The corresponding X-ray diffraction patterns (XRD) are shown in Figure A.2-1 a. Hydrothermal synthesis is carried out at 150°C for 60 min residence time, according to a procedure first described by Liu et al. ⁽³⁵⁾ For synthesizing the anatase phase, the samples are subject to spray pyrolysis following a methodology described elsewhere⁽³⁴⁾. ETL structures are confirmed to fully cover the electrode surface, as measured through cyclic voltammetry (Figure A.2-1 b). It should be noted that in the case of the AR structure, the base anatase layer is deposited on FTO by spray pyrolysis and acts as seed during hydrothermal synthesis⁽³⁶⁾ to give rise to the vertically aligned rutile titania nanorods. For RA, on the other hand, the anatase layer coats the titania nanorods and forms a very thin conformal layer. Correspondingly, no anatase diffraction peaks were detected in the XRD pattern (Figure A.2-2 a). For more information, see Supplementary Note 1. The effective conductivity (σ) of FTO/ETL stacks was measured using two-probe measurements (Figure A.2-1 c) by scanning from -1 V to 1

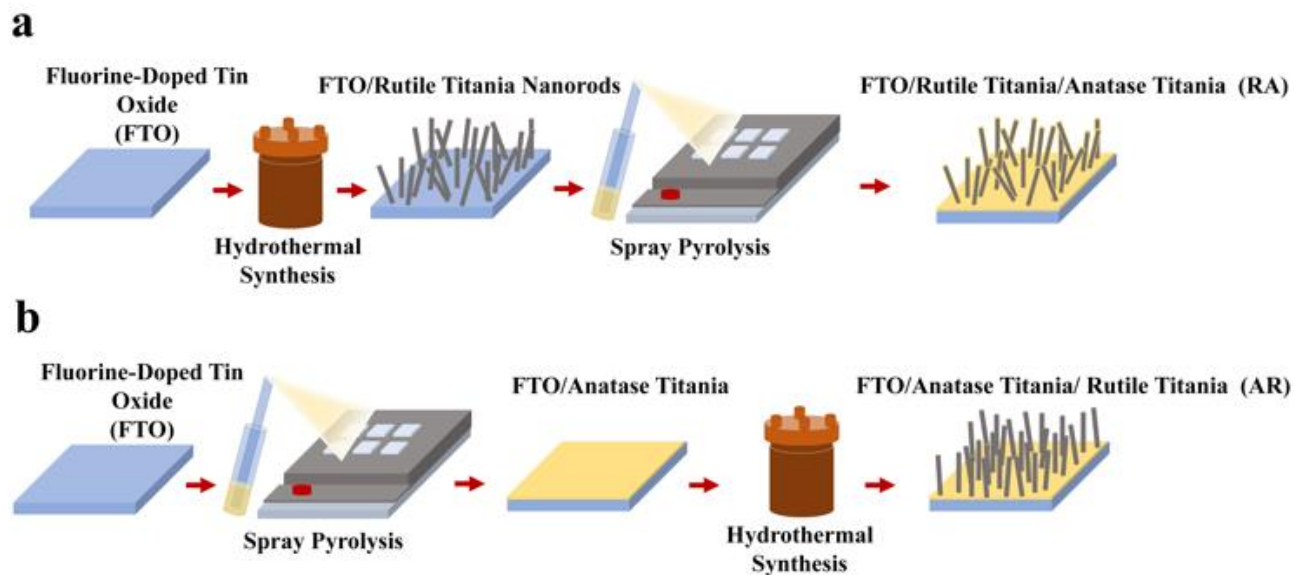


Figure 5.1: Schematics of synthesis methodology for (a) RA and (b) AR ETL structures.

V. Both stacks render a linear trend in the studied voltage range. Since FTO/RA presents a much larger slope ($=\sigma$) compared with FTO/AR (206.05 S vs. 24.63 S), the effective conductivity of FTO/RA is indeed higher than that of the AR counterpart (see Supplementary Note 2 for more information). Additionally, the UV-Vis absorption spectra of the ETLs are shown in Figure A.2-1 d. Cross-section and top view SEM images of the ETLs are shown in Figure 5.2 a and Figure 5.2 b, respectively. To compare surface roughness of the ETL structures, AFM was conducted, as shown in Figure 5.2 c. The estimated root mean square (RMS) values for RA is 86.24 nm and for AR is 69.77 nm. The lower surface roughness value obtained for AR can be attributed to the vertical growth of the nanorods (as opposed to the multi growth directions in RA), since pre-deposited anatase titania acts as a seed layer.

ETLs are then infiltrated/capped with the perovskite layer which has the nominal composition of $(\text{Cs}_5\text{Rb}_5\text{MA}_{0.15}\text{FA}_{0.75})\text{Pb}(\text{I}_{0.83}\text{Br}_{0.17})_3$ ⁽³⁷⁾. The corresponding XRD patterns show analogous peaks for perovskite layer filling ETL structures (Figure A.2- 2a). Full stack PSCs were assembled by using spiro-OMeTAD as HTL and gold (Au) as metallic contact. The cross-section SEM images of the resulting devices are presented in Figure 5.2 d, where perovskite layer and HTL show thickness values of around 500 nm and 200 nm, respectively. Additionally, the top-view SEM images of perovskite layer filling the ETL architectures (Figure 5.2 e) show enhanced crystallite

size for the AR structure compared with RA. To dope the HTL, a two-stage doping process was utilized whereby samples were left in a dark and dry room (relative humidity of 20 %) overnight prior to Au evaporation, followed by 15 hours of storage in 20% relative humidity under ambient light after the deposition of metal contact. The effectiveness of our doping strategy was evaluated using space-charge limited current (SCLC) measurement on FTO/HTL/Au stacks (Figure A.2- 2b).

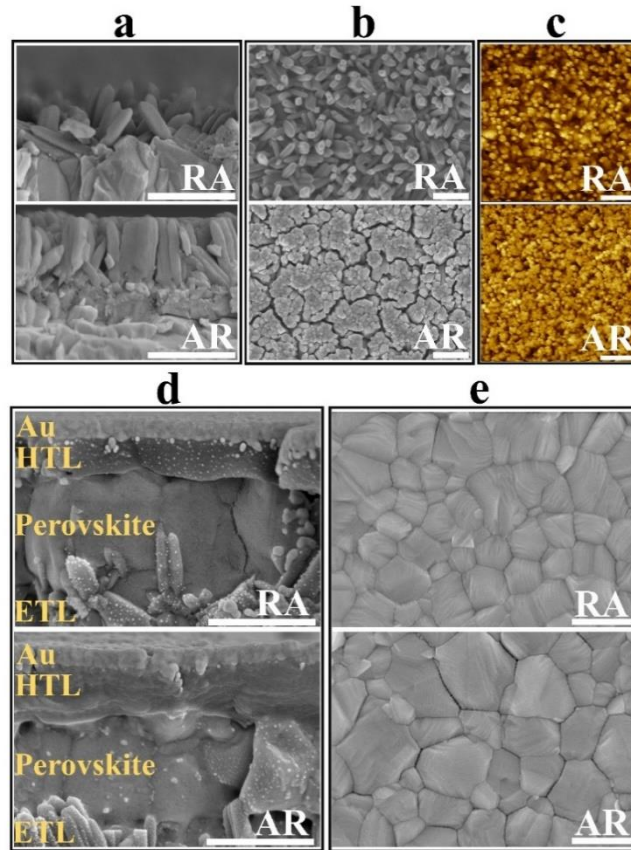


Figure 5.2: Cross section (a) and top view (b) SEM images, as well as the corresponding AFM images (c) of AR and RA structures, and (d) cross section SEM images of the full stack PSC devices as well as (e) the corresponding perovskite layer coating AR and RA structures. The scale bar on SEM and AFM images denotes 500 nm and 1 μm , respectively.

The mobility (μ) is calculated from the trap-free SCLC region using Mott-Gurney's square law according to Equation 5.1:

$$J = \frac{9\varepsilon\varepsilon_0\mu V^2}{8L^3} \quad (\text{Equation 5.1})$$

Where ϵ_0 and ϵ are the vacuum permittivity and dielectric constant, respectively. Additionally, L is the thickness while J and V are current density and voltage at the onset of SCLC regime. The mobility of doped HTL films is calculated to be $4.35 \times 10^{-4} \text{ cm}^2 \cdot \text{V}^{-1} \cdot \text{s}^{-1}$ which is in excellent agreement with the value reported for spiro-OMeTAD film tested with SCLC using the same configuration(38).

Next, to measure photovoltaic (PV) metrics, J - V measurements were performed for both forward scan (FS) and reverse scan (RS) directions, at different scan rates of 100 mV/s, and 10 mV/s. In **Error! Reference source not found.** a-d, a comparison is made for PSCs based on each of the ETL structures, in terms of short-circuit current density (J_{SC}), open-circuit voltage (V_{OC}), fill factor (FF) and power conversion efficiency (PCE). Under 100 mV/s, PSCs based on RA show higher J_{SC} compared with their AR counterpart, while delivering similar values at lower scan rates (**Error! Reference source not found.** a). It should be noted that for both ETL structures the average of J_{SC} between the two scan directions stays relatively similar. Under both scan rates, RA-based PSCs deliver higher V_{OC} than that of AR (**Error! Reference source not found.** b). Additionally, PSCs based on RA display closer V_{OC} values between the two scan directions compared with AR-based PSCs. With regards to FF (**Error! Reference source not found.** c) slightly higher values are obtained, upon utilization of AR as ETL compared with RA-based PSCs. Lastly, PSCs based on RA display higher PCE s than their AR counterpart (**Error! Reference source not found.** d). The PV metrics for each PSC type, as well as the corresponding champion device in this case, are summarized in Table A.2-1. It should be noted that since the composition, deposition and doping parameters corresponding to HTL is not subject to variation, then the observed changes can be majorly attributed to the ETL/perovskite interface.

Photoluminescence (PL) and time-resolved photoluminescence (TRPL) measurements were performed to gain insight into ETL/perovskite interface. To isolate the effect of ETL and its interface with the perovskite layer, the PL/TRPL measurements were conducted on FTO/ETL/Perovskite stacks, with the surface of the perovskite layer passivated using trioctylphosphine oxide (TOPO)(39). The PL spectra for perovskite layer coating AR and RA are presented in **Error! Reference source not found.** e, whereby RA shows slightly enhanced PL intensity compared with AR. This observation is in line with higher V_{OC} values recorded for RA

structure compared with AR (**Error! Reference source not found. b). Error! Reference source not found. f**, shows the TRPL decay profiles for the two ETL configurations. The exponential decay curves were fitted using the biexponential decay model of Equation 5.2⁽⁴⁰⁾:

$$I = I_0 + A_1 \exp\left(-\frac{t-t_0}{\tau_1}\right) + A_2 \exp\left(-\frac{t-t_0}{\tau_2}\right) \quad (\text{Equation 5.2})$$

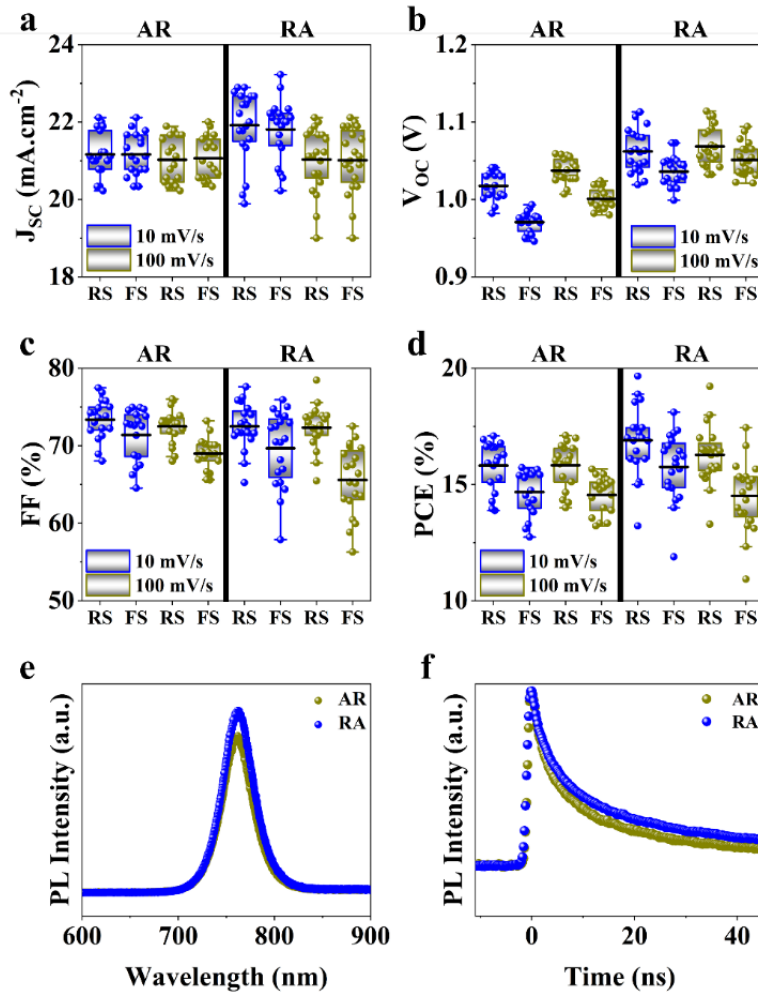


Figure 5.3: Comparison of the PV metrics in reverse scan (RS) as well as forward scan (FS) for PSCs based on AR and RA ETL structures: (a) J_{sc} , (b) V_{oc} , (c) FF , and (d) PCE , PL spectra with

emission centered around 760 nm (e) and TRPL profiles (f) with excitation wavelength set to 504nm.

Table 5.1: Extracted charge carrier lifetimes from fitting TRPL decays.

Sample	τ_1 (ns)	τ_2 (ns)	τ_{ave} (ns)
AR	4.22 ± 0.04	35.99 ± 0.30	32.65
RA	5.28 ± 0.05	48.34 ± 0.32	44.09

Additionally, the average lifetime (τ_{ave}) is calculated using $\tau_{ave} = \frac{(\tau_1)^2 + (\tau_2)^2}{\tau_1 + \tau_2}$. The shorter τ_1 and longer τ_2 lifetime components are associated with non-radiative trap-assisted recombination and bulk radiative recombination, respectively.⁽⁴⁰⁾ The corresponding fitting values of TRPL decay profiles are shown in Table 5.1. The smaller τ_1 for AR compared with RA configuration, can be attributed to better charge extraction by the ETL⁽⁴¹⁾, conforming to the trends observed for *FF* (**Error! Reference source not found.** c). The improved charge extraction of AR structure can be ascribed to larger perovskite crystallite size, a smoother interface⁽⁴²⁾ (Figure 5.2 c), as well as favorable pathway for electron movement from rutile to anatase⁽⁴³⁾. In the literature, enhanced τ_2 has been attributed to longer charge carrier lifetimes and hence longer diffusion lengths⁽⁴⁴⁾. Therefore, the higher τ_2 for RA compared with AR, is in line with their enhanced V_{OC} . Overall, RA demonstrates a higher τ_{ave} . We hypothesize that the higher conductivity of RA compared with the AR counterpart (Figure A.2-1 c), translates into a higher Fermi level, enabling this ETL to better match that of photoexcited electrons in perovskite. The correlation between absolute PL intensity and PV metrics such as *FF* and V_{OC} , is discussed thoroughly in the literature (45, 46), and is out of the scope of this work.

The external quantum efficiency (EQE) spectra for the best performing PSCs based on each ETL structure is presented in Figure A.2- 3a. A broad EQE plateau exceeding 80% is observed for both ETL structures between 400 nm and 750 nm. Additionally, the hysteresis index (HI) distribution for the PSCs utilized in this work is shown in Figure A.2- 3b. In the present study, HI is defined

based on the variation in FF in reverse and forward scan direction (denoted as FF_{RS} and FF_{FS} , respectively), according to Equation 5.3⁽⁴⁷⁾:

$$HI_{FF} = \frac{FF_{RS} - FF_{FS}}{FF_{RS}} \text{ (Equation 5.3)}$$

PSCs based on RA demonstrate mostly higher hysteresis compared with AR. Conventionally, the metric of HI has been utilized to gauge PSCs performance. However, in recent years questions have been raised with respect to the actual practicality of HI considering it is merely a transient measure. (48, 49) In this work, we focus our attention on analyzing the locus of hysteresis as appearing on the representative J - V curves under 100 and 10 mV/s (Figure 5.4). More specifically, AR shows divergence of the J - V curves starting shortly before V_{OC} and extending to voltages exceeding that (Figure 5.4 a and Figure 5.4 c). In the case of RA (Figure 5.4 b and Figure 5.4 d), under both scan rates, the hysteresis locus appears to extend up to V_{OC} and does not extend much beyond that. To better inspect the implications of hysteresis locus with regards to charge carrier dynamics, EIS measurements were performed under 1 Sun illumination and forward bias. As discussed previously, the major difference in J - V curves for PSCs based on the RA and AR is the range of voltage within which the FS and RS diverge. Therefore, we surveyed the evolution of EIS for both of ETL structures when scanned from V_{OC} to 1.4 V. The corresponding Nyquist plots for PSCs based on AR and RA are shown in Figure 5.5. In the following, we first analyze the implication of EIS patterns obtained under open-circuit conditions through presenting a band diagram in Figure 5.6 a-c, which focuses on ETL/perovskite interface.

In principle, the electronic charge carrier dynamics in the high frequency range (10^6 - 10^3 Hz) of EIS measurements, should be dominated only through electronic conductivity of the perovskite bulk as well as that of interfaces, since this frequency range is too fast for ions to follow. The band diagram in this region (Figure 5.6 a) shows a built-in field across the perovskite layer which favors funneling of the electronic charge carriers into their respective transport layers (for both AR and RA structures, denoted as ETL to represent the general case). At high frequency, such a band alignment is prevalent across the entire perovskite bulk film since the ionic effects take longer to modify the interfacial energetics. Note that our obtained Nyquist plots under V_{OC} (Figure 5.6 a and Figure 5.6 b) display two full semicircles (in high and low frequency).

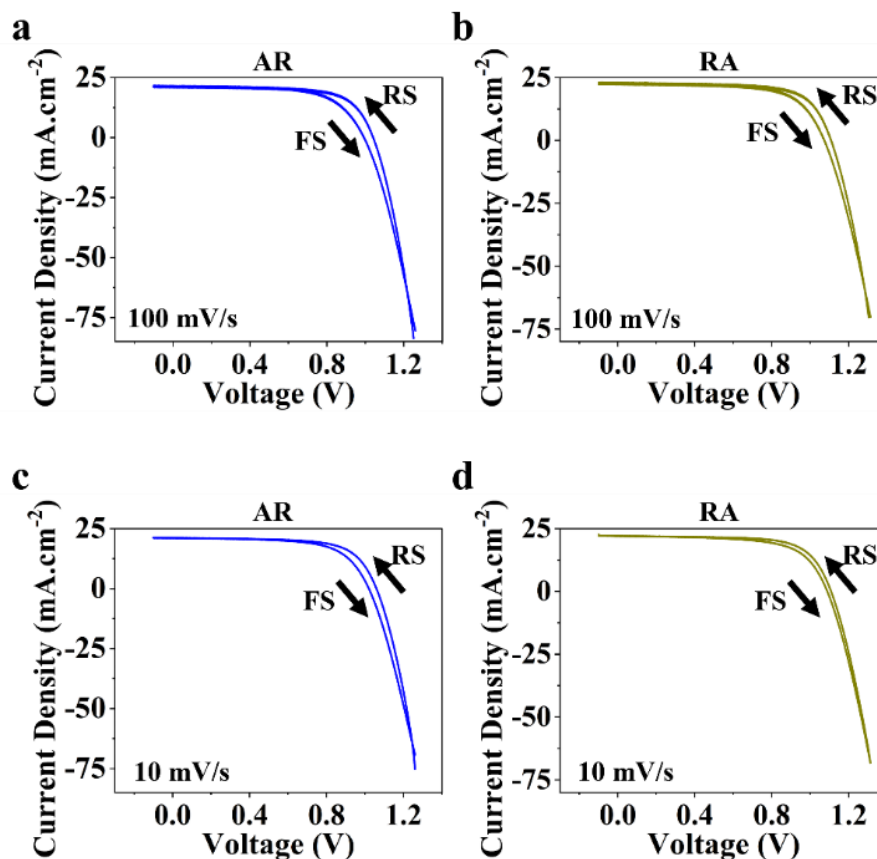


Figure 5.4: Representative current-voltage (J - V curves) measured under 100 mV/s and 10 mV/s in RS and FS for PSCs utilizing AR (a,c) and RA (b,d) as ETL structure

To fit the high frequency (HF) and low frequency (LF) arcs in the EIS patterns, we have utilized an equivalent circuit shown in Figure A.2- 4a, where the series resistance element (R_{Series}) is connected in series with two RC branches (with R and C being resistance and capacitance, respectively), corresponding to HF and LF arcs. The higher R_{Series} values of PSCs based on AR compared with that of RA (Figure A.2- 4b), can be attributed to the lower conductivity of AR structure as ETL. The observed capacitance response of the high frequency arc (C_{HF}) has been associated with geometrical capacitance (C_g) and diverse dipolar mechanisms of the bulk perovskite material⁽⁵⁰⁾. The high and low frequency arc diameter (denoted as R_{HF} and R_{LF} , respectively) values are compared for different ETL structures in Figure A.2- 4c and Figure A.2- 4d, under open-circuit condition. Notably, the observed trends for the two resistance parameters are in line with that of FF (**Error! Reference source not found.** c); PSCs based RA display the larger R_{HF} and R_{LF} , compared to their AR counterpart. In literature, both resistance parameters have

been majorly attributed to recombination resistance^(51, 52). However, it can be readily seen from **Error! Reference source not found. b** that while RA structure indeed shows higher V_{OC} than AR (in accordance with the “recombination resistance” definition), their corresponding FF values are lower (**Error! Reference source not found. c**). Based on our observations, we attribute R_{HF} and R_{LF} to charge transfer resistance across the interface, similar to the conclusion drawn by Ebadi et al.⁽²⁷⁾ Due to the higher conductivity of RA, a larger built-in field is expected to be generated across the perovskite bulk for the resulting PSCs (because of a larger difference between the Fermi level in ETL and HTL).

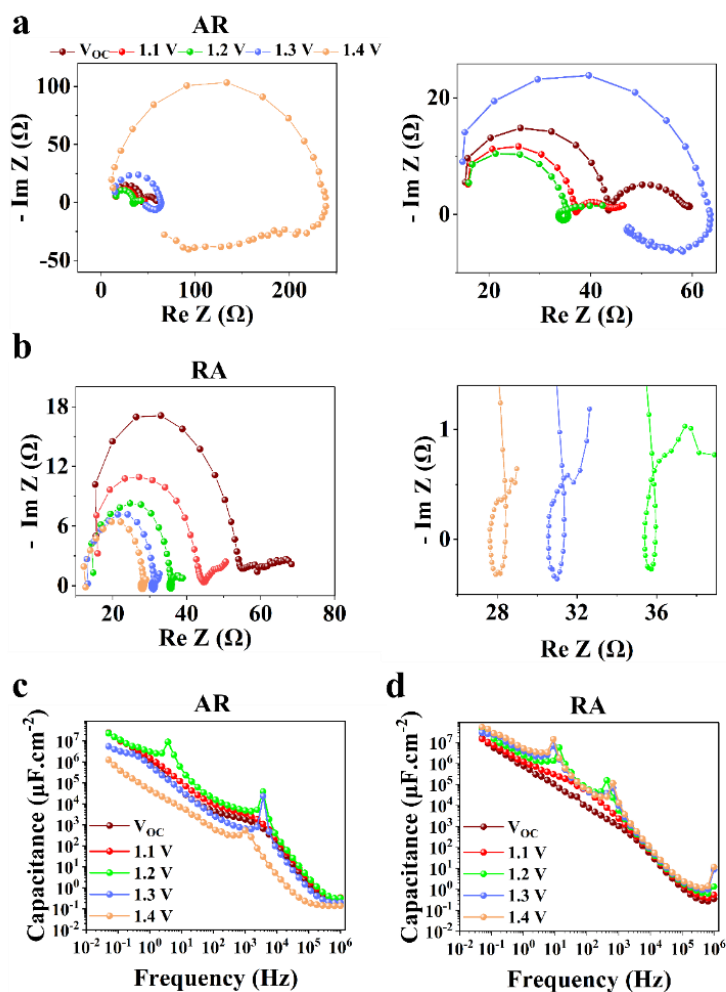


Figure 5.5: Comparison of Nyquist plots measured under 1 Sun illumination and increasing forward bias for PSCs based on (a) AR and (b) RA as ETL. The panel on the right columns show the zoomed-in view of the adjacent panel on the left, C-f plots for PSCs based on (c) AR and (d) RA.

Such an effect would accelerate ionic movement towards contacts for the purpose of screening the field, resulting in an earlier appearance of flat band conditions in RA-based devices (Figure 5.6 b) compared with the AR counterpart (Figure 5.6 c). Once the ionic motion is triggered, then the electronic current across the interface is no longer independent of ionic effects and is rather modulated through ionic migration and resulting interfacial potential barrier height as a result.⁽³⁰⁾ Hence, in Figure 5.6 b and Figure 5.6 c, the electronic current at the interface is denoted as J_e^* (modulated electronic current) on right column, while the bulk electronic current is kept as J_e on the left column. Reaching flat band conditions earlier leads to a larger portion of the built-in field to drop across the RA/perovskite interface which can enhance the rate of recombination between free holes and electrons at interfacial recombination sites as the predominant pathway⁽⁵³⁾. Hence, within the range of 0 V to V_{OC} , the charge extraction landscape in PSCs based on RA would be dominated by recombination (to a larger extent than AR), which manifests in the deteriorated FF .

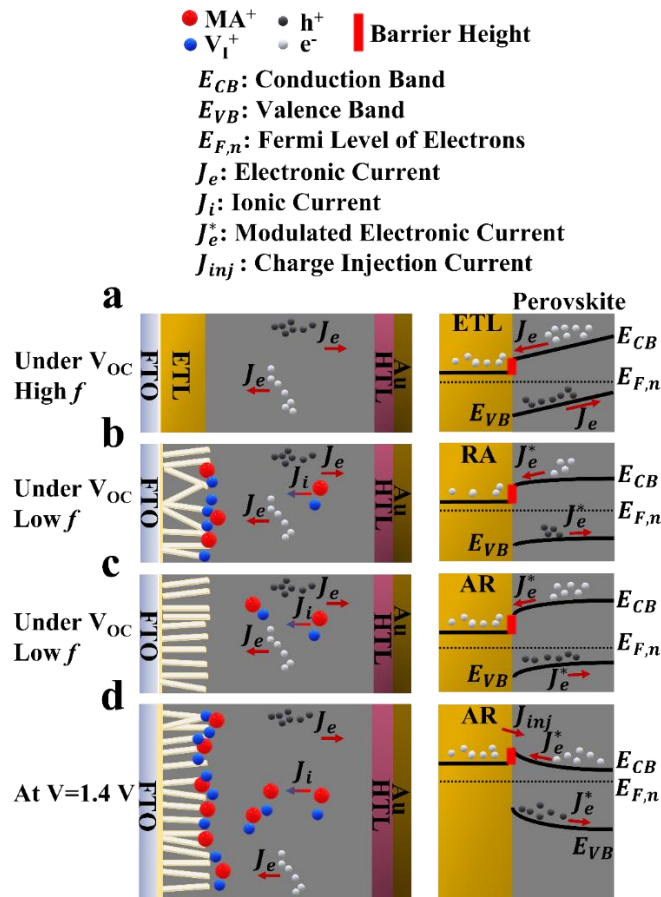


Figure 5.6: Charge carrier dynamics in PSCs under 1 Sun illumination; a) generalized scheme of ETL/perovskite interface and band energy alignment in the high frequency region of EIS under V_{OC} (before the effect of ionic charge appears), and under ionic pile up upon longer illumination times at lower frequencies for b) RA and c) AR ETL structures under V_{OC} , d) the dynamics under increased forward bias leading to the appearance of low frequency hook in EIS spectra of AR.

Next, to understand the divergence of J - V curves around V_{OC} for AR-based structures, EIS measurements are conducted under 1 Sun illumination and increasing forward biases (V_{OC} to 1.4 V). The resulting spectra (Figure 5.5 a and Figure 5.5 b) demonstrate the appearance of inductance (in the form of loop and hook) in response to bias values larger than V_{OC} . Occurrence of both such features indicates decreased differential resistance. However, since a loop appears in mid frequency while a hook takes place in lower frequency range, we are inclined to consider them as manifestation of different interfacial processes. There have been several experimental observations of inductance as well as theoretical understandings of this feature in PSCs^(26, 32, 54, 55, 56). For both structures (Figure 5.5 a and Figure 5.5 b), increasing voltage from V_{OC} to 1.2 V, leads to reduction of R_{HF} . Therefore, based on our Interpretation of R_{HF} as charge transfer resistance, its reduction as a function of increasing voltage can be taken as a sign of increased conductivity across ETL/perovskite interface. From Figure 5.5 a and Figure 5.5 b, the inductive loop appears, in the mid frequency range, earlier in the Nyquist plot for RA (1.1 V) than that of AR (1.2 V). Because of an earlier triggering of ionic migration, at a given time, a larger density of ionic charge is accumulated at RA/perovskite. Increasing forward bias further accelerates migration and accumulation⁽²⁷⁾, leading to higher accumulation of ionic charge at the interface than perovskite bulk, eventually resulting in conduction band discontinuity (local downward and upward spikes) at ETL/perovskite. As an implication of the higher interfacial doping density, the photoexcited electrons from perovskite would be scattered at a higher rate in moving towards ETL, leading to increased mobility⁽⁵⁷⁾, as has been shown previously for GaAs⁽⁵⁸⁾. This, in turn, decreases resistance which results in the appearance of inductive loop in the Nyquist plot. Conversely, and based on our hypothesis, if the photogenerated electrons experience a consistent movement in one direction (for example consistent downward from perovskite into ETL without encountering spikes), then inductive loop would not take place (e.g., Nyquist plots for both ETLs under V_{OC}). Correspondingly, at 1.1 V, ionic pile-up and hence band discontinuity at RA/perovskite interface, is already considerable enough that results in observing inductive loop. Therefore, the reason AR

shows a delayed inductive loop compared with RA, can be attributed to its slower pace of ionic movement which would require larger applied voltages to create comparable ionic accumulation as that of RA, at a given doping density. Noticeably, the two ETL structures diverge considerably for 1.3 V and 1.4 V; while RA still shows decreased R_{HF} , AR demonstrates a drastic increase of R_{HF} in addition to displaying a hook in low frequency region. The coupled increase of R_{HF} and appearance of a hook in the Nyquist plots can be attributed to band inversion at AR/Perovskite interface, as illustrated in Figure 5.6 d. Band inversion, due to dipole formation, has been suggested to take place in earlier(59) as well as more recent studies(26). To gain further insight, capacitance vs. frequency ($C-f$) representations are also provided, as shown in Figure 5.5 b and Figure 5.5 c. In $C-f$ plots, low frequency capacitance is associated with surface capacitance of accumulated charge at the interface and termed as surface capacitance (C_s).⁽²⁰⁾ The frequency at which the spikes in capacitance occur correlate with that of both mid and low frequency inductance, as observed from corresponding Nyquist plots (Figure 5.5 a and Figure 5.5 b). For RA, the C_s continuously increases from V_{OC} to 1.4 V. Conversely, for AR, C_s at 1.4 V displays the lowest value among all the studied biases (about an order of magnitude lower than the value obtained under V_{OC}).

Next, we set to understand the connotations of low frequency inductance as observed in the Nyquist plots of AR, as shown in Figure 5.5 a. If we assume that AR surface has a lower capacity for accommodating positively charged ionic species than RA, then it would follow that due to the increased concentration of accumulated ionic species (because of increased forward bias), the resulting interfacial p -doping density in perovskite would be sufficient to induce band inversion in perovskite/AR interface. Therefore, for a given ETL, there would be threshold of accumulated ionic density within the perovskite layer before it can be considered p -doped and induce inversion of the bands as a result. In this interpretation the inductive loop, which appears as a semicircle in the fourth quadrant, is indicative of electron injection from ETL into perovskite. Concomitantly, the apparent negative differential resistance associated with low frequency inductance, is in fact indicative of charge carrier movement in the opposite direction of what gives rise to HF and LF semicircles. Therefore, the appearance of low-frequency inductance in Nyquist plots of AR can be indicative of inverted bands at the perovskite interface resulting in the diminished V_{OC} in FS. Overall, our interpretation of hysteresis in PSC is in line with the results of previous works^{(27, 28,}

^{29, 30}), attributing hysteresis and low frequency dynamics to out-of-phase electronic recombination current amplified through out-of-phase ionic current.

Moreover, we attempt to establish a correlation between hysteresis locus and recombination regime. As we argued earlier, conductivity can play a key role in determining band alignment at the interface, whereby for a higher *n*-doped ETL, the perovskite can afford to have a larger ionic pile up at the interface before the perovskite/ETL can be considered a sufficiently doped *n-p* heterojunction with the bands becoming inverted on the p side (perovskite) as shown in Figure 5.6 d. PSCs based on AR, demonstrate diminished V_{OC} in FS (more pronounced compared with RA), which, we believe, stems from conductivity of ETL. Specifically, conductivity determines how fast the ionic movement across the perovskite layer is initiated. Therefore, since it was shown earlier that AR has lower electronic conductivity, meaning the free accumulated electrons in AR cannot be dissipated from the interface towards ETL bulk as fast as RA, then in the presence of inverted bands (under 1.3 and 1.4 V as shown in Figure 5.6 d), non-radiative recombination (between electrons in ETL and holes in perovskite, close to the interface) would be enhanced leading to reduced V_{OC} in FS. While under RS, the bands in AR would recover towards a more favorable alignment (Figure 5.6 c), due to the dissipation of positively charged ionic species towards HTL, therefore giving rise to larger V_{OC} values compared with FS. Additionally, based on the obtained results for PSCs based on RA, we can conclude that a mid-frequency loop has a less detrimental effect on the V_{OC} measured in FS (Table A.2-1). Hence, depending on the band alignment under which recombination takes place, the locus of hysteresis can be varied; recombination under inverted band alignment leads to widening of $J-V$ curves around V_{OC} and exceeding voltages (Figure 5.4 a and Figure 5.4 c) while recombination under flat band conditions results in $J-V$ divergence up to V_{OC} (Figure 5.4 b and Figure 5.4 d).

Lastly, the shelf stability of the non-encapsulated PSCs was tested by storing them for 200 hours under dark and 25% relative humidity. The resulting distribution of PV metrics is shown in Figure A.2- 5 and summarized in Table A.2- 2. The average *PCE* after storage is seen to slightly drop for both ETL architectures (AR and RA) under both scan rates and direction. The most prominent change after storage relates to the reduction of J_{SC} . The V_{OC} also is seen to decrease upon storage in the case of RA-based PSCs but surprisingly to increase after storage (except for 10 mV/s which renders very close values) in the case of AR architecture. The *FF* values remain relatively similar

under most scan conditions. The observed divergence in the evolution of V_{OC} under storage can be attributed to ETL/perovskite interface since the HTL-related parameters were not subject to change.

5.4. Conclusion

In summary, we have studied hysteresis locus in PSCs and origin of inductive features by analyzing the Nyquist plot patterns under 1 Sun illumination. The measurements were done on ETL architectures synthesized through a combination of hydrothermal synthesis and spray pyrolysis, rendering AR and RA structures. The high and low frequency resistance parameters, under open-circuit condition from Nyquist plots was attributed to charge transfer resistance across perovskite interfaces. Importantly, in the EIS measurements performed under increasing forward bias, inductive features (loop and hook) were observed in the Nyquist plot. We attributed the mid-frequency loop to increased scattering of photoexcited electrons due to enhanced interfacial doping density (because of increased ionic accumulation at the ETL interface compared with that of perovskite bulk). Occurrence of low frequency inductive hook, in Nyquist plots of PSCs based on both AR structures was attributed to inversion of the perovskite bands at the interface. It was postulated that the higher conductivity of a given ETL structure could enhance the pace of ionic migration from perovskite towards interfaces resulting in accumulation (of ionic species) that consequently affects the band alignment for electronic charge transfer to respective contacts due to ionic-electronic current amplification. Additionally, we pointed to the conductivity of a given ETL as a potential cause for observing low frequency inductance. We believe that the low frequency hook observed in Nyquist plots of PSCs is directly related with diminished V_{OC} values in forward scan direction.

5.5. Bridge

The work in Chapter 5 was conducted to understand the correlation between the interfacial ETL structure (nanorod scaffold) with the hysteresis locus on J - V curves which gives rise to inductive features on EIS patterns, obtained under 1 Sun illumination and voltages exceeding V_{OC} .

For this purpose, two titania nanorod scaffolds were generated through varying the sequence between spray pyrolysis and hydrothermal synthesis. When spray pyrolysis was conducted first, the resulting c -TiO₂ seed layer gave rise to vertically aligned rutile titania nanorods (on FTO) forming an interface with the perovskite layer. On the other hand, performing hydrothermal synthesis first resulted in a randomly oriented rutile titania nanorod scaffold which was then covered with anatase c -TiO₂, the latter forming the interface with the perovskite medium. The variation in magnitude and locus of hysteresis as a function of the type of scaffold supporting the perovskite layer was investigated by studying the J - V curves under 100 and 10 mV/s. The results were correlated with EIS patterns obtained under 1 Sun illumination and increasing forward bias. It was demonstrated that the conductivity of ETL as well as interfacial defect states exert a heavy influence over the voltage range under which non-radiative recombination is more predominant, dictating the locus of hysteresis. By considering multiple factors such as the rate of ionic defect equilibration at the interface and ETL conductivity, it was concluded that the divergence between J - V curves under voltages exceeding V_{OC} was indicative of band inversion on the perovskite side of the interface, which manifested as inductive hook and loop in the corresponding EIS patterns.

Thus, the research described in Chapters 4 and 5 studied in detail the evolution of hysteresis dynamics in PSCs for both planar and scaffold-based architectures from the perspective of ETL interfacing with the perovskite layer. What motivated the work presented in Chapter 6, was the drive to discover whether for a given ETL structure exhibiting inductive hysteresis, modifications made to the HTL side could alter hysteresis dynamics with respect to both locus and magnitude. In addition, it was important to understand the modifications done to the PV metrics under light soaking, scan direction and rate that give rise to the corresponding hysteresis dynamics. For this purpose, in Chapter 6, quadruple perovskite based-PSCs were assembled in n - i - p architecture with spiro-OMeTAD as HTL and the vertically aligned titania nanorod scaffold that displayed inductive hysteresis in Chapter 5. Correspondingly, the doping conditions for HTL were varied (with respect to duration, and type of storage). The resulting PSCs were studied under prolonged light soaking

as well as two different scan rates to understand the evolution of hysteresis dynamics as a function of the parameters employed to effect *p*-doping of spiro-OMeTAD.

5.6. References

1. Kojima A, Teshima K, Shirai Y, Miyasaka T. *Journal of the American Chemical Society*. 2009;131:6050-1.
2. Jeong J, Kim M, Seo J, Lu H, Ahlawat P, Mishra A, et al. *Nature*. 2021;592(7854):381-5.
3. Yoo JJ, Seo G, Chua MR, Park TG, Lu Y, Rotermund F, et al. Efficient perovskite solar cells via improved carrier management. *Nature*. 2021;590(7847):587-93.
4. Stranks SD, Eperon GE, Grancini G, Menelaou C, Alcocer MJ, Leijtens T, et al. Electron-hole diffusion lengths exceeding 1 micrometer in an organometal trihalide perovskite absorber. *Science*. 2013;342(6156):341-4.
5. De Wolf S, Holovsky J, Moon S-J, Loper P, Niesen B, Ledinsky M, et al. Organometallic halide perovskites: sharp optical absorption edge and its relation to photovoltaic performance. *The Journal of Physical Chemistry Letters*. 2014;5(6):1035-9.
6. Xing G, Mathews N, Sun S, Lim SS, Lam YM, Grätzel M, et al. Long-range balanced electron-and hole-transport lengths in organic-inorganic CH₃NH₃PbI₃. *Science*. 2013;342(6156):344-7.
7. Das B, Liu Z, Aguilera I, Rau U, Kirchartz TJMA. Defect tolerant device geometries for lead-halide perovskites. *Materials Advances* 2021;2(11):3655-70.
8. Snaith HJ, Abate A, Ball JM, Eperon GE, Leijtens T, Noel NK, et al. Anomalous Hysteresis in Perovskite Solar Cells. *J Phys Chem Lett*. 2014;5(9):1511-5.
9. Tress W, Marinova N, Moehl T, Zakeeruddin SM, Nazeeruddin MK, Grätzel M. Understanding the rate-dependent J–V hysteresis, slow time component, and aging in CH₃NH₃PbI₃ perovskite solar cells: the role of a compensated electric field. *Energy & Environmental Science*. 2015;8(3):995-1004.
10. Meloni S, Moehl T, Tress W, Franckevičius M, Saliba M, Lee YH, et al. Ionic polarization-induced current–voltage hysteresis in CH₃NH₃PbX₃ perovskite solar cells. *Nature Communications*. 2016;7(1):10334.

11. Abdi-Jalebi M, Andaji-Garmaroudi Z, Cacovich S, Stavrakas C, Philippe B, Richter JM, et al. Maximizing and stabilizing luminescence from halide perovskites with potassium passivation. *Nature*. 2018;555(7697):497-501.
12. Saliba M, Matsui T, Domanski K, Seo J-Y, Ummadisingu A, Zakeeruddin Shaik M, et al. Incorporation of rubidium cations into perovskite solar cells improves photovoltaic performance. *Science*. 2016;354(6309):206-9.
13. van Reenen S, Kemerink M, Snaith HJ. Modeling Anomalous Hysteresis in Perovskite Solar Cells. *The Journal of Physical Chemistry Letters*. 2015;6(19):3808-14.
14. Calado P, Telford AM, Bryant D, Li X, Nelson J, O'Regan BC, et al. Evidence for ion migration in hybrid perovskite solar cells with minimal hysteresis. *Nature Communications*. 2016;7(1):13831.
15. Ye J, Byranvand MM, Martínez CO, Hoye RLZ, Saliba M, Polavarapu L. Defect Passivation in Lead-Halide Perovskite Nanocrystals and Thin Films: Toward Efficient LEDs and Solar Cells. *Angewandte Chemie International Edition*. 2021;60(40):21636-60.
16. Kang D-H, Park N-G. On the Current–Voltage Hysteresis in Perovskite Solar Cells: Dependence on Perovskite Composition and Methods to Remove Hysteresis. *Advanced Materials*. 2019;31(34):1805214.
17. Liu P, Wang W, Liu S, Yang H, Shao Z. Fundamental understanding of photocurrent hysteresis in perovskite solar cells. *Advanced Energy Materials*. 2019;9(13):1803017.
18. von Hauff E, Klotz DJJoMCC. Impedance spectroscopy for perovskite solar cells: characterisation, analysis, and diagnosis. *Journal of Materials Chemistry C*. 2022.
19. Guerrero A, Garcia-Belmonte G, Mora-Sero I, Bisquert J, Kang YS, Jacobsson TJ, et al. Properties of contact and bulk impedances in hybrid lead halide perovskite solar cells including inductive loop elements. *The Journal of Physical Chemistry C*. 2016;120(15):8023-32.
20. Zarazua I, Bisquert J, Garcia-Belmonte G. Light-induced space-charge accumulation zone as photovoltaic mechanism in perovskite solar cells. *The journal of physical chemistry letters*. 2016;7(3):525-8.
21. Bisquert J, Guerrero A. Chemical Inductor. *Journal of the American Chemical Society*. 2022;144(13):5996-6009.

22. Gonzales C, Guerrero A, Bisquert J. Transition from Capacitive to Inductive Hysteresis: A Neuron-Style Model to Correlate I–V Curves to Impedances of Metal Halide Perovskites. *The Journal of Physical Chemistry C*. 2022.
23. Hernández-Balaguera E, Bisquert J. Negative Transient Spikes in Halide Perovskites. *ACS Energy Letters*. 2022;7:2602-10.
24. Muñoz-Díaz L, Rosa AJ, Bou A, Sánchez RS, Romero B, John RA, et al. Inductive and Capacitive Hysteresis of Halide Perovskite Solar Cells and Memristors Under Illumination. *Frontiers in Energy Research*. 2022:911.
25. Fabregat-Santiago F, Kulbak M, Zohar A, Vallés-Pelarda M, Hodes G, Cahen D, et al. Deleterious Effect of Negative Capacitance on the Performance of Halide Perovskite Solar Cells. *ACS Energy Letters*. 2017;2(9):2007-13.
26. Ghahremanirad E, Bou A, Olyaei S, Bisquert J. Inductive Loop in the Impedance Response of Perovskite Solar Cells Explained by Surface Polarization Model. *J Phys Chem Lett*. 2017;8(7):1402-6.
27. Ebadi F, Taghavinia N, Mohammadpour R, Hagfeldt A, Tress W. Origin of apparent light-enhanced and negative capacitance in perovskite solar cells. *Nat Commun*. 2019;10(1):1574.
28. Pockett A, Eperon GE, Sakai N, Snaith HJ, Peter LM, Cameron PJ. Microseconds, milliseconds and seconds: deconvoluting the dynamic behaviour of planar perovskite solar cells. *Phys Chem Chem Phys*. 2017;19(8):5959-70.
29. Jacobs DA, Shen H, Pfeffer F, Peng J, White TP, Beck FJ, et al. The two faces of capacitance: new interpretations for electrical impedance measurements of perovskite solar cells and their relation to hysteresis. *Journal of Applied Physics*. 2018;124(22):225702.
30. Moia D, Gelmetti I, Calado P, Fisher W, Stringer M, Game O, et al. Ionic-to-electronic current amplification in hybrid perovskite solar cells: ionically gated transistor-interface circuit model explains hysteresis and impedance of mixed conducting devices. *Energy & Environmental Science*. 2019;12(4):1296-308.
31. Feng Y, Bian J, Wang M, Wang S, Zhang C, Dong Q, et al. Interfacial negative capacitance in planar perovskite solar cells: An interpretation based on band theory. *Materials Research Bulletin*. 2018;107:74-9.
32. Anaya M, Zhang W, Hames BC, Li Y, Fabregat-Santiago F, Calvo ME, et al. Electron injection and scaffold effects in perovskite solar cells. *J Mater Chem C Mater*. 2017;5(3):634-44.

33. Liu B, Aydil ES. Growth of oriented single-crystalline rutile TiO₂ nanorods on transparent conducting substrates for dye-sensitized solar cells. *Journal of the American Chemical Society*. 2009;131(11):3985-90.
34. Saliba M, Correa-Baena J-P, Wolff CM, Stolterfoht M, Phung N, Albrecht S, et al. How to Make over 20% Efficient Perovskite Solar Cells in Regular (n-i-p) and Inverted (p-i-n) Architectures. *Chemistry of Materials*. 2018;30(13):4193-201.
35. Liu B, Aydil ES. Growth of Oriented Single-Crystalline Rutile TiO₂ Nanorods on Transparent Conducting Substrates for Dye-Sensitized Solar Cells. *Journal of the American Chemical Society*. 2009;131(11):3985-90.
36. Kalb J, Folger A, Zimmermann E, Gerigk M, Trepka B, Scheu C, et al. Controlling the density of hydrothermally grown rutile TiO₂ nanorods on anatase TiO₂ films. *Surfaces and Interfaces*. 2019;15:141-7.
37. Saliba M, Matsui T, Domanski K, Seo J-Y, Ummadisingu A, Zakeeruddin SM, et al. Incorporation of rubidium cations into perovskite solar cells improves photovoltaic performance. *Science*. 2016;354(6309):206-9.
38. Kim SG, Le TH, de Monfreid T, Goubard F, Bui TT, Park NG. Capturing mobile lithium ions in a molecular hole transporter enhances the thermal stability of perovskite solar cells. *Advanced Materials*. 2021;33(12):2007431.
39. Braly IL, deQuilettes DW, Pazos-Outón LM, Burke S, Ziffer ME, Ginger DS, et al. Hybrid perovskite films approaching the radiative limit with over 90% photoluminescence quantum efficiency. *Nature Photonics*. 2018;12(6):355-61.
40. Bi D, Yi C, Luo J, Décoppet J-D, Zhang F, Zakeeruddin Shaik M, et al. Polymer-templated nucleation and crystal growth of perovskite films for solar cells with efficiency greater than 21%. *Nature Energy*. 2016;1(10):16142.
41. Chen J, Seo JY, Park NG. Simultaneous improvement of photovoltaic performance and stability by in situ formation of 2D perovskite at (FAPbI₃)_{0.88} (CsPbBr₃)_{0.12}/CuSCN interface. *Advanced Energy Materials*. 2018;8(12):1702714.
42. Kakavelakis G, Maksudov T, Konios D, Paradisanos I, Kioseoglou G, Stratakis E, et al. Efficient and Highly Air Stable Planar Inverted Perovskite Solar Cells with Reduced Graphene Oxide Doped PCBM Electron Transporting Layer. *Advanced Energy Materials*. 2017;7(7):1602120.

43. Scanlon DO, Dunnill CW, Buckeridge J, Shevlin SA, Logsdail AJ, Woodley SM, et al. Band alignment of rutile and anatase TiO₂. *Nature materials*. 2013;12(9):798-801.
44. Kim S-G, Chen J, Seo J-Y, Kang D-H, Park N-G. Rear-Surface Passivation by Melaminium Iodide Additive for Stable and Hysteresis-less Perovskite Solar Cells. *ACS Applied Materials & Interfaces*. 2018;10(30):25372-83.
45. Stolterfoht M, Caprioglio P, Wolff CM, Márquez JA, Nordmann J, Zhang S, et al. The impact of energy alignment and interfacial recombination on the internal and external open-circuit voltage of perovskite solar cells. *Energy & environmental science*. 2019;12(9):2778-88.
46. Kirchartz T, Márquez JA, Stolterfoht M, Unold T. Photoluminescence-based characterization of halide perovskites for photovoltaics. *Advanced energy materials*. 2020;10(26):1904134.
47. Unger EL, Czudek A, Kim H-S, Tress W. Current-voltage analysis: Lessons learned from hysteresis. *Characterization Techniques for Perovskite Solar Cell Materials*: Elsevier; 2020. p. 81-108.
48. Habisreutinger SN, Noel NK, Snaith HJ. Hysteresis index: A figure without merit for quantifying hysteresis in perovskite solar cells. *ACS Energy Letters*. 2018;3(10):2472-6.
49. Le Corre VM, Diekmann J, Peña-Camargo F, Thiesbrummel J, Tokmoldin N, Gutierrez-Partida E, et al. Quantification of efficiency losses due to mobile ions in perovskite solar cells via fast hysteresis measurements. *Solar RRL*. 2022;6(4):2100772.
50. Pockett A, Eperon GE, Peltola T, Snaith HJ, Walker A, Peter LM, et al. Characterization of planar lead halide perovskite solar cells by impedance spectroscopy, open-circuit photovoltage decay, and intensity-modulated photovoltage/photocurrent spectroscopy. *The Journal of Physical Chemistry C*. 2015;119(7):3456-65.
51. Zarazua I, Han G, Boix PP, Mhaisalkar S, Fabregat-Santiago F, Mora-Sero I, et al. Surface Recombination and Collection Efficiency in Perovskite Solar Cells from Impedance Analysis. *J Phys Chem Lett*. 2016;7(24):5105-13.
52. Correa-Baena J-P, Turren-Cruz S-H, Tress W, Hagfeldt A, Aranda C, Shooshtari L, et al. Changes from bulk to surface recombination mechanisms between pristine and cycled perovskite solar cells. *ACS Energy Letters*. 2017;2(3):681-8.

53. Stolterfoht M, Wolff CM, Márquez JA, Zhang S, Hages CJ, Rothhardt D, et al. Visualization and suppression of interfacial recombination for high-efficiency large-area pin perovskite solar cells. *Nature Energy*. 2018;3(10):847-54.
54. Ulf M, Zhu T, Goubard F, Pauporté T, JomCA. Molecular versus polymeric hole transporting materials for perovskite solar cell application. *Journal of Materials Chemistry A*. 2018;6(27):13350-8.
55. Alvarez AO, Arcas R, Aranda CA, Bethencourt L, Mas-Marza E, Saliba M, et al. Negative Capacitance and Inverted Hysteresis: Matching Features in Perovskite Solar Cells. *J Phys Chem Lett*. 2020;11(19):8417-23.
56. Fabregat-Santiago F, Kulbak M, Zohar A, Vallés-Pelarda M, Hodes G, Cahen D, et al. Deleterious effect of negative capacitance on the performance of halide perovskite solar cells. *ACS Energy Letters*. 2017;2(9):2007-13.
57. Neamen DA. *Semiconductor physics and devices: basic principles*: McGraw-hill; 2003.
58. Cardona MJPR. Electron effective masses of InAs and GaAs as a function of temperature and doping. *Physical Review*. 1961;121(3):752.
59. Guerrero A, You J, Aranda C, Kang YS, Garcia-Belmonte G, Zhou H, et al. Interfacial degradation of planar lead halide perovskite solar cells. *ACS nano*. 2016;10(1):218-24.

Chapter 6: Controlling Photo-Induced Doping of Spiro-OMeTAD in Perovskite Solar Cells

This chapter addresses the 3rd objective of the thesis, which is to evaluate how the doping process employed for increasing *p*-type conductivity of spiro-OMeTAD, as HTL, impacts the corresponding PSC behavior under light soaking at different scan rates. This chapter is replication of a manuscript submitted for peer reviewed publication, the citation of which is the following:

- Yekani, R., Wang, H., Ghamari, P., Bessette, S., Gauvin, R., and Demopoulos, G.P., 2023. “The Importance of Controlling Photo-Induced Doping of Spiro-OMeTAD as HTL in Perovskite Solar Cells”. *Submitted to J. Phys. Chem. C*.

Abstract

The doping strategy employed for enhancing hole conductivity of spiro-OMeTAD as hole transport layer (HTL) in perovskite solar cells (PSCs) is rarely specified in the literature. However, as revealed in this work, the specifics of the doping process with respect to the type of storage and its duration can have important consequences on the evolution of hysteresis dynamics in PSCs. The variability in photovoltaic metrics and hysteresis loci in current-voltage (*J-V*) curves are studied before and after light soaking, as well as different scan rates, to determine operational differences as a result of a given doping processes. X-ray photoelectron spectroscopy (XPS) shows formation of deleterious compounds such as Li₂O and LiF, which are used to propose operational band alignments. Finally, with the aid of electrochemical impedance spectroscopy (EIS), signatures of HTL bulk and interfacial conductivity modulation are identified. The propagation of a third semicircle in the low frequency Nyquist plot is ascribed to performance loss caused by unfavorable interfacial electrochemical reactions, while the shrinkage of the high frequency arc is linked with performance gain, due to increased HTL bulk conductivity. This work underlines the important correlation between spiro-OMeTAD doping strategy with loss and gain in PSC performance under operational conditions.

Keywords

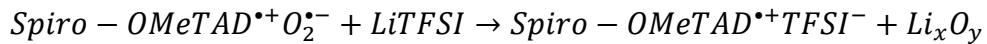
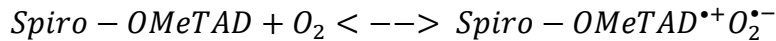
perovskite solar cells, hole transport layer, spiro-OMeTAD, doping, light soaking, hysteresis

6.1. Introduction

During the past decade, perovskite solar cells (PSCs) have witnessed unparalleled research interest enabling them to close in on the competition with other leading photovoltaic (PV) technologies(1). Such progress is owed not only to intense research efforts but also to numerous advantageous properties such as tunable band gap(2) , defect tolerance(3), long charge carrier diffusion length(4, 5) , high absorption coefficient(6) , and ambipolar transport(7), to name a few . The absorber layer in PSCs possesses ABX_3 perovskite crystal structure where A is a monovalent cation (organic/inorganic), B is a divalent cation (inorganic), and X is a halide. Most commonly, PSCs are assembled in the *n-i-p* architecture, whereby the perovskite layer (assumed to be an intrinsic semiconductor-*i*)(8, 9) is sandwiched between an electron transport layer (ETL) and hole transport layer (HTL), which are *n*-doped and *p*-doped semiconductors, respectively. Despite the beneficial properties of halide perovskite semiconductors, PSCs face serious shortcomings such as hysteresis that hamper their large-scale development. Hysteresis is the term applied to the mismatch between current-voltage (*J-V*) curves when the solar cell is scanned in reverse scan (RS) and forward scan (FS) directions.(10) Among the many hypotheses put forward to explain this phenomenon,(10, 11, 12, 13, 14) ionic migration across the perovskite layer in combination with interfacial defects has garnered the most support(15, 16, 17, 18, 19). This synergetic effect is believed to modulate the interfacial charge extraction efficiency depending on the ionic arrangement under the given scan direction,(20) which then leads to divergence in *J-V* curves. Hysteresis has been addressed from different fronts in the literature. Through elemental substitution, composition of the perovskite layer has been engineered (from fully inorganic such as $CsPbI_3$ to hybrid organic inorganic such as $FAPbI_3$)(2) to optimize for not only lower hysteresis but also higher PV metrics. An example of this compositional tuning is the quadruple cation composition of $(Cs_5Rb_5MA_{0.15}FA_{0.75})Pb(I_{0.83}Br_{0.17})_3$ which was first introduced by Saliba et al.(21) and has been widely used in the literature due to its superior performance. In addition to compositional engineering, there have also been extensive efforts on the perovskite layer with respect to defect passivation(22) and tuning of dimensionality(23).

Another side by which hysteresis can be addressed and ultimately controlled is to consider the role of the transport layers. With reference specifically to HTL, its most vital role in PSCs is transporting the photogenerated holes from the perovskite layer to the metal contact. In doing so,

the HTL must fulfill certain requirements. Apart from thermal and chemical stability, the appropriate band alignment of the highest unoccupied molecular level (HOMO) of HTL with the valence band (VB) of the perovskite layer and its low bulk series resistance are of paramount importance as they ultimately translate into efficient hole extraction and high conductivity.(24) The most common HTL choice in PSCs is the small molecule 2,2',7,7'-tetrakis[N,N-di(4-methoxyphenyl)amino]-9,9'-spirobifluorene (spiro-OMeTAD), which is prevalently utilized among the solid-state dye-sensitized solar cells (ss-DSSCs) community and remains to be a popular choice for PSCs. (24) However, spiro-OMeTAD is a very poor conductor (nearly an insulator) in its pristine form. Therefore, *p*-doping is required to increase its conductivity(25, 26) in order to function as an effective HTL in PSCs. Over the years, a common combination of additives to *p*-dope spiro-OMeTAD has been a mix of lithium bis(trifluoromethanesulfonyl)imide (LiTFSI) and 4-tertbutyl pyridine (4-TBP). LiTFSI is believed to play a critical role in enabling the stabilizing of *p*-doping of spiro-OMeTAD in the presence of oxygen.(27) On the other hand, 4-TBP has been shown to significantly improve the solubility of LiTFSI in the spiro-OMeTAD precursor solution and therefore improve the composition and morphology of HTL film.(28) Overall, oxidation of spiro-OMeTAD, in the presence of LiTFSI and O₂, is suggested to take place via(27):



where Li_xO_y denotes lithium oxide species (Li_2O_2 or Li_2O). The *p*-type doping results from $\text{Spiro} - \text{OMeTAD}^{\bullet+}$ radical cation being weakly bound to TFSI^- because of the highly delocalized charge of the latter anion. It is the Li_xO_y complexes that stabilize *p*-doping via the consumption of O₂^[17]. Despite *p*-doping, the conductivity and mobility values reported for Spiro-OMeTAD remain far below those of the perovskite layer(29), making the corresponding interface a bottleneck for efficient charge carrier transport in *n-i-p* architectures.(24) While there has been considerable progress with respect to hysteresis and overall performance regarding thickness, surface passivation and composition, of the transport layers (22, 29, 30), there has rarely been any investigation into how the procedure employed in the doping of spiro-OMeTAD, when employing the conventional LiTFSI and 4-TBP combination impacts the hysteresis dynamics in PSCs. Moreover, the details of doping procedure for spiro-OMeTAD are hardly discussed in the

literature. Therefore, in this study, we have undertaken to address these knowledge gaps by varying the doping processes in terms of storage conditions (dark/ambient light), sequence thereof and duration. Additionally, PSCs have been known to display either a gain or loss in performance with light soaking, and even presenting a mix of both behaviors under prolonged illumination.(31, 32, 33) These observations suggest complex interfacial dynamics that warrant a better understanding. Hence, in this study, the $J-V$ curves and the corresponding PV metrics are studied before and after light soaking, under 1 Sun, in order to understand the variation in hysteresis dynamics as well as the influence of doping condition on the PSC tolerance towards 1 Sun illumination during operation. In understanding the corresponding trends, X-ray photoelectron spectroscopy (XPS) measurements are conducted on the HTL films before and after light soaking to assess the possible changes in the bonding environment of spiro-OMeTAD as well as interfacial reactions. Additionally, through employing electrochemical impedance spectroscopy (EIS), signatures of bulk and interfacial conductivity are identified. Overall, this work demonstrates that depending on the employed doping strategy for spiro-OMeTAD, the corresponding PSC performance can evolve differently under light soaking and reduced scan rate. As such, this study sheds new light on hysteresis dynamics from the perspective of HTL conductivity modulation on ionic migration and arrangement in the perovskite layer, which for a given ETL effectively dictates the band alignment under operating conditions.

6.2. Experimental

Synthesis of the Electron Transport Layer (ETL)

For all ETL-related synthesis purposes, the FTO glass substrates (2 cm by 2 cm in dimension and pre-patterned) were purchased from Solaronix (with surface resistivity of 7 Ohm/ Square and thickness of 2.2 mm-part number: TCO22-7/LI). The substrates were ultrasonically cleaned sequentially in a 2% Hellmanex solution in DI water, 2-propanol, and acetone, for 15 min in each solvent. Eventually, the substrates were treated for 15 min with UV-ozone.

To synthesize the AR structure as ETL, the procedures described in our previous work [28] were followed. This involved deposition initially of a seed anatase phase using spray pyrolysis. Cleaned FTO substrates were placed on a hotplate and heated gradually to 450°C. Then a precursor solution containing 9 mL ethanol, 0.6 mL Ti(IV) diisopropoxide bis acetylacetonate (Sigma Aldrich) and

0.4 mL acetylacetone (Sigma Aldrich) was sprayed over the samples using O₂ as carrier gas. When the spraying process was finished, the substrates were left on the hotplate for another 10 min before turning it off and letting the samples cool down to room temperature. Growth of the rutile nanorod film was carried out using hydrothermal synthesis(34) over the anatase seed layer. The reaction solution was made with 0.02 L DI water and 0.02 L concentrated hydrochloric acid (36.5%-38% by weight from Fisher Scientific). The mixture was stirred at room temperature in a sealed beaker for 5 minutes before the addition of 0.001 L Ti (IV) butoxide (Reagent grade 97%, Sigma Aldrich). After stirring for another 40 min, the precursor solution was added to a Teflon-lined stainless-steel autoclave (0.125 L volume, Parr Instrument Co.), where two substrates (FTO covered with anatase layer) were placed at an angle with their conductive sides facing the wall. The autoclave was then sealed and placed in the oven with a heating ramp of 10°C/hour to reach the final temperature of 150°C where they were held for 60 minutes before cooling down inside the oven, which took approximately 3 hours. After the synthesis was done, the substrates were taken out and washed thoroughly with DI water. Afterwards, they underwent an annealing step at a heating ramp of 4°C/min to 550°C with a holding time of 30 minutes before cooling down.

Synthesis of Perovskite Layer and Hole Transport Layer (HTL)

The perovskite layer is synthesized and deposited according to the procedure described by Saliba et al.(35). In short, the perovskite precursor was prepared by mixing FAI (1M), PbI₂ (1.1 M), MABr (0.2M) and PbBr₂ (0.2M) in DMF/DMSO (4:1 v/v). CsI (1.5M in DMSO) and RbI (1.5M in DMF:DMSO 4:1 v/v) were added to the perovskite precursor to obtain quadruple cation composition of (Cs₅Rb₅MA_{0.15}FA_{0.75})Pb(I_{0.83}Br_{0.17})₃. The perovskite layer is deposited through the anti-solvent method by using 150 µL of the final perovskite precursor and using a two-step spinning program; 1000 rpm for 10 seconds followed by 6000 rpm for 20 seconds. Five seconds before the end of spinning, 200 µL of chlorobenzene was poured on the spinning substrate. The substrates were then annealed at 100 °C for 45 minutes. Except for PbI₂ and PbBr₂ which were sourced from TCI America, all other chemicals were purchased from Sigma Aldrich.

Spiro-OMeTAD was chosen as the HTL material. To make the precursor, 72.3 mg of spiro-OMeTAD, 28.3 µL 4-TBP and 17.5 µL LiTFSI (520 mg/mL in acetonitrile) are added to 1 mL chlorobenzene. Deposition of HTL was conducted by spin casting 30 µL the precursor solution at

3000 rpm. Finally, 80 nm of gold was thermally evaporated (NexDep, Angstrom Engineering) in 2E-6 mbar vacuum at the rate of 1 Å/s.

Current Density- Voltage (J - V) and Electrochemical Impedance Spectroscopy (EIS) Measurements

The J - V and EIS measurements were conducted with a class A solar simulator (Sol1A 94021A, Newport) which was calibrated with a silicon KG5 reference cell (Abet Technologies). To obtain the PV metrics, J - V curves were recorded under 1 Sun at 100 and 10 mV/s from -0.2 V (vs. reference electrode) to 0.2 V above V_{OC} . All EIS measurements were conducted under 1 Sun illumination and various forward bias values with a Biologic potentiostat (SP-300) and controlled by EC lab software from 1 MHz to 50 mHz, with a perturbation potential of 20 mV over 40 data points. There was a total of four devices on each sample, with an active area of 0.09 cm².

Cyclic Voltammetry Measurements

Cyclic voltammetry measurements were carried out in a one-compartment cell using Biologic potentiostat (SP-300) and controlled by EC lab software. Ag/AgCl (sat. KCl) and Au were used as reference and counter electrode, respectively. The electrolyte was 0.5 mM K₄Fe(CN)₆ (Sigma Aldrich) + 0.5mM K₃Fe(CN)₆ (Sigma Aldrich) in aqueous 0.5 M KCl (Sigma Aldrich). The voltage was scanned from -1 V to 1V at a rate of 25 mV/s. The effective electrode area was 1 cm².

X-Ray Diffraction (XRD)

XRD patterns were acquired using a Bruker D8 Advance. Copper source (K α line) was used with a voltage of 40 kV and a current of 40 mA. Scan parameters were 2Theta from 6° to 70° with an increment of 0.02°, and integration time of 1s. The experiment was performed in the grazing incidence diffraction mode with a low incident angle of 3°. Both the primary and secondary axial soller was 2.5° while the secondary twin optic was set to soller 0.2°. The LynxEye detector was set to 0D mode.

Ultraviolet-visible (UV-Vis) Measurements

The absorbance spectra were measured using integrating sphere (PV Measurements, Inc.) and chopping frequency of 100 Hz. The specimens were obtained by spin casting spiro-OMeTAD precursor solution over FTO pieces (surface resistivity of 7 Ohm/Square from Sigma Aldrich).

X-Ray Photoelectron Spectroscopy (XPS) Measurements

XPS spectra were collected with Nexsa G2 (Thermo Scientific), using Al K α radiation (1486.6 eV) and an X-ray spot size of 200 μm . The flood gun was turned on for the measurements to prevent charging effects. Samples were sealed into the sample holder inside a nitrogen-filled glovebox to prevent oxidation of spiro-OMeTAD. For all elemental spectra, 20 scans with a dwell time of 50 ms and pass energy of 50 eV were used. Charge correction was carried out using adventitious C 1s set to a binding energy of 284.8 eV, while charge neutralization was carried out using an electron flood gun.

Scanning Electron Microscopy (SEM)

Cross sectional and top view SEM images were obtained with a SU8230 Hitachi cold-field emission scanning electron microscope (CFE-SEM), utilizing the in-lens upper secondary electron detector, and using 2mm of working distance with 3 kV acceleration voltage and emission current of 20 μA . To increase the conductivity of the cross-section specimen and help with drifting, 4 nm of platinum was sputtered on them with a Quorum Q150TS sputter coater. The cross-sectional samples were prepared by mechanically cleaving the specimen with diamond scribe.

Determination of Space-Charge Limited Current Density (SCLC)

To prepare the samples for SCLC measurements, 30 μL of the spiro-OMeTAD precursor solution was spin cast on the spinning FTO substrate at 3000 rpm for 30 seconds. Additionally, 80 nm of Au was thermally evaporated on top of spiro-OMeTAD films. The measurements were conducted by sweeping the voltage from 0 V to 10 V at 10 mV/s scan rate, using a Keithley 2400 semiconductor characterization system.

6.3. Results and Discussion

In this work, we have employed the *n-i-p* device architecture of FTO/ETL/perovskite/HTL/metal contact, as schematically shown in Figure 6.1 a. The ETL is deposited through hydrothermal growth of rutile titania nanorods over anatase seed layer (deposited via spray pyrolysis) which will be nominally denoted as AR (for FTO-**A**natase-**R**utile).(36) Both the perovskite layer, with the composition of $(\text{Cs}_5\text{Rb}_5\text{MA}_{0.15}\text{FA}_{0.75})\text{Pb}(\text{I}_{0.83}\text{Br}_{0.17})_3$, and HTL (spiro-OMeTAD) are deposited using spin coating. All studied HTL films contain LiTFSI and 4-TBP as additives. At times

throughout this manuscript, a comparison has been made to pristine HTL, which in this work by “pristine” we refer to Spiro-OMeTAD impregnated with LiTFSI and 4-tbp and of which its properties (e.g. conductivity) were measured outside the glovebox under 20% relative humidity (RH) as with the other devices. Finally, gold (Au) – the metal contact - is deposited by thermal evaporation again outside the glovebox, during which time the samples were exposed to air. Details of all procedures are provided in the *Experimental Methods* section.

Cross-sectional and top-view scanning electron microscopy (SEM) images of the AR structure, as ETL, are shown in Figure 6.1 b and Figure 6.1 c, respectively. Full coverage of FTO electrode by ETL is confirmed through cyclic voltammetry measurements (Figure 6.1 d). Additionally, in Figure 6.1 e, the X-ray diffraction (XRD) pattern of FTO/AR is displayed, with the peak along [001] direction indicating the vertical alignment of rutile titania nanorods with respect to FTO. The cross-sectional view of the ETL/Perovskite/HTL/Au stack is shown in Figure 6.1 f, with the top-view image of the corresponding perovskite layer, covering the AR film structure, displayed in Figure 6.1 g. Moreover, Figure 6.1 h demonstrates the UV-Vis absorption results, conducted over FTO/AR stack. Finally, the XRD pattern of FTO/AR/Perovskite is displayed in Figure 6.1 i.

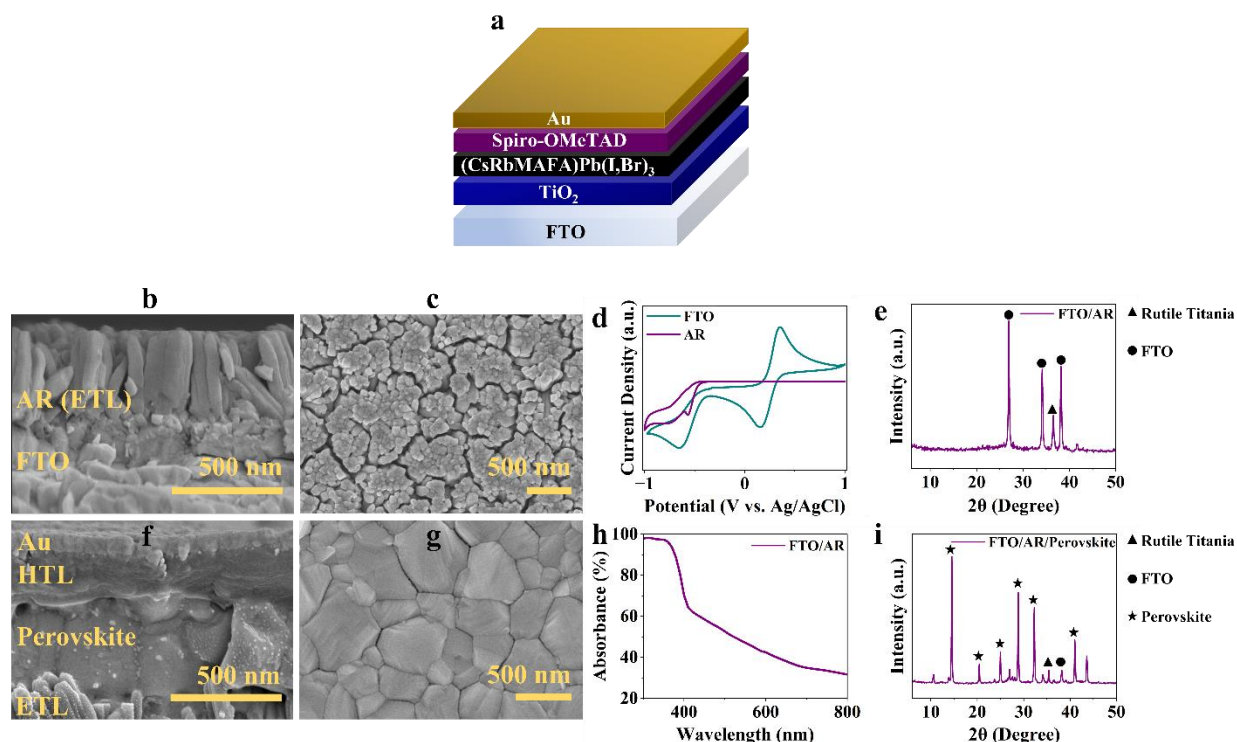


Figure 6.1: (a) The *n-i-p* configuration used in constructing the PSCs in this work; SEM images of (b) cross-section and (c) top-view of the TiO₂ (AR) structure serving as ETL; (d) cyclic voltammogram and (e) XRD pattern of FTO/ETL; (f) cross-sectional image of the FTO/ ETL/ Perovskite/ HTL/Au and (g) top-view image of the perovskite layer covering the AR ETL; (h) UV-Vis spectrum of FTO/ETL and (i) the XRD pattern of FTO/ETL/Perovskite.

To demonstrate the extent to which spiro-OMeTAD doping process can affect the resulting PSC properties, a total of four conditions were employed by varying the ambient light exposure/storage regime, sequence and duration (Table 6.1). Both the light and dark doping stages were conducted after the HTL film deposition under 20% RH. It should be noted that the doped HTL solution was prepared with spin casting inside the glovebox and never exposed to air. As the first step in characterizing the HTLs, ultraviolet-visible (UV-Vis) absorption spectra were obtained over FTO/HTL stacks (Figure 6.2 a). The oxidation of spiro-OMeTAD can be deduced from the enhancement of absorption bands around 460 nm and 520 nm (compared with that of pristine spiro-OMeTAD), which correspond to generation of spiro-OMeTAD radical cation.(37, 38, 39)

Table 6.1: Different doping conditions tested.

	Before Au Deposition	After Au Deposition
LL	Ambient Light (12 Hours)	Ambient Light (12 Hours)
LD	Ambient Light (12 Hours)	Dark (12 Hours)
DL	Dark (12 Hours)	Ambient Light (12 Hours)
DL(15)	Dark (12 Hours)	Ambient Light (15 Hours)

Overall, the differently doped HTL layers present similar absorption spectra, with negligible difference in their corresponding peak intensities. Additionally, the results of space-charge limited current density (SCLC) measurements performed on FTO/HTL/Au stacks are shown in Figure 6.2 b. From these, the hole mobility (μ) is calculated from the trap-free SCLC region using Mott-Gurney's square law according to Equation 6.1(40) :

$$J = \frac{9\varepsilon\varepsilon_0\mu V^2}{8L^3} \text{ (Equation 6.1)}$$

Where ε_0 and ε are the vacuum permittivity and dielectric constant of the organic medium, respectively. Also in Equation 6.1, L is the HTL thickness while J and V are current density and voltage at the onset of SCLC regime. From Figure 6.1 f, thickness of spiro-OMeTAD is estimated to be ~ 200 nm. The mobility of various HTL films synthesized in this work is calculated to be relatively similar in the range of $10^{-5} \text{ cm}^2 \text{ V}^{-1} \text{ s}^{-1}$, which is in good agreement with the values reported elsewhere(41). Moreover, conductivity measurements were performed under dark and under 1 Sun illumination, following a procedure described elsewhere(42). The corresponding results are summarized in Table A.3-1 and can be seen in Figure 6.2 c (conductivity under dark) and Figure 6.2 d (conductivity under 1 Sun illumination). All doped HTL films (as well as pristine spiro-OMeTAD) show enhanced conductivity under illumination, which is in accordance with previous reports. (43) Overall, DL(15) and LL samples demonstrate the highest and lowest conductivity, under a given testing condition, respectively. Pristine spiro-OMeTAD, under dark, shows an order of magnitude lower conductivity than the other tested processes, which is enhanced under illumination to about half the value obtained for LL. We emphasize that the conductivity value obtained for pristine spiro-OMeTAD in our work is an order of magnitude higher than the reported value in the literature(27) and this is so because in present work spiro-OMeTAD contained LiTFSI and its measurement was made under 20% relative humidity (RH) as with the other devices.

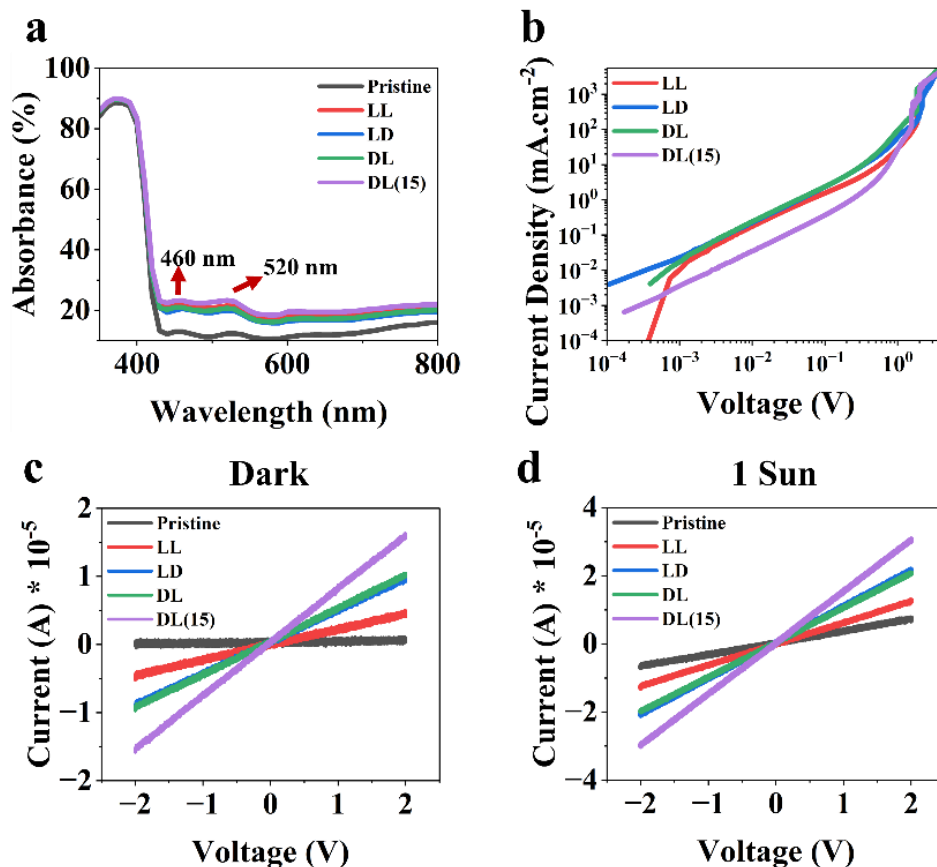


Figure 6.2: Optoelectronic characterization of the spiro-OMeTAD films: (a) UV-Vis absorbance, (b) space-charge limited current density (SCLC), conductivity of glass/HTL films (c) under dark and (d) under 1 Sun illumination.

To obtain PV metrics, each PSC sample (comprising four devices) was exposed to increasing pre-illumination from 0 to 60 minutes, with a 20-minute interval, before recording the J - V curves. The distribution of PV metrics is displayed in Figure 6.3 a-d. As seen in Figure 6.3 a, DL(15) delivers the highest J_{SC} , while other conditions show similar average values. Except for LD, the average of J_{SC} , for a given scan direction, decreases with decreasing scan rate. In terms of V_{OC} (Figure 6.3 b), the highest and lowest values are shown by LD and LL, respectively. Additionally, all doped samples show a higher V_{OC} distribution upon decreasing the scan rate. PSCs based on LL also show the lowest FF values while DL(15) displays the highest averages (Figure 6.3 c). Although the low V_{OC} and FF values for LL-based PSCs are in accordance with their conductivity (Figure 6.2 c and Figure 6.2 d), no conclusive correlation is obtained between conductivity measurements and V_{OC} or FF trends for other doping conditions. Meanwhile, in the case of PCE (Figure 6.3 d),

DL(15) shows the highest average while LL displays particularly low values. Except for LD, the *PCE* in the FS direction experiences a drop vis-a-vis RS under either scanning speed. The J_{SC} trends are also registered in the collected external quantum efficiency (EQE) spectra, as shown in Figure 6.3 e. Here again, DL(15) is displaying the highest plateau of over 80%, correlating with the highest J_{SC} values measured for PSCs based on this doping condition. On the other hand, LL demonstrates the lowest values in the range of 600-800 nm.

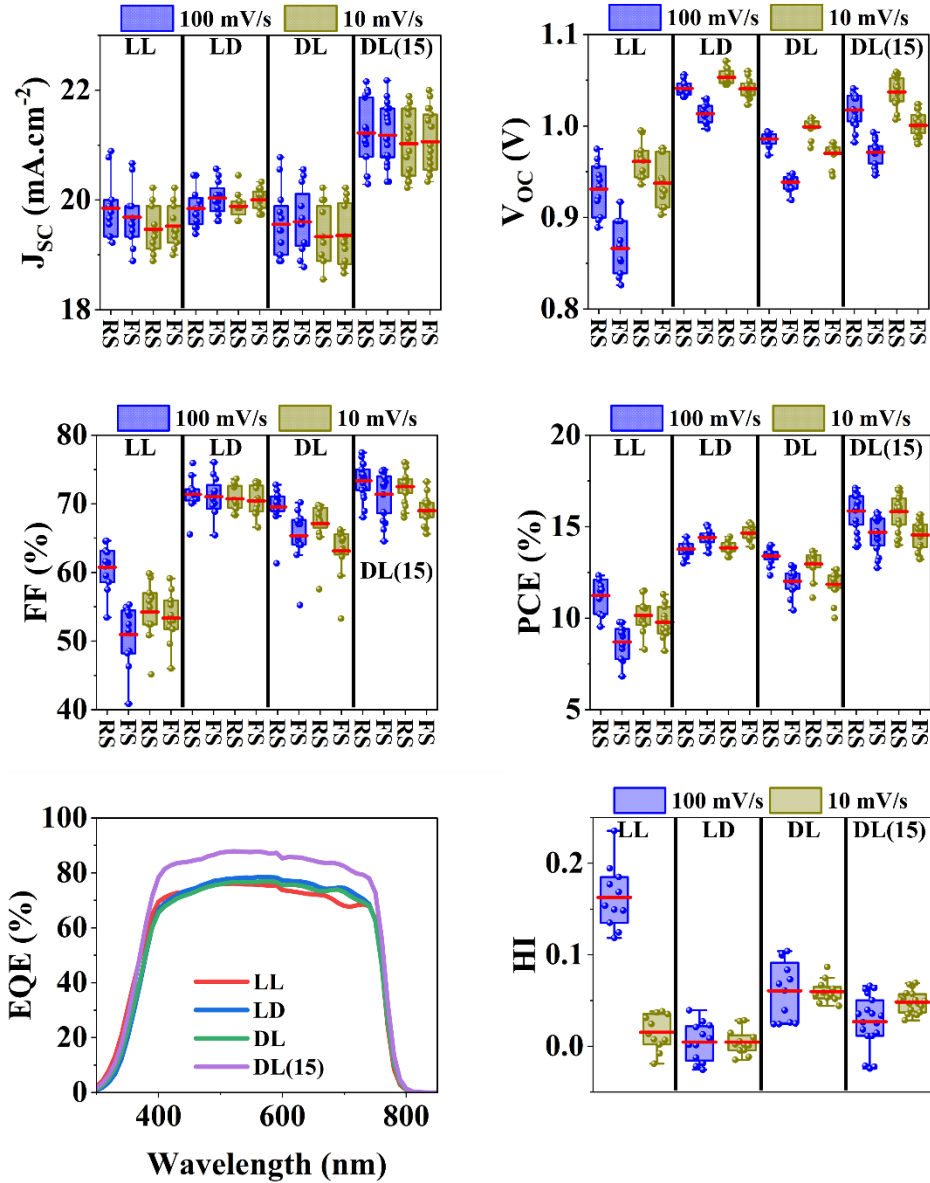


Figure 6.3: Distribution of PV metrics of PSCs assembled with HTL doped under the different conditions listed in Table 6.1: (a) J_{SC} , (b) V_{OC} , (c) FF , and (d) PCE obtained from $J-V$ scans under 100 mV/s and 10 mV/s speeds, (e) EQE spectra, and (f) hysteresis index (HI).

In this work, the hysteresis index (HI) is defined based on the variation of FF in reverse (FF_{RS}) and forward scan (FF_{FS}) according to: $HI = \frac{FF_{RS} - FF_{FS}}{FF_{RS}}$. (15) Figure 6.3 f displays the distribution of HI for all the doping conditions considered in this work. Under 100 mV/s, LL and LD show the highest and lowest HI values, respectively. Except for DL(15), all doping processes display reduced HI with decreased scan rate. Additionally, under 10 mV/s, DL and DL(15) show enhanced

HI compared with the other two doping processes. . There has been some controversy over the use of HI to gauge the performance of PSCs, as this metric is calculated based on parameters that are interdependent and therefore is not a reflection of what truly affects PSC hysteresis behavior. In particular, in our previous work(36), we demonstrated how despite similar HI, the phenomenon of hysteresis can take place at a different locus in $J-V$ curves, which is indicative of the band alignment for a given scan direction, under which the rate of non-radiative recombination is enhanced. Consequently, we find the analysis of the hysteresis locus and changes in PV metrics between RS and FS, instead of HI, to be a better approach in understanding charge carrier phenomena in PSCs. For this purpose, the representative $J-V$ curves (Figure 6.4) and PV metrics (Table A.3- 2 Table A.3- 5) for all the doping conditions were studied before and after 60 min of light soaking, at 100 and 10 mV/s scan speeds.

We will be developing our arguments on the basis that under FS, the photogenerated field drives the ionic species towards the “wrong” contact (cation vacancies towards ETL and anion vacancies towards HTL(31)), which opposes the built-in field and generates an unfavorable band alignment, resulting in field-dependent charge extraction landscape.(42) Conversely, under RS, the arrangement of the ionic species at the interfaces results in a favorable band alignment, assisting with charge extraction and consequently higher FF as well as V_{OC} . This situation results in the rise of the so-called normal hysteresis.(43, 44, 45) Overall, due to ionic migration in the perovskite layer and the subsequent accumulation, narrow Debye layers are formed at the interfaces.(46) In understanding the limitations imposed on FF we consider a combination of low bulk conductivity of HTL with interfacial phenomena such as slow equilibration of ionic species in Debye layers at the HTL interface, inverted bands on the perovskite side and adverse electrochemical reactions at the interface. The equilibration of ionic species within interfacial Debye layers has been previously discussed by Domanski et al.(31), and in this work we will approach this concept from a different angle to explain the hysteresis variation between differently doped spiro-OMeTAD as HTL within the same PSC architecture. We believe that in cases where the loss mechanism under FS is due to unfavorable band alignment (for example inverted bands or flat bands), then under RS, FF would be limited by the slow recovery of bands towards a favorable alignment. The pace of this recovery process would then depend on how fast ions can rearrange and equilibrate in the interfacial Debye layers under reverse bias which ultimately depends on the conductivity of the HTL. More specifically, a higher HTL film conductivity would mean a larger built-in field across the

perovskite layer, resulting in an earlier triggering of ionic motion towards the interfaces. This would eventually cause an earlier equilibration of ionic species at the HTL/perovskite interface which results in an earlier restoration of the band alignment to the favorable direction. On the other hand, it should be noted that the ionic species are believed to shield the coulombic charge enabling long charge carrier diffusion lengths in perovskites. Concomitantly, we suggest that slower equilibration of ions, in addition to not being able to restore the desired band alignment under RS, can delay the benign shielding effect and therefore cause a higher rate of non-radiative recombination. In addition to lower HTL conductivity, irreversible electrochemical reactions at the interface and bulk HTL could limit the band recovery under RS. And finally for the perovskite/HTL interface to be considered an n-p doped heterojunction (in which the bands would be inverted on the perovskite side), the density of the accumulated n-type ionic species in the perovskite layer must surpass a threshold that is determined by the p-doping density on the HTL side. As such, this situation is more feasible for an HTL with a lower p-doping density. Moreover, under inverted band alignment hole injection from HTL back in the perovskite layer becomes a possibility (indicated as J_{inj} in Figure 6.5c), which can lead to non-radiative recombination.

For LL doping condition (Figure 6.4 a and Table A.3-2), HI is reduced with decreasing scan rate, both before and after light soaking. However, this is far from a positive outcome, as it is majorly due to decreased FF_{RS} , while FF_{FS} is retained. We propose that for LL-based PSCs, the lower scanning speed is on par with the pace of ionic migration (as dictated by the HTL conductivity). As a result, the extent to which the bands can recover under RS towards a more favorable state for charge extraction will be lowered with reduced scanning speed, which lowers FF_{RS} as a result. After light soaking, FF is reduced considerably for both scan rates and directions. The overall changes lead to enhanced and reduced HI under 100 mV/s and 10 mV/s, respectively. Considering these observations, we suggest that prolonged illumination can result in an adverse electrochemical reaction at the interface, diminishing interfacial conductivity. Such a reaction could lead to reduction of HTL(47, 48), i.e. decrease of cation radical concentration or otherwise decrease of its p-doping density, resulting in an inverted band structure(49) (Figure 6.5c). Ultimately, this reduction in HTL conductivity could lead to unfavorable charge extraction landscape such as inverted band alignment or earlier appearance of flat band conditions exacerbating non-radiative recombination.

In LD-based PSCs (Figure 6.4 b and Table A.3-3) HI is reduced with decreased scan rate, for before and after light soaking, because of increased FF_{FS} . Therefore, in this case, the reduction of HI is indeed a positive outcome. Additionally, the fact that the FF_{FS} does not change much compared with that of RS, indicates that charge extraction efficiency is not considerably modulated between the two scan directions. Thus, we suggest that the band alignment under RS shows an upward bend in the perovskite towards HTL (Figure 6.5 a), enabling efficient hole extraction whose current is denoted as J_h in Figure 6.5. However, under FS, and due to the tendency of ionic species to screen the built-in field(20), a flat band condition would be attained (Figure 6.5 b). In particular we suggest that, for LD-based PSCs, the photo-induced electrochemical reactions discussed for the LL counterpart are less enhanced.

For DL (Figure 6.4 c and Table A.3-4), for both before and after light soaking, decreasing the scan rate leads to a larger reduction of FF_{RS} than FF_{FS} , leading to reduction of HI. In DL(15) (Figure 6.4 d and Table A.3-5), the FF under both directions are retained reasonably well with reducing the scan rate for both before and after light soaking. However, the FF_{FS} and FF_{RS} are severely diminished under light soaking, much more considerably compared with DL. This observation could be ascribed to adverse electrochemical reactions that diminish FF_{FS} and limit the extent of band recovery and therefore attainable FF_{RS} , similar to the proposed mechanism for LL. However, in the case of DL and DL(15)-based PSCs, owing to their higher HTL conductivity compared to that of LL, the proposed electrochemical reactions are potentially less likely to reduce the HTL p -doping to the extent that band inversion can be induced.

Through performing conductivity measurements, it was confirmed that the bulk conductivity of HTL does not decrease after 60 minutes of light soaking, therefore hinting at potential interfacial phenomena that give rise to the observed dynamics with prolonged light soaking as a function of the employed doping strategy (Figure A.3-1 and Table A.3- 6).

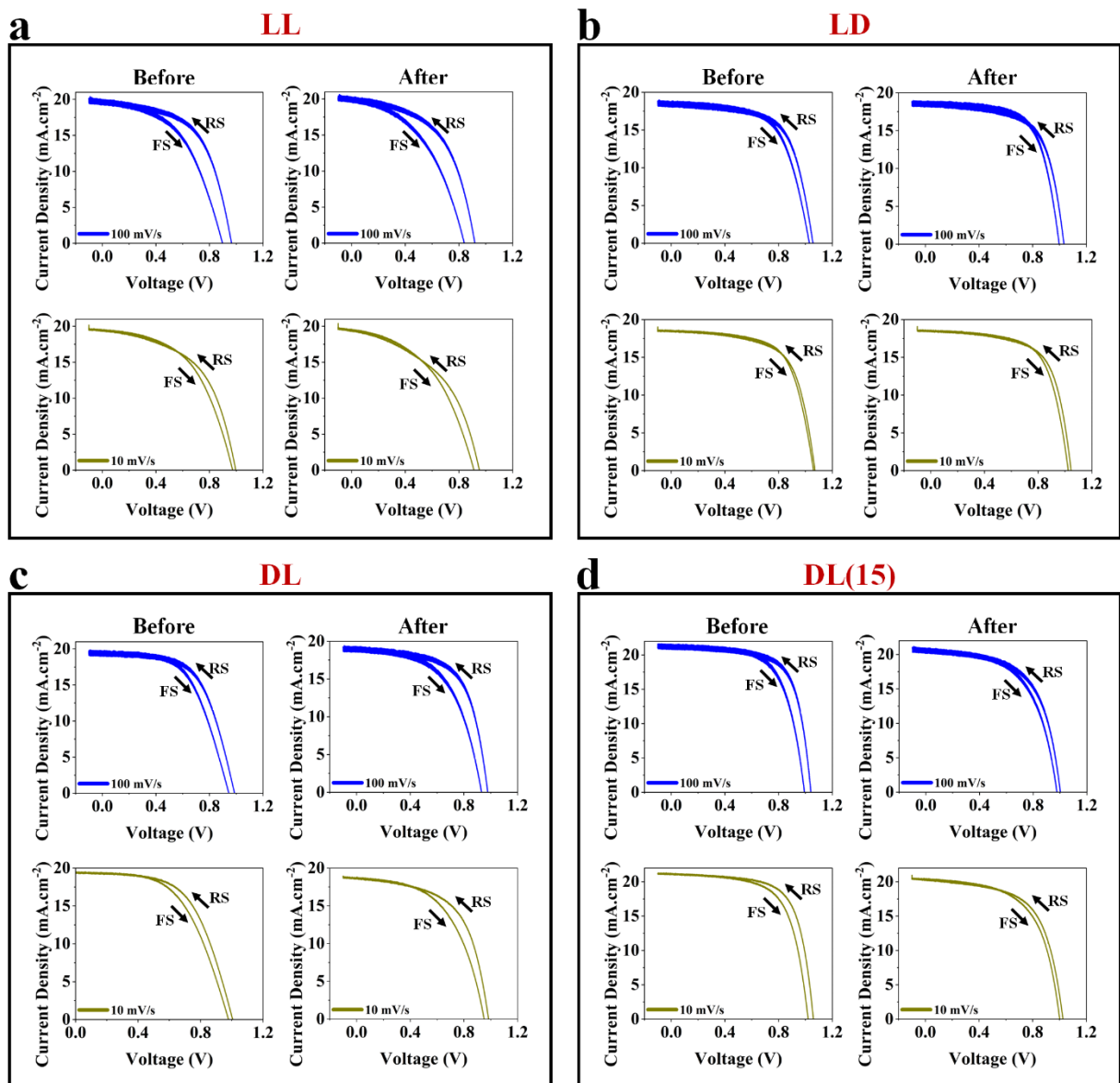


Figure 6.4- Representative J - V curves for PSCs using spiro-OMeTAD as HTL, doped according to the conditions listed in Table 6.1. The curves are displayed at either 100 or 10 mV/s scan

speed, as well before and after 60 minutes of light soaking, denoted as Before and After, respectively.

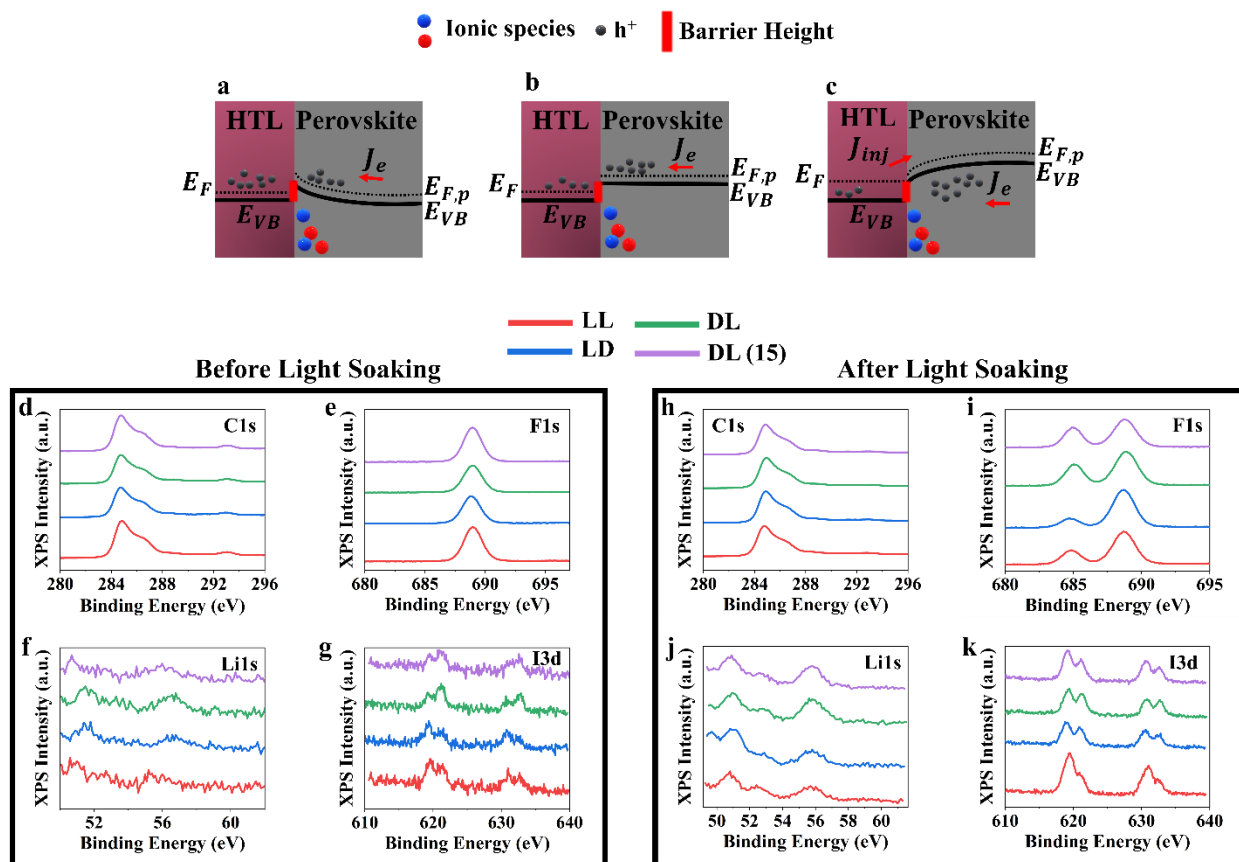


Figure 6.5: Proposed band diagrams at Perovskite/HTL interface: (a) favorable upward band bending which aids with the movement of photogenerated holes into HTL, (b) flat band conditions as a result of ionic accumulation at the interface and screening the built-in field, and (c) unfavorable inverted band alignment which inhibits efficient extraction of photogenerated holes by HTL. E_V , E_F and $E_{F,p}$ denote valance band, Fermi level in spiro-OMeTAD, and quasi hole Fermi level in the perovskite layer, respectively, in addition to comparison of XPS spectra obtained over the FTO/ETL/perovskite/HTL stacks before (d-g) and after (h-k) 60 minutes of light soaking under 1 Sun illumination.

To probe the potential reactions responsible for performance degradation of some doping conditions under prolonged illumination such as LL, XPS measurements were conducted on the HTL, before and after 60 minutes of light soaking. The corresponding results are shown in Figure 6.5 d-k. The fittings of XPS spectra are displayed in Figure A.3- 2 and Figure A.3- 3, and

summarized in Table A.3- 7 and Table A.3- 8. For all doping processes, the C1s spectra (Figure A.3- 2a and Figure A.3- 3a) consists of multiple components which correspond to carbon atoms in different functional groups. The adventitious carbon peak at 284.8 eV is correlated with C-C/C=C, while the peaks at the binding energy around 285 eV are ascribed to C-H group.(44, 45) Moreover, the peak centered around 286 eV is attributed to C-N bonding.(46) The small peak centered around 288 eV has been previously attributed to C=O bonding, which is interpreted as oxygen and moisture interaction with the perovskite surface.(30) .Finally, the small peaks centered around 291 and 293 eV can be attributed to CF₂ and CF₃ bonding, corresponding to LiTFSI salt at the surface.(44, 47) After light soaking, the peak centered around 285 eV is no longer present for any of the doping processes (Figure A.3- 3a). Moreover, the C1s spectra for DL(15) both before and after light soaking are fitted with an additional peak (compared with other doping conditions), which is centered around 289 eV (Table A.3- 7 and Table A.3- 8). This peak has been attributed to C=O bonding. Additionally, in the F1s spectra (Figure 6.5 e and Figure A.3- 2b) obtained prior to light soaking, only one peak at around 688 eV is detected which is correlated with -CF₃ bonding in TFSI group.(47, 48) However, after light soaking, a new peak around 685 eV (Figure 6.5 i and Figure A.3- 3b) appears which corresponds to F⁻(48), which the least pronounced in the case of LD. Previous studies had suggested that the F⁻ is an intrinsic part of spiro-OMeTAD spectrum(48), while others(49) assumed it appeared due to X-ray-induced decomposition of LiTFSI. However, in the present study, the presence of this peak is a direct consequence of LiTFSI decomposition due to light soaking, which is in accordance with enhanced Li1s signal after illumination. Therefore, based on the peak centered around 685 eV, LiF is expected to form in accordance with previous reports.(47) Correspondingly, the peak centered around 56 eV in Li1s spectra after light soaking (Figure A.3- 3c) can be ascribed to LiF, in agreement with previous reports.(50) Moreover, two additional peaks in Li1s are observed at around 50 eV and 52 eV. The latter has been attributed to Li₂O(57) which is absent in the case of LD only, and we ascribe the former to LiI formation. It should be noted that prior to light soaking, Li1s signal is rather insignificant (Figure 6.5 f) which becomes detectable after pre-illumination (Figure 6.5 j), despite with low intensity, which is indicative of lithium segregation/migration towards the HTL surface. This redistribution was previously reported for spiro-OMeTAD upon long air exposure.(49) Our results indicate that this behavior can also be observed upon light soaking.

The I3d signal prior to light soaking (Figure A.3-2c), despite being relatively low in intensity displays doublets, due to spin-orbit coupling, showing splitting which becomes more visible and better separated after light soaking (Figure A.3-3d). Within each state, the peak at lower binding energy is attributed to iodide ions (I^-), while the higher binding energy component is ascribed to iodine (I_2). Taking these observations into considerations, it can be concluded that I^- diffusion from the perovskite layer into spiro-OMeTAD readily takes place after doping (showing the highest intensity for LL), and is further exacerbated through light soaking (in this case showing the lowest intensity for LD), as seen in Figure 6.5 g and Figure 6.5 k, respectively. It has been previously shown, that I^- diffusion into spiro-OMeTAD decreases its electrical conductivity because iodide ions behave as reducing agents.(51, 52, 53) Additionally, this can lead to deepening the HOMO level of spiro-OMeTAD(53) potentially lowering it below that perovskite VB, and therefore leading to unfavorable band alignment under operation. Although I^- diffusion was previously reported for elevated temperatures,(51, 52, 53) our results indicate that it can also take place under prolonged light soaking. Overall, the XPS results point towards the absence of Li_2O as well as the lowest LiF and I^- peak intensity for LD, which might be able to explain the better performance of PSCs based on this doping condition.

Although the XPS results point to a potential gradient of concentration (and bonding environment) for different elements across HTL thickness, they cannot render conclusive information regarding the perovskite/HTL interface. As such, the trends obtained so far as a result of varying the doping of HTL and the corresponding discussion are cross examined with the aid of EIS patterns in order to more conclusively explain their origin. For this purpose, EIS measurements were conducted before and after light soaking, under open-circuit condition as shown in Figure 6.6.

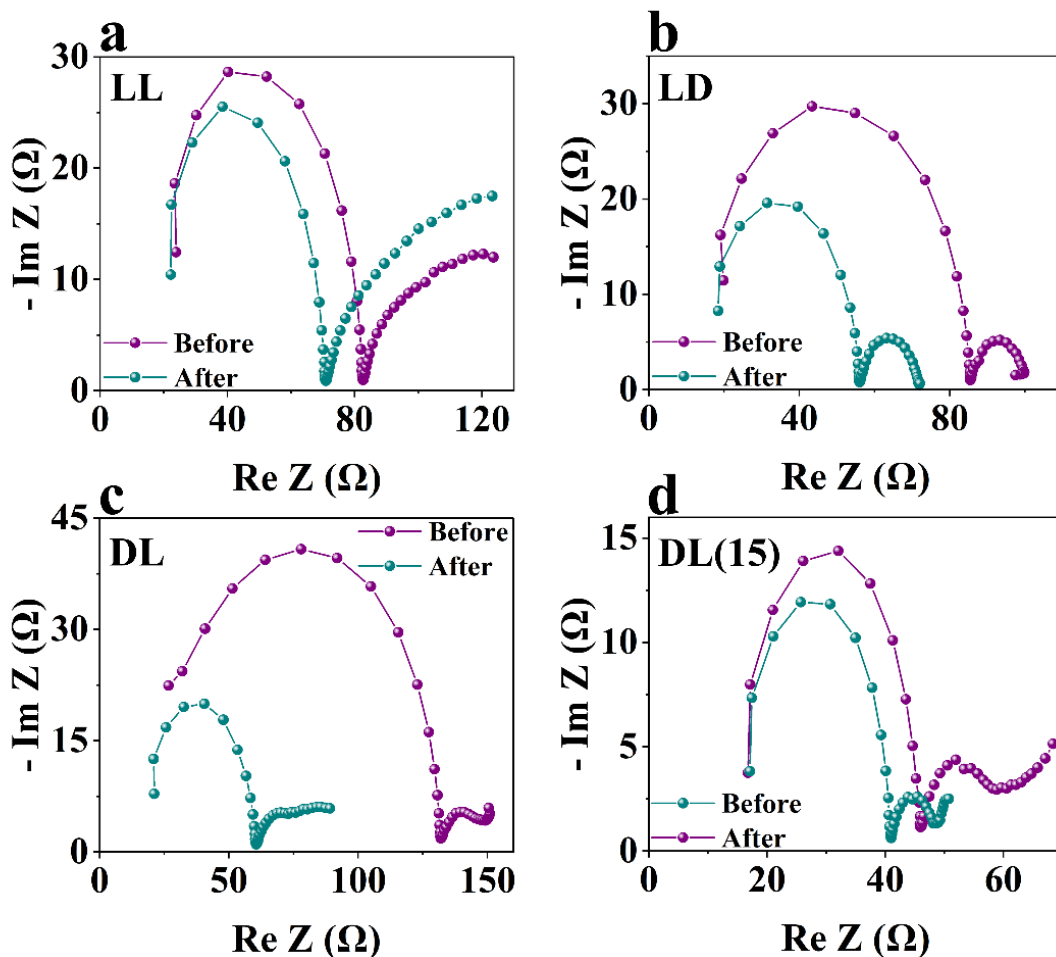


Figure 6.6: Comparison of Nyquist plots for HTL exposed to different doping conditions, obtained under open-circuit condition and 1 Sun illumination before and after 60 min of light soaking.

The spectra for LL (Figure 6.6 a) are best fitted with an equivalent circuit consisting of three RC elements.⁽⁴³⁾ For LD (Figure 6.6 b), DL (Figure 6.6 c) and DL(15) (Figure 6.6 d), only two well-separated arcs are observed prior to light soaking. However, after pre-illumination, the spectra for DL and DL(15) develop a third arc in the low frequency region. For the spectra showing two arcs, the equivalent circuit in Figure A.3- 4a was utilized, while for the three-arc patterns (either well-separated or merged), the equivalent circuit in Figure A.3- 4b was chosen. In both equivalent circuits, R_{Series} denotes the series resistance by the wires and contacts. Additionally, to fit the low, mid, and high frequency features, the RC elements indicated by LF, MF and HF are employed, respectively. It should be noted the choice of equivalent circuits and the interpretation of Nyquist

patterns have been the subject of controversy in the literature(54, 55, 56). In the present study, we will interpret each feature through considering the explained changes in PV metrics and $J-V$ curves, as well as comparing Nyquist plots before and after light soaking. The fitting results for R_{Series} , R_{HF} , R_{MF} and R_{LF} as well as the corresponding capacitance parameters are shown in Table A.3- 9. We note that for all doping conditions, R_{Series} is reduced with light soaking. LL shows reduced R_{HF} and R_{MF} , while it displays enhanced R_{LF} with light soaking. LD, DL and DL(15) show reduced R_{HF} with light soaking. On the other hand, while DL and DL(15) show enhanced R_{LF} after illumination, the corresponding values for LD remain rather similar. Overall, regardless of the doping strategy, R_{HF} decreases with light soaking, in accordance with increased conductivity upon illumination (Figure 6.2, Table A.3-1, Figure A.3-1 and Table A.3- 6). We suggest that this increased bulk conductivity is able to overcome the deleterious conductivity effects suggested for I^- migration (as indicated from XPS results) for all doping conditions. We note that this reduction is more drastic for LD and DL which we attribute to the dark storage period known to reversibly decrease spiro-OMeTAD conductivity(43). Whereas in the case of DL(15), the longer ambient light doping stage is able to recover the conductivity after the dark doping period. Although Bach et al.(43), attributed the decrease of R_{HF} with illumination to reduction of hole injection barrier at the perovskite/HTL interface, we assign this parameter to charge transport resistance in the HTL bulk, decreasing with illumination. On the other hand, we believe that the changes observed for R_{MF} and R_{LF} have other physical implications than R_{HF} . Noticeably, while the mid and low frequency arcs in LL (before and after light soaking) and DL (after light soaking) are rather merged, the low frequency semicircle in DL(15) is well-separated from the mid frequency one. Hence, the enlargement or appearance of the low frequency semicircle can be attributed to deteriorated charge extraction at the interface. Consequently, we can correlate the increased R_{LF} to the formation of Li_2O and LiF (as shown through XPS results), which are known to be insulators(57, 58) , which can therefore prevent effective charge extraction at the interface. As such, the rather unchanged charge extraction efficiency and therefore FF in the case of LD are manifested as similar R_{LF} values (for both before and after light soaking). We attribute this observation to the fact that LD shows the least intense LiF peak, as well as the absence of Li_2O peak, in the corresponding XPS spectra (Figure 6.5 i and Figure 6.5 f). Therefore, in line with our previous work(36), we suggest that larger combined magnitude of R_{HF} , R_{MF} and R_{LF} indicates higher charge transfer resistance. Since the perovskite layer and ETL are not subject to variation in this work, then the changes in

R_{MF} and R_{LF} can be majorly attributed to injection barrier at the perovskite/HTL interface. To further corroborate this view, additional EIS measurements were conducted on PSCs which were left in the dark both before and after gold deposition (Figure 6.7 a), which will be denoted as DD henceforth. The corresponding results for UV-Vis, SCLC and conductivity measurements on DD are displayed in Figure A.3- 5.

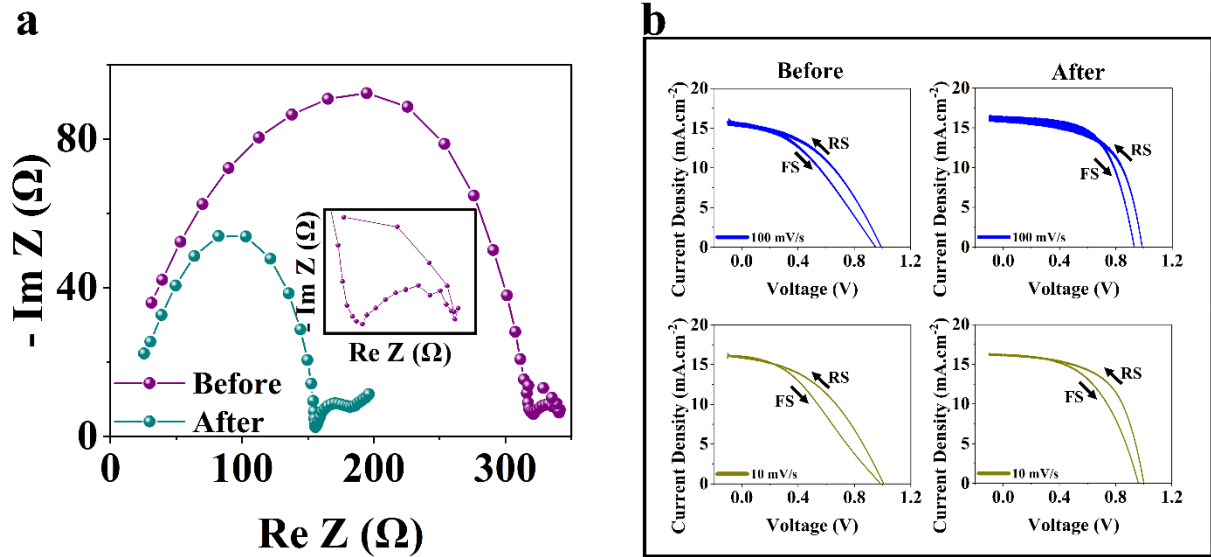


Figure 6.7: Characterization of PSCs left under dark before and after gold deposition (DD): (a) Nyquist plots obtained under open-circuit condition and 1 Sun illumination, and (b) J - V curves under 100 and 10 mV/s scan speed before and after 60 min of light soaking.

The distribution of PV metrics and HI for spiro-OMeTAD doped according to DD procedure is shown in Figure A.3- 6. Under both dark and 1 Sun illumination, a similar value of conductivity as LL is obtained for DD (Table A.3- 10). Yet, interestingly, the J - V curves for DD evolve differently under prolonged illumination (Figure 6.7 b) compared with that of LL (Figure 6.4 a). The metrics corresponding to Figure 6.7 b are summarized in Table A.3- 11. In the case of the doping process of DD, the best fitting of the Nyquist plots for both illumination conditions are rendered with the three-RC equivalent circuit of Figure A.3- 4b. Contrary to LL where the low frequency arc is comprised of two semicircles, for DD it is the high frequency arc that is a merger of two components. After light soaking, R_{HF} is reduced drastically, confirming that this resistance parameter is indeed correlated with bulk HTL conductivity. In contrast to what was observed for LL, the FF for both scan directions and scan rates are considerably improved with light soaking

(Figure 6.7 b and Table A.3- 11). The fitting results of the corresponding EIS patterns are listed in Table A.3- 12. Therefore, based on EIS results, while an arc in the high frequency range of Nyquist plot can prove benign by shrinking under light and resulting in improved performance (e.g., DD), a low frequency arc and its propagation under illumination is tied to performance loss in PSCs (e.g., LL). In other words, depending on the underlying cause for the low PV metrics, the performance could either improve or become worse under prolonged light soaking.

In the following, we offer our overall understanding of the results discussed in this work. We suspect that the overall conductivity of spiro-OMeTAD, within the context of conductivity measurement over the HTL film deposited on glass, has a complex dependency on the starting concentration of spiro-OMeTAD and LiTFSI, as well as how they evolve after the storage steps introduced to enhance their conductivity. The conductivity enhancement of spiro-OMeTAD, under the same ambient condition, in principle should be higher under light than dark. (59) The evolution of the said concentrations could be the result of competing between generation of oxidized spiro-OMeTAD radical cations and photo-decomposition of TFSI anion. As expected, the pristine HTL shows a lower conductivity than the films deliberately exposed to humidity. However, the substantial rise of conductivity can be attributed the higher rate of spiro-OMeTAD radical generation than photo-dissociation of TFSI anion, which is potentially an effect taking effect for longer light exposure times than what is considered for the scope of this work. Correspondingly, it is possible that two consecutive light storage steps (LL) lead to reduced conductivity overall compared with a dark and light storage combined.

Perhaps what enables PSCs based on LD to perform better is the dark storage period in which doping still takes place (albeit at a lower rate than under ambient light), which further enhances the HTL conductivity, yet allows for recovery from ambient light exposure. This eventually results in higher HTL conductivity as well as PV metrics for LD. On the other hand, for processes such as DL and DD which undergo dark doping first, appreciable conductivity can only be achieved upon ambient light exposure. This is evident from the staggering difference between performance metrics obtained for DL and DD-based PSCs. However, when devices experience dark doping first, then the length of light doping would have to be extended, as compared to when the light doping stage is performed first to render comparable V_{OC} and FF . However, the enhanced performance metrics (in RS) for DL(15) come at the cost of enhanced hysteresis which was also

present among other doping conditions, with LD displaying the smallest magnitude. Thus, the strategic placement of light and dark doping stages bears much significance for the device operation. For the PSCs studied in this work, the deteriorated performance metrics in FS were attributed to a combination of factors such as low HTL conductivity and adverse interfacial reactions specifically with the formation of LiF and Li₂O formation. In particular, we demonstrated that depending on the mechanism causing inferior metrics, the corresponding PSC can experience either a loss or gain in performance after prolonged light soaking under 1 Sun illumination. Overall, the strategy employed in doping spiro-OMeTAD can dictate long lasting effects with respect to performance metrics but also hysteresis dynamics and tolerance towards 1 Sun illumination.

6.4. Conclusion

In this work, the influence of spiro-OMeTAD doping conditions on the hysteresis evolution in PSCs was studied. Multiple doping conditions were chosen which differ with respect to storage conditions (dark/ ambient light), sequence and duration. Through SCLC and UV-Vis measurements, it was confirmed that the different employed strategies result in relatively similar traces in hole mobility and absorption, respectively. However, the different conductivities obtained for the HTLs indicates that the utilized doping strategies indeed modulate the charge carrier density within spiro-OMeTAD films. The PV metrics of the corresponding PSCs displayed a strong dependence on the exact doping condition. The most tolerant PSCs towards prolonged illumination under 1 Sun, were obtained by placing the ambient light exposure step only prior to Au deposition, followed by a dark storage step afterwards. On the contrary, having two consecutive light storage periods (before and after Au deposition) resulted in deteriorating PV metrics with light soaking. To understand the origin of these differences and evaluate how variation in PV metrics depending on the locus and extent of hysteresis, J - V curves were thoroughly studied under scan rates of 100 mV/s and 10 mV/s, both before and after light soaking treatment of 60 minutes under 1 Sun illumination. From this analysis, the change in FF between RS and FS was attributed to different band alignments at perovskite/HTL interface as result of the different doping condition. It was hypothesized that under FS for an HTL with lower p -type conductivity, the density of accumulated ionic species on the perovskite side required for its sufficient n -doping and subsequently forming

an *n-p* type heterojunction with HTL is less likely. Such a condition results in inverted band alignment on the perovskite side, exacerbating interfacial recombination which translates into lower *FF* and *V_{OC}* in FS than RS. Through XPS measurements, decomposition of LiTFSI (as dopant for spiro-OMeTAD) and LiF formation was demonstrated. Moreover, by utilizing EIS, the signatures of deteriorated interfacial conductivity are identified from the appearance and propagation of the third arc in low frequency region of Nyquist plots. In contrast, the shrinkage of high frequency semicircle was shown to be beneficial for PSC performance. Moreover, from EIS spectra, the reduction in high frequency resistance was attributed to increased bulk conductivity of HTL, due to light soaking, while the low and mid frequency resistance parameters were correlated with interfacial charge transfer resistance. Thus, it was concluded that ambient light exposure is a necessary doping step for adequate *p*-doping of spiro-OMeTAD, but more importantly the sequence of light exposure plays a key role in determining the gain/loss of PSC under prolonged light soaking. Overall, this work demonstrated that depending on the spiro-OMeTAD doping strategy, different PV metrics and hysteresis dynamics during operation can be expected. This points towards the need for a more accurate reporting of the employed process as well as a standardized doping strategy to be developed and adopted by the perovskite PV research community.

6.5. References

1. Yoo JJ, Seo G, Chua MR, Park TG, Lu Y, Rotermund F, et al. Efficient perovskite solar cells via improved carrier management. *Nature*. 2021;590(7847):587-93.
2. Correa-Baena J-P, Abate A, Saliba M, Tress W, Jacobsson TJ, Grätzel M, et al. The rapid evolution of highly efficient perovskite solar cells. *Energy & Environmental Science*. 2017;10(3):710-27.
3. Das B, Liu Z, Aguilera I, Rau U, Kirchartz T. Defect tolerant device geometries for lead-halide perovskites. *Materials advances*. 2021;2(11):3655-70.
4. DeQuilettes DW, Koch S, Burke S, Paranjli RK, Shropshire AJ, Ziffer ME, et al. Photoluminescence lifetimes exceeding 8 μ s and quantum yields exceeding 30% in hybrid perovskite thin films by ligand passivation. *ACS Energy Letters*. 2016;1(2):438-44.

5. Ni Z, Bao C, Liu Y, Jiang Q, Wu W-Q, Chen S, et al. Resolving spatial and energetic distributions of trap states in metal halide perovskite solar cells. *Science*. 2020;367(6484):1352-8.
6. Park N-G. Perovskite solar cells: an emerging photovoltaic technology. *Materials Today*. 2015;18(2):65-72.
7. Giorgi G, Fujisawa J-I, Segawa H, Yamashita K. Small photocarrier effective masses featuring ambipolar transport in methylammonium lead iodide perovskite: a density functional analysis. *The journal of physical chemistry letters*. 2013;4(24):4213-6.
8. Miyano K, Tripathi N, Yanagida M, Shirai Y. Lead Halide Perovskite Photovoltaic as a Model p-i-n Diode. *Accounts of Chemical Research*. 2016;49(2):303-10.
9. Wetzelaer G-JAH, Scheepers M, Sempere AM, Momblona C, Ávila J, Bolink HJ. Trap-Assisted Non-Radiative Recombination in Organic-Inorganic Perovskite Solar Cells. *Advanced Materials*. 2015;27(11):1837-41.
10. Snaith HJ, Abate A, Ball JM, Eperon GE, Leijtens T, Noel NK, et al. Anomalous hysteresis in perovskite solar cells. *The journal of physical chemistry letters*. 2014;5(9):1511-5.
11. Unger EL, Hoke ET, Bailie CD, Nguyen WH, Bowring AR, Heumüller T, et al. Hysteresis and transient behavior in current-voltage measurements of hybrid-perovskite absorber solar cells. *Energy & Environmental Science*. 2014;7(11):3690-8.
12. Tress W, Marinova N, Moehl T, Zakeeruddin SM, Nazeeruddin MK, Grätzel M. Understanding the rate-dependent J-V hysteresis, slow time component, and aging in CH₃NH₃PbI₃ perovskite solar cells: the role of a compensated electric field. *Energy & Environmental Science*. 2015;8(3):995-1004.
13. Dualeh A, Moehl T, Tétreault N, Teuscher J, Gao P, Nazeeruddin MK, et al. Impedance spectroscopic analysis of lead iodide perovskite-sensitized solid-state solar cells. *ACS nano*. 2014;8(1):362-73.
14. Butler KT, Frost JM, Walsh A. Ferroelectric materials for solar energy conversion: photoferroics revisited. *Energy & Environmental Science*. 2015;8(3):838-48.
15. Unger EL, Czudek A, Kim H-S, Tress W. Chapter 4 - Current-voltage analysis: lessons learned from hysteresis. In: Pazoki M, Hagfeldt A, Edvinsson T, editors. *Characterization Techniques for Perovskite Solar Cell Materials*: Elsevier; 2020. p. 81-108.

16. Contreras L, Idígoras J, Todinova A, Salado M, Kazim S, Ahmad S, et al. Specific cation interactions as the cause of slow dynamics and hysteresis in dye and perovskite solar cells: a small-perturbation study. *Physical Chemistry Chemical Physics*. 2016;18(45):31033-42.
17. Frost JM, Butler KT, Walsh A. Molecular ferroelectric contributions to anomalous hysteresis in hybrid perovskite solar cells. *Apl Materials*. 2014;2(8):081506.
18. Correa Baena JP, Steier L, Tress W, Saliba M, Neutzner S, Matsui T, et al. Highly efficient planar perovskite solar cells through band alignment engineering. *Energy & Environmental Science*. 2015;8(10):2928-34.
19. Weber SAL, Hermes IM, Turren-Cruz S-H, Gort C, Bergmann VW, Gilson L, et al. How the formation of interfacial charge causes hysteresis in perovskite solar cells. *Energy & Environmental Science*. 2018;11(9):2404-13.
20. Moia D, Gelmetti I, Calado P, Fisher W, Stringer M, Game O, et al. Ionic-to-electronic current amplification in hybrid perovskite solar cells: ionically gated transistor-interface circuit model explains hysteresis and impedance of mixed conducting devices. *Energy & Environmental Science*. 2019;12(4):1296-308.
21. Saliba M, Matsui T, Domanski K, Seo J-Y, Ummadisingu A, Zakeeruddin SM, et al. Incorporation of rubidium cations into perovskite solar cells improves photovoltaic performance. *Science*. 2016;354(6309):206-9.
22. Ye J, Byrannvand MM, Martínez CO, Hoye RL, Saliba M, Polavarapu L. Defect passivation in lead-halide perovskite nanocrystals and thin films: toward efficient LEDs and solar cells. *Angewandte Chemie*. 2021;133(40):21804-28.
23. Quan LN, Yuan M, Comin R, Voznyy O, Beauregard EM, Hoogland S, et al. Ligand-stabilized reduced-dimensionality perovskites. *Journal of the American Chemical Society*. 2016;138(8):2649-55.
24. Rombach FM, Haque SA, Macdonald TJ. Lessons learned from spiro-OMeTAD and PTAA in perovskite solar cells. *Energy & Environmental Science*. 2021.
25. Cappel UB, Daeneke T, Bach U. Oxygen-induced doping of spiro-MeOTAD in solid-state dye-sensitized solar cells and its impact on device performance. *Nano letters*. 2012;12(9):4925-31.

26. Pfeiffer M, Leo K, Zhou X, Huang J, Hofmann M, Werner A, et al. Doped organic semiconductors: Physics and application in light emitting diodes. *Organic Electronics*. 2003;4(2-3):89-103.
27. Abate A, Leijtens T, Pathak S, Teuscher J, Avolio R, Errico ME, et al. Lithium salts as “redox active” p-type dopants for organic semiconductors and their impact in solid-state dye-sensitized solar cells. *Physical Chemistry Chemical Physics*. 2013;15(7):2572-9.
28. Schloemer TH, Christians JA, Luther JM, Sellinger A. Doping strategies for small molecule organic hole-transport materials: impacts on perovskite solar cell performance and stability. *Chemical science*. 2019;10(7):1904-35.
29. Le Corre VM, Stolterfoht M, Perdigon Toro L, Feuerstein M, Wolff C, Gil-Escrig Ln, et al. Charge transport layers limiting the efficiency of perovskite solar cells: how to optimize conductivity, doping, and thickness. *ACS Applied Energy Materials*. 2019;2(9):6280-7.
30. Jiang Q, Zhao Y, Zhang X, Yang X, Chen Y, Chu Z, et al. Surface passivation of perovskite film for efficient solar cells. *Nature Photonics*. 2019;13(7):460-6.
31. Domanski K, Roose B, Matsui T, Saliba M, Turren-Cruz S-H, Correa-Baena J-P, et al. Migration of cations induces reversible performance losses over day/night cycling in perovskite solar cells. *Energy & Environmental Science*. 2017;10(2):604-13.
32. Huang F, Jiang L, Pascoe AR, Yan Y, Bach U, Spiccia L, et al. Fatigue behavior of planar CH₃NH₃PbI₃ perovskite solar cells revealed by light on/off diurnal cycling. *Nano Energy*. 2016;27:509-14.
33. Khenkin MV, KM A, Visoly-Fisher I, Kolusheva S, Galagan Y, Di Giacomo F, et al. Dynamics of photoinduced degradation of perovskite photovoltaics: from reversible to irreversible processes. *ACS Applied Energy Materials*. 2018;1(2):799-806.
34. Liu B, Aydil ES. Growth of oriented single-crystalline rutile TiO₂ nanorods on transparent conducting substrates for dye-sensitized solar cells. *Journal of the American Chemical Society*. 2009;131(11):3985-90.
35. Saliba M, Correa-Baena J-P, Wolff CM, Stolterfoht M, Phung N, Albrecht S, et al. How to Make over 20% Efficient Perovskite Solar Cells in Regular (n-i-p) and Inverted (p-i-n) Architectures. *Chemistry of Materials*. 2018;30(13):4193-201.

36. Yekani R, Chiu H-c, Strandell D, Wang Z, Bessette S, Gauvin R, et al. Correlation between hysteresis dynamics and inductance in hybrid perovskite solar cells: studying the dependency on ETL/perovskite interfaces. *Nanoscale*. 2023.
37. Noh JH, Jeon NJ, Choi YC, Nazeeruddin MK, Grätzel M, Seok SI. Nanostructured TiO₂/CH₃NH₃PbI₃ heterojunction solar cells employing spiro-OMeTAD/Co-complex as hole-transporting material. *Journal of Materials Chemistry A*. 2013;1(38):11842-7.
38. Sanchez RS, Mas-Marza E. Light-induced effects on Spiro-OMeTAD films and hybrid lead halide perovskite solar cells. *Solar Energy Materials and Solar Cells*. 2016;158:189-94.
39. Burschka J, Kessler F, Nazeeruddin MK, Grätzel M. Co (III) complexes as p-dopants in solid-state dye-sensitized solar cells. *Chemistry of Materials*. 2013;25(15):2986-90.
40. Mott NF, Gurney RW. *Electronic processes in ionic crystals*: Clarendon Press; 1948.
41. Nakka L, Cheng Y, Aberle AG, Lin F. Analytical Review of Spiro-OMeTAD Hole Transport Materials: Paths Toward Stable and Efficient Perovskite Solar Cells. *Advanced Energy and Sustainability Research*. 2022;3(8):2200045.
42. Nguyen WH, Bailie CD, Unger EL, McGehee MD. Enhancing the Hole-Conductivity of Spiro-OMeTAD without Oxygen or Lithium Salts by Using Spiro(TFSI)₂ in Perovskite and Dye-Sensitized Solar Cells. *Journal of the American Chemical Society*. 2014;136(31):10996-1001.
43. Tan B, Raga SR, Rietwyk KJ, Lu J, Furer SO, Griffith JC, et al. The impact of spiro-OMeTAD photodoping on the reversible light-induced transients of perovskite solar cells. *Nano Energy*. 2021;82:105658.
44. Watts JF. High resolution XPS of organic polymers: The Scienta ESCA 300 database. G. Beamson and D. Briggs. 280pp.,£ 65. John Wiley & Sons, Chichester, ISBN 0471 935921,(1992). Wiley Online Library; 1993.
45. Luo Q, Zhang Y, Liu C, Li J, Wang N, Lin H. Iodide-reduced graphene oxide with dopant-free spiro-OMeTAD for ambient stable and high-efficiency perovskite solar cells. *Journal of Materials Chemistry A*. 2015;3(31):15996-6004.
46. Zhu H, Liu Y, Eickemeyer FT, Pan L, Ren D, Ruiz-Preciado MA, et al. Tailored Amphiphilic Molecular Mitigators for Stable Perovskite Solar Cells with 23.5% Efficiency. *Advanced Materials*. 2020;32(12):1907757.

47. Dedryvère R, Leroy S, Martinez H, Blanchard F, Lemordant D, Gonbeau D. XPS valence characterization of lithium salts as a tool to study electrode/electrolyte interfaces of Li-ion batteries. *The Journal of Physical Chemistry B*. 2006;110(26):12986-92.
48. Wang S, Cabrerós A, Yang Y, Hall AS, Valenzuela S, Luo Y, et al. Impacts of the hole transport layer deposition process on buried interfaces in perovskite solar cells. *Cell Reports Physical Science*. 2020;1(7):100103.
49. Hawash Z, Ono LK, Raga SR, Lee MV, Qi Y. Air-exposure induced dopant redistribution and energy level shifts in spin-coated spiro-MeOTAD films. *Chemistry of Materials*. 2015;27(2):562-9.
50. Schroder KW, Celio H, Webb LJ, Stevenson KJ. Examining solid electrolyte interphase formation on crystalline silicon electrodes: influence of electrochemical preparation and ambient exposure conditions. *The Journal of Physical Chemistry C*. 2012;116(37):19737-47.
51. Mesquita I, Andrade L, Mendes A. Temperature impact on perovskite solar cells under operation. *ChemSusChem*. 2019;12(10):2186-94.
52. Kim S, Bae S, Lee S-W, Cho K, Lee KD, Kim H, et al. Relationship between ion migration and interfacial degradation of CH₃NH₃PbI₃ perovskite solar cells under thermal conditions. *Scientific Reports*. 2017;7(1):1200.
53. Tumen-Ulzii G, Qin C, Matsushima T, Leyden MR, Balijipalli U, Klotz D, et al. Understanding the degradation of Spiro-OMeTAD-based perovskite solar cells at high temperature. *Solar RRL*. 2020;4(10):2000305.
54. Calado P, Telford AM, Bryant D, Li X, Nelson J, O'Regan BC, et al. Evidence for ion migration in hybrid perovskite solar cells with minimal hysteresis. *Nature communications*. 2016;7(1):13831.
55. Jacobs DA, Shen H, Pfeffer F, Peng J, White TP, Beck FJ, et al. The two faces of capacitance: New interpretations for electrical impedance measurements of perovskite solar cells and their relation to hysteresis. *Journal of Applied Physics*. 2018;124(22):225702.
56. Ravishankar S, Almora O, Echeverría-Arrondo C, Ghahremanirad E, Aranda C, Guerrero A, et al. Surface polarization model for the dynamic hysteresis of perovskite solar cells. *The journal of physical chemistry letters*. 2017;8(5):915-21.
57. Chaney RC, Lafon EE, Lin CC. Energy band structure of lithium fluoride crystals by the method of tight binding. *Physical Review B*. 1971;4(8):2734.

58. Liu L, Henrich VE, Ellis W, Shindo I. Bulk and surface electronic structure of Li₂O. *Physical review B*. 1996;54(3):2236.
59. Seo J-Y, Akin S, Zalibera M, Preciado MAR, Kim H-S, Zakeeruddin SM, et al. Dopant Engineering for Spiro-OMeTAD Hole-Transporting Materials towards Efficient Perovskite Solar Cells. *Advanced Functional Materials*. 2021;31(45):2102124.

Chapter 7: Global Discussion

7.1. Thesis Overview

As detailed in Chapters 1 and 2, perovskite solar cells (PSCs) are a promising alternative to the conventional c-Si photovoltaics due to a combination of extremely beneficial optoelectronic properties of metal halide perovskite semiconductors such as possessing long charge carrier diffusion length,(1) high absorption coefficient,(2, 3) and defect tolerance,(4, 5) next to relative ease of synthesis and low cost of manufacturing(6, 7). However, the phenomenon of hysteresis prevents at least partially realization of these favorable properties of metal halide perovskites in fully functional photovoltaic devices. Hysteresis is the term applied to the mismatch between $J-V$ curves in FS and RS directions,(8) and is closely related as well with instability problems exhibited by PSCs.(9) This phenomenon is believed to be a manifestation of ionic conduction across the perovskite layer and their subsequent pile up at interfaces, modulating interfacial potential barriers and therefore electronic charge carrier extraction efficiency.(10) As discussed in Section 2.6.3, there has been a myriad of strategies for mitigating hysteresis that ranges from choice of transport layers (ETL and HTL), passivation strategies, defect management, composition of the perovskite layer, encapsulation, etc.(11) The results have, in times, led to the rather erroneous term of “hysteresis-free” to be used by some authors. However, in practice, it has been proved many times over that the absence of hysteresis under a given testing condition does not negate its presence under all others.(12, 13) As such, the phenomenon of hysteresis remains to be a complex challenge with its extent and appearance dependent heavily on the specifics of not only the PSC components but also the framework of operation. Such observations set the general objective of this thesis, i.e., to better understand the transport layer-dependent evolution of hysteresis dynamics under different testing conditions, in PSCs with quadruple perovskite composition of $(\text{Cs}_5\text{Rb}_5\text{MA}_{0.15}\text{FA}_{0.75})\text{Pb}(\text{I}_{0.83}\text{Br}_{0.17})_3$, in $n-i-p$ device architecture, as the latter are heralded as the most promising ones among the different compositions and configurations.

The work in this thesis was initially started with titania nanorod scaffolds as ETL structure due to two prominent reasons. One was the ease of tuning the nanorods with respect to length, diameter and vertical alignment (*vs.* the FTO substrate), which in turn facilitated a systematic characterization of the perovskite layer properties as a function of the underlying ETL scaffold.

Secondly, the perovskite layer infiltrating/capping the nanorod scaffolds demonstrated superior stability compared with that of planar ETL which was a requirement to still have a functioning solar cell after the spiro-OMeTAD *p*-doping in air was completed. Later, it was discovered that the type of titania nanorod scaffold (with respect to the sequence of interfacing with c-TiO₂) had a considerable impact over the PSC performance evolution under different testing conditions. Another issue as will be explained later in this chapter, *p*-doping of spiro-OMeTAD through air exposure proved to be a pivoting step significantly influencing the functioning of PSCs and their hysteresis behavior. Prior to this understanding, PSCs would be left in a dark desiccator (RH less than 10%) for 12 hours prior to gold deposition. However, the resulting devices failed to show any rectification behavior. Light soaking was able to induce only small degrees of improvement. Considering that our HTL-free PSCs could display better charge rectification behavior, insufficient spiro-OMeTAD *p*-doping was suspected to be the culprit behind the poor full-stack device performance. As such, and due to reports on light-induced oxidation of spiro-OMeTAD(14), the cells were left under room light at RH of 20% for 12 hours. This resulted in considerable performance improvement which was further complemented by extending the light exposure stage to 15 hours and conducting both the light and dark steps under 20% RH. This resulted in the DL(15) doping process discussed in Chapter 6 and which became the only *p*-doping process employed in Chapter 4 and Chapter 5. During conducting the work for Chapter 6, it became clear that even the same doping process could result in different performance evolution depending on the prevailing ambient RH. Therefore, this necessitated the conducting of this work when the RH value was at similar steady value (20%) to enable “season-free” acquisition of results in a meaningful way. In the following, the results of Chapter 4 to Chapter 6 are summarized and discussed together to offer a global picture of the transport layer-dependent evolution of hysteresis in quadruple perovskite-based PSCs in *n-i-p* architecture.

In **Chapter 4**, the influence of light soaking, scan rate and applied bias on ETL-dependent hysteresis modulation was investigated by comparing two different ETL configurations: *i*) the conventional planar, whereby compact-TiO₂ (anatase) film (deposited on FTO by spray pyrolysis) constituted the ETL, and *ii*) a scaffold-based ETL, where c-TiO₂ was coated on a TiO₂ (rutile) scaffold made of hydrothermally grown nanorods on FTO. The former configuration was denoted as Planar c-TiO₂, while the latter was labeled as TNR. Moreover, the thickness of c-TiO₂ in each configuration was increased by using a higher volume of precursor solution (four times as much

as the base level) during spray pyrolysis, rendering Planar c-TiO₂ (x4) and TNR (x4). The different ETL structures were fabricated into PSCs by spin coating on them the perovskite absorber layer and using on top of that spiro-OMeTAD as HTL.

Planar PSCs displayed considerable gain in FF under light soaking for both scan directions and rates (albeit more enhanced for thinner c-TiO₂), in contrast to their scaffold-based counterparts. This increase was attributed to the enhanced p -type conductivity of spiro-OMeTAD (as HTL) under prolonged illumination -as determined during the study reported in Chapter 6, which would facilitate charge extraction at the corresponding interface, especially under FS, without compromising charge extraction capability at the ETL interface. Accordingly, HI was reduced under light soaking for both Planar configurations. This reduction was accompanied by enhanced FF and reduced V_{OC} . On the other hand, for scaffold-based PSCs, light soaking was found to adversely affect the ETL/perovskite interface to a larger extent than the positive influence of p -doping of spiro-OMeTAD at the other interface, resulting in deteriorated FF for both scan rates and directions. The reduction of HI in the case of scaffold-based PSCs was accompanied by reduced FF and V_{OC} . As a result of such changes, we suggested that the trends of FF follow the conductivity modulation at both interfaces, as deduced from the respective EIS spectra. The reduction of charge transfer resistance for planar configurations under light soaking was attributed to enhanced conductivity induced by the p -doping of HTL, and which had as consequence to obtain enhanced FF . On the other hand, the Nyquist plots of both scaffold-based PSCs displayed unexpectedly increased charge transfer resistance upon light soaking and as a decrease in FF . This manifestation pointed towards increased charge transport resistance at the ETL interface apparently due to some adverse electrochemical reactions that were not identified. Turning our attention to the effect of scan rate, it was observed that the standard planar PSCs displayed considerably reduced FF especially in FS, while the corresponding V_{OC} values were increased, when the scan rate was reduced from 100 mV/s to 10 mV/s. This resulted in enhanced HI. However, we demonstrated that this effect on FF could be largely alleviated by utilizing a thicker compact titania planar configuration as both FF and V_{OC} were increased upon decreasing the scan rate in the case of Planar c-TiO₂ (x4) ETL. As such, the planar PSCs utilizing a thicker c-TiO₂ proved to be less sensitive to changes in the scan direction and rate. This set of results reveals how sensitive the functioning of PSC is on fabrication and operating conditions demanding very careful optimization and control of all processing steps and components.

Apart from the changes in the magnitude of HI, the results indicated that the locus of hysteresis can substantially change depending on the specific properties and testing conditions of the ETL/perovskite. Thus, by comparing EIS spectra before and after J - V scans, we determined that forward bias has a negative effect on the band alignment at ETL/perovskite interface in PSCs based on Planar c-TiO₂ due to the increased charge transfer resistance. This negative effect, however, was removed by increasing the thickness of c-TiO₂ in the planar configuration, similar to what was observed for scaffold-based PSCs. Therefore, depending on the ETL configuration (planar vs. modified mesoporous) and the thickness of c-TiO₂ different hysteresis evolution as a function of light soaking, scan rate and forward bias can be expected for the corresponding PSC.

Up until this point, the impact of c-TiO₂ as part of ETL on the evolution of charge carrier dynamics and therefore hysteresis behavior as a function of illumination, scan rate and applied bias in PSCs was elucidated. Next, we placed a narrow focus on the type of titania nanorod scaffold and how it controlled the hysteresis locus, specifically under voltages exceeding V_{OC} .

In **Chapter 5**, the structure of nanorod scaffold interface (modified with c-TiO₂ coating) on hysteresis was probed. More specifically two sets of titania nanorod scaffolds were built featuring rutile nanorods grown on c-TiO₂ (anatase)-coated FTO (termed **AR** (for Anatase-Rutile) or nanorods (rutile) grown on FTO and coated afterwards with c-TiO₂ (anatase) (termed **RA** (for Rutile-Anatase). The AR sequence of synthesis placed rutile titania nanorods in direct contact with the infiltrating perovskite medium. On the other hand, the RA ETL structure interfaced anatase titania with the perovskite layer. The RA scaffold is the same as the TNR scaffold studied in Chapter 4. Of the two ETL scaffold structures, PSCs with RA proved to have the higher J_{SC} and V_{OC} and this was correlated to the higher effective conductivity of FTO/RA compared with FTO/AR. Representative J - V curves for PSCs based on both ETL structures were studied under 100 and 10 mV/s and inspected for hysteresis locus and magnitude. Under 100 mV/s, PSCs constructed based on both scaffolds display similar hysteresis locus starting around 0.8 V and extending to voltages beyond V_{OC} (although larger in magnitude for AR). Under 10 mV/s, the magnitude of hysteresis for both PSC types is reduced. However, the mismatch between J - V curves in RA-based PSCs does not extend beyond V_{OC} , while for AR a considerable widening persists in that region. It was suggested that due to the higher effective conductivity of RA, ionic migration is triggered earlier across the perovskite layer to screen the built-in field. As a result, ionic species

arrive at the interface and equilibrate earlier in the case of RA-based PSCs than their AR counterparts. This leads to an earlier formation of the flat band condition in RA-based PSCs than their AR counterpart. Since under this situation, a larger portion of the field will drop across the interfaces, then the presence of interfacial defects can lead to increased non-radiative recombination especially with the RA-based PSCs.

To inspect the manifestation of charge carrier dynamics responsible for the different hysteresis loci, EIS measurements were conducted under 1 Sun illumination and applied bias from V_{OC} to 1.4 V. It was observed the AR-based PSCs to display an inductive loop in the low frequency segment of Nyquist plots, in addition to the inductive hook in the mid frequency range exhibited by both ETLs. The observation of an inductive hook was attributed to a higher density of accumulated ionic species at the interface, as a result of increased applied bias, resulting in interfacial band discontinuity. This then gives rise to a higher scattering rate of photoexcited electrons moving from the perovskite layer to the ETL, leading to increased mobility of charge carriers. On the other hand, the low frequency inductive hook was hypothesized to be correlated with the band inversion at ETL/perovskite interface, resulting in charge transfer from ETL into perovskite which would exacerbate non-radiative recombination of charge carriers and widen the gap between $J-V$ curves as a result. This band inversion was attributed to the lower effective conductivity (and therefore lower n -type doping) of AR compared with RA. An ETL with lower conductivity would, in turn, require a lower extent of ionic accumulation in the perovskite layer to achieve sufficient p -doping which would then result in the formation of a $p-n$ heterojunction and have the bands inverted on the perovskite side. Overall, this work demonstrated that the conductivity of the ETL scaffold can have a considerable impact not only on the pace of ionic migration across the perovskite layer but also on the interfacial band alignment and non-radiative recombination as a result of interfacial ionic accumulation. The results of Chapter 5 are summarized in Figure 7.1.

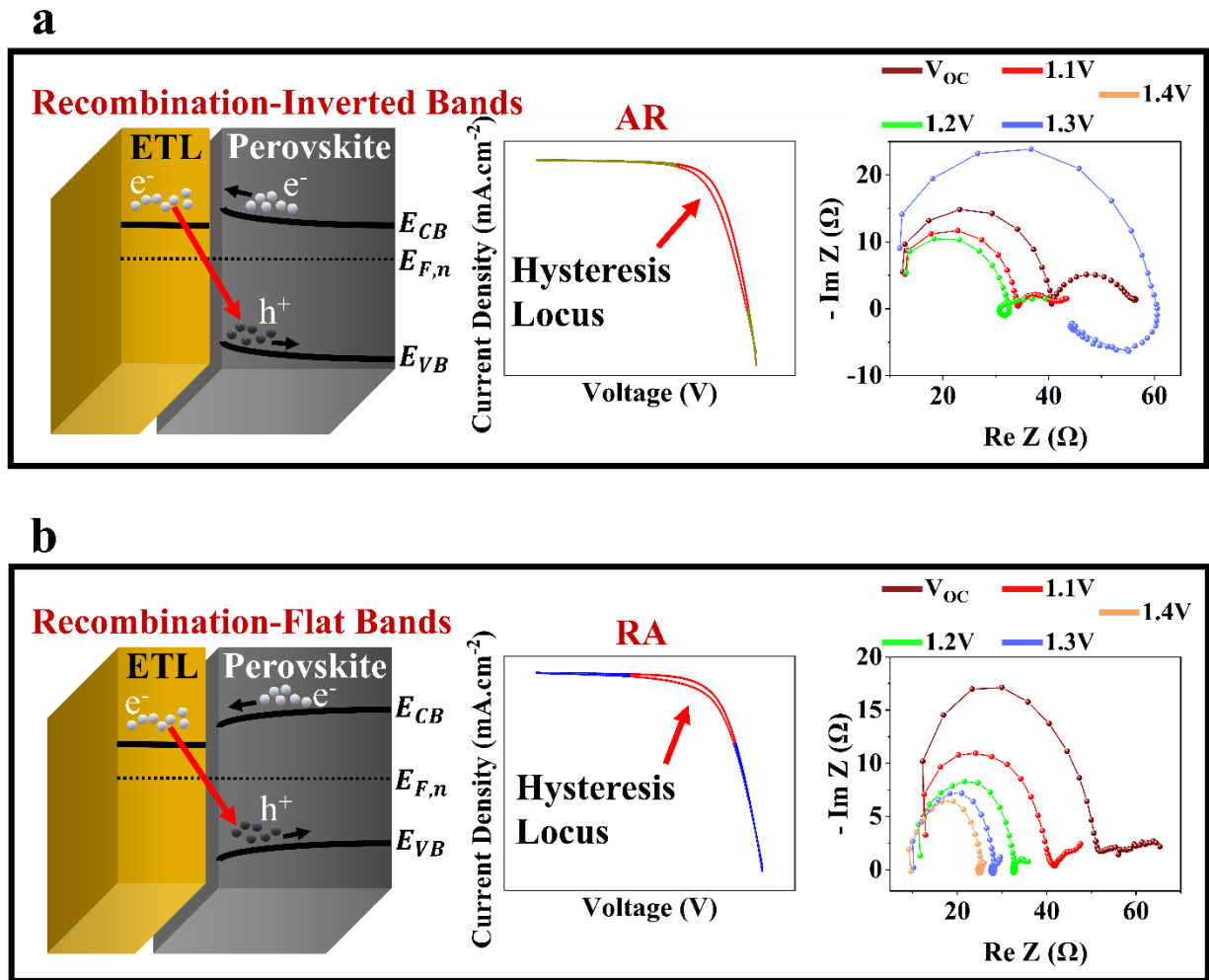


Figure 7.1: Illustration of band bending at ETL/perovskite interface showing the dominant recombination mechanism giving rise to the hysteresis locus observed on J - V curves at 10 mV/s, as well as probing the corresponding charge carrier dynamics using EIS under 1 Sun illumination and increasing forward bias in excess of V_{oc} for PSCs based on (a) AR and (b) RA as ETL.

For a comprehensive overview, Figure 7.2 compares the distribution of PV metrics as a function of the utilized ETL structure, at 100 mV/s and 10 mV/s under various light soaking times of 0 to 60 minutes. Additionally, representative J - V curves are compared in Figure 7.3.

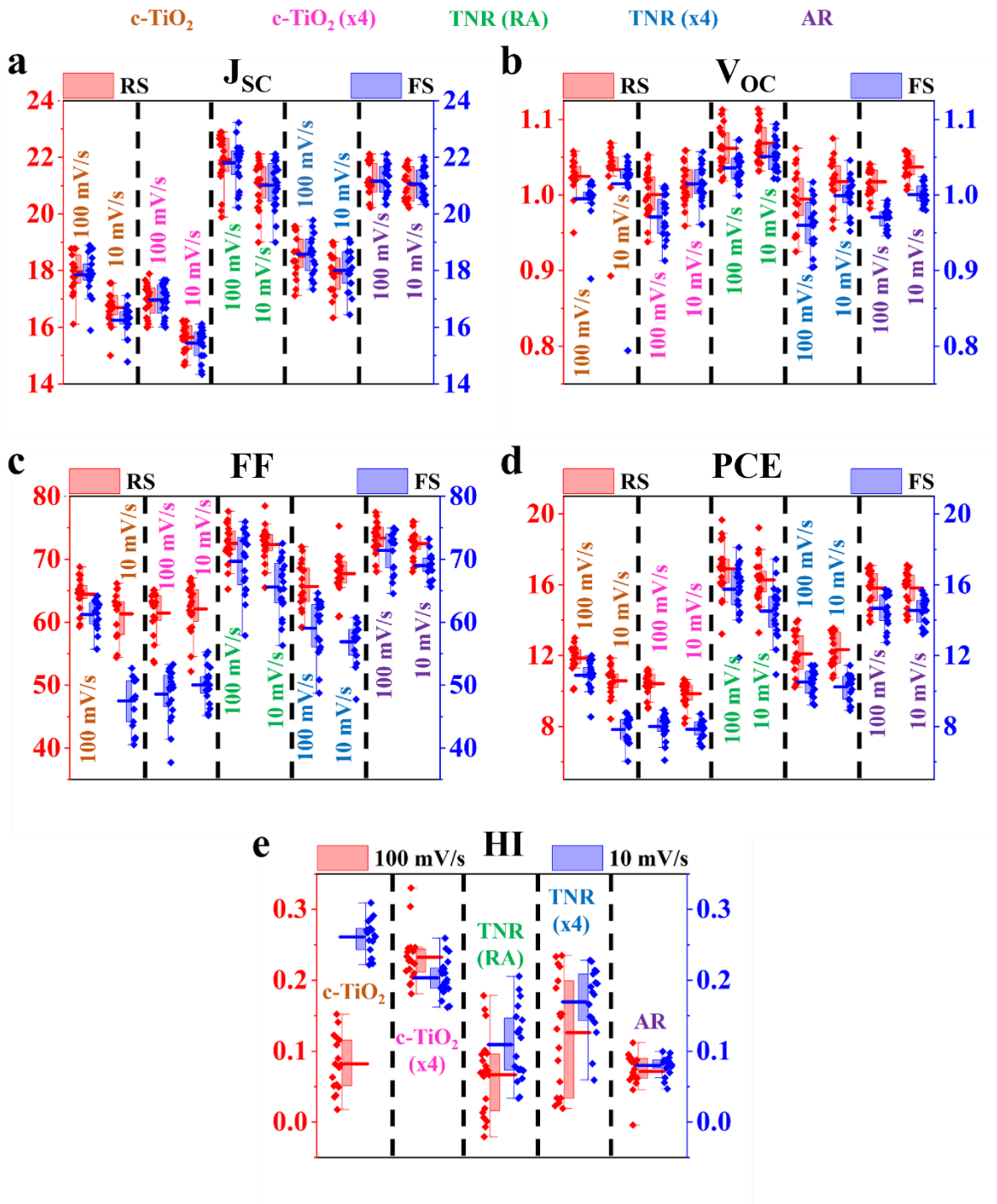


Figure 7.2: PV metrics (a) J_{SC} , (b) V_{OC} , (c) FF , and (d) PCE , as well as (e) HI for PSCs with quadruple perovskite composition in *n-i-p* architecture assembled using $c\text{-TiO}_2$, $c\text{-TiO}_2$ (x4), TNR (same as RA in Chapter 5), TNR (x4) and AR.

100 mV/s 10 mV/s

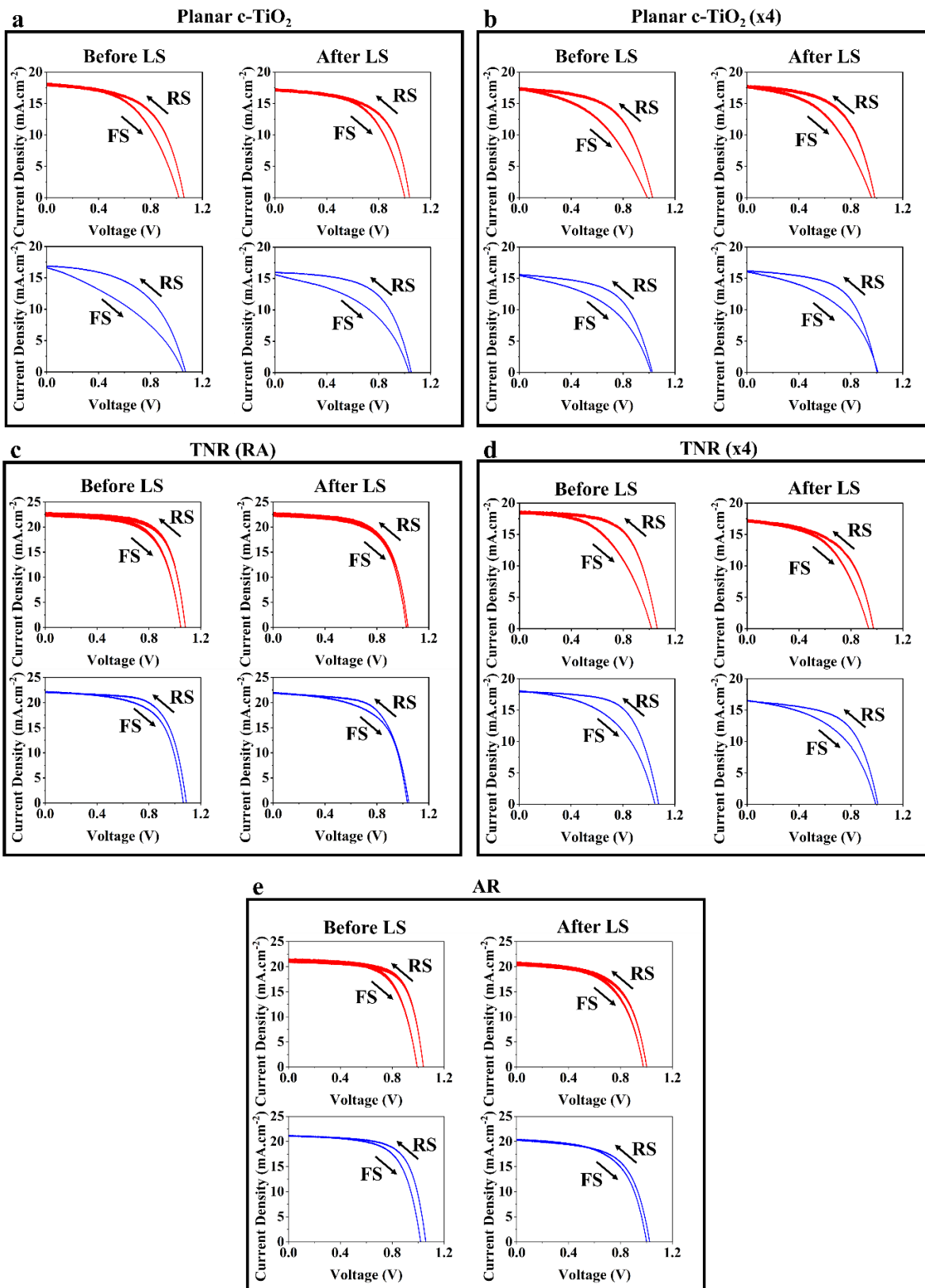


Figure 7.3: Comparison of J - V curves at 100 and 10 mV/s before and after light soaking (LS) for PSCs with quadruple perovskite composition in n - i - p architecture assembled using c-TiO₂, c-TiO₂ (x4), TNR (same as RA in Chapter 5), TNR (x4) and AR.

In summary to this point, the phenomenon of hysteresis in PSCs and its evolution as a function of light soaking, scan rate and applied bias was studied from the perspective of ETL structure in either planar (c-TiO₂) and/or titania nanorod scaffolds. Obtaining a complete picture of hysteresis though also necessitated an understanding of the role of spiro-OMeTAD in perovskite/HTL interface, in particular the effect of p -doping.

The method of p -doping of spiro-OMeTAD had always proved to be a key element in making functioning PSCs. In particular, spiro-OMeTAD is insulating in its pristine form, therefore cannot provide the required charge carrier rectification when utilized without the addition of dopants.(15) The most widely used combination of chemical dopants are LiTFSI and 4-TBP.(14) However, in the early stages of this thesis even with the chemical dopants present, the PSCs displayed nearly insulating behavior, lacking the required level of rectification. During the later stages, it became evident that spiro-OMeTAD, despite having chemical dopants, still needed to be exposed to low-humidity air to be able to function. One interesting observation was that type of storage (dark, ambient light, or both), as well as its length could have a significant effect on not only the efficiency but also hysteresis behavior of the corresponding PSCs. Another important observation was that light soaking under 1 Sun was able to induce gain in efficiency only for certain doping methods and there was a limit to the extent of the enhancement by prolonged illumination. In other words, insufficient p -doping of spiro-OMeTAD by not having been exposed to low-humidity air, could not be fully compensated by mere light soaking.

Such observations shaped the motivation behind the work described in **Chapter 6**, whereby a narrow focus was placed on systematically studying the doping methodology of spiro-OMeTAD and its impact on charge carrier dynamics and hysteresis evolution under light soaking. The corresponding PSCs were assembled using AR structure (investigated in Chapter 5) as ETL. An important sub-objective of this chapter was to determine whether the locus and magnitude of hysteresis for a given ETL could be modulated depending on the specific spiro-OMeTAD doping process. In that Chapter, we argued that not every apparent reduction in hysteresis can be regarded as a positive influence. As an example, reduced HI can be a result of different changes to PV

metrics such as reduction of FF in one direction, while FF in the other direction remains constant. Alternatively, increased HI could be the result of enhanced FF in one direction while it stays the same in the other. Therefore, the mere increase or decrease in HI cannot necessarily be taken as indication of worsened or improved PSC performance, respectively, under different testing conditions. Instead, we demonstrated that comparing the magnitude of hysteresis is only meaningful when accompanied by analyzing the corresponding changes in PV metrics.

The utilized processes in Chapter 6 consisted of two separate storage steps for low-humidity air exposure, one being before and the other one after Au deposition. The storage was conducted under dark (D) and ambient light (L), generating the following doping conditions: DD, DL, LL and LD. The letter to the left indicates the storage step before gold while the one on the right corresponds to the storage after gold. The length of all stages was set to 12 hours. To study the influence of exposure duration, the ambient light stage for DL was extended to 15 hours, resulting in DL(15) doping condition. All doping processes were conducted under a fixed relative humidity of 20%. Like the work conducted in Chapters 4 and 5, in Chapter 6 each PSC group (comprising four devices) was exposed to increasing pre-illumination from 0 to 60 minutes, with 20 minutes interval, before recording the $J-V$ curves. While DL(15) and LD displayed close averages for FF and V_{OC} , the considerably higher J_{SC} recorded for DL(15) resulted in the highest PCE for the corresponding PSCs. The representative $J-V$ curves for each doping condition were compared under 100 and 10 mV/s, before and after light soaking. Of the considered doping conditions, LD displayed negligible change between the curves in FS and RS under both light soaking and reduced scan rate. The corresponding reduction was due to increased FF in FS, which was in sharp contrast to all other doping conditions displaying reduced FF in RS, FS or both. The reason behind deteriorated FF was investigated through XPS, whereby it was revealed that the formation of deleterious products such as LiF and Li₂O (as a result of LiTFSI decomposition under light soaking) could prevent efficient charge extraction at perovskite/HTL. The combination of adverse interfacial electrochemical reactions (decomposition of LiTFSI to Li₂O and LiF) with low HTL bulk conductivity was considered as the reason behind deteriorating PSC performance under light soaking, which was correlated with the propagation of low frequency semicircle in Nyquist plot, leading to performance loss under operation. In contrast, it was demonstrated that for sufficient p-doping of spiro-OMeTAD, exposure to ambient light, in addition to dry air is necessary. This became evident for DD-based PSCs which displayed very low FF prior to light soaking. However,

after prolonged illumination, the FF was considerably enhanced under both scan rates. This change resulted in performance gain and was manifested as a reduction of charge transfer resistance in the corresponding Nyquist plot. In particular, we demonstrated that depending on the mechanism causing inferior metrics, the corresponding PSC can experience either a loss or gain in performance after prolonged light soaking under 1 Sun illumination, and correspondingly dictate evolution of hysteresis dynamics. This point is summarized in Figure 7.4.

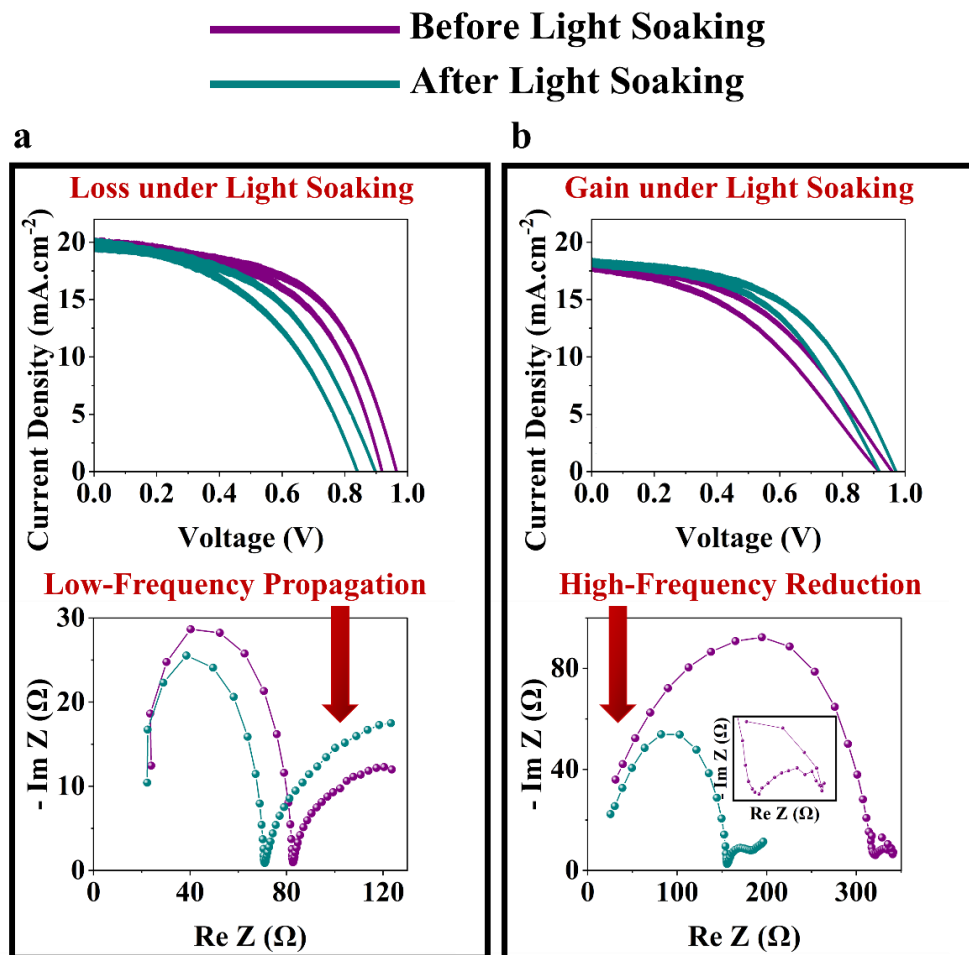


Figure 7.4: Comparison of J - V curves as well as EIS spectra obtained under 1 Sun illumination before and after light soaking for PSCs with quadruple perovskite composition in n - i - p architecture assembled using two different doping processes of spiro-OMeTAD, as HTL, per (a) LL and (b) DD.

7.2. References

1. Xing G, Mathews N, Sun S, Lim SS, Lam YM, Grätzel M, et al. Long-range balanced electron-and hole-transport lengths in organic-inorganic CH₃NH₃PbI₃. *Science*. 2013;342(6156):344-7.
2. Park N-G. Perovskite solar cells: an emerging photovoltaic technology. *Materials Today*. 2015;18(2):65-72.
3. Lin Q, Armin A, Nagiri RCR, Burn PL, Meredith P. Electro-optics of perovskite solar cells. *Nature Photonics*. 2015;9(2):106-12.
4. Huang H, Bodnarchuk MI, Kershaw SV, Kovalenko MV, Rogach AL. Lead halide perovskite nanocrystals in the research spotlight: stability and defect tolerance. *ACS energy letters*. 2017;2(9):2071-83.
5. Das B, Liu Z, Aguilera I, Rau U, Kirchartz T. Defect tolerant device geometries for lead-halide perovskites. *Materials advances*. 2021;2(11):3655-70.
6. Song Z, McElvany CL, Phillips AB, Celik I, Krantz PW, Wathage SC, et al. A techno-economic analysis of perovskite solar module manufacturing with low-cost materials and techniques. *Energy & Environmental Science*. 2017;10(6):1297-305.
7. Mujahid M, Chen C, Hu W, Wang Z-K, Duan Y. Progress of high-throughput and low-cost flexible perovskite solar cells. *Solar RRL*. 2020;4(8):1900556.
8. Snaith HJ, Abate A, Ball JM, Eperon GE, Leijtens T, Noel NK, et al. Anomalous Hysteresis in Perovskite Solar Cells. *The Journal of Physical Chemistry Letters*. 2014;5(9):1511-5.
9. Miyasaka T. *Perovskite Photovoltaics and Optoelectronics: From Fundamentals to Advanced Applications*: John Wiley & Sons; 2021.
10. Calado P, Telford AM, Bryant D, Li X, Nelson J, O'Regan BC, et al. Evidence for ion migration in hybrid perovskite solar cells with minimal hysteresis. *Nature communications*. 2016;7(1):13831.
11. Kim S-G, Park N-G. Hysteresis of I – V Performance: Its Origin and Engineering for Elimination. *Perovskite Photovoltaics and Optoelectronics*2022. p. 215-32.
12. Unger EL, Czudek A, Kim H-S, Tress W. Chapter 4 - Current-voltage analysis: lessons learned from hysteresis. In: Pazoki M, Hagfeldt A, Edvinsson T, editors. *Characterization Techniques for Perovskite Solar Cell Materials*: Elsevier; 2020. p. 81-108.

13. Kim S-G, Li C, Guerrero A, Yang J-M, Zhong Y, Bisquert J, et al. Potassium ions as a kinetic controller in ionic double layers for hysteresis-free perovskite solar cells. *Journal of Materials Chemistry A*. 2019;7(32):18807-15.
14. Rombach FM, Haque SA, Macdonald TJ. Lessons learned from spiro-OMeTAD and PTAA in perovskite solar cells. *Energy & Environmental Science*. 2021;14(10):5161-90.
15. Snaith HJ, Grätzel M. Enhanced charge mobility in a molecular hole transporter via addition of redox inactive ionic dopant: Implication to dye-sensitized solar cells. *Applied physics letters*. 2006;89(26):262114.

Chapter 8: Synopsis

This Chapter comprises the major conclusions, contributions to original knowledge and future perspectives.

8.1. Global Conclusions

Hysteresis index (HI), and its corresponding decrease or increase, cannot be utilized as the sole metric for determining whether the perovskite solar cell (PSC) performance has improved or declined, respectively. Instead, for a correct interpretation of hysteresis and the underlying charge carrier dynamics, changes in HI must be coupled with analyzing the modifications in PV metrics between the two scan directions, under different testing conditions.

1. The absence of hysteresis under a certain testing condition does not necessarily guarantee the same trend under other scenarios. The obtained results from the perspective of both electron transport layer (ETL) and hole transport layer (HTL) conclusively proved that the divergence between current-voltage ($J-V$) curves in forward scan (FS) and reverse scan (RS) can be subject to considerable change as a result of prolonged illumination and lowered scan rate, due to the concomitant modulation of interfacial charge carrier extraction efficiency.
2. PSCs with even the optimized perovskite composition of $(\text{Cs}_5\text{Rb}_5\text{MA}_{0.15}\text{FA}_{0.75})\text{Pb}(\text{I}_{0.83}\text{Br}_{0.17})_3$ can demonstrate varying locus and magnitude of hysteresis depending on the type of charge transport layers, their configuration, conductivity and thickness as well as the corresponding interfaces within the $n-i-p$ architecture. Obtaining a PSC device with minimal hysteresis is a target contingent on optimization of all the involved components not only with respect to properties of the individual layer but also its combination with other layers.
3. The thickness of compact titania (c- TiO_2) and its combination with a supporting titania nanorod scaffold underneath, as part of ETL, can exert a significant influence over the evolution of hysteresis dynamics as a function of light soaking, applied bias and scan rate. The results showed that for PSCs with planar configuration, fill factor (FF) is significantly improved under prolonged light soaking. The stronger enhancement under FS leads to lower HI under light soaking, despite reduced open-circuit voltage (V_{OC}). Observation of

the opposite trend in FF for scaffold-based PSCs indicates detrimental light-induced electrochemical reactions at ETL/perovskite interface. Yet, the corresponding reduction in HI for these structures proved that this metric is not a reliable route to comment on hysteresis dynamics. The scan-rate dependent trends displayed a strong dependence on c-TiO₂ thickness and the ETL configuration. Thicker c-TiO₂ coating as well as the presence of a scaffold proved pivotal in sustaining FF under FS especially at 10 mV/s.

4. The appearance of an inductive hook in the low frequency part of the Nyquist plot was attributed to an inverted band alignment at the ETL/perovskite interface, enabling charge carrier injection into the perovskite layer and the corresponding non-radiative recombination to be the dominant interfacial process. This was shown to be heavily dictated by interfacial properties as well as ETL bulk conductivity. Presence of an inductive loop in the mid-frequency segment of the EIS spectra was assigned to band discontinuity at the ETL/perovskite interface, due to ionic accumulation, enhancing the rate of photoelectron scattering and hence mobility. Such a band discontinuity would, in turn, enable injection of charge from ETL into the perovskite material to be taking place at a similar time constant compared with electron transfer from perovskite into ETL, leading to the appearance of inductive loop.
5. Depending on the underlying mechanism responsible for low p -doping density of spiro-OMeTAD, the corresponding PSC can experience either a loss or gain of performance under light soaking and therefore experience a different extent and locus of hysteresis depending on the PV metrics most affected in each scan direction. Deteriorated performance under prolonged illumination was attributed to the diffusion of iodide ions from the perovskite material into the HTL, as well as generation of detrimental compounds such as Li₂O and LiF, impeding efficient charge extraction. This was manifested as propagation of low frequency semicircle on the Nyquist plot. On the other hand, enhanced performance was reflected as reduction of high frequency semicircle of EIS patterns.

8.2. Contributions to the Original Knowledge

The major contributions to original scientific knowledge achieved by the studies in Chapter 4 to Chapter 6 of this thesis, are listed in the following:

1. For the first time, a systematic study associating evolution of hysteresis locus and magnitude on J - V curves to the choice of charge transport layers, their thickness and bulk conductivity as well as modulation of interfacial conductivity for the corresponding majority charge carrier was demonstrated.
2. Through studying J - V curves at different scan rates and under light soaking as well as EIS patterns obtained before and after J - V curves, for the first time, a correlation between the c-TiO₂ layer thickness and interfacing with titania nanorod scaffold, within the ETL structure, and hysteresis dynamics in corresponding PSCs was established.
3. This thesis contains the first-ever study on the influence of the type of titania nanorod scaffold, as ETL, on the appearance and interpretation of inductive hysteresis in PSCs as probed through EIS patterns obtained under 1 Sun illumination and applied voltages exceeding V_{OC} .
4. This thesis presents, for the first time, the considerable influence of the variation in spiro-OMeTAD p -doping process from the perspective of ambient light exposure and duration on the modulation of locus and magnitude of hysteresis, as a function of light soaking and scan rate.

8.3. Future Research Direction

In the research works conducted in Chapter 4 to Chapter 6, as comprehensively summarized in Section 7.1, the transport layer- dependent evolution of hysteresis dynamics in PSCs with n - i - p architecture as a function of light soaking, scan rate and applied bias were evaluated. Some of the properties of the transport layers that were considered to explain the observed hysteresis patterns consisted of conductivity, mobility, surface coverage, crystallinity, morphology, light absorption, composition, valance band, and Fermi level position.

One aspect of the transport layers that could potentially provide an interesting pathway for future studies is the corresponding dielectric constant. This parameter can affect the electric field

distribution between the perovskite and transport layers and ultimately prove important in controlling hysteresis in PSCs. The chosen materials should be able to passivate the interface between the perovskite medium and transport layers. For materials with a high dielectric constant, the thickness should not exceed a few nm to allow for tunnelling of charge carriers through. Altogether, a correlation between thickness- k and hysteresis evolution under different testing conditions would be of interest.

Another perspective that could contribute to a more in-depth understanding, would be a fundamental study regarding the variation of doping density in both transport layers and study the resulting trends in hysteresis. Much like dielectric constant, doping density can also affect the field distribution across the device and therefore modulate hysteresis.

Although some theoretical studies have predicted the variation in PV metrics with properties such as doping density, mobility, and conductivity, a comprehensive experimental study on the thickness-dielectric constant-doping density correlation with modulation of PV metrics in both scan directions under different testing conditions is still lacking.

A.1. Supplementary Information- Chapter 4

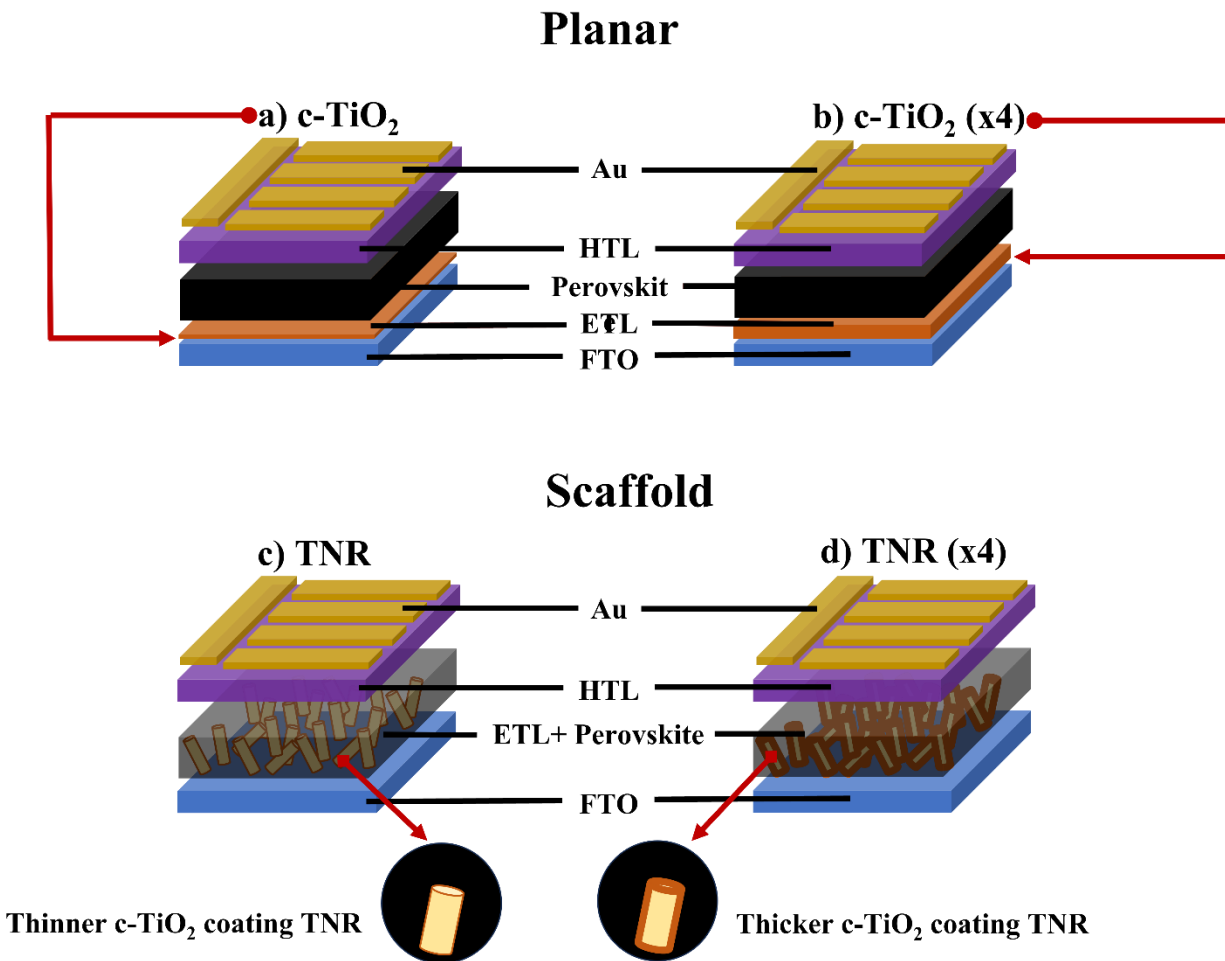


Figure A.1- 1: Schematic illustration of *n-i-p* PSCs studied in this work based on the ETL configuration: (a) planar c-TiO₂, (b) planar c-TiO₂ (x4), (c) TNR and (d) TNR(x4).

Table A.1-1: Valence band energy (E_{VB}) and work function (Φ) values of different ETL structures

	c-TiO ₂	c-TiO ₂ (x4)	TNR	TNR (x4)
IE (eV)	6.90	6.94	6.82	6.93
Φ (eV)	3.21	3.18	3.19	3.20

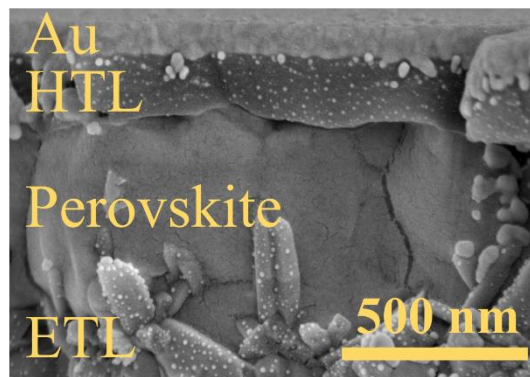


Figure A.1-2: Cross-section SEM image of the full stack PSC in *n-i-p* architecture, using TNR as ETL

Table A.1- 2: Change of PV metrics for PSCs based on Planar c-TiO₂ before and after 60 minutes light soaking. In each column, 100 and 10 denote the scan speeds of 100 mV/s and 10 mV/s, respectively. Additionally, LS stands for light soaking.

	100 RS w/o	100 FS w/o	10 RS w/o	10 FS w/o	100 RS LS	100 FS LS	10 RS LS	10 FS LS
J_{SC} (mA.cm ⁻²)	17.77	17.88	16.88	16.55	17.11	17	16	15.55
V_{OC} (V)	1.058	1.018	1.069	1.051	1.037	1.001	1.050	1.034
FF (%)	64.98	59.00	57.72	41.37	67.62	64.18	65.27	50.70
PCE (%)	12.22	10.73	10.41	7.19	11.99	10.92	10.96	8.15
HI_{PCE}	0.12		0.3		0.08		0.25	

Table A.1- 3: Change of PV metrics for PSCs based on Planar c-TiO₂ (x4) before and after 60 minutes light soaking. In each column, 100 and 10 denote the scan speeds of 100 mV/s and 10 mV/s, respectively. Additionally, LS stands for light soaking.

	100	100	10	10	100	100	10	10
	RS	FS	RS	FS	RS	FS	RS	FS
	w/o	w/o	w/o	w/o	LS	LS	LS	LS
J_{SC} (mA.cm ⁻²)	17.44	17.33	15.55	16.44	17.44	17.66	16.11	16.11
V_{OC} (V)	1.027	0.983	1.025	1.015	0.985	0.959	1.003	1.009
FF (%)	62.63	49.88	64.04	51.26	64.53	52.66	66.00	51.45
PCE (%)	11.22	8.49	10.21	8.55	11.08	8.91	10.66	8.36
HI_{PCE}	0.24		0.15		0.19		0.21	

Table A.1- 4: Change of PV metrics for PSCs based on TNR before and after 60 minutes light soaking. In each column, 100 and 10 denote the scan speeds of 100 mV/s and 10 mV/s, respectively. Additionally, LS stands for light soaking.

	100	100	10	10	100	100	10	10
	RS	FS	RS	FS	RS	FS	RS	FS
	w/o	w/o	w/o	w/o	LS	LS	LS	LS
J_{SC} (mA.cm ⁻²)	22.77	22.11	21.88	22.00	22.66	22.88	21.77	21.88
V_{OC} (V)	1.080	1.045	1.088	1.065	1.039	1.027	1.045	1.033
FF (%)	75.88	73.09	75.58	71.13	71.71	70.9	72.25	67.32
PCE (%)	18.66	16.88	17.99	16.65	16.88	16.66	16.44	15.22
HI_{PCE}	0.09		0.07		0.01		0.07	

Table A.1- 5: Change of PV metrics for PSCs based on TNR (x4) before and after 60 minutes light soaking. In each column, 100 and 10 denote the scan speeds of 100 mV/s and 10 mV/s, respectively. Additionally, LS stands for light soaking.

	100	100	10	10	100	100	10	10
	RS	FS	RS	FS	RS	FS	RS	FS
	w/o	w/o	w/o	w/o	LS	LS	LS	LS
J_{SC} (mA.cm ⁻²)	18.33	18.66	17.88	17.88	17.33	17.33	16.33	16.44
V_{oc} (V)	1.062	1.017	1.075	1.046	0.973	0.936	1.007	0.990
FF (%)	71.33	57.12	70.48	57.30	61.59	57.32	66.33	54.73
PCE (%)	13.88	10.83	13.54	10.71	10.38	9.29	10.90	8.91
HI_{PCE}	0.21		0.20		0.10		0.18	

Table A.1- 6: Valence band energy E_{VB} and Φ values of perovskite layer interfacing different ETL structures. LS stands for light soaking.

	c-TiO ₂	c-TiO ₂ (x4)	TNR	TNR (x4)
IE- Before LS (eV)	6.70	6.69	6.62	6.60
IE- After LS (eV)	6.72	6.71	6.64	6.68
Φ - Before LS (eV)	5.32	5.27	5.17	4.9
Φ - After LS (eV)	4.88	4.89	4.97	4.88

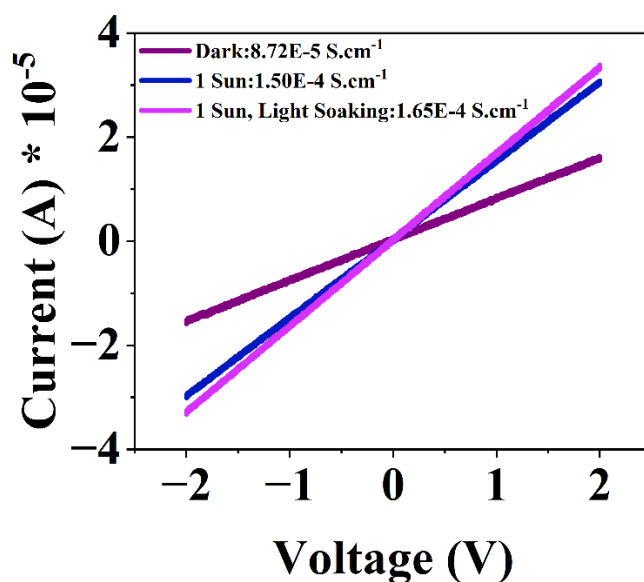


Figure A.1- 3: Results of the conductivity measurements on glass/spiro-OMeTAD film under dark, illumination and light soaking for 60 minutes.

— Planar c-TiO₂
 — Planar c-TiO₂ (x4)
 — TNR
 — TNR(x4)

Before Light Soaking

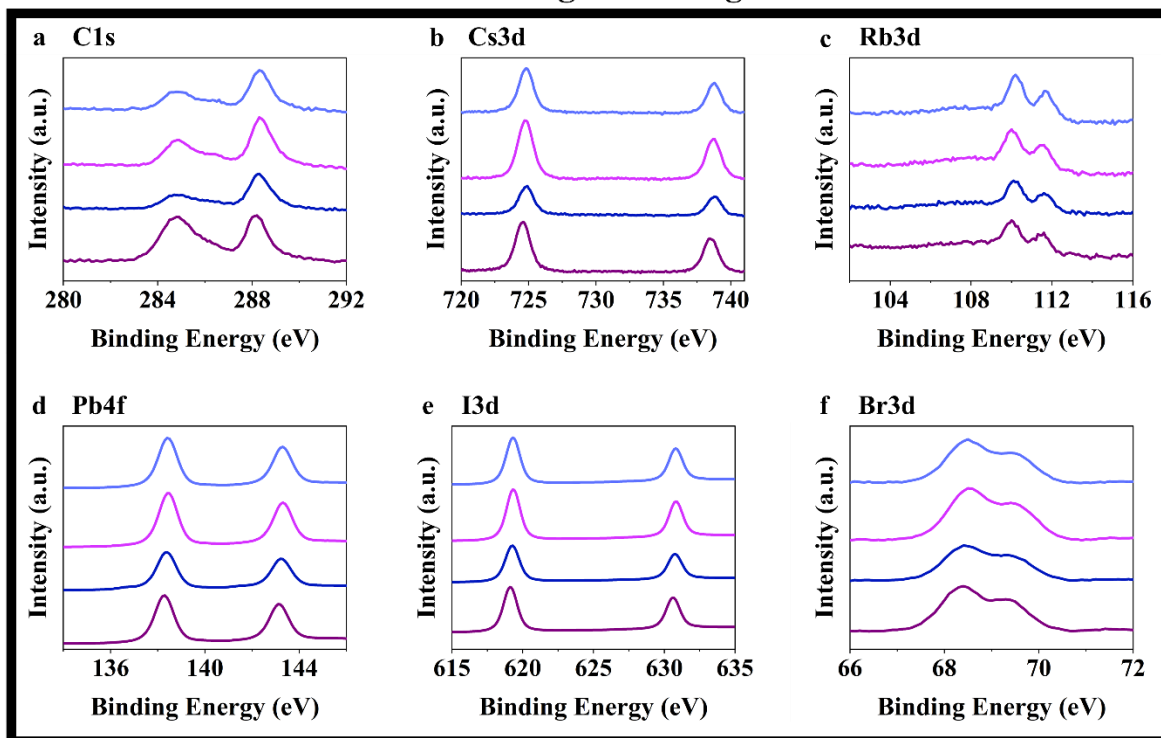


Figure A.1- 4: Comparison of the XPS core-level spectra for perovskite layers interfacing different ETLs before light soaking: (a) C1s, (b) Cs3d, (c) Rb3d, (d) Pb4f, (e) I3d and (f) Br3d.

Table A.1- 7: Summary of the values obtained through fitting the XPS spectra displayed in Figure A.1- 4.

		c-TiO ₂		c-TiO ₂ (x4)		TNR		TNR (x4)	
		BE	FWHM	BE	FWHM	BE	FWHM	BE	FWHM
		(eV)	(eV)	(eV)	(eV)	(eV)	(eV)	(eV)	(eV)
C1s	1	284.9	1.94	284.7	1.14	284.62	1.67	284.8	1.44
	2	287.6	0.77	286.1	1.42	286.4	1.58	286.39	1.5
	3	288.2	0.75	288.3	1.56	288.3	1.08	288.33	1.04
	4	288.8	0.52	290.4	0.75	289.3	1.25	289.7	1.04
Cs3d	1	724.6	1.77	724.9	1.17	724.7	1.33	724.8	1.25
	2	738.4	1.25	738.8	2.87	738.7	2.42	738.8	2.56
Rb3d	1	107.8	3.08	107.32	3.65	107.46	2.56	107.7	3.02
	2	110	1.29	110.1	0.93	110	1.06	110.2	1.06
	3	111.6	0.87	111.6	1.27	111.6	1.29	111.7	0.94
Pb4f	1	138.3	1.04	138.4	1.08	138.5	1.04	138.4	1.04
	2	143.1	0.94	143.2	0.96	143.3	0.93	143.3	0.94
I3d	1	619.1	1.19	619.3	1.23	619.3	1.19	619.3	1.21
	2	630.6	1.14	630.7	1.15	630.8	1.14	630.8	1.14
Br3d	1	68.4	0.96	68.4	1.15	68.5	0.98	68.5	1
	2	69.3	0.77	69.49	0.58	69.4	0.58	69.4	0.58

— Planar c-TiO₂
 — Planar c-TiO₂ (x4)
 — TNR
 — TNR(x4)

After Light Soaking

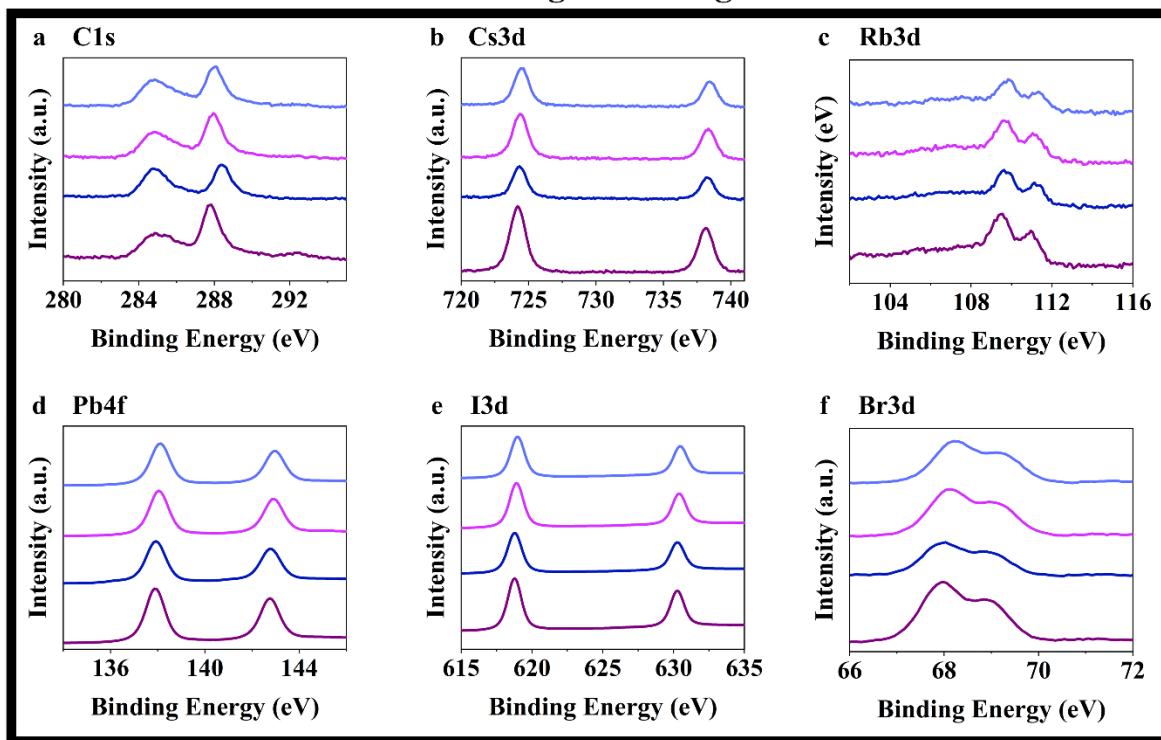


Figure A.1- 5: Comparison of the XPS core-level spectra for perovskite layers interfacing different ETLs after light soaking: (a) C1s, (b) Cs3d, (c) Rb3d, (d) Pb4f, (e) I3d and (f) Br3d.

Table A.1- 8: Summary of the values obtained through fitting the XPS spectra displayed in Figure

A.1- 5

		c-TiO ₂		c-TiO ₂ (x4)		TNR		TNR (x4)	
		BE (eV)	FWHM (eV)	BE (eV)	FWHM (eV)	BE (eV)	FWHM (eV)	BE (eV)	FWHM (eV)
C1s	1	284.9	2.14	284.7	1.58	284.8	1.75	284.8	2.19
	2	286.1	0.98	286.2	1.27	286	1.04	286.5	0.43
	3	287.9	1.48	288.3	1.42	287.9	1.42	288	1.38
	4	290	1.79	289.8	0.47	289.5	1.85	289.8	1.67
	5	292.4	1.17	-	-	-	-	-	-
Cs3d	1	724.2	2.44	724.9	1.21	724.3	1.27	724.4	1.27
	2	738.2	1.31	738.8	2	738.3	2.31	738.4	2.62
Rb3d	1	106.55	2.71	108.2	1.9	107.1	2.46	107.5	3.25
	2	109.6	1.23	110.2	1.15	109.6	1.23	109.8	1.1
	3	110.88	1.23	111.75	1.15	111	1.14	111.3	1.37
Pb4f	1	137.9	1.04	138.5	1.08	138	1.06	138.1	1.06
	2	142.8	0.94	143.3	0.98	142.9	0.96	142.9	0.96
I3d	1	618.8	1.19	619.3	1.23	618.9	1.21	618.9	1.23
	2	630.3	1.12	630.8	1.15	630.3	1.14	630.4	1.15
Br3d	1	68.9	0.58	68.6	0.98	68.1	0.96	68.1	1
	2	68	1	69.4	0.58	68.9	0.58	69	0.58

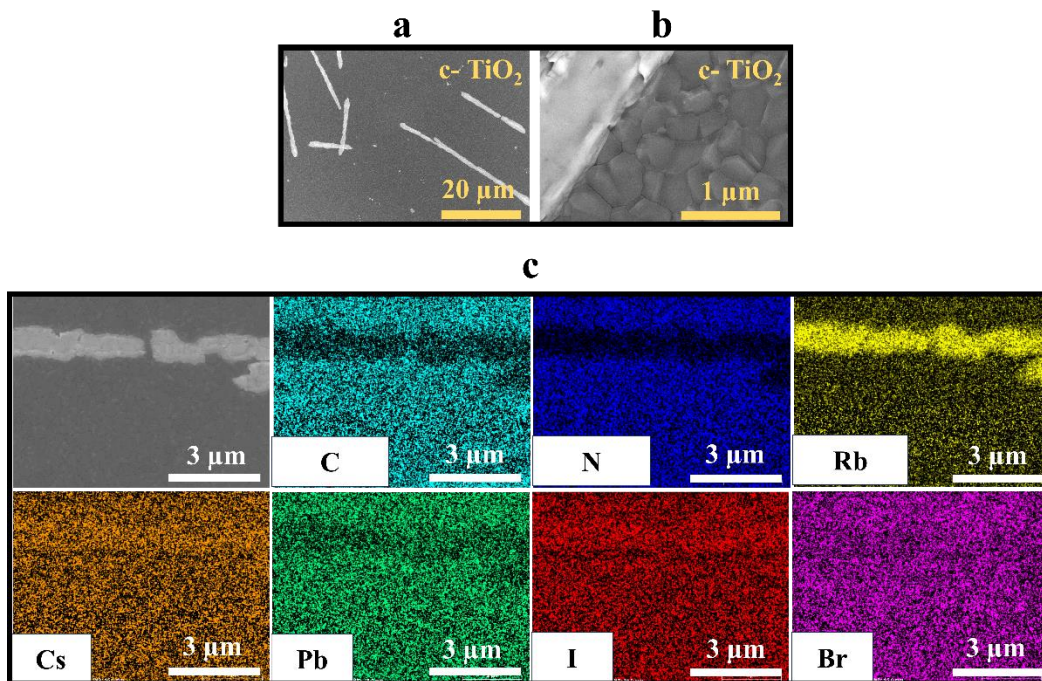


Figure A.1- 6: Top-view SEM image of the perovskite layer, interfacing c-TiO₂ as ETL, after light soaking at (a) 15k and (b) 50k magnification, as well EDS mapping (c) obtained over the precipitate displaying similar morphology and composition to Figure 4.2 a.

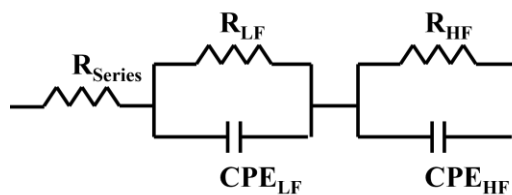


Figure A.1- 7: Equivalent circuit used in fitting the EIS patterns of Figure 4.7.

Table A.1- 9: The extracted parameters from fitting the Nyquist plots of Figure 4.7 a with the equivalent circuits of Figure A.1- 7 , for PSCs based on c-TiO₂.

	R_{Series} (Ω)	R_{LF} (Ω)	C_{LF} (F)	R_{HF} (Ω)	C_{HF} (F)
Before JV	28.15	20.32	0.02	54.47	2.49E-8
After JV	26.3	19.75	0.01	97.73	2.89E-8
LS-Before JV	22.58	20.01	0.02	39.85	2.31E-8
LS-After JV	27.34	24.08	0.01	67.23	9.10E-9

Table A.1- 10: The extracted parameters from fitting the Nyquist plots of Figure 4.7 b with the equivalent circuits of Figure A.1- 7, for PSCs based on c-TiO₂ (x4).

	R_{Series} (Ω)	R_{LF} (Ω)	C_{LF} (F)	R_{HF} (Ω)	C_{HF} (F)
Before JV	28.69	34.63	0.000585	64.78	1.61E-8
After JV	26.24	26.79	0.000498	60.82	1.39E-8
LS-Before JV	21.84	31.69	0.000566	48.97	1.90E-8
LS-After JV	22.66	34.42	0.00072	55.31	1.59E-8

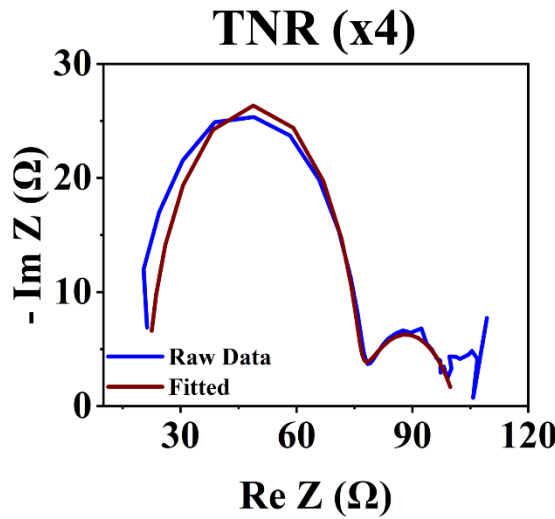
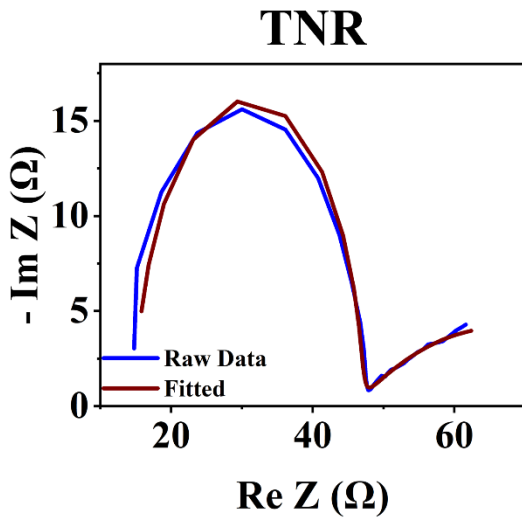
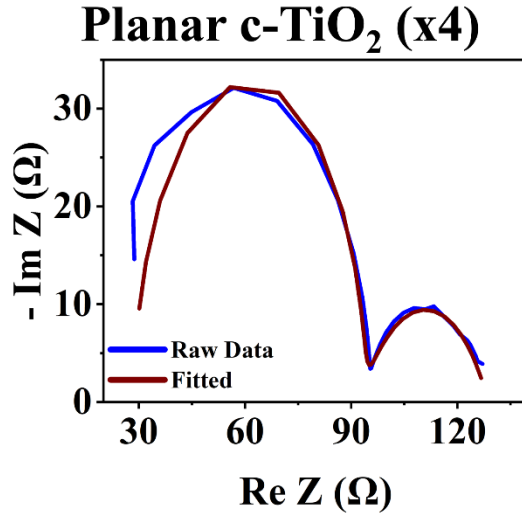
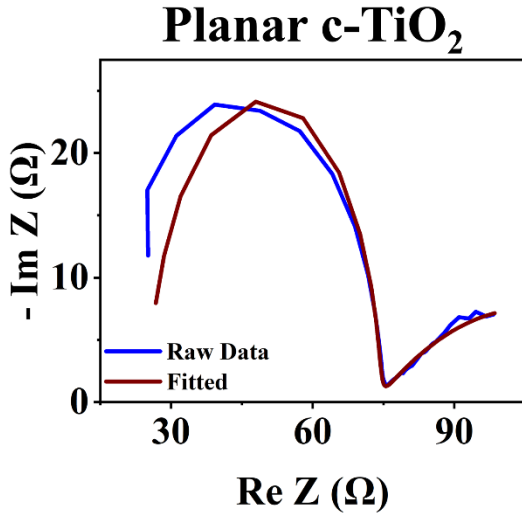
Table A.1- 11: The extracted parameters from fitting the Nyquist plots of Figure 4.7 c with the equivalent circuits of Figure A.1- 7, for PSCs based on TNR.

	$R_{Series} (\Omega)$	$R_{LF} (\Omega)$	$C_{LF} (F)$	$R_{HF} (\Omega)$	$C_{HF} (F)$
Before JV	14.66	7.97	0.012	27.65	2.89E-8
After JV	15.07	6.81	0.026	25.87	2.61E-8
LS-Before JV	15.44	11.49	0.028	28.34	2.17E-8
LS-After JV	15.74	11.24	0.034	29.94	1.54E-8

Table A.1- 12: The extracted parameters from fitting the Nyquist plots of Figure 4.7 d with the equivalent circuits of Figure A.1- 7, for PSCs based on TNR (x4).

	$R_{Series} (\Omega)$	$R_{LF} (\Omega)$	$C_{LF} (F)$	$R_{HF} (\Omega)$	$C_{HF} (F)$
Before JV	32.15	16.67	0.00462	52.35	3.51E-8
After JV	28.11	13.53	0.00361	45.76	3.78E-8
LS-Before JV	21.31	24.91	0.000858	54.61	3.83E-8
LS-After JV	21.83	27.35	0.000984	61.94	3.18E-8

Examples of EIS Fittings



A.2. Supplementary Information- Chapter 5

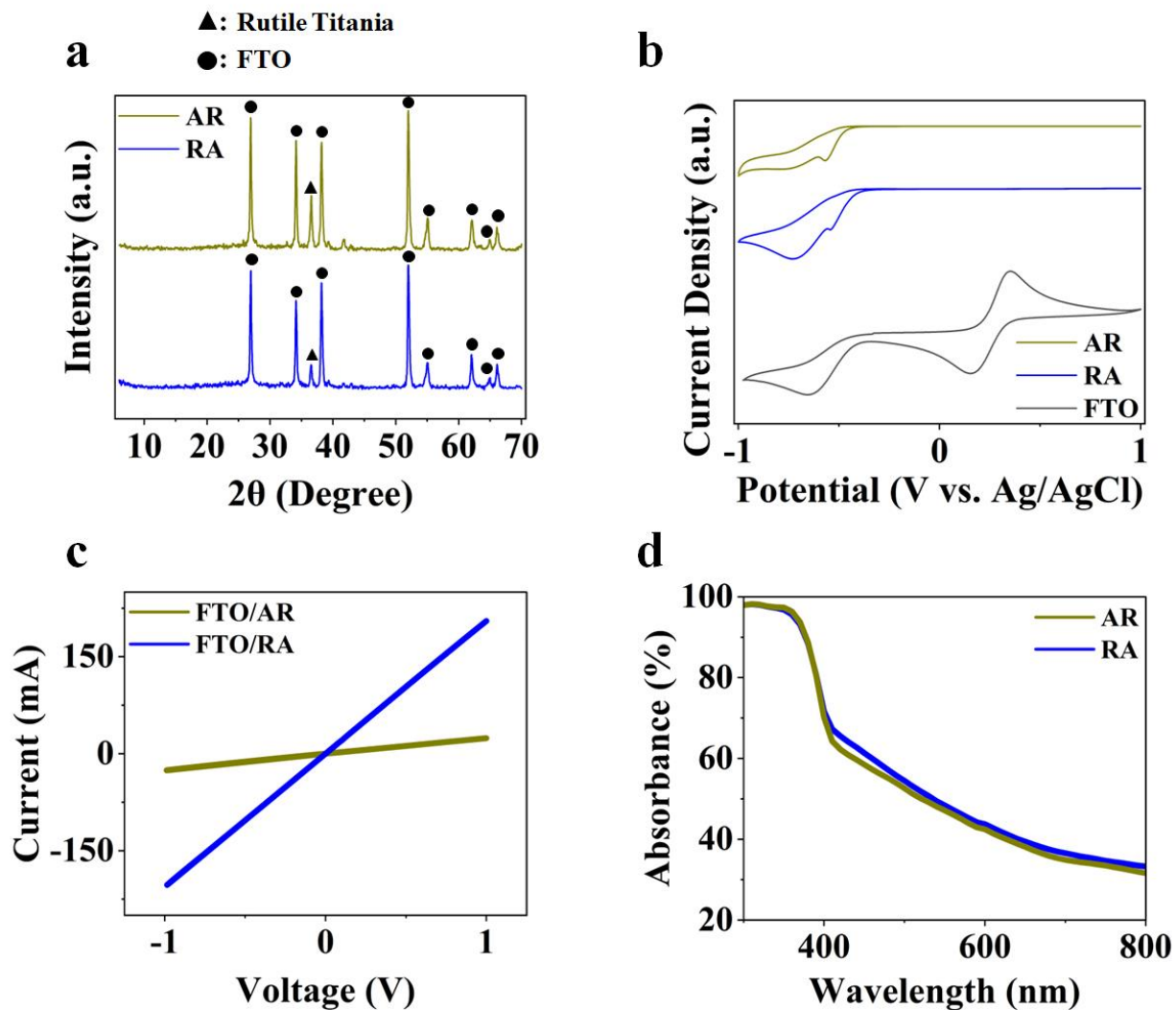


Figure A.2- 1: a) XRD patterns (peaks marked by filled triangle and circle denote diffraction from rutile titania and FTO, respectively), b) cyclic voltammetry scans, (c) effective conductivity of the ETL structures, (d) the UV-Vis absorbance spectra. All the presented results are obtained over FTO/ETL stacks.

Supplementary Note 1:

The single diffraction peak corresponding to titania conforms with the tetragonal rutile phase of P42/mmm space group (JCPDS No. 88-1175, $a=b=0.4517$ nm and $c=0.2940$ nm). This peak corresponds to the [001] direction, which is the theoretically preferential growth direction for rutile titania nanorods(1, 2). Since spray pyrolysis typically results in very thin layers(3), the corresponding peaks could not be detected in our XRD patterns. However, deposition of titania through spray pyrolysis is known to produce anatase phase(4, 5).

Supplementary Note 2:

The effective conductivity of FTO/ETL stacks is obtained from the slope associated with each trend line according to:

$$\sigma = \frac{I}{V} = \frac{I}{R}. \sigma \text{ is calculated to be } 206.05 \text{ S for FTO/RA and } 24.63 \text{ S for FTO/AR.}$$

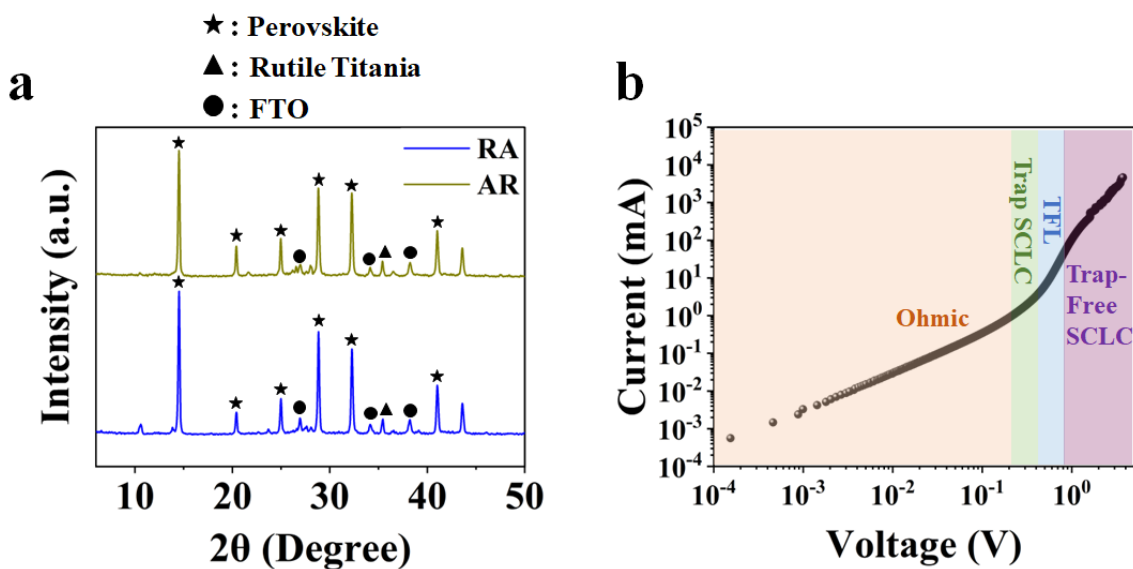


Figure A.2- 2: (a) XRD pattern of the perovskite layer infiltrating AR and RA ETL structures. (b) dark current- voltage curve for FTO/spiro-OMeTAD/Au architecture.

Table A.2- 1: PV metrics variation of PSCs based on AR and RA ETL structure for forward scan (FS) and reverse scan (RS), under 100 and 10 mV/s scan rates. The champion device in each case is highlighted in the row underneath.

	J_{sc} (RS)	V_{oc} (RS)	FF (RS)	PCE (RS)	J_{sc} (FS)	V_{oc} (FS)	FF (FS)	PCE (FS)
100 mV/s	21.16	1.017	73.36	15.81	21.16	0.97	71.39	14.67
AR	± 0.56	± 0.01	± 2.48	± 1.02	± 0.52	± 0.01	± 3.25	± 0.94
Champion Device	21.88	1.041	75.01	17.09	21.77	0.985	72.51	15.55
10 mV/s	20.98	1.035	72.44	15.75	21.01	0.999	68.97	14.49
AR	± 0.55	± 0.014	± 2.24	± 0.95	± 0.51	± 0.01	± 2.04	± 0.76
Champion Device	21.88	1.058	73.88	17.10	21	1.019	73.21	15.66
100 mV/s	21.91	1.06	72.5	16.90	21.80	1.036	69.67	15.75
RA	± 0.89	± 0.02	± 2.88	± 1.43	± 0.75	± 0.01	± 4.71	± 1.40
Champion Device	22.88	1.10	77.61	19.66	22.22	1.073	75.95	18.10
10 mV/s	21.03	1.06	72.34	16.27	21.01	1.05	65.57	14.51
RA	± 0.81	± 0.02	± 2.70	± 1.21	± 0.82	± 0.02	± 4.32	± 1.46
Champion Device	22.11	1.10	78.46	19.22	22.11	1.08	72.51	17.44

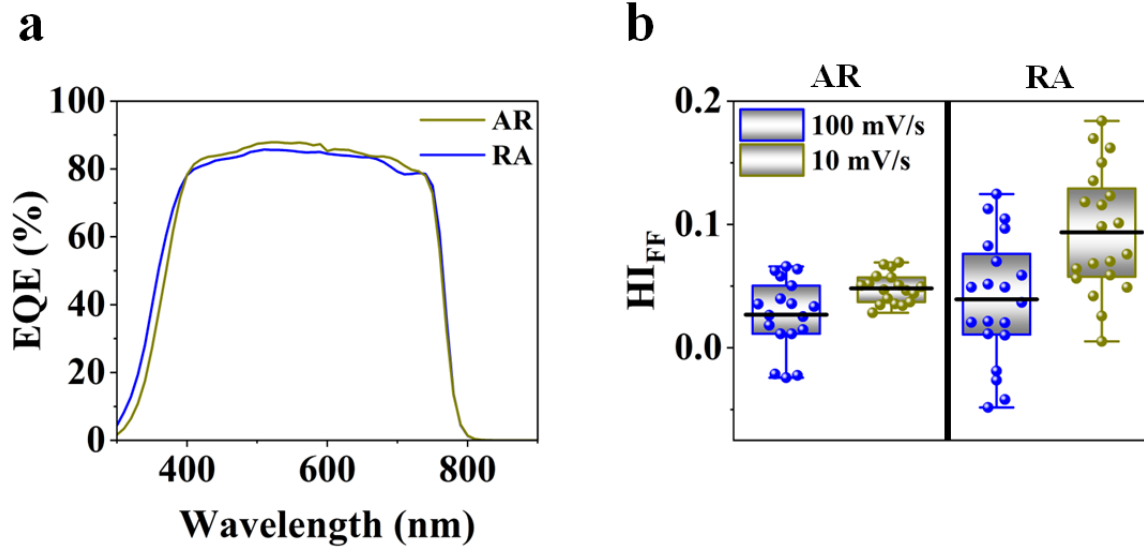


Figure A.2- 3: (a) EQE spectra obtained for PSCs based on AR and RA ETL structures (b) Distribution of HI_{FF} for PSCs based on AR and RA ETL structures.

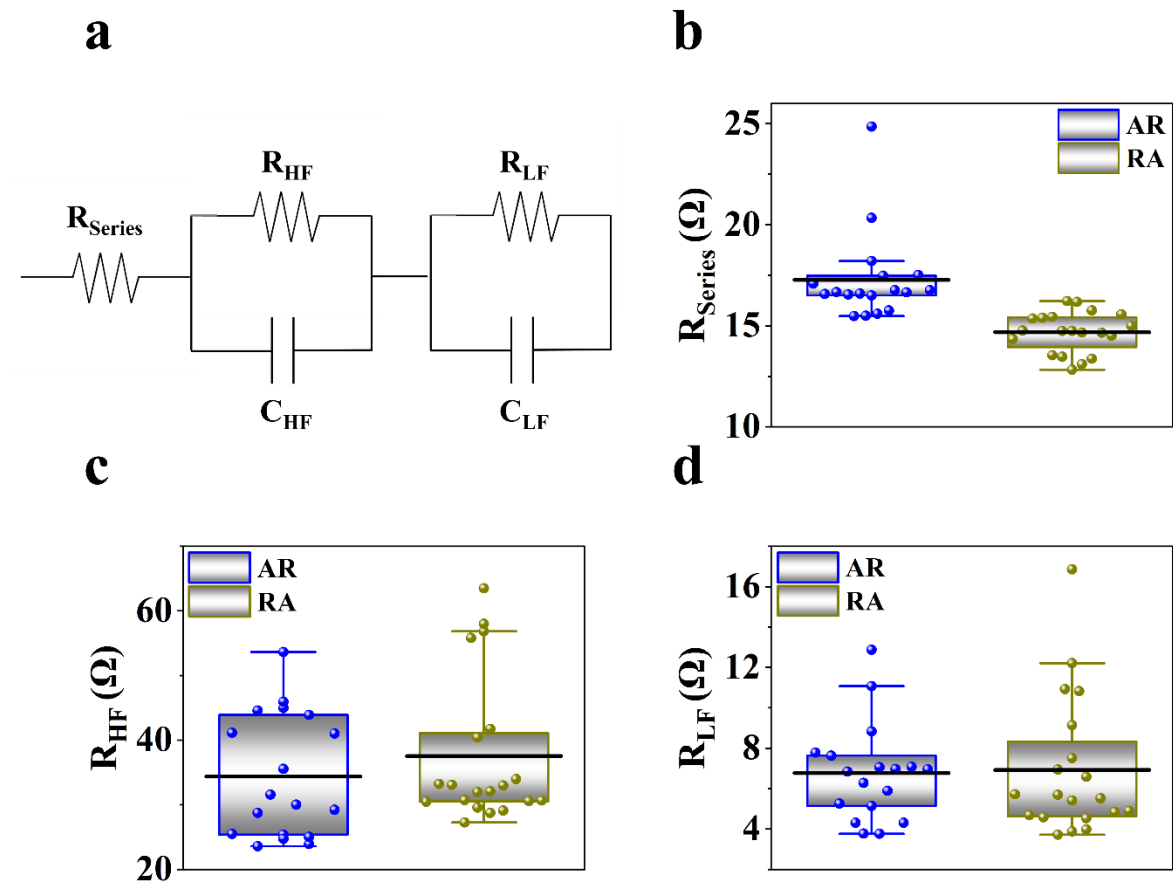


Figure A.2- 4: (a) Equivalent circuit used for fitting the EIS spectra recorded under open-circuit condition, comparison of (b) R_{Series} , (c) R_{HF} , and (d) R_{LF} for PSCs based on AR and RA.

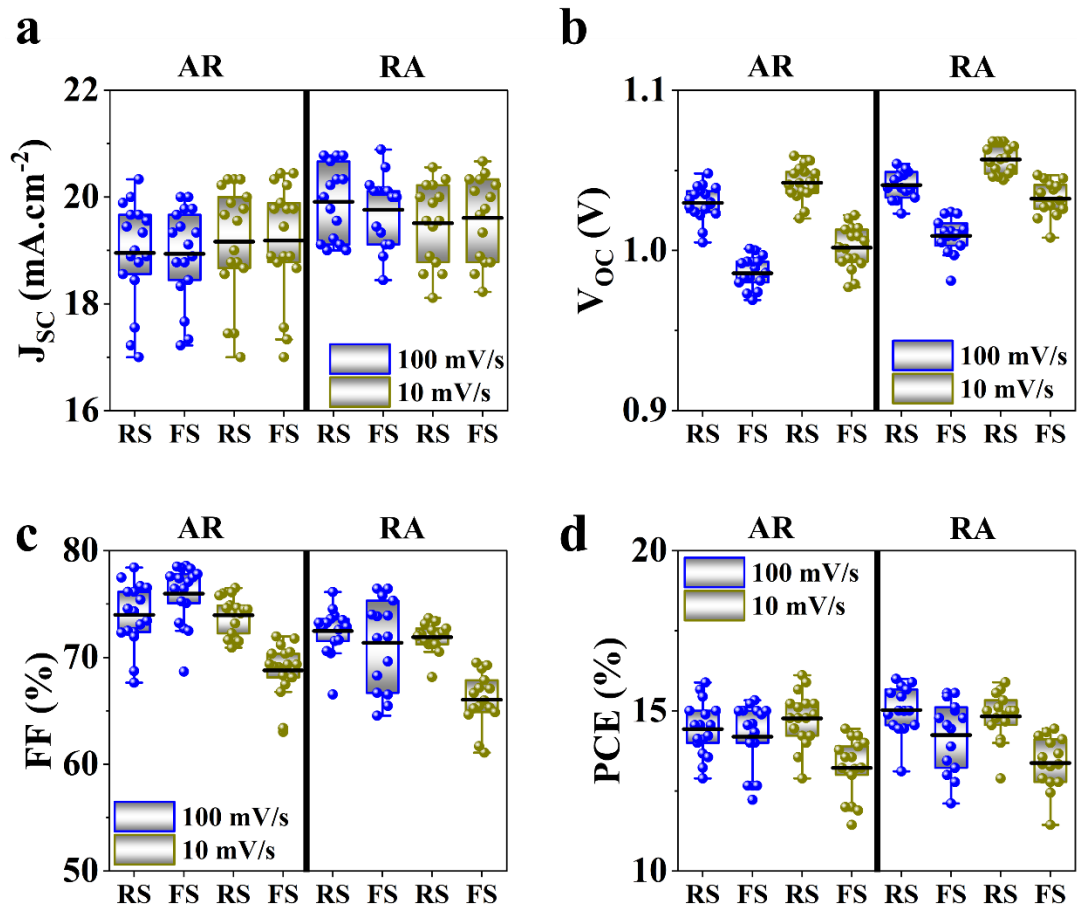
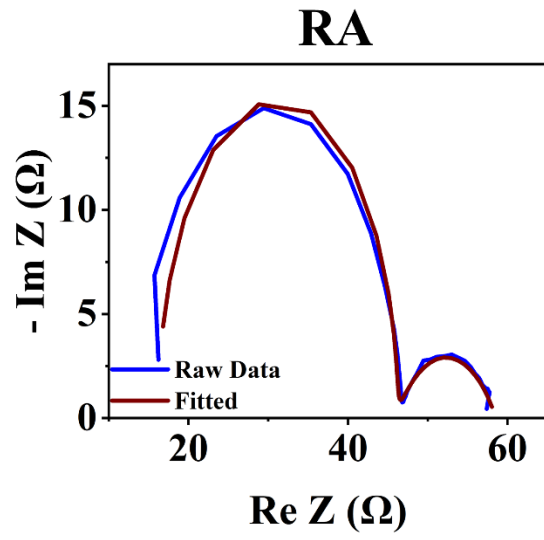
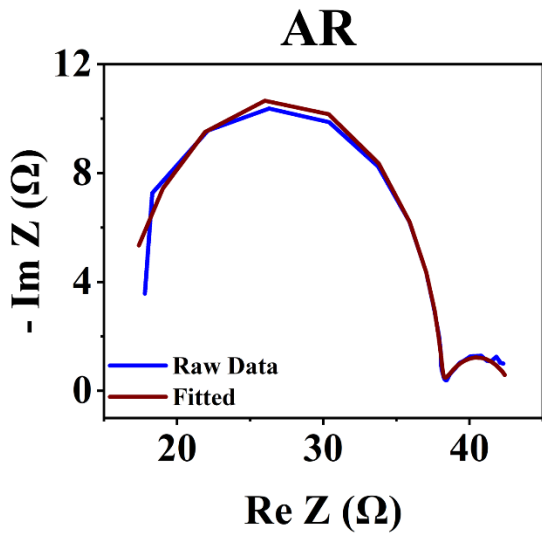


Figure A.2- 5: The distribution of PV metrics after storing the devices for 200 hours under dark and 25% relative humidity: (a) J_{SC} , (b) V_{OC} , (c) FF , (d) PCE

Table A.2- 2: PV metrics variation of PSCs based on AR and RA ETL structure for forward scan (FS) and reverse scan (RS), under 100 and 10 mV/s scan rates, corresponding to storing the devices for 200 hours under dark and 25% relative humidity. The champion device in each case is highlighted in the row underneath.

	J_{sc} (RS)	V_{oc} (RS)	FF (RS)	PCE (RS)	J_{sc} (FS)	V_{oc} (FS)	FF (FS)	PCE (FS)
100 mV/s	18.95	1.029	73.97	14.43	18.93	0.985	75.96	14.19
AR	± 0.93	± 0.01	± 2.84	± 0.81	± 0.86	± 0.009	± 2.67	± 0.991
Champion Device	19.33	1.048	78.41	15.88	19.66	0.992	77.58	15.22
10 mV/s	19.16	1.042	73.94	14.76	19.18	1.001	68.95	13.21
AR	± 1.05	± 0.01	± 1.71	± 0.8	± 1.04	± 0.01	± 2.45	± 0.87
Champion Device	19.88	1.059	76.49	16.11	19.88	1.009	71.97	14.44
100 mV/s	19.91	1.04	72.43	15.02	19.76	1.009	71.37	14.24
RA	± 0.67	± 0.008	± 2.13	± 0.72	± 0.65	± 0.01	± 4.04	± 1.06
Champion Device	20.77	1.046	73.61	15.99	20.11	1.012	76.43	15.55
10 mV/s	19.51	1.056	71.89	14.82	19.60	1.032	66.04	13.37
RA	± 0.73	± 0.008	± 1.298	± 0.723	± 0.76	± 0.01	± 2.38	± 0.79
Champion Device	20.55	1.063	72.71	15.88	20.33	1.03	68.96	14.44

Examples of EIS Fittings



A.3. Supplementary Information- Chapter 6

Table A.3- 1: Conductivity values obtained for HTL films doped according to processes of Table 6.1, under dark as well as 1 Sun illumination.

	Dark Conductivity (S.cm ⁻¹)* E-5	1 Sun Conductivity (S.cm ⁻¹) *E-4
LL	2.26 ± 0.18	0.6 ±0.08
LD	4.88 ±0.21	1.04 ±0.1
DL	5.09 ±0.23	1.11 ±0.05
DL(15)	8.64 ±0.27	1.54 ±0.06
Pristine	0.14 ±0.01	0.33 ±0.01

Table A.3- 2: Change of PV metrics for the LL process before and after 60 minutes of light soaking. In each column, 100 and 10 denote the scan speeds of 100 mV/s and 10 mV/s, respectively.

	100 RS w/o	100 RS 60min	100 FS w/o	100 FS 60min	10 RS w/o	10 RS 60min	10 FS w/o	10 FS 60min
<i>J_{sc}</i> (mA.cm⁻²)	19.88	19.55	19.88	19.44	19.22	19.33	19.44	19.44
<i>V_{oc}</i> (V)	0.964	0.918	0.896	0.839	0.995	0.951	0.972	0.911
<i>FF</i> (%)	63.16	61.58	55.30	52.44	59.83	52.45	57.55	51.74
<i>PCE</i> (%)	12.10	11.05	9.85	8.55	11.44	9.64	10.87	9.16

Table A.3- 3: Change of PV metrics for the LD process before and after 60 of minutes light soaking. In each column, 100 and 10 denote the scan speeds of 100 mV/s and 10 mV/s, respectively.

	100	100	100	100	10	10	10	10
	RS	RS	FS	FS	RS	RS	FS	FS
	w/o	60min	w/o	60min	w/o	60min	w/o	60min
J_{sc} (mA.cm ⁻²)	18.55	18.77	18.66	18.77	18.33	18.33	18.55	18.44
V_{oc} (V)	1.056	1.032	1.028	0.997	1.071	1.045	1.060	1.023
FF (%)	72.01	72.24	70.06	73.59	72.43	73.07	72.30	73.01
PCE (%)	14.10	13.99	13.43	13.77	14.21	13.99	14.21	13.77

Table A.3- 4: Change of PV metrics for the DL process before and after 60 minutes of light soaking. In each column, 100 and 10 denote the scan speeds of 100 mV/s and 10 mV/s, respectively.

	100	100	100	100	10	10	10	10
	RS	RS	FS	FS	RS	RS	FS	FS
	w/o	60min	w/o	60min	w/o	60min	w/o	60min
J_{sc} (mA.cm ⁻²)	19	19.22	19.11	18.88	19.33	18.55	19.33	18.66
V_{oc} (V)	0.986	0.977	0.944	0.931	1.005	0.983	0.978	0.950
FF (%)	69.81	68.20	64.05	62.55	65.76	65.17	62.28	59.52
PCE (%)	13.07	12.80	11.55	10.99	12.77	11.88	11.77	10.55

Table A.3- 5: Change of PV metrics for the DL(15) process before and after 60 of minutes light soaking. In each column, 100 and 10 denote the scan speeds of 100 mV/s and 10 mV/s, respectively.

	100 RS w/o	100 RS 60min	100 FS w/o	100 FS 60min	10 RS w/o	10 RS 60min	10 FS w/o	10 FS 60min
J_{sc} (mA.cm ⁻²)	21.00	20.22	20.77	20.77	21.11	20.22	21	20.33
V_{oc} (V)	1.041	1.001	0.993	0.976	1.059	1.025	1.019	1.00
FF (%)	77.47	68.93	74.73	64.54	76.03	68.61	73.21	66.66
PCE (%)	16.93	13.95	15.41	13.08	16.99	14.21	15.66	13.55

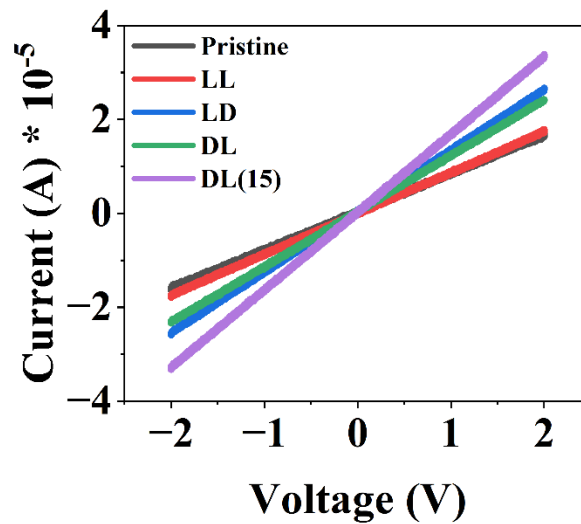


Figure A.3- 1: Comparison of conductivity trends, performed after 60 minutes of light soaking.

Table A.3- 6: Conductivity values obtained for HTL films doped according to processes of Table 6.1, after 60 minutes of light soaking.

	1 Sun Conductivity (S.cm ⁻¹) *E-4
LL	0.81 ±0.03
LD	1.18 ±0.08
DL	1.16 ±0.05
DL(15)	1.63 ±0.01
Pristine	0.82 ±0.01

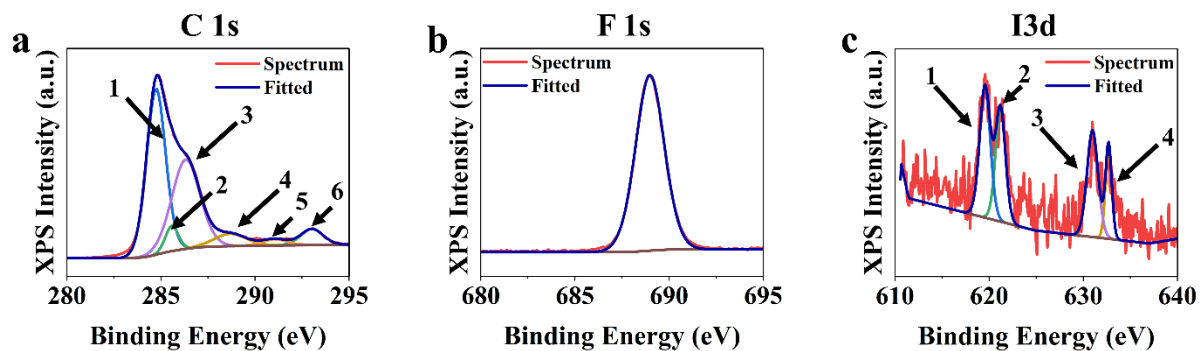


Figure A.3- 2: Fittings of XPS spectra obtained over FTO/ETL/perovskite/HTL films prior to light soaking.

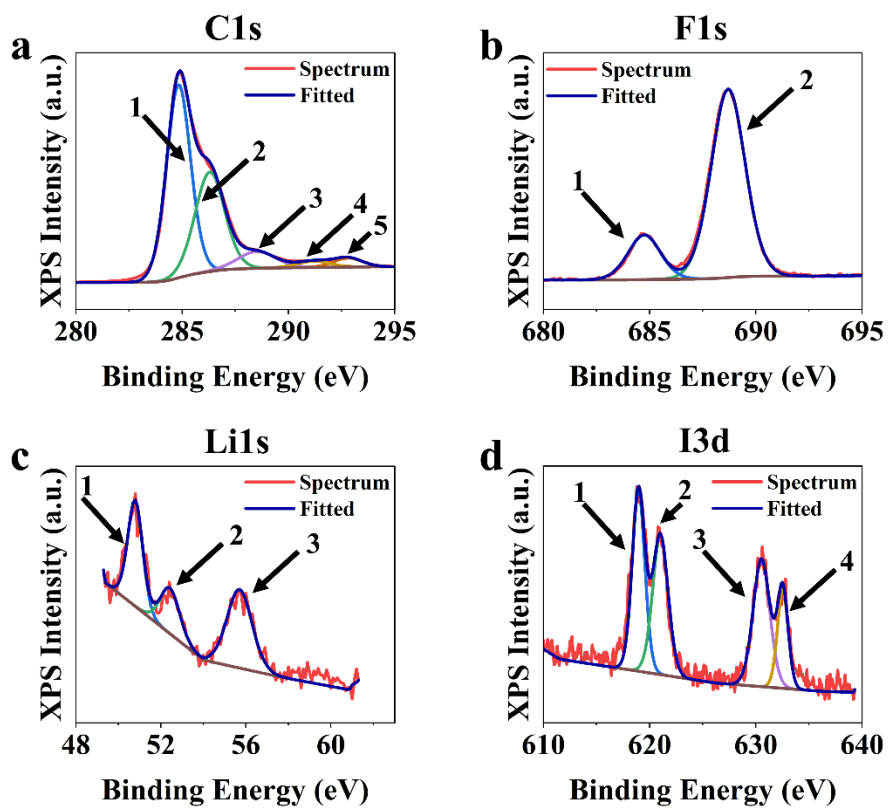


Figure A.3- 3: Fittings of XPS spectra obtained over FTO/ETL/perovskite/HTL films after light soaking for 60 minutes.

Table A.3- 7: Binding energy (BE) and full-width half maximum (FWHM) values obtained from XPS spectra of the HTL films deposited over FTO/ETL/perovskite stacks, prior to light soaking for 60 minutes.

		LL		LD		DL		DL(15)	
		BE (eV)	FWHM (eV)	BE (eV)	FWHM (eV)	BE (eV)	FWHM (eV)	BE (eV)	FWHM (eV)
C1s	1	284.74	1.23	284.80	1.27	284.80	1.20	284.72	1.30
	2	285.58	0.84	285.70	0.84	285.63	0.82	285.58	0.72
	3	286.32	1.81	286.45	1.63	286.41	1.78	286.38	1.76
	4	288.68	2.07	288.62	1.98	288.98	1.96	288.48	1.10
	4*	-	-	-	-	-	-	289.68	1.50
	5	291.06	1.59	290.93	1.68	291.28	1.62	291.28	1.36
	6	293.02	1.44	293.02	1.52	293.18	1.48	292.98	1.44
F1s		688.98	1.86	688.93	1.85	688.95	1.83	688.93	1.80
I3d	1	619.55	1.38	619.26	1.69	619.34	1.84	619.62	1.80
	2	621.21	1.29	621.23	1.80	621.18	1.28	621.32	1.17
	3	630.98	1.57	630.87	1.24	631.04	1.89	631.12	1.17
	4	632.69	0.8	632.59	1.14	632.88	1.14	632.58	1.10

Table A.3- 8: Binding energy (BE) and full-width half maximum (FWHM) values obtained from XPS spectra of the HTL films deposited over FTO/ETL/perovskite stacks, after light soaking for 60 minutes.

		LL		LD		DL		DL(15)	
		BE	FWHM	BE	FWHM	BE	FWHM	BE	FWHM
		(eV)	(eV)	(eV)	(eV)	(eV)	(eV)	(eV)	(eV)
C1s	1	284.83	1.38	284.83	1.32	284.75	1.24	284.81	1.22
	2	286.30	1.70	286.21	1.74	286.10	1.82	286.13	2.10
	3	288.50	2.16	288.40	2.84	288.48	3.20	288.62	1.33
	4	291.20	1.88	291.20	1.58	291.52	1.42	291.40	1.56
	4*	-	-	-	-	-	-	289.62	1.89
	5	292.80	1.64	292.90	1.50	293.00	1.38	293.00	1.40
F1s	1	684.75	1.86	684.80	2.69	685.04	1.78	684.96	1.78
	2	688.70	1.00	688.70	1.52	688.86	2.09	688.77	1.92
Li1s	1	50.79	0.85	51.03	0.84	50.99	1.31	50.85	1.32
	2	52.43	1.12	-	-	52.86	1.03	52.80	1.31
	3	55.70	1.44	55.75	1.41	55.85	1.49	55.80	1.28
I3d	1	618.96	1.46	619.50	2.17	619.28	1.83	619.10	1.46
	2	621.01	1.78	621.50	1.12	621.29	1.34	621.11	1.85
	3	630.53	1.92	631.00	1.50	630.80	1.82	630.63	1.86
	4	632.53	1.24	632.70	1.12	632.70	1.28	632.60	1.30

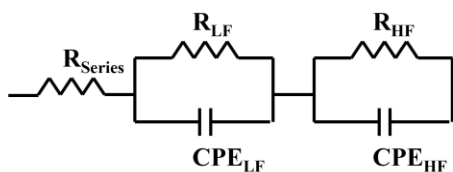
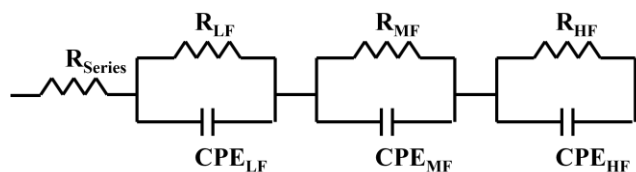
a**b**

Figure A.3- 4: Equivalent circuits utilized for fitting the Nyquist plots of Figure 6.6, with R_{Series} being the series resistance. Equivalent circuits shown in (a) and (b) include elements in low frequency (LF), as well as high frequency (HF). The equivalent circuit displayed in (b) has additional mid frequency (MF) components.

Table A.3- 9: The extracted parameters from fitting the Nyquist plots of Figure 6.6 with the equivalent circuits of Figure A.3- 4. The unit for the extracted resistance and CPE values are Ohm (Ω) and Farad (F), respectively.

	LL	LD	DL	DL(15)
R_{Series}- Before	23.89	19.81	26.68	17.08
R_{Series}- After	22.23	18.40	21.12	16.77
R_{HF}- Before	57.16	64.4	104.1	28.3
R_{HF}- After	47.28	36.93	38.22	23.16
R_{MF}- Before	51.61	-	-	-
R_{MF}- After	47.27	-	6.004	10.78
R_{LF}- Before	28.07	17.01	21.69	9.33
R_{LF}- After	43.4	16.83	40.13	43.69
CPE_{HF}- Before	7.51E-9	1.78E-8	6.10E-8	1.39E-8
CPE_{HF}- After	5.08E-9	7.24E-8	1.55E-8	2.07E-8
CPE_{MF}- Before	0.059	-	-	-
CPE_{MF}- After	0.066	-	0.0029	0.0011
CPE_{LF}- Before	0.01	0.004	0.0059	0.0035
CPE_{LF}- After	0.009	0.002	0.027	0.078

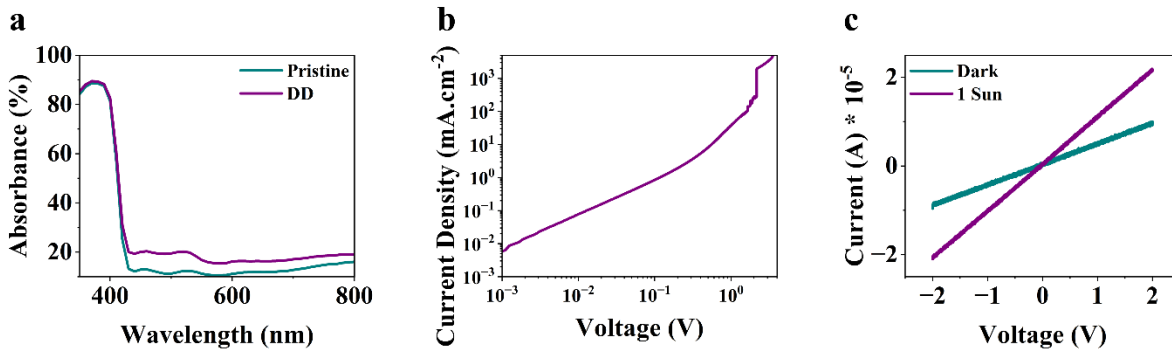


Figure A.3- 5: Characterization results obtained from DD doping condition: (a) comparison of UV-Vis spectra for DD and pristine spiro-OMeTAD, (b) SCLC trend, and (c) evolution of conductivity for DD from dark to 1 Sun illumination

Table A.3- 10: Conductivity values obtained for spiro-OMeTAD film doped according to DD process.

	Dark Conductivity (S.cm ⁻¹)	1 Sun Conductivity (S.cm ⁻¹)
DD	2.84E-5	6.49E-5

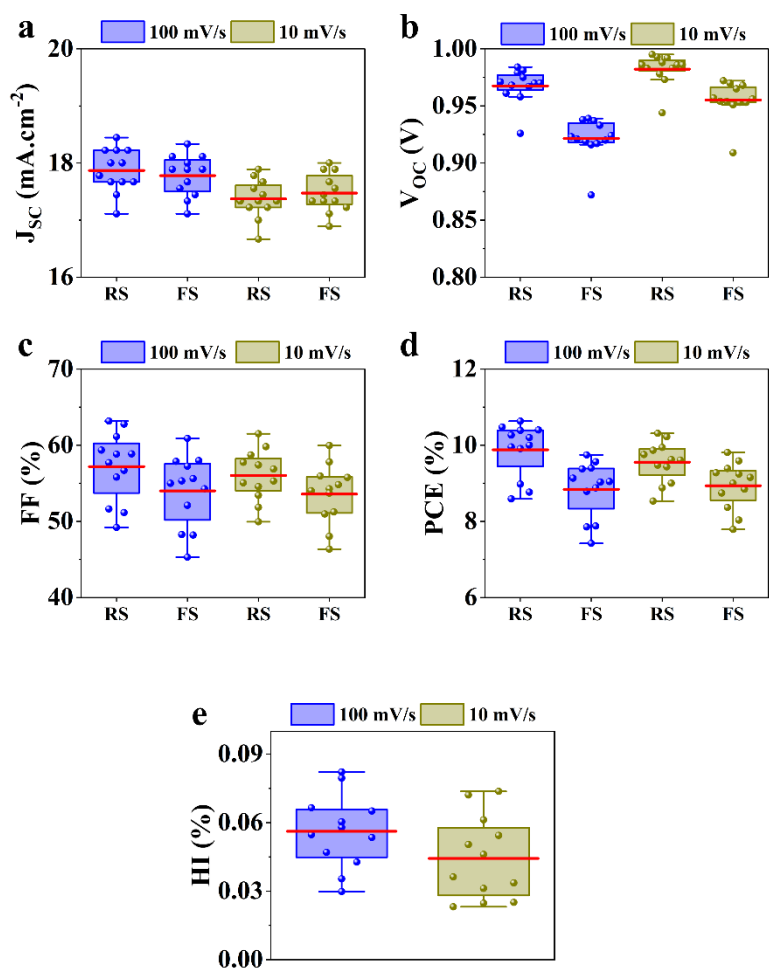


Figure A.3- 6: Distribution of PV metrics obtained for PSCs using DD as the doping process for spiro-OMeTAD films: (a) J_{SC} , (b) V_{OC} , (c) FF, and (d) PCE, as well as (e) HI values, under scan rates of 100 and 10 mV/s.

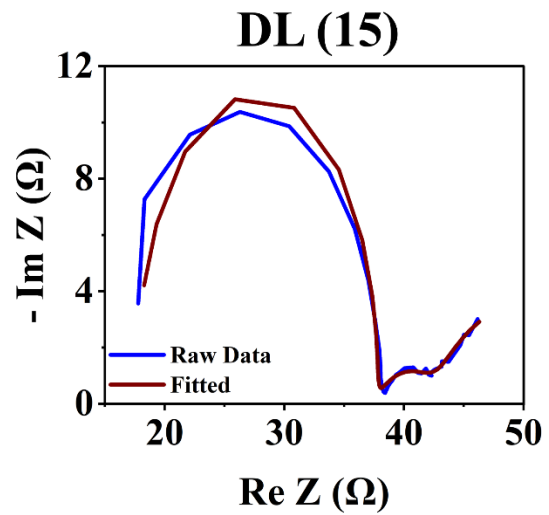
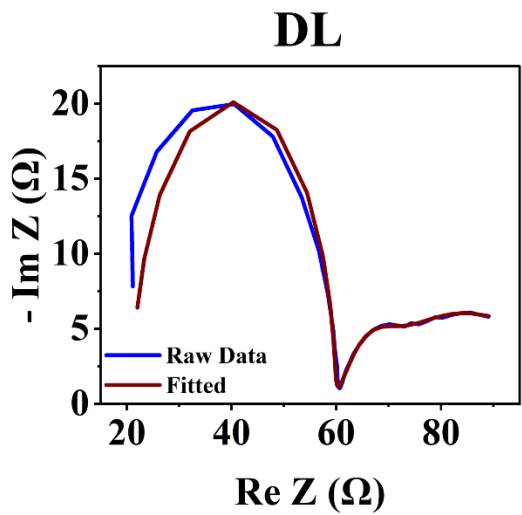
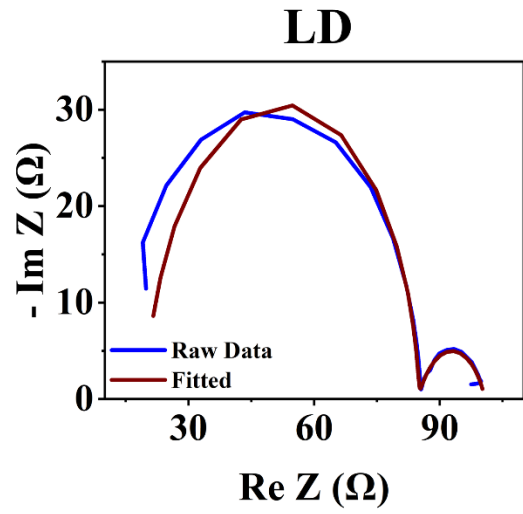
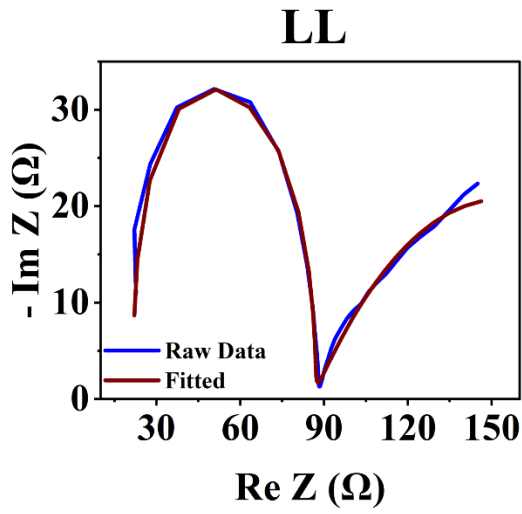
Table A.3- 11: Change of PV metrics for the DD process before and after 60 minutes light soaking. In each column, 100 and 10 denote the scan speeds of 100 mV/s and 10 mV/s, respectively. Additionally, RS and FS indicate forward and reverse scan directions, respectively.

	100	100	100	100	10	10	10	10
	RS	RS	FS	FS	RS	RS	FS	FS
	w/o	60min	w/o	60min	w/o	60min	w/o	60min
J_{sc} (mA.cm ⁻²)	15.55	16.22	15.55	15.77	15.88	16.11	16.00	16.11
V_{oc} (V)	0.991	0.986	0.951	0.930	1.007	1.00	0.983	0.961
FF (%)	43.02	65.36	37.59	69.81	42.64	65.17	34.84	57.26
PCE (%)	6.62	10.45	5.55	10.23	6.81	10.49	5.47	8.86

Table A.3- 12: The extracted parameters from fitting the Nyquist plots for DD with the equivalent circuits of Figure A.3- 4b. The unit for the extracted resistance and CPE values are Ohm (Ω) and Farad (F), respectively.

	DD
R_{Series}- Before	27.11
R_{Series}- After	23.28
R_{HF}- Before	295.3
R_{HF}- After	36.78
R_{MF}- Before	26.17
R_{MF}- After	27.04
R_{LF}- Before	59.17
R_{LF}- After	11.46
CPE_{HF}- Before	3.67E-8
CPE_{HF}- After	4.94E-8
CPE_{MF}- Before	0.00324
CPE_{MF}- After	0.00403
CPE_{LF}- Before	7.41E-10
CPE_{LF}- After	3.68E-10

Examples of EIS Fittings



A.4. References

1. Kalb J, Dorman JA, Siroky S, Schmidt-Mende LJC. Controlling the spatial direction of hydrothermally grown rutile TiO₂ nanocrystals by the orientation of seed crystals. *Crystals* 2019;9(2):64.
2. Wisnet A, Betzler SB, Zucker RV, Dorman JA, Wagatha P, Matich S, et al. Model for hydrothermal growth of rutile wires and the associated development of defect structures. *Crystal Growth & Design*. 2014;14(9):4658-63.
3. Saliba M, Matsui T, Seo JY, Domanski K, Correa-Baena JP, Nazeeruddin MK, et al. Cesium-containing triple cation perovskite solar cells: improved stability, reproducibility and high efficiency. *Energy Environ Sci*. 2016;9(6):1989-97.
4. Conde A, Guerrero M, Castillo N, Soto AB, Fragoso R, Cabanas-Moreno J. TiO₂ anatase thin films deposited by spray pyrolysis of an aerosol of titanium diisopropoxide. *Thin Solid Films*. 2005;473:68-73.
5. Raj AME, Agnes V, Bena Jothy V, Ravidhas C, Wollschläger J, Suendorf M, et al. Spray deposition and property analysis of anatase phase titania (TiO₂) nanostructures. *Thin Solid Films*. 2010;519(1):129-35.

